UCTEA Turkish Chamber of Civil Engineers

Teknik Dergi

Technical Journal

Volume 32 Issue 4 July 2021

TEKNİK DERGİ PUBLICATION PRINCIPLES

Teknik Dergi is a scientific and technical journal indexed by the Science Citation Index Expanded. Annually six issues are published, three in Turkish in the months of January, May and September, three in English in March, July and November. Its main principles of publication are summarized below:

1. Articles reporting original scientific research and those reflecting interesting engineering applications are accepted for publication. To be classified as original, the work should either produce new scientific knowledge or add a genuinely new dimension to the existing knowledge or develop a totally new method or substantially improve an existing method.
2. Articles reporting preliminary results of scientific studies and those which do not qualify as full articles but provide useful information for the reader can be considered for publication as technical notes.
3. Discussions received from the readers of the published articles within three months from publication are reviewed by the Editorial Board and then published together with the closing remarks of the author.
4. Manuscripts submitted for publication are evaluated by two or three reviewers unknown to the authors. In the light of their reports, final decision to accept or decline is taken by the Editorial Board. General policy of the Board is to get the insufficient manuscripts improved in line with the reviewers' proposals. Articles that fail to reach the desired level are declined. Reasons behind decisions are not declared.
5. A signed statement is taken from the authors, declaring that the article has not been published as a "journal article or book chapter". In case the Editorial Board is in the opinion that the article has already been published elsewhere with minor changes or suspects plagiarism or a similar violation of ethics, then not only that article, but none of the articles of the same authors are published.
6. Papers reporting works presented as conference papers and developed further may be considered for publication. The conference it was presented to is given as a footnote in the first page.
7. Additionally, a document signed by all authors, transferring the copyright to UCTEA Chamber of Civil Engineers is submitted together with the manuscript.

UCTEA Turkish Chamber of Civil Engineers

Teknik Dergi

Technical Journal

Volume 32 Issue 4 July 2021

UCTEA *(TMMOB)*
Turkish Chamber of Civil Engineers *(İnşaat Mühendisleri Odası)*
Necatibey St. No: 57, Kızılay 06440 Ankara, Turkey
Tel: +90.312.294 30 00 - Faks: +90.312.294 30 88
E-mail: imo@imo.org.tr - www.imo.org.tr

Publisher *(Sahibi)*:
Taner YÜZGEÇ
On behalf of UCTEA Turkish Chamber of Civil Engineers

Administrative Officer *(Yazı İşleri Müdürü)*:
Özer AKKUŞ

Volume 32 - Issue 4 - July 2021 *(Cilt 32 - Sayı 4 - Temmuz 2021)*
Published bi-monthly. Local periodical. *(İki ayda bir yayınlanır, yerel süreli yayın)*
Date of Print: 1 July 2021 *(Baskı Tarihi: 1 Temmuz 2021)*
Number of copies: 1.000 *(1.000 adet basılmıştır)*

ISSN: 1300-3453

Teknik Dergi is indexed by
- Science Citation Index Expanded
- Scopus
- Journal Citation Reports / Science Edition
- Engineering Index
- Concrete Abstracts (American Concrete Institute)
- National Technical Information Service (US NTIS)
- CITIS
- Ulrich's International Periodical's Directory
- TR Index

Teknik Dergi is a peer reviewed open access periodical publishing papers of original research and interesting practice cases. It addresses both the research community and the practicing engineers.

Printed by *(Baskı)*:
Boyut Tanıtım Matbaa Basım Yayın San. Tic. Ltd. Şti.
İvedik Organize Sanayi 1354. Cad. Fora İşmerkezi No: 138/18 - Yenimahalle /Ankara
Tel: 0.312.385 72 12 - Faks: 0.312.385 72 13

UCTEA Turkish Chamber of Civil Engineers
Teknik Dergi

Reviewers:

This list is renewed each year and includes reviewers who served in the last two years of publication.

Süleyman ADANUR
Ali Mardani AGHABAGLOU
Ayda Şafak AĞAR ÖZBEK
Perviz AHMEDZADE
Ragıp AKBAŞ
Sami Oğuzhan AKBAŞ
Şeref Doğuşcan AKBAŞ
Rıfat AKBIYIKLI
Özge AKBOĞA KALE
Hüseyin AKBULUT
Burcu AKÇAY ALDANMAZ
Cihan Taylan AKDAĞ
Adem AKPINAR
Muhammet Vefa AKPINAR
Atakan AKSOY
Hafzullah AKSOY
Hakan AKSU
Tülay AKSU ÖZKUL
Büşra AKTÜRK
Güzin AKYILDIZ ALÇURA
Zuhal AKYÜREK
Uğurhan AKYÜZ
Sadık ALASHAN
Cenk ALHAN
Sinan ALTIN
Selim ALTUN
Adlen ALTUNBAŞ
Ahmet Can ALTUNIŞIK
Yalçın ALVER
Egemen ARAS
Ergin ARIOĞLU
Yalçın ARISOY
Musa Hakan ARSLAN
Deniz ARTAN İLTER
Şenay ATABAY
Ali Osman ATAHAN
Hakan Nuri ATAHAN
Abdullah AVEY
Ersin AYDIN
İsmail AYDIN
Mustafa Tamer AYVAZ
Ela BABALIK
Can Elmar BALAS
Selim BARADAN
Türkay BARAN
Bekir Oğuz BARTIN
Eyüp Ensar BAŞAKIN
Cemal BAŞARAN
Özgür BAŞKAN
İdris BEDİRHANOĞLU
Niyazi Özgür BEZGİN
Senem BİLİR MAHÇİÇEK
Ahmet BİRİNCİ
İlknur BOZBEY
Zafer BOZKUŞ
Atıl BULU
Burcu BURAK BAKIR
Halil İbrahim BURGAN
Yusuf CALAYIR
Erdem CANBAY
Zekai CELEP
Cihan CENGİZ
Halim CEYLAN
Hüseyin CEYLAN
Ömer CİVALEK
Özgür ÇAKIR
Melih ÇALAMAK
Gülben ÇALIŞ
Erkan ÇELEBİ
Kutay ÇELEBİOĞLU
Tevfik Kutay ÇELEBİOĞLU
Ahmet Ozan ÇELİK
Oğuz Cem ÇELİK
Osman Nuri ÇELİK
Semet ÇELİK
Hilmi Berk ÇELİKOĞLU
Mecit ÇETİN
Gökhan ÇEVİKBİLEN
Mesut ÇİMEN
Safiye Feyza ÇİNİCİOĞLU
Erdal ÇOKÇA
Şevket ÇOKGÖR
İsa ÇÖMEZ
Atilla DAMCI
Yakup DARAMA
Osama M.F. DAWOUD
Özgür DEĞERTEKİN
Abdullah DEMİR
Cem DEMİR
Uğur DEMİR
Ender DEMİREL
Mehmet Cüneyd DEMİREL
Fatih DİKBAŞ
Seyyit Ümit DİKMEN
İrem DİKMEN TOKER
Ali Ersin DİNÇER
Selim DÜNDAR
Nurhan ECEMİŞ ZEREN
Alper ELÇİ
Şebnem ELÇİ
Muhammet Emin EMİROĞLU
Hakan ERDEM
Sinan Turhan ERDOĞAN
Esin ERGEN PEHLEVAN
Ayşen ERGİN
Gökmen ERGÜN
Ebru ERİŞ
Bülent ERKMEN
Barış ERKUŞ
Esra Ece ESELLER BAYAT
Tuğba ESKİŞAR TEFÇİ
Burak FELEKOĞLU
Okan FISTIKOĞLU
Abdullah GEDİKLİ
Ergun GEDİZLİOĞLU
Mohammad Ali GHORBANİ
Ömer GİRAN
Konuralp GİRGİN
Zehra Canan GİRGİN
Ilgın GÖKAŞAR
Çağlar GÖKSU
Serdar GÖKTEPE
Fazlı Erol GÜLER
Hakan GÜLER
Ilgın GÜLER
Gürkan GÜNAY
Taylan GÜNAY
Abdurrahman GÜNER
Samet GÜNER
Ülker GÜNER BACANLI
Oğuz GÜNEŞ
Mehmet Şükrü GÜNEY
Tuba GÜRBÜZ
BÜYÜKKAYIKÇI
Melike GÜREL
İbrahim GÜRER
Aslı Pelin GÜRGÜN
Gürşans GÜVEN IŞIN
Iman HAJİRASOULİHA
Soner HALDENBİLEN
Murat HAMDERİ
Ufuk HANCILAR
Ingo A. HANSEN
Mustafa HATİPOĞLU
Nejan HUVAJ SARIHAN
Metin HÜSEM
Zeynep IŞIK
Hande IŞIK ÖZTÜRK
Sabriye Banu İKİZLER
Ragıp İNCE
Eren İNCİ
Pınar İNCİ KOÇAK
Sedat KABDAŞLI
Volkan KAHYA
Mehmet Rifat KAHYAOĞLU
Volkan KALPAKÇI
Alper KANYILMAZ
Murat KARACASU
Tanay KARADEMİR
Halil KARAHAN
Ali KARAİPEKLİ
Cenk KARAKURT
Mustafa KARAŞAHİN
Zülküf KAYA
Mustafa Kubilay KELEŞOĞLU
Mustafa Erol KESKİN
Havvanur KILIÇ
İsmail Emrah KILIÇ
Sami And KILIÇ
Fahriye KILINÇKALE
Ufuk KIRBAŞ
Veysel Şadan Özgür KIRCA
Güven KIYMAZ
Young Hoon KİM
Gökhan KİRKİL
Salih KOÇAK
Niyazi Uğur KOÇKAL
Önder KOÇYİĞİT
Mehmet Melih KOŞUCU
Baha Vural KÖK
Mete KÖKEN
Fuat KÖKSAL
Şerife Yurdagül KUMCU
Murat KURUOĞLU
Akif KUTLU
Semih KÜÇÜKARSLAN
Abdullah KÜRKÇÜ
Hilmi LUŞ
Kasım MERMERTAŞ
Mehmet Murat MONKUL
Hamid MORTEZAİE
Yetiş Şazi MURAT
Sepanta NAİMİ
Öcal NECMİOĞLU
Sinan Melih NİĞDELİ
Elif OĞUZ
Didem OKTAY
Derviş Volkan OKUR
Volkan OKUR
Mehmet Hakkı OMURTAG
Engin ORAKDÖĞEN
Şeref ORUÇ
Akın ÖNALP
Halil ÖNDER
Jülide ÖNER
Bihrat ÖNÖZ
Mustafa ÖZAKÇA
Bergüzar ÖZBAHÇECİ
Ceyhun ÖZÇELİK
Gökhan ÖZDEMİR
İlker ÖZDEMİR
Osman Nuri ÖZDEMİR
Halit ÖZEN
Murat ÖZEN
Pelin ÖZENER
Cem ÖZER
Hasan ÖZER
Serkan ÖZGEN
Eren Arman ÖZGÜVEN
Hakkı Oral ÖZHAN
Yener ÖZKAN
M. Hulusi ÖZKUL
Gülen ÖZKULA
Turan ÖZTURAN
Hasan Tahsin ÖZTÜRK
Mustafa ÖZUYSAL
Polat ÖZYİĞİT
Gülizar ÖZYURT
TARAKÇIOĞLU
Onur PEKCAN
Elişan Filiz PİROĞLU
Cengiz POLAT
Selim PUL
Selçuk SAATÇİ
Selman SAĞLAM
Mehmet SALTAN
İlyas SARIBAŞ
Afşin SARITAŞ
Altuğ SAYGILI
Serdar SELAMET
Senem SEYİS
Alper SEZER
Faiz Uddin Ahmed SHAİKH
Osman SİVRİKAYA
Behzad SOLTANBEİGİ
Celal SOYARSLAN
Serdar SOYÖZ
Tayfun Altuğ SÖYLEV
Aleksandar STEVANOVİC
Erol ŞADOĞLU
Güvenç ŞAHİN
Remzi ŞAHİN
Yuşa ŞAHİN
Mustafa ŞAHMARAN
Nermin ŞARLAK
Ömer Lütfi ŞEN
Burak ŞENGÖZ
Aynur ŞENSOY ŞORMAN
Okan ŞİRİN
Ali Arda ŞORMAN
Ali Ünal ŞORMAN
Özcan TAN
Gülüm TANIRCAN
Kürşat TANRIÖVEN
Serhan TANYEL
Yüksel TAŞDEMİR
Kerem TAŞTAN
Gökmen TAYFUR
İlker TEKİN
Beytullah TEMEL
Egemen TEOMETE
Serdal TERZİ
Berrak TEYMUR
H. Onur TEZCAN
Hüseyin Onur TEZCAN
Mesut TIĞDEMİR
Şahnaz TİĞREK
Salih TİLEYLİOĞLU
Vedat TOĞAN
Onur Behzat TOKDEMİR
Cengiz TOKLU
Nuray TOKYAY
Ali TOPAL
İlker Bekir TOPÇU
Cem TOPKAYA
Selçuk TOPRAK
Kamile TOSUN FELEKOĞLU
Gökçe TÖNÜK
Nursu TUNALIOĞLU
Kağan TUNCAY
Gürsoy TURAN
Ö. Tuğrul TURAN
Cüneyt TÜZÜN
Latif Onur UĞUR
Mehmet Fevzi UĞURYOL
Berna UNUTMAZ
Volkan Emre UZ
Nihal UZCAN ERATLI
İbrahim Mert UZUN
Deniz ÜLGEN
Mehmet ÜLKER
Cüneyt VATANSEVER
Syed Tanvir WASTI
Nazmiye YAHNİOĞLU
Cem YALÇIN
Mehmet Cem YALÇIN
Aslı YALÇIN DAYIOOĞLU
Ahmet Cevdet YALÇINER
İsmail Özgür YAMAN
Arcan YANIK
Mert Yücel YARDIMCI
Ufuk YAZGAN
Anıl YAZICI
Halit YAZICI
Kasım YENİGÜN
Seda YEŞİLMEN
İrem Zeynep YILDIRIM
Mehmet YILDIRIMOĞLU
Osman YILDIZ
Çetin YILMAZ
Fatih YILMAZ
Koray Kamil YILMAZ
Mehmet YILMAZ
Murat YILMAZ
Mustafa Tuğrul YILMAZ
Veysel YILMAZ
Yüksel YILMAZ
Fatih YONAR
Recep YURTAL
İsmail YÜCEL
Ömer YÜKSEK
Ercan YÜKSEL
Yeliz YÜKSELEN AKSOY
Ahmet Şahin ZAİMOĞLU
Abdullah Can ZÜLFİKAR

UCTEA Turkish Chamber of Civil Engineers

Teknik Dergi

Volume: 32 Issue: 4 July 2021

CONTENTS

Foreword

SOME CHANGES AND THEIR STATISTICAL REFLECTIONS

Teknik Dergi (Technical Journal), the open access scientific and technical journal of the Turkish Chamber of Civil Engineers (TCCE), publishes articles reflecting original research studies and novel contributions to practice of civil engineering.

The main purpose of Teknik Dergi is to inform the Turkish and international civil engineering communities, especially the members of TCCE, about the current scientific and technical developments, thus to contribute to the improvement of civil engineering practices. In other words, to serve as a bridge between the world of research and the world of practice.

Initially, only articles in Turkish were accessible in print. In 2004, "online" access was also made available. Starting from 2017, all articles accepted for publication have been assigned a DOI. Thus, the accepted articles became effectively published worldwide. In 2018, two fundamental statutory changes were made in order to improve international recognition. Since then, Teknik Dergi is bilingual and publishes six issues per year, three in Turkish and three in English.

After the changes introduced in 2017-2018

- Until 2017, the number of articles submitted for consideration per year gradually increased from 40 to 80. After statutory changes there has been an abrupt increase in the number of articles to the range of 80 to 160 per year. Furthermore, based on the limited data available, rate of increase of the submitted articles has risen too.
- Before 2017, on the average 20 articles were published per year. After 2017, this number gradually increased and in 2020 it was almost doubled to 40.
- The number of articles in each issue gradually increased from 5 to 6, on the average. The change from 4 issues per year to 6 issues per year, effective 2018 and onward, was apparently the reason for keeping the number of articles per issue within the range of 5-6.
- The duration of the manuscript review processes decreased steadily from 450 days on the average in the pre-change period to an average of 230 days in 2020.

Technical Journal strives unceasingly to improve the quality of its service in view of the demands without compromising its main principles.

Prof. A. Metin Ger
On behalf of the Editorial Board

Teknik Dergi, 2021 10919-10945, Paper 618

Discharge Coefficients for Radial-Gated Ogee Spillways by Laboratory Data and by *Design of Small Dams*

Tefaruk HAKTANIR[1]
Mohammed A. KHALAF[2]

ABSTRACT

Using the measured data on 15 laboratory models in USA, six models and one prototype in Turkey, the discharge coefficients (*C*'s) of radial-gated ogee spillways for various gate openings and lake water surface elevations are computed. Comparison of these *C*'s for 22 spillways with the ones given by Figure 9-31 of *Design of Small Dams* does not show close agreements. It is determined that *C* depends on both the angle Θ and the ratio d/H_1, rather than Θ only where *d* and H_1 are the gate opening and the upstream head, and statistically significant regression equations are computed individually for each one of 22 cases.

Keywords: Discharge coefficient for partially-opened radial-gated spillways.

1. INTRODUCTION

Design of Small Dams [1, 2] is a classical reference book for design of dams all over the world including Turkey [e.g. 3, 4, 5, 6]. Some dams have free-flow (un-gated) ogee flood spillways while some others have ogee spillways equipped with radial gates. The apex of a radial-gated ogee spillway is lower than the maximum operation elevation (top of the active storage), and the upper tip of the gates at closed position is usually about 1 m or so above top of the active storage. During routing of a flood the recommended operation policy is to lift all of the gates simultaneously and to have the same gate opening for all. At first glance, the total cost of a radial-gated spillway may seem to be more than that of an un-gated spillway because of the additional cost of the radial gates, their trunnion pins and hoisting mechanisms. However, a much longer free-flow spillway is needed to attain the same maximum water surface elevation (WSE) during routing of the design flood. This is because the crest elevation of the free-flow spillway necessarily equals the top of the active storage allowing a small net head for the spilling discharge. And, the excavation work needed to place the longer free-flow spillway will increase its cost. In short, comparing the relevant costs of both

Note:
- This paper has been received on March 15, 2019 and accepted for publication by the Editorial Board on January 7, 2020.
- Discussions on this paper will be accepted by September 30, 2021.
- https://doi.org/10.18400/tekderg.540640

1 Nuh Naci Yazgan University, Department of Civil Engineering, Kayseri, Turkey
thaktanir@nny.edu.tr - https://orcid.org/0000-0002-8111-4557

2 Erciyes University, Department of Civil Engineering, Kayseri, Turkey -
mohammed077080812@gmail.com - https://orcid.org/0000-0002-8111-4557

types of spillways may lead to a radial-gated one as the optimum design. There are many dams equipped with radial-gated spillways, and the routing of the critical design flood hydrograph or any other less intense hydrograph from a dam having a radial-gated ogee spillway is important both for design and for real life operations.

The methods for computing the spilled discharge over the partially-opened radial-gated ogee spillways are different in both the previous and recent editions of *Design of Small Dams* [1, 2]. The subsection 201 of the second edition of *Design of Small Dams* [1] gives the equation (a dimensionally homogeneous one) to compute this discharge as:

$$Q = (2/3)\cdot(\sqrt{2g})\cdot C\cdot L_e\cdot(H_1^{3/2} - H_2^{3/2}) \tag{1}$$

where, g is the acceleration of gravity, C is the discharge coefficient, L_e is the effective spillway length, H_1 and H_2 are defined as: "*H_1 and H_2 are the total heads (including the velocity head of approach) to the bottom and top of the orifice, respectively*." [1], and Q is the discharge. Figure 257 of the 1973 edition of *Design of Small Dams*, whose copy is given here as Figure 1, depicts the terms in equation (1) and presents a curve for the C coefficient as a function of the ratio d/H_1, where d is the vertical gate opening ($d = H_1 - H_2$). The effective length L_e is shorter than the net length due to the contraction effects on the discharging water during entrance into the spillway bays caused by the piers and the approach embankments, and it is computed by [1]:

$$L_e = L - 2\cdot(N_p\cdot k_p + k_a)\cdot H \tag{2}$$

where, L is the net length of the spillway crest excluding the piers, N_p is the number of piers on the crest, k_p is the pier contraction coefficient, k_a is the approach abutments contraction coefficient, and H is the total head above the spillway apex. Three values for k_p and k_a are suggested as 0, 0.01, 0.02, and 0, 0.1, 0.2, respectively, depending on the geometrical shapes of pier noses and abutment headwalls [1].

In subsection 9.16 of the third edition of *Design of Small Dams* [2] however, a different equation is given for discharge over a radial-gated ogee spillway while the gates are partially opened, which is:

$$Q = C\cdot D\cdot L\cdot(2g\cdot H)^{1/2} \tag{3}$$

where, C is the discharge coefficient, D is the shortest distance between the gate lip and the spillway crest curve, L is the net length (not the effective length) of the spillway crest, and H is the vertical difference between the total head just upstream of the gate and the center of the gate opening. C in equation (3) is different from the C in equation (1), and in this study we symbolize C in equation (1) by *C-73* and C in equation (3) by *C-87*. Equation (3) also is dimensionally homogeneous. Figure 9-31 on page 379 of the third edition of *Design of Small Dams* [2], whose copy is given here as Figure 2, depicts the terms in equation (3) and presents a curve defining *C-87* as a function of the angle Θ, which is the angle between the tangent to the gate lip and the tangent to the crest curve at the point nearest to the lip.

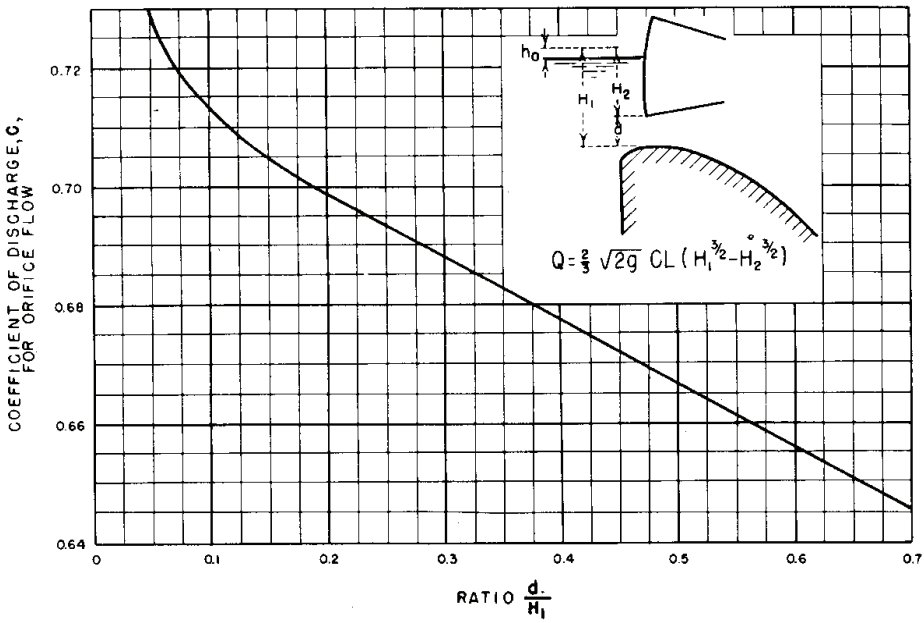

Figure 1 - Copy of Figure 257 of the second edition of 'Design of Small Dams' [1] depicting the terms in equation (1) and giving the curve for discharge coefficient C-73 as a function of the ratio d/H_1.

Equation (3) and Figure 9-31 of *Design of Small Dams* [2] are originally due to *Hydraulic Design Criteria, Volume 2, Tainter Gates on Spillway Crests, Sheets 311-1 to 311-5* by US Army Corps of Engineers [7]. Figure 9-31 of *Design of Small Dams* [2] is a replica of 'Hydraulic Design Chart 311-1' in reference no.7, whose copy is given here as Figure 3. The symbols of β, Go, and B are used in 'Hydraulic Design Chart 311-1' [7] for the symbols of Θ, *D*, and *L* in Figure 9-31 of *Design of Small Dams* [2], respectively. Otherwise, the diagrams and the numbers on both axes of these two figures are exactly the same. There are two curves in these figures, and the longer one is for those spillways where the gate seat is a little downstream from the apex, and the shorter curve is for those spillways where the gate lip is seated on the apex. 'Hydraulic Design Chart 311-1' (Figure 3 here) presents the plotted points about the best-fit curves also, which were obtained from the data taken on six cases [7].

As seen in Figure 3, the longer curve is derived using the measured data on spillways of two laboratory models and of three actual dams. It is clearly visible that the plotted points for those five cases around the best-fit curve exhibits considerable noises for Θ's smaller than 72º. The second curve in 'Hydraulic Design Chart 311-1' is derived as the best-fit curve to the points measured in only one laboratory model study, meaning a general curve is suggested which is derived out of one laboratory model only, even not an actual size prototype [7]. We believe, the relationship for such a crucial coefficient as *C-87* for the case of the gate lip being seated some distance downstream from the apex having been derived using only five cases of measured data may not reflect a true generalization, and inclusion of many more measured

data may improve that relationship. Similarly, for the case of the gate seat being on the apex, data from one laboratory model is definitely too few, and the second curve in Figure 3 cannot represent the general case. This has been the main theme of our study, and accordingly we have aimed to enrichen these two relationships using many more relevant data obtained on many laboratory models performed by renowned facilities in USA and in Turkey.

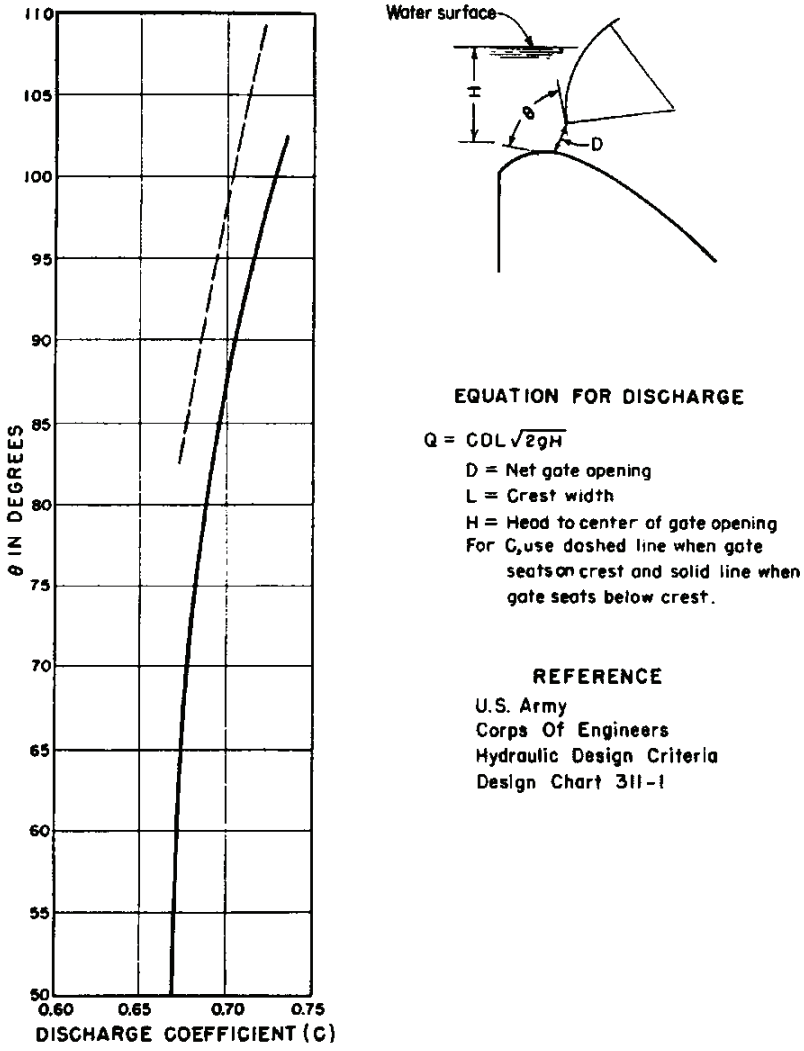

Figure 9-31.—Discharge coefficient for flow under gates. 103-D-1875.

Figure 2 - Copy of Figure 9-31 of the third edition of 'Design of Small Dams' [3] depicting the terms in equation (3) and giving the curve for discharge coefficient C-87 as a function of the angle Θ.

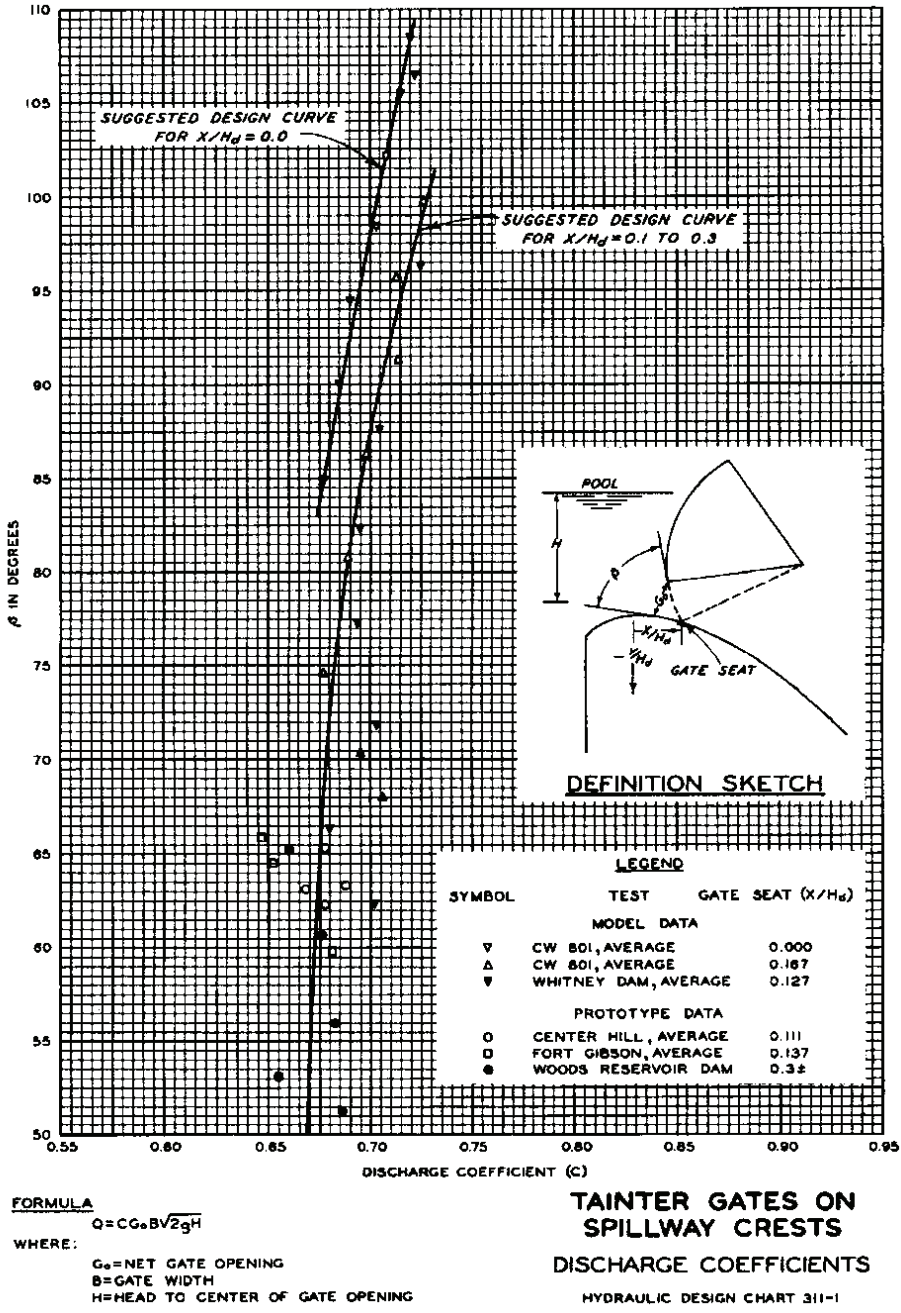

Figure 3 - Copy of Hydraulic Design Chart 311-1 in 'Hydraulic Design Criteria, Volume 2, Tainter Gates on Spillway Crests, Sheets 311-1 to 311-5' by USACE [7].

We have noticed that in designs of even the recently built dams in Turkey, equation (1) in 1973 edition of *Design of Small Dams* is used instead of equation (3) in 1987 edition of *Design of Small Dams*, although the newer edition is used for the designs of the other units of the dams [e.g. 3, 4, 5, 6]. Hence, the first objective of this study has been a quantitative comparison of equations (1) and (3) using the measured data on a few laboratory model study reports by Hydraulic Investigation and Laboratories Services of USBR, Waterways Experimentation Station of USACE, and Hydraulic Laboratories of General Directorate of State Water Works of Republic of Turkey (DSI). Since the 1987 edition of *Design of Small Dams* is the recent one, equation (1) has been repealed and a new method of computing the spillway discharge through partially-opened radial gates is valid now, which is equation (3) here. Therefore, more emphasis is given to evaluation of the discharge coefficient of equation (3), denoted by *C-87* here, using measured data of 22 different model studies performed by the mentioned organizations.

Computation of discharge over ogee spillways has been investigated by various researchers [e.g. 8, 9, 10, 11, 12]. There are other methods for computing discharge through partially-opened gates. For example, Ansar and Chen [13] presented generalized equations for discharge over ogee spillways with sharp-edged sluice gates using the data measured at many canal control structures in South Florida. Bahajantri et al [14] proposed a numerical method based on finite element approach. Saunders et al [15] developed a method using the Smoothed Particle Hydrodynamics model. Schohl [16] used the data measured on six laboratory models whose spillways had downstream face profiles defined by the method of Tennessee Valley Authority (TVA). Schohl [16] computed the discharge coefficient of the equation used by TVA, which is different from both equations (1) and (3), with many different gate openings and water surface elevations using all of the data in these six spillway model studies and noticed that they were not in close harmony. Schohl [16] additionally plotted the discharge coefficients of the TVA equation against the angle Θ of the method of *Design of Small Dams* [2] in a figure which also showed a fairly wide scatter. Haug [17] computed the discharge coefficients of equation (3) using the laboratory model data on the radial-gated ogee spillways of five dams in the USA. The laboratory models were repeated twice with different scales for two of these dams, 1:48 and a larger scale for Hells Canyon Dam spillway model, and 1:50 and 1:120 for Wanapum Dam spillway model. The relationships of the *C* coefficient of equation (3) as a function of the angle Θ computed by Haug [17] using all measured data of these cases in the same figure also revealed a fairly wide scatter and not a close cluster around the curve in Figure 9-31 of *Design of Small Dams* [2].

The reason for avoiding the usage of the method in the recent edition of *Design of Small Dams* [2] is most probably because it is analytically more difficult to apply than the method in its previous edition [1]. The difficulty is caused by (1) trigonometric complexity for computation of the angle Θ and (2) geometrical hardship for *D*, which is the smallest distance between the gate lip and the surface of the ogee profile. A method for computation of both Θ and *D* is given in the technical report: *Hydraulic Design Criteria, Sheets 311-1 to 311-5* [7], which involves a cumbersome path necessitating two tables, the first one having 20 columns and the second one 15 columns, plus a log-log graph having two lines, one for the analytical expression of the crest curve of the ogee profile and the other for its derivative. An alternative method, which computes both Θ and *D* by a more concise numerical scheme having no need for any table or any graph, is presented by Haktanir et al [18].

The first objective of this study is to compute the discharge coefficients of the formulas for the partially-opened radial-gated ogee spillways given in the previous and recent editions of *Design of Small Dams* [1, 2] for a few dams for which the laboratory model data are available and to compare such obtained coefficients with the ones given in the pertinent figures in those books. Finally, it is aimed that a new equation be developed for the *C* coefficient of equation (3), *C-87*, using the measured data available in these laboratory reports.

2. THE DATA USED IN THE STUDY

We have searched through the web sites of the Hydraulic Investigation and Laboratories Services of USBR and the Waterways Experimentation Station of USACE and we have found many relevant reports dated as early as 1949 and as recent as 2014. We have officially applied for permission for usage of the numerical data contained in those reports separately to the concerned bureaus of both USBR and USACE. And, we have received replies from USBR and USACE stating: "You are welcome to use and translate the material as long as you provide credit to the Bureau of Reclamation and include a disclaimer that states: 'The Bureau of Reclamation is not responsible for the accuracy of this translation.'", and: "All government work and images that are in the public domain need no permission to use. We just ask that they are attributed correctly to the source.", respectively. We are grateful to both USBR and USACE. We have also acquired similar consensus from DSI.

Although we have downloaded quite a few USBR and USACE reports containing hydraulic models of radial-gated spillways, unfortunately we have not been able to use some of them because (1) some crucial data like elevation of the gate trunnion were missing which were not possible to extract from scaled figures, and (2) some of the spillways did not have ogee profiles. Altogether, we have been able to collect 22 reports, six from USBR, nine from USACE, and seven from DSI, respectively [19, 20, 21, 22, 23, 24, 25, 26, 27, 28, 29, 30, 31, 32, 33, 34, 35, 36, 37, 38, 39, 40]. Hence, altogether, we have been able to collect measured data for 22 different radial-gated ogee spillways. 21 of these are of laboratory model studies, and one contains data consisting of five different discharges measured in the approach channel of Seyhan Dam for various gate openings in Turkey in the year 1959 [34]. Five data triplets of lake water surface elevation, gate opening, and discharge at the actual spillway of Seyhan Dam were measured during a high incoming water period which happened in the first two weeks of the month of February in the year 1959 [34]. Each of these five discharges were determined by integration of small area flows computed by multiplying the point velocities measured with the help of a current meter at many points in the cross-section of the approach channel which was 12 meters upstream from the nose of the piers. The coordinates of the measurement points were away from each other 1.0 meter vertically and 4.3 meters horizontally [34].

All of the needed numerical data are taken from these reports by double checking. Table 1 presents some introductory information about these reports. The relevant numerical data of all of these 22 cases are presented in the M.Sc. thesis of Khalaf [41], which can be reached in the web site for theses of graduate studies of Council of Higher Education of Republic of Turkey, which is: tez.yok.gov.tr/ulusaltezmerkezi/

3. DISCHARGE COEFFICIENTS FOR RADIAL-GATED OGEE SPILLWAYS BY MEASURED DATA AND BY 1973 AND 1987 EDITIONS OF *DESIGN OF SMALL DAMS*

If all of the other terms in either equation (1) or equation (3) can be computed using the measured data, then the C coefficient remains as the only unknown. Hence, the discharge coefficient denoted by *C-73* here is computed by equation (1) leaving C alone at one side, and the discharge coefficient denoted by *C-87* here is computed by equation (3) again taking C alone to one side. The relative difference of any one of the two C coefficients taken out of the relevant charts in either the previous or the latest edition of *Design of Small Dams* [1, 2] from the C coefficient determined by either equation (1) or equation (3) using the measured data is computed by:

$$RD_C = (C_{chart} - C_{measured}) \div C_{measured} \quad (4)$$

where, C_{chart} is the coefficient taken from the relevant chart in either the 1973 or the 1987 edition of *Design of Small Dams* [1, 2], and $C_{measured}$ is the coefficient computed using the measured data.

Table 1 - List of the dams whose laboratory reports are used in this study

	Name	**Stream**	**Country**	**Organization**	**Scale of the model**
1	Boysen	Bighorn	USA	USBR	1:48
2	Norton	Missouri	USA	USBR	1:42
3	Glen Elder	Solomon	USA	USBR	1:72
4	Toa Vaca	Toa Vaca	USA	USBR	1:48
5	McPhee	Dolores	USA	USBR	1:36
6	Folsom	American	USA	USBR	1:36
7	Kaysinger Bluff	Osage	USA	USACE	1:60
8	Oakley	Sangamon	USA	USACE	1:60
9	Oakley (Revised)	Sangamon	USA	USACE	1:60
10	Burnsville	Ohio	USA	USACE	1:40
11	Tombigbee A	Tombigbee	USA	USACE	1:15
12	Tombigbee B	Tombigbee	USA	USACE	1:25
13	Cooper	Sulphur	USA	USACE	1:36
14	Bloomington	Potomac	USA	USACE	1:60
15	Lake Darling	Souris	USA	USACE	1:36
16	Kigi	Perisuyu	Turkey	DSI	1:60
17	Yedigoze	Seyhan	Turkey	DSI	1:70
18	Kavsak	Zamanti	Turkey	DSI	1:50

Table 1 - List of the dams whose laboratory reports are used in this study (continue)

	Name	Stream	Country	Organization	Scale of the model
19	Beyhan-1	Murat	Turkey	DSI	1:70
20	Incir	Buyuk	Turkey	DSI	1:50
21	Yusufeli	Coruh	Turkey	DSI	1:40
22	Seyhan	Seyhan	Turkey	DSI	1:1 (actual dam, not the model)

4. RESULTS AND DISCUSSIONS

In those 22 reports whose data are analyzed in this study, the dams had ogee spillways with radial-gates, and we have used all of the data measured for various partial gate openings and for various lake water surface elevations. Out of these 22 cases, we are presenting the results of the spillways of Norton Dam and of the Cooper Dam in USA in this paper here. The reasons for this are manifold. First of all, the data of the Norton Dam contains many more points than those of the other reports. Secondly, its results seem to be more consistent. Thirdly, its results are in parallel to the chart in Figure 257 of the previous edition of *Design of Small Dams* [1] and to some degree to the chart in Figure 9-31 of the recent edition of *Design of Small Dams* [2]. Fourthly, the *C-87* coefficient shows a positive relationship with the ratio d/H_1. This is another result of our study that the *C-87* coefficient depends not only on the angle Θ but also on the ratio d/H_1, which is noticed for the first time by our study. The first reason for presenting the results of the spillway of the Cooper Dam is because both the experimentally observed relationships for the *C-73* and *C-87* coefficients exhibit tendencies contradicting the charts in the mentioned figures of the previous and recent editions of *Design of Small Dams* [1, 2]. The second reason is that the *C-87* coefficient shows a negative relationship with the ratio d/H_1. All of the data and the results both in numerical and graphical forms are given in the M. Sc. Thesis of Mohammed Khalaf [41], which can be reached in the web site for theses of graduate studies of Council of Higher Education of Republic of Turkey, which is: tez.yok.gov.tr/ulusaltezmerkezi/

Table 2.a gives the data for the spillway of Norton Dam taken from the report: *Hydraulic Model Studies on Norton Dam Spillway, Missouri River Basin Project, Kansas* [20] needed by the computer program coded for this study which computes the discharge coefficients for the partially-opened radial gates first by equation (1), *C-73*, and next by equation (3), *C-87*. Table 2.b presents the output of the mentioned computer program using the data given in Table 2.a as the input. The data presented in Table 2.a are necessary to compute both *C-73* and *C-87* for various combinations of gate openings (*d*'s) and lake water surface elevations (WSE's); and therefore, they are included here for anyone interested in these computations and wishing to verify the results given in Table 2.b.

For the spillway of Norton Dam, Figure 4 shows the plots of the experimentally obtained points of *C-87* against the angle Θ together with the points of *C-87* given by Figure 9-31 of the 1987 edition of *Design of Small Dams* [2]. Figure 5.a shows the plots of the experimentally obtained points of *C-73* against d/H_1 together with the points of *C-73* given by Figure 257 of the 1973 edition of *Design of Small Dams* [1], and Figure 5.b shows the

plots of the experimentally obtained points of *C-87* against d/H_1. As another example, Figures 6, 7.a, and 7.b show the same relationships for the spillway of Cooper Dam as those of Figures 4, 5.a, and 5.b, respectively. Similar figures of the other 20 dams are given in the M. Sc. thesis of Khalaf [41]. In the parts following Figure 7.b, the analyses of these triplet figures of all of the 22 dams are summarized and discussed.

Table 2.a - The data for computing both of the discharge coefficients of C-73 and C-87 for the radial-gated ogee spillway of Norton Dam taken from its laboratory model report by USBR [20]

Net spillway length (L): 90.0 ft, sill height of spillway: 11 ft,
angle with vertical of the upstream face of spillway: 45º ,
elevation difference between upstream and downstream toes of spillway: 1.0 ft,
spillway apex elevation: 2296.0 ft, spillway design head (Hd): 44.7 ft,
number of piers on the spillway (N_p): 3,
abutment contraction coefficient (k_p): 0.1, piers contraction coefficient (k_a): 0.01,
radius of the radial gate (Rg): 45.0 ft,
radius of the first circle of the spillway crest profile upstream of the apex (R_1): 20.1 ft,
K and n coefficients of the downstream crest (ogee) curve: 0.52, 1.75,
elevation of the gate trunnion center: 2328.0 ft,
elevations of gate seat and top of gate at closed position: 2295.65 ft, 2332.0 ft
Spillway discharges and water surface elevations for the partial gate openings:

d (ft)	Q (cfs)	WSE (ft)
2	3000	2304
2	3900	2308
2	4800	2312
2	5300	2316
2	5900	2320
2	6300	2324
2	6900	2328
2	7100	2332
4	6600	2308
4	8000	2312
4	9200	2316
4	10500	2320
4	11500	2324
4	12200	2328
4	13000	2332
6	9000	2308
6	11000	2312
6	12800	2316

6	14500	2320
6	15800	2324
6	17100	2328
6	18200	2332
6	19500	2336
8	13500	2312
8	16100	2316
8	18200	2320
8	20100	2324
8	21800	2328
8	23400	2332
8	24900	2336
10	18900	2316
10	21700	2320
10	24000	2324
10	26400	2328
10	28800	2332
10	30500	2336
10	32100	2340
12	21500	2316
12	24700	2320
12	27900	2324
12	30600	2328
12	33000	2332
12	35500	2336
12	37600	2340
14	24000	2316
14	27900	2320
14	31400	2324
14	34500	2328
14	37600	2332
14	40500	2336
14	43000	2340
16	30500	2320
16	34500	2324
16	38400	2328
16	41800	2332
16	45000	2336
16	48000	2340
18	33000	2320
18	37800	2324

18	42000	2328
18	46000	2332
18	49500	2336
18	52800	2340
20	40300	2324
20	44800	2328
20	49200	2332
20	53000	2336
20	57500	2340
22	47800	2328
22	52600	2332
22	57100	2336
22	61600	2340
24	50500	2328
24	55800	2332
24	60700	2336
24	65400	2340
26	58800	2332
26	64000	2336
26	69000	2340
28	61500	2332
28	67200	2336
28	72800	2340
30	70300	2336
30	76100	2340
32	73400	2336
32	79800	2340
34	82800	2340

Table 2.b - Output of the computer program for the discharge coefficients for the partially-opened gates (1) by the 1973 edition and (2) by the 1987 edition of Design of Small Dams [1, 2] using the laboratory model data of the spillway of Norton Dam [20]

All lengths are in ft and discharges are in cfs
Gate trunnion coordinates (y, x): 32.00 35.35
Gate seat coordinates (y, x): -0.35 4.07
Discharge coefficients and their relative differences for
the partially-opened flow case:

Hmsrd	dmsrd	Qmsrd	C-73	Cexp-73	RD-C-73	C-87	Cexp-87	RD-C-87
8.07	2.	3000.	.6927	.7621	-9%	.6690	.7538	-11%
12.07	2.	3900.	.7025	.7934	-11%	.6690	.7825	-15%

16.07	2.	4800.	.7076	.8395	-16%	.6690	.8250	-19%
20.07	2.	5300.	.7117	.8267	-14%	.6690	.8096	-17%
24.07	2.	5900.	.7155	.8396	-15%	.6690	.8193	-18%
28.07	2.	6300.	.7190	.8306	-13%	.6690	.8075	-17%
32.07	2.	6900.	.7222	.8521	-15%	.6690	.8255	-19%
36.07	2.	7100.	.7250	.8283	-12%	.6690	.7995	-16%
12.00	4.	6600.	.6845	.7315	-6%	.6693	.7226	-7%
16.00	4.	8000.	.6934	.7515	-8%	.6693	.7402	-10%
20.00	4.	9200.	.6987	.7647	-9%	.6693	.7507	-11%
24.00	4.	10500.	.7031	.7921	-11%	.6693	.7750	-14%
28.00	4.	11500.	.7059	.8009	-12%	.6693	.7808	-14%
32.00	4.	12200.	.7082	.7938	-11%	.6693	.7711	-13%
36.00	4.	13000.	.7103	.7974	-11%	.6693	.7719	-13%
12.03	6.	9000.	.6666	.6994	-5%	.6719	.6878	-2%
16.03	6.	11000.	.6799	.7122	-5%	.6719	.6996	-4%
20.03	6.	12800.	.6879	.7268	-5%	.6719	.7120	-6%
24.03	6.	14500.	.6933	.7432	-7%	.6719	.7257	-7%
28.03	6.	15800.	.6971	.7447	-6%	.6719	.7248	-7%
32.03	6.	17100.	.7000	.7510	-7%	.6719	.7284	-8%
36.03	6.	18200.	.7030	.7520	-7%	.6719	.7267	-8%
40.03	6.	19500.	.7050	.7637	-8%	.6719	.7354	-9%
16.09	8.	13500.	.6664	.6784	-2%	.6744	.6625	2%
20.09	8.	16100.	.6771	.7021	-4%	.6744	.6846	-1%
24.09	8.	18200.	.6842	.7119	-4%	.6744	.6924	-3%
28.09	8.	20100.	.6893	.7201	-4%	.6744	.6982	-3%
32.09	8.	21800.	.6931	.7256	-4%	.6744	.7011	-4%
36.09	8.	23400.	.6961	.7312	-5%	.6744	.7041	-4%
40.09	8.	24900.	.6985	.7362	-5%	.6744	.7064	-5%
20.17	10.	18900.	.6663	.6781	-2%	.6773	.6574	3%
24.17	10.	21700.	.6752	.6934	-3%	.6773	.6710	1%
28.17	10.	24000.	.6816	.6992	-3%	.6773	.6748	0%
32.17	10.	26400.	.6863	.7122	-4%	.6773	.6853	-1%
36.17	10.	28800.	.6901	.7277	-5%	.6773	.6978	-3%
40.17	10.	30500.	.6930	.7279	-5%	.6773	.6956	-3%
44.17	10.	32100.	.6955	.7284	-5%	.6773	.6936	-2%
20.24	12.	21500.	.6556	.6647	-1%	.6803	.6401	6%
24.24	12.	24700.	.6662	.6744	-1%	.6803	.6491	5%

28.24	12.	27900.	.6738	.6908	-2%	.6803	.6636	3%
32.24	12.	30600.	.6796	.6991	-3%	.6803	.6698	2%
36.24	12.	33000.	.6840	.7043	-3%	.6803	.6726	1%
40.24	12.	35500.	.6876	.7142	-4%	.6803	.6798	0%
44.24	12.	37600.	.6905	.7181	-4%	.6803	.6812	0%
20.29	14.	24000.	.6450	.6616	-3%	.6837	.6320	8%
24.29	14.	27900.	.6573	.6721	-2%	.6837	.6433	6%
28.29	14.	31400.	.6662	.6818	-2%	.6837	.6519	5%
32.29	14.	34500.	.6729	.6884	-2%	.6837	.6569	4%
36.29	14.	37600.	.6781	.6988	-3%	.6837	.6649	3%
40.29	14.	40500.	.6822	.7081	-4%	.6837	.6716	2%
44.29	14.	43000.	.6856	.7125	-4%	.6837	.6736	2%
24.34	16.	30500.	.6485	.6644	-2%	.6877	.6321	9%
28.34	16.	34500.	.6586	.6725	-2%	.6877	.6402	7%
32.34	16.	38400.	.6662	.6848	-3%	.6877	.6509	6%
36.34	16.	41800.	.6721	.6921	-3%	.6877	.6563	5%
40.34	16.	45000.	.6769	.6992	-3%	.6877	.6612	4%
44.34	16.	48000.	.6808	.7055	-4%	.6877	.6651	3%
24.37	18.	33000.	.6397	.6632	-4%	.6919	.6267	10%
28.37	18.	37800.	.6510	.6739	-3%	.6919	.6386	8%
32.37	18.	42000.	.6596	.6814	-3%	.6919	.6455	7%
36.37	18.	46000.	.6662	.6904	-4%	.6919	.6529	6%
40.37	18.	49500.	.6715	.6954	-3%	.6919	.6559	5%
44.37	18.	52800.	.6759	.7004	-3%	.6919	.6587	5%
28.39	20.	40300.	.6435	.6674	-4%	.6966	.6292	11%
32.39	20.	44800.	.6530	.6709	-3%	.6966	.6333	10%
36.39	20.	49200.	.6603	.6789	-3%	.6966	.6402	9%
40.39	20.	53000.	.6662	.6825	-2%	.6966	.6424	8%
44.39	20.	57500.	.6711	.6976	-4%	.6966	.6549	6%
32.40	22.	47800.	.6464	.6689	-3%	.7022	.6291	12%
36.40	22.	52600.	.6545	.6750	-3%	.7022	.6350	11%
40.40	22.	57100.	.6610	.6817	-3%	.7022	.6403	10%
44.40	22.	61600.	.6663	.6912	-4%	.7022	.6479	8%
32.40	24.	50500.	.6398	.6673	-4%	.7074	.6251	13%
36.40	24.	55800.	.6486	.6726	-4%	.7074	.6310	12%
40.40	24.	60700.	.6557	.6782	-3%	.7074	.6359	11%
44.40	24.	65400.	.6615	.6850	-3%	.7074	.6411	10%

36.39	26.	58800.	.6428	.6715	-4%	.7128	.6281	13%
40.39	26.	64000.	.6504	.6746	-4%	.7128	.6314	13%
44.39	26.	69000.	.6567	.6799	-3%	.7128	.6356	12%
36.38	28.	61500.	.6369	.6707	-5%	.7187	.6251	15%
40.38	28.	67200.	.6452	.6732	-4%	.7187	.6288	14%
44.38	28.	72800.	.6519	.6794	-4%	.7187	.6344	13%
40.36	30.	70300.	.6399	.6736	-5%	.7245	.6277	15%
44.36	30.	76100.	.6471	.6768	-4%	.7245	.6312	15%
40.34	32.	73400.	.6346	.6769	-6%	.7300	.6288	16%
44.34	32.	79800.	.6423	.6802	-6%	.7300	.6332	15%
44.31	34.	82800.	.6375	.6798	-6%	.7350	.6315	16%

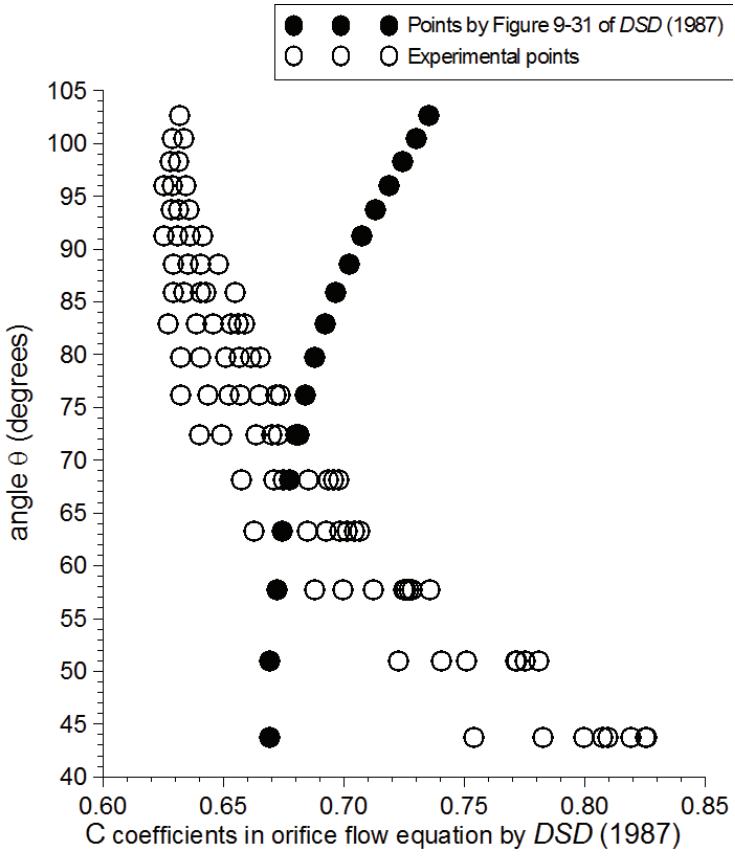

Figure 4 - Plot of the discharge coefficients C-87 against the angle Θ obtained by the data measured on the laboratory model of the spillway of Norton Dam [20] together with the points given by Figure 9-31 of the third edition of Design of Small Dams [2] for the same Θ's

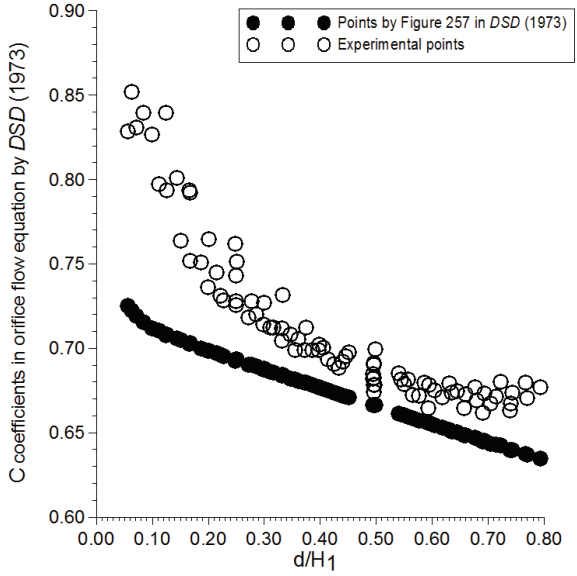

Figure 5.a - Plot of the discharge coefficients C-73 against the ratio d/H_1 obtained by the data measured on the laboratory model of the spillway of Norton Dam [20] together with the points given by Figure 257 of the second edition of Design of Small Dams [1]

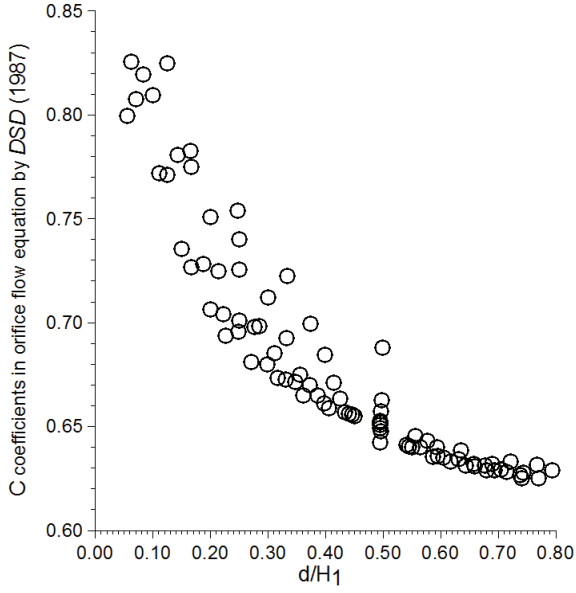

Figure 5.b - Plot of the discharge coefficients C-87 against the ratio d/H1 obtained by the data measured on the laboratory model of the spillway of Norton Dam [20]

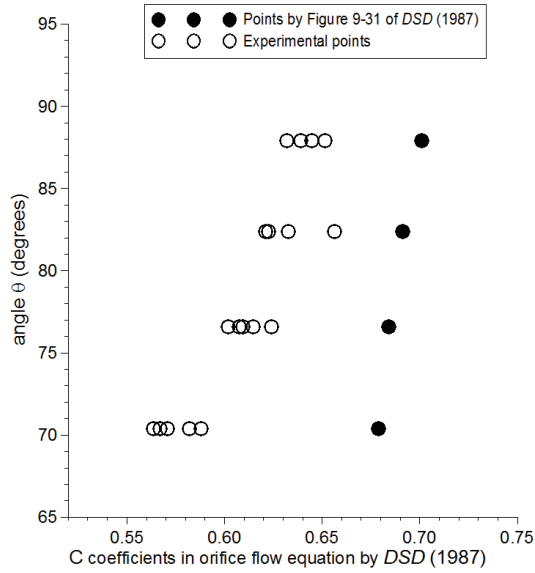

Figure 6 - Plot of the discharge coefficients C-87 against the angle Θ obtained by the data measured on the laboratory model of the spillway of Cooper Dam [30] together with the points given by Figure 9-31 of the third edition of Design of Small Dams [2] for the same Θ's

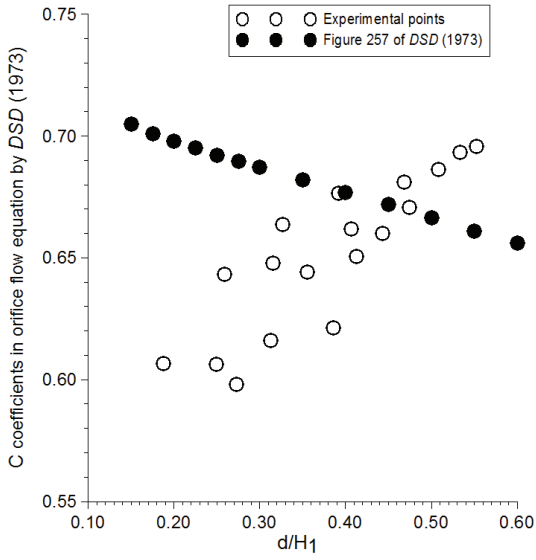

Figure 7.a - Plot of the discharge coefficients C-73 against the ratio d/H_1 obtained by the data measured on the laboratory model of the spillway of Cooper Dam [30] together with the theoretical points given by Figure 257 of the second edition of Design of Small Dams [2]

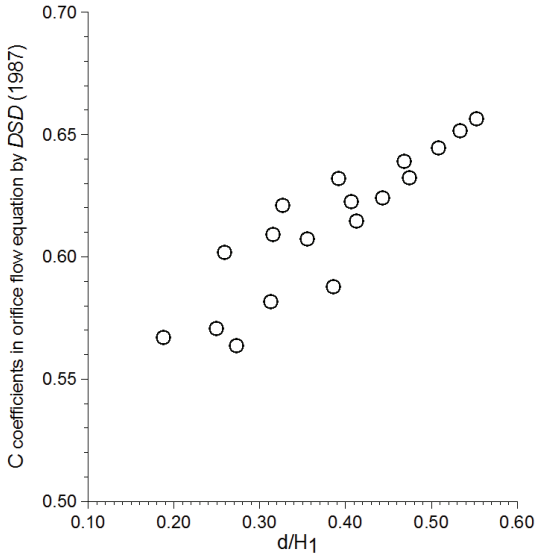

Figure 7.b - Plot of the discharge coefficients C-87 against the ratio d/H_1 obtained by the data measured on the laboratory model of the spillway of Cooper Dam [30]

First of all, we have noticed that a few different-magnitude *C-87*'s exist against the same numerical value of the angle Θ, which can be clearly seen in both Figures 4 and 6. It is a geometrical fact that the angle Θ assumes a constant value when the gate opening is fixed, because the tangents to the gate lip and to the crest curve of the spillway will be at fixed positions in that case. Therefore, it is obvious that there being different magnitudes of the *C-87* coefficient corresponding to the same value of the angle Θ means that *C-87* depends on another independent variable together with Θ. Yet again, it is analytically evident that the other explanatory variable must be related to the lake water surface elevation simply because the other *C-87*'s for the same Θ correspond to different water surface elevations at the same gate opening position. Therefore, the other explanatory variable is deemed to be the ratio of the vertical gate opening to the total head with respect to the spillway apex, which is symbolized by d/H_1. In the 1973 edition of *Design of Small Dams* [1], the discharge coefficient *C-73* is determined as a function of d/H_1. Similary, the analyses in our study indicate that the discharge coefficient of the new method, *C-87*, should be a function of d/H_1 together with the angle Θ. Figures of pairs of both Figures 5.a, 5.b, and 6.a, 6.b reveal plots verifying this so-far-ignored fact. Figure 5.a shows the variation of the measured values of the *C-73* coefficient together with the values given by Figure 257 of the 1973 edition of *Design of Small Dams* [1] for the spillway of Norton Dam. Although there is not a close fit, still, the measured *C-73*'s exhibit parallel values to those given by Figure 257 of the 1973 edition of *Design of Small Dams* [1]. Interestingly, the plots of the measured *C-87* values against d/H_1 also exhibit a trend parallel to the measured *C-73* values. In other words, as can be appreciated easily by inspecting Figure 5.b, although unnoticed so far, the discharge coefficient of the 1987 method, *C-87*, also indicates a close relationship to the ratio d/H_1. The measured data of the spillway of Norton Dam is one of a total of 22 such reports we have

been able to obtain. In Figure 7.a, an interesting relationship is observed between the discharge coefficient of the previous method, *C-73*, and the ratio d/H_1, which is contradictory to the theoretical curve. So, for the spillway of Cooper Dam, the relationship between *C-73* and d/H_1 is opposite of what is expected according to Figure 257 of the 1973 edition of *Design of Small Dams* [1]. Yet, as seen in Figure 7.b, for Cooper Dam the relationship between the discharge coefficient of the recent method, *C-87*, and the ratio d/H_1 also exhibits an increasing *C-87* with an increasing d/H_1, parallel to the relationship of *C-73* with d/H_1.

In short, out of 22 reports, 9 cases revealed *C-73* and d/H_1 and also *C-87* and d/H_1 relationships parallel to the curve given in Figure 257 of the 1973 edition of *Design of Small Dams* [1], which is decreasing *C-73* with increasing d/H_1 and also decreasing *C-87* with increasing d/H_1, and 13 cases showed contradictory behavior, namely, increasing *C-73* with increasing d/H_1 and also increasing *C-87* with increasing d/H_1. The reason for the relationship between *C-87* and d/H_1 having a negative slope for some spillways and a positive slope for some other spillways must be related to the dimensions of the spillway and of the gates. Therefore, we have computed many ratios of dimensions, which are: (sill height)/(spillway length), (trunnion height)/(spillway length), (trunnion height)/(sill height), (design head)/(spillway length), (design head)/(sill height), (gate height)/(spillway length), (gate height)/(sill height), and (radius of gate)/(spillway length), which are symbolized as P/L, T_H/L, T_H/P, H_d/L, H_d/P, G_H/L, G_H/P, Rg/L, respectively, with the expectation of relating the behavior of positive or negative slope for the relationship of *C-87* against d/H_1 to a tangible dimensionless quantity. Trunnion height, T_H, is the difference in elevations of the gate trunnion and of the gate seat, sill height (P) is the difference of elevations of the spillway apex and bottom of the approach channel at the upstream toe of the spillway, design head (H_d) is the net head over the spillway apex for the design discharge, gate height (G_H) is the difference of elevations of the top and bottom lips of the gate in closed position, and radius of gate (Rg) is the outer radius of the gate. Tables 3.a and 3.b present these ratios for all of the 22 cases, the former having those spillways with negative slope for the *C-87* against *d/H1* relationship and the latter with positive slope. Investigation of these tables suggests that the ratios of (trunnion height)/(spillway length) and/or (radius of gate)/(spillway length) can be taken as guides for the slope of the relationship between *C-87* and the second explanatory variable d/H_1. As the outcome of the analyses, whose summaries are given in Tables3.a and 3.b, it can be said that the slope of the relationship between *C-87* and d/H_1 is negative when $T_H/L > 0.25$ and positive if $T_H/L < 0.25$. Aside from that, the slope of this relationship is negative when $Rg/L > 0.5$ and positive if $Rg/L < 0.5$.

Leaving these observations aside, we have plotted the *C-87* coefficients against the angle Θ obtained by the measured data of all of these 22 spillways all in one figure, which is Figure 8. Six of these 22 spillways have gate seats directly at the top of the apex, while the gate seats of the other 16 are placed downstream from the apex at a distance about a small percentage of the design head. Because the trajectories of the shooting jet under the partially-opened radial gate by these two distinct cases should be different, the relationship of *C-87* with the angle Θ is also deemed to be different; and hence, although not too far apart, there are two different charts for these two cases [2, 7]. In Figure 8, those charts from Figure 9-31 of *Design of Small Dams* [2] are shown by green and yellow lines extended within the same ranges as in Figure 9-31. The points of *C-87* against Θ are shown in blue for those spillways whose gate seats are downstream from the apex, and the points of *C-87* against Θ are shown in red for those spillways whose gate seats are right on top of the apex in Figure 8. First of all, the

overall appearance of the plotted points in Figure 8 does not give hope for a generalizable clustering around a potential curve, and we come to the conclusion that a generalized model for the discharge coefficient *C-87* does not look to be meaningfully unique. Another noteworthy observation in Figure 8 is that, the end points of the green and yellow lines in the figure, which are taken from Figure 9-31 of *Design of Small Dams* [2], are actually too short to cover the experimentally measured ranges.

Table 3.a - Various ratios pertaining to some spillway and gate dimensions for those dams for which the discharge coefficient C-87 exhibits a decreasing relationship with increasing d/H_1

Dam	L	P	$\frac{P}{L}$	$\frac{T_H}{L}$	$\frac{T_H}{P}$	$\frac{H_d}{L}$	$\frac{H_d}{P}$	$\frac{G_H}{L}$	$\frac{G_H}{P}$	$\frac{Rg}{L}$
Boysen	60 ft	10 ft	0.17	0.35	2.1	0.9	5.2	0.42	2.5	0.70
Mcphee	56 ft	8 ft	0.14	0.28	2.0	0.6	3.9	0.50	3.5	0.50
Norton	90 ft	11 ft	0.12	0.36	3.0	0.5	4.1	0.40	3.3	0.50
Toa Vaca	90 ft	13 ft	0.14	0.33	2.3	0.4	3.1	0.38	2.6	0.46
Bloomington	210 ft	13 ft	0.06	0.06	1.0	0.2	3.1	0.15	2.5	0.17
Yusufeli	57.5 m	11.7 m	0.20	0.11	0.5	0.2	1.1	0.15	0.8	0.22
Kigi	28 m	4 m	0.14	0.25	1.8	0.4	3.1	0.40	2.8	0.60
Yedigoze	66 m	4 m	0.06	0.11	1.7	0.3	4.2	0.28	4.7	0.25
Kavsak	37.8 m	10 m	0.26	0.22	0.8	0.6	2.1	0.70	2.6	0.47

Table 3.b - Various ratios pertaining to some spillway and gate dimensions for those dams for which the discharge coefficient C-87 exhibits an increasing relationship with increasing d/H_1

Dam	L	P	$\frac{P}{L}$	$\frac{T_H}{L}$	$\frac{T_H}{P}$	$\frac{H_d}{L}$	$\frac{H_d}{P}$	$\frac{G_H}{L}$	$\frac{G_H}{P}$	$\frac{Rg}{L}$
Burnsville	126 ft	37 ft	0.30	0.14	0.47	0.33	1.1	0.28	0.9	0.27
Cooper	200 ft	28.2 ft	0.14	0.04	0.25	0.13	0.9	0.11	0.8	0.11
Glen Elder	600 ft	9.5 ft	0.02	0.03	1.74	0.04	2.7	0.04	2.3	0.04
Lake Darling	215 ft	12.5 ft	0.06	0.03	0.64	0.12	2.0	0.10	1.8	0.11
Oakley	168 ft	18 ft	0.11	0.06	0.58	0.22	2.0	0.16	1.5	0.20
Oakley (Rvsd)	160 ft	11 ft	0.07	0.09	1.35	0.18	2.7	0.15	2.2	0.16
Folsom	210 ft	154 ft	0.73	0.07	0.10	0.30	0.4	0.25	0.3	0.21
Kaysinger	160 ft	58.3 ft	0.36	0.10	0.28	0.27	0.7	0.30	0.8	0.30
Tombigbee A	104 ft	5 ft	0.05	0.03	0.55	0.14	3.0	0.07	1.6	0.20
Tombigbee B	495 ft	5 ft	0.01	0.01	1.40	0.04	3.7	0.03	3.0	0.04
Incir	21.8 m	3 m	0.14	0.26	1.94	0.53	3.8	0.36	2.7	0.50
Seyhan	42 m	2 m	0.05	0.08	1.75	0.28	6.0	0.14	3.1	0.21
Beyhan-1	69 m	5 m	0.07	0.13	1.76	0.26	3.6	0.24	3.4	0.23

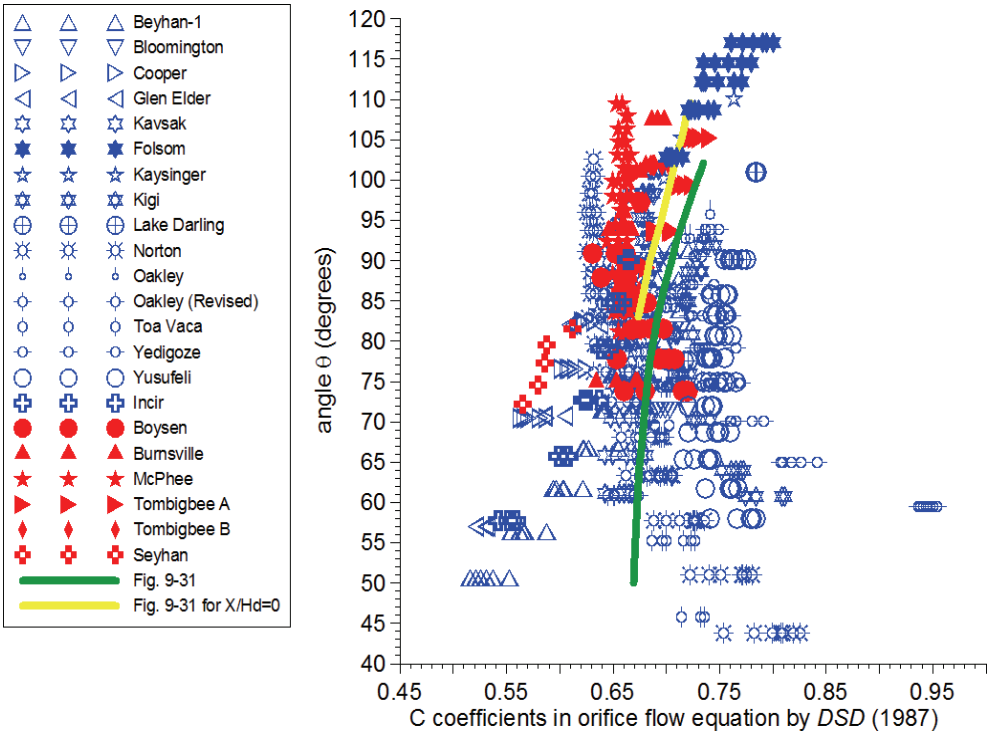

Figure 8 - Plot of the discharge coefficients C-87 against the angle Θ obtained by the measured data in all of 22 reports used in this study together with the charts given in Figure 9-31 of the third edition of 'Design of Small Dams' [2]

The scales of those laboratory models vary between 1:15 to 1:72, eight with scales greater than 1:60, four with scales 1:48 and 1:50, seven within scales 1:36 and 1:42, and two having the scales of 1:15 and 1:25. Seyhan Dam's spillway has a scale 1:1. And hence, there should be scale effects on the measured values. As noted by Haug [17], for small gate openings, surface tension and viscosity effects may be significant which may have affected the hydraulic behavior of the spilling jet for small-scale models. Haug [17] commented: "Scale models smaller than 1/50 can have more than 15 % error just due to viscous scale effects." The scales of the spillway models of Yedigoze and Beyhan-1 Dams are 1:70 and that of Glen Elder Dam is 1:72 [36, 38, 21], which are the smallest size models out of the 22 cases analyzed in our study. For these three spillway models, the plotted points with small Θ angles, meaning small gate openings, look appreciably deviant from those of larger openings in Figure 8 and in the individually drawn figures [41]. Looking at Figure 3 above, which contains the original form of the diagram given in Figure 9-31 in the recent edition of *Design of Small Dams* [2], it can be observed that the plotted points of *C-87* against Θ measured on the spillways of five cases only also show a fairly wide scatter around the averaging curve for angles smaller than 72°. In short, we believe it is difficult to expect close clustering of relationships obtained out of laboratory measurements from different scale models.

Yet, there are geometrical properties of the approach conditions and the spillway configuration peculiar to each dam. For example, some spillways are located at either the left-hand side or the right-hand side of the embankment, and yet some others are located right in the middle of a concrete arch dam with no approach channel. The geometrical shapes of the approach channels are also different from each other. In short, even if the needed quantities affecting the discharge characteristics of a spillway were measured directly on the prototype structure, still there would be differences which would be off from a generalized relationship.

Therefore, our final result is that for an important dam, a laboratory model study, with a scale no smaller than 1:50, must be carried out beforehand, and the discharge coefficient of the analytical model had much better be individually obtained rather than using a generalized chart like Figure 9-31 of the third edition of *Design of Small Dams* [2]. Inspecting the relationships of *C-87* against Θ and against d/H_1 for each report separately implicates that indeed individually for each dam *C-87* may be significantly related to both of these explanatory variables, Θ and d/H_1. Hence, regression equations are computed separately for each one of these 22 cases analyzed in this study. Table 5 presents the magnitudes of the coefficients, of the **t** values of the coefficients, and of the determination coefficients of the regressions for the Norton and Cooper Dams. The others are given in the M.Sc. thesis by Khalaf [41], and for most of them the regression coefficients are significant at 95 % level and their determination coefficients are around 0.90.

*Table 5 - Values of the coefficients, of their **t** values (in parentheses), and of the determination coefficients (R^2, adjusted for degree of freedom) of the regression equations for C-87 for Norton and Cooper Dams*

Regression equation for *C-87* is: $C\text{-}87 = c_0 + c_1\times\Theta + c_2\times\Theta^2 + c_3\times(d/H_1) + c_4\times(d/H_1)^2$

Dam / R^2_{adj}	c_0	c_1	c_2	c_3	c_4
Norton	1.12	-0.00888	0.000052	-0.259	0.144
$R^2_{adj} = 0.92$	(65.1)	(-15.4)	(13.1)	(-10.2)	(5.2)
Cooper	-0.649	0.0285	-0.000165	0.127	0.0
$R^2_{adj} = 0.97$	(-3.0)	(5.2)	(-4.7)	(7.4)	

During the construction of the approach channel of the spillway of a dam, a safe and sound steel rope and cable car unit can be mounted over it. As compared to the total cost of the spillway and its appurtenances, the cost of this cable car unit will be negligibly small. During days of high incoming flows, either by a conventional current meter or another instrument like an Acoustic Doppler Anemometer, point velocities all over the cross-section of the approach channel can be measured and the total discharge can be determined by integration of small area flow rates over the entire section. This experiment can be repeated for various gate openings and lake water surface elevations in any day of any year whenever suitable. The occurrences of high waters during the service life of a dam most probably will be smaller than the critical design flood. Therefore, real-life experiments will probably be carried out for fairly small gate openings and not too high lake water surface elevations. This should be

an advantage actually, because at small gate openings and low water surface elevations the viscous and surface tension effects may yield unrealistic measurements for small-scale laboratory models. Hence, real-life measurements on prototype spillways would yield realistic data for low values. The actual spillway measurements at low heads and small gate openings could be conjunctively evaluated with high heads and large gate openings obtainable in laboratory models.

5. CONCLUSIONS

Technical reports of six laboratory studies by USBR, nine by USACE, six by DSI (General Directorate of State Water Works of Turkey) containing measured data for partial gate openings of radial-gated ogee spillway models are analyzed. Five points of lake water surface elevation, gate opening, and spillway discharge, which are based on actual point velocity measurements across the entire section of the approach channel of Seyhan Dam in Turkey are also included in the study. The conclusions reached are as follows.

Figure 9-31 in the recent edition of *Design of Small Dams* [2] is insufficient for accurately estimating the discharge coefficient of the equation used by USBR for computing the discharge over an ogee spillway for the case of partially-opened gates. Analyses of these 22 reports indicate that the discharge coefficient, symbolized by *C-87* here, should be calculated relating it (1) to the angle between the tangent to the gate lip and the tangent to the crest curve closest to the gate lip (Θ) and (2) to the ratio of the gate opening to the head with respect to the spillway apex (d/H_1). Figure 9-31 in *Design of Small Dams* [2] however, relates *C-87* to Θ only.

The relationship between the coefficient *C-87* as the dependent variable against both the angle Θ and the ratio d/H_1 must be determined separately for each dam by a comprehensive laboratory model study having a scale no smaller than 1:50, while a generalized curve will not yield accurate results for the (Spillway discharge) ↔ (Head) relationship for the case of the partially-opened gates for a specific dam.

Symbols

$\mathbf{c_i}$: Coefficients of the regression equation relating *C-87* to d/H_1 and Θ (i = 0, 1, 2, 3, 4)

C : Coefficient of discharge in general equations for partially-opened radial-gated ogee spillways

C-73 : Symbol used in this study for coefficient of discharge in equation (1)

C-87 : Symbol used in this study for coefficient of discharge in equation (3)

C_{chart} : Magnitude of coefficient of discharge taken from the relevant chart given in either 1973 or 1987 edition of the book: *Design of Small Dams*

$C_{measured}$: Magnitude of coefficient of discharge computed by the inverse of either equation (1) or equation (3) using the measured data

d : Vertical opening of the partially-opened radial gate

g : Acceleration of gravity

H : Total head just upstream of the gate with respect to the spillway apex in equation (2)

H : Total head just upstream of the gate with respect to the center of the gate opening in equation (3)

H_1, H_2 : Total heads to the bottom and top of the gate opening, respectively

k_a : Approach abutments contraction coefficient

k_p : Pier contraction coefficient

L : Net length of the spillway crest excluding the piers

L_e : Effective length of the spillway crest

N_p : Number of piers on the spillway crest

P : Sill height of the spillway

Q : Discharge of water spilling over the radial-gated ogee spillway when the gates are partially-opened

R^2_{adj} : Determination coefficient of the regression equation adjusted for degree of freedom

RDc : Relative difference of a *C* coefficient taken out of the relevant chart in either 1973 or 1987 edition of the book: *Design of Small Dams* from the experimental *C* coefficient

Θ : Angle between the tangent to the gate lip and the tangent to the crest curve at the point nearest to the lip

References

[1] USBR, *Design of Small Dams*, Second edition, US Department of The Interior, Bureau of Reclamation, US Government Printing Office, Washington DC, 1973.

[2] USBR, *Design of Small Dams*, A Water Resources Technical Publication, Third edition, US Department of The Interior, Bureau of Reclamation, US Government Printing Office, Washington DC, 1987.

[3] DSI, *Ilısu Dam and Hydroelectric Power Plant, Hydraulic Report of Flood Spillway, Rep–14.160/0030–Rev.1.* Colenco Power Engineering Ltd, IM Magia Engineering, Dolsar Engineering, Rast Engineering Ltd., Dams and Hydroelectric Power Plants Department, General Directorate of State Water Works, Ankara, Turkey, 2010.

[4] Enerjisa, *Hydraulic Design of Flood Spillway of Kavsak Dam*. Enerjisa Engineering Ltd, Istanbul, Turkey, 2009.

[5] Sanko, *Final Feasibility Report of Yedigoze Dam and HPP Volume 1, Appendix-4: Hydraulic Design of Flood Spillway* (in Turkish). Sanko Engineering and Consulting Inc., Cetin Emec Boulevard, 6th Street, No: 61/7, 06520 Balgat, Ankara, Turkey, 2007.

[6] Temelsu, *Final Design Project of Bayramhacılı Dam and HPP, Chapter 3.1: Hydraulic Design of Flood Spillway* (in Turkish). Temelsu Engineering and Consulting Inc., Ankara, Turkey, 2007.

[7] USACE, *Hydraulic Design Criteria, Volume 2, Tainter Gates on Spillway Crests, Sheets 311-1 to 311-5*. Department of the Army, Corps of Engineers, Mississippi River Commission, Waterways Experimentation Station, Vicksburg, Mississippi, USA, 1987.

[8] Mazumdar, S. K. and Roy, I. D., Orifice flow in a gated spillway. *ISH Journal of Hydraulic Engineering*, 3(2), 44–52, DOI: 10.1080/09715010.1997.10514609, 1997.

[9] Savage, B. M. and Johnson, M. C., Flow over ogee spillway: Physical and numerical model case study. *Journal of Hydraulic Engineering, ASCE*, 127(8), 640–649, 2001.

[10] Kim, G. D. and Park, J. H., Analysis of flow structure over ogee-spillway in consideration of scale and roughness effects by using CFD model. *KSCE Journal of Civil Engineering*, 9(2), 161–169, DOI: 10.1007/BF02829067, 2005.

[11] Alhashimi, S. A. M., CFD modeling of flow over ogee spillway by using different turbulent models. *International Journal of Scientific Engineering and Technology Research*, 2(15), 1682–1687, 2013.

[12] Bagatur, T. and Onen, F., Computation of design coefficients in ogee-crested spillway structure using GEP and regression models. *KSCE Journal of Civil Engineering*, 20(2), 951–959. DOI 10.1007/s12205–015–0648–x, 2016.

[13] Ansar, M. and Chen, Z., Generalized flow rating equations at prototype gated spillways. *Journal of Hydraulic Engineering, ASCE*, 135(7), 602–608, 2009.

[14] Bahajantri, M. R., Eldho, T. I., Deolalikar, P. B., Numerical modeling of turbulent flow through spillway with gated operation. *International Journal for Numerical Methods in Engineering*, 72, 221–243. DOI: 10.1002/nme.2016, 2007.

[15] Saunders, K., Prakash, M., Cleary, P. W., Cordell, M., Application of Smoothed Particle Hydrodynamics for modeling gated spillway flows. *Applied Mathematical Modelling*, 38, 4308–4322, DOI: 10.1016/j.apm.2014.05.008, 2014.

[16] Schohl, G. A., Discharge Correlations for Spillways with Radial Gates. In B. Crookston & B. Tullis (Eds.), *Hydraulic Structures and Water System Management*. 6th IAHR International Symposium on Hydraulic Structures, Portland, OR, 27–30 June (pp. 641–651). Doi: 10.15142/T34106228160853 (ISBN 978–1–884575–75–4), 2016.

[17] Haug, P. E., Spillway Capacity and Discharge Uncertainty – Why Do Rating Curves Rarely Agree with Flow Measurement Records? (http://www.ayresassociates.com/wp-content/uploads/2014/02/Spillway-Rating-Curves-Flow-Studies.pdf), 2014.

[18] Haktanir, T., Citakoglu, H., Kucukgoncu, H., An efficient algorithm for ogee spillway discharge with partially-opened radial gates by the method of *Design of Small Dams* and comparison of current and previous methods. *The International Journal of Engineering and Science (IJES)*, 5(7), 13–26, ISSN (e): 2319 – 1813 ISSN (p): 2319 – 1805, 2016.

[19] USBR, *Hydraulic Model Studies of Boysen Dam Spillway, Report No: 212,US* Department of The Interior, Bureau of Reclamation, Engineering Laboratories Branch, Design and Construction Division, Denver, Colorado, USA, 1952.

[20] USBR, *Hydraulic Model Studies on Norton Dam Spillway*, Missouri River Basin Project, Kanas, *Report No:* Hyd-493*, US* Department of The Interior, Bureau of Reclamation, Hydraulic Branch, Division of Research, Office of Assistant Commissioner and Chief Engineer, Denver, Colorado, USA, 1962.

[21] USBR, *Hydraulic Model Studies of the Spillway Glen Elder Dam*, Missouri River Basin Project, Kansas, *Report No:* Hyd-561*, US* Department of The Interior Bureau of Reclamation, Hydraulic Branch, Division of Research, Office of Chief Engineer, Denver, Colorado, USA, 1966.

[22] USBR, *Hydraulic Model Studies of Toa Vaca Dam Spillway*, Puerto Rico Water Resources Authority, *Report No:* REC-OCE-70-42*,* US Engineering and Research Center Bureau of Reclamation, Division of General Research, Denver, Colorado, USA, 1970.

[23] USBR, *Hydraulic Model Studies of McPhee Dam Spillway*, *Report No:* GR-81-2*, US* Engineering and Research Center Bureau of Reclamation, Hydraulic Branch, Division of Research, Denver, Colorado, USA, 1981.

[24] USBR, *Physical Hydraulic Model Studies of Folsom Dam Emergency Spillway, Tainter Gate Alternatives*, *Report No:* HL-2014-01*, US* Department of The Interior Bureau of Reclamation, Technical Service Center, Hydraulic Investigation and Laboratories Services, Denver, Colorado, USA, 2014.

[25] USACE, *Report on Model Studies of Spillway for Kaysinger Bluff Dam Osage River, Missouri, Hydraulic Model Investigation*, *Report No:* TR/2-809, US Department of The Army Engineer, Waterways Experiment Station, Vicksburg, Miss., USA, 1968.

[26] USACE, *Report on Model Studies of Spillway for Oakley Dam, Sangamon River, Hydraulic Model Investigation,* Technical Report TR-H-70-13. Hydraulics Laboratory, US Department of The Army Engineer, Waterways Experiment Station, Vicksburg, Miss., USA, 1970.

[27] USACE, *Report on Model Studies of Spillway for Oakley Dam Sangamon River, Illinois. Appendix A: Type 2 (Revised) Spillway, Hydraulic Model Investigation, Report No:* TR/H-70-13-App-A, US Department of The Army Engineer, Waterways Experiment Station, Vicksburg, Miss., USA, 1972.

[28] USACE, *Report on Model Studies of Spillway for Burnsville Dam, Little Kanawha River, West Virginia, Hydraulic Model Investigation, Report No:* TR/H-75-5, US Department of The Army Engineer, Waterways Experiment Station, Vicksburg, Miss., USA, 1975.

[29] USACE, *Report on Model Studies of Typical Tennessee-Tombigbee Canal Section Spillways, Spillways A and B,* Hydraulic Model Investigation*,* Technical Report H-78-21, Hydraulics Laboratory, US Department of The Army Engineer, Waterways Experiment Station, Vicksburg, Miss., USA, 1978.

[30] USACE, *Report on Model Studies of Spillway for Cooper Dam, Sulphur River, Texas. Hydraulic Model Investigation, Report No:* TR/HL-80-15, US Department of The Army Engineer, Waterways Experiment Station, Vicksburg, Miss., USA, 1980.

[31] USACE, *Report on Model Studies of Bloomington Spillway North Branch Potomac River Maryland and West Virginia, Hydraulic Model Investigation*, *Report No:*TR/HL-83-9, US Department of The Army, Waterways Experiment Station, Vicksburg, Miss., USA, 1983.

[32] USACE, *Report on Model Studies of Lake Darling Spillway Souris River, North Dakota, Hydraulic Model Investigation, Report No:* TR/HL-88-9, US Department of The Army Engineer, Waterways Experiment Station, Vicksburg, Miss., USA, 1988.

[33] USACE, *Report on Model Studies of Pompton Dam Spillway, Pompton Lake Ramapo River Basin, New Jersey, Hydraulic Model Investigation, Technical Report* HL-91-19, US Department of The Army Engineer, Waterways Experiment Station, Vicksburg, Miss., USA, 1991.

[34] DSI, *Report on Flowrate Measurements at the Flood Routing Spillway of Seyhan Dam* (in Turkish). Ministry of Housing and Development, General Directorate of State Water Works, Ankara, Turkey, 1959.

[35] DSI, *Report on Model Studies of Flood Spillway of Kigi Dam, Model no:356, Publication no: 969* (in Turkish). Technical Research and Quality Control Department, General Directorate of State Water Works, Ankara, Turkey, 2004.

[36] DSI, *Report on Model Studies of Flood Spillway of Yedigoze Dam, Model no:381, Publication no: 995* (in Turkish). Technical Research and Quality Control Department, General Directorate of State Water Works, Ankara, Turkey, 2008.

[37] DSI, *Report on Model Studies of Flood Spillway of Kavsak Dam, Model no:385, Publication no: 1005* (in Turkish). Technical Research and Quality Control Department, General Directorate of State Water Works, Ankara, Turkey, 2010.

[38] DSI, *Report on Model Studies of Flood Spillway of Beyhan-1 Dam, Model no:392, Publication no: 1017* (in Turkish). Technical Research and Quality Control Department, General Directorate of State Water Works, Ankara, Turkey, 2012.

[39] DSI, *Report on Model Studies of Flood Spillway of Incir Dam, Model no:402, Publication no: 1026* (in Turkish). Technical Research and Quality Control Department, General Directorate of State Water Works, Ankara, Turkey, 2013.

[40] DSI, *Report on Model Studies of Flood Spillway of Yusufeli Dam, Model no:406, Publication no: 1033* (in Turkish). Technical Research and Quality Control Department, General Directorate of State Water Works, Ankara, Turkey, 2015.

[41] Khalaf M., *Comparison of Discharge Coefficients for Partially-Opened Radial-Gated Ogee Spillways*, M. Sc. Thesis. Graduate School of Natural and Applied Sciences, Erciyes University, Kayseri, Turkey, 2017, tez.yok.gov.tr/ulusaltezmerkezi/

Teknik Dergi, 2021 10947-10965, Paper 619

Detecting Drought Variability by using Two-Dimensional Correlation Analysis

Fatih DIKBAŞ[1]
Ülker Güner BACANLI[2]

ABSTRACT

The Standardized Precipitation Index (SPI) has been recognized as the standard index that should be used for quantifying and reporting meteorological drought. This study aims to present the application of the two-dimensional correlation method for determining the spatial and temporal variability of drought among the SPI series. Heatmaps were used as a new way of visualizing SPI series which enables visual inspection of dry and wet periods. The developed method was applied on 13 meteorological stations in Central Anatolia. Significant variations in drought behaviour were found in the investigated region even for the stations close to each other.

Keywords: Drought variability, standardized precipitation index, two-dimensional correlation, drought visualization, Central Anatolia.

1. INTRODUCTION

Drought is an extreme natural weather event posing a threat to available water resources and it has been associated with human-induced global warming [1]. Together with the slow but continuous worldwide decrease of total available water [2, 3] and rapidly rising human population, the intensity and frequency of drought events is likely to increase worldwide. Droughts can cause devastating impacts on the environment and on society resulting with higher economic damages than the other catastrophes like earthquakes. Droughts influence both surface water and groundwater resources, therefore, drought modelling has drawn attention of researchers in many fields including ecology, hydrology, meteorology and agriculture [4]. The current research shows that drought will continue to be one of the most important natural disasters faced by the future generations. This increasing threat of extreme weather events also increases the requirement for reliable modelling, estimation and prediction of drought. Accurate evaluation of the existing data on drought allows us to

Note:
- This paper has been received on April 30, 2019 and accepted for publication by the Editorial Board on January 7, 2020.
- Discussions on this paper will be accepted by September 30, 2021.

• https://doi.org/10.18400/tekderg.559195

1 Pamukkale University, Civil Engineering Department, Denizli, Turkey
f_dikbas@pau.edu.tr - https://orcid.org/0000-0001-5779-2801

2 Pamukkale University, Civil Engineering Department, Denizli, Turkey
ugbacanli@pau.edu.tr - https://orcid.org/0000-0002-2279-9138

monitor and predict changing drought patterns in spatial and temporal scales. There is a continuous research to understand the behavior of droughts under climate change due to the changes in spatio-temporal variability of precipitation [4].

Drought contrasts from other natural hazards in that it is difficult to determine the initiation and the end of drought. The effects of drought are seen in many areas including economic, social, and environmental processes. Drought has been classified into four groups: socioeconomic, agricultural, hydrological and meteorological [5]. Generally, the first observed drought is the meteorological (or climatological) drought, later the effects of agricultural drought are seen. Socio-economic drought occurs either together with or after meteorological drought if water supply does not satisfy water demand.

Determination of drought is also a difficult task. Different drought parameters were proposed by researchers in order to define drought as well as to identify the interactions between drought and hydrological/meteorological events (e.g. the Rainfall Anomaly Index (RAI) [6], the Crop Moisture Index (CMI) [7], the Standardized Precipitation Index (SPI) [8], the Surface Water Supply Index (SWSI) [9], the Percent of Normal Precipitation Index (PNPI) [10] and the Standardized Precipitation-Evapotranspiration Index (SPEI) [11].

With the aim of detecting, observing and analysing drought events, the SPI has been widely used by researchers as a well-reviewed and robust index since it has a clear computation procedure and a multi-scalar character. The calculation of the SPI, the drought index recommended by the World Meteorological Organisation, requires only the precipitation data as input [12].

The following are some examples in current literature applying SPI together with other methods aiming at identification of drought. A comparison of SPI and Palmer Drought Severity Index (PDSI) was presented by Guttmann [13]. Drought in the south-western United States was examined using the SPI by Hayes et al. [14]. Keyantash and Dracup [15] used 14 drought indices in United States. Morid et al. [16] used seven meteorological indices which included the Percent of Normal (PN), the Deciles Index (DI), the China-Z index (CZI), the SPI, the Modified CZI (MCZI), the Z-Score and the Effective Drought Index (EDI) for the assessment of drought in Iran. Livada and Assimakopoulos [17] calculated the SPI values by utilising data from 23 stations in Greece. They investigated drought's intensity and duration for a period of 51 years.

A comparison of the Reconnaissance Drought Index (RDI) and SPI was carried out in Iran by Jamshidi et al. [18]. A study by Jain et al. [19] compared SPI, Statistical Z-Score, EDI, Rainfall Departure (RD), CZI, and Rainfall Decile based Drought Index (RDDI) in central India. Bandyopadhyay and Saha used four drought indices (SPI, RAI, Normalized Difference Vegetation Index (NDVI) Anomaly Index (NAI) and Vegetation Condition Index (VCI)) for the analysis of drought in India [20].

The previous works generally make use of time series graphs for investigating SPI values. This paper presents a new approach where matrices and heatmaps are evaluated for revealing temporal and spatial relationships among SPI series. This approach allows visual and quantitative comparison of SPI series with different durations and also provides information on differences of drought behaviour among stations.

1.1. Drought in Turkey

In a climatological viewpoint, the majority of Turkish mainland has a dry and semi-dry property and influence of drought has been frequently experienced in the region throughout history [21]. Even though drought is a serious problem and the severe drought in 1876 had killed about 200.000 people [21, 22], there is a limited number of scientific studies on drought in Turkey. Some of the existing research were focused on water supply system and drought in Istanbul [23]; analysis of spatial and temporal patterns [24] and probabilities [25] of drought in Turkey based on the SPI; application of meteorological drought modelling for drought in Turkey [26] and in Central Anatolia [27]; drought analysis in Antakya-Kahramanmaraş Graben [28]; analysis of the 2007 and 2013 droughts in Turkey by NOAH Hydrological Model [29], trend analysis of precipitation and drought in the Aegean region [30] and long-term spatio-temporal drought variability in Turkey [31, 32].

The drought document of the Turkish Ministry of Agriculture and Forestry states that drought occurs in connection with the irregularities in precipitation events [21]. Figure 1 shows that these significant precipitation variations cause droughts in different severity levels in widespread or local scales in Turkey which is within the Mediterranean macro climate zone in the subtropical belt [33]. The figure shows that Central Anatolia is the most vulnerable region in terms of drought. Therefore, the Central Anatolian Region was selected for the application of the two-dimensional correlation method [34] for a quantitative identification and comparison of temporal drought patterns among selected meteorological observation stations in the region.

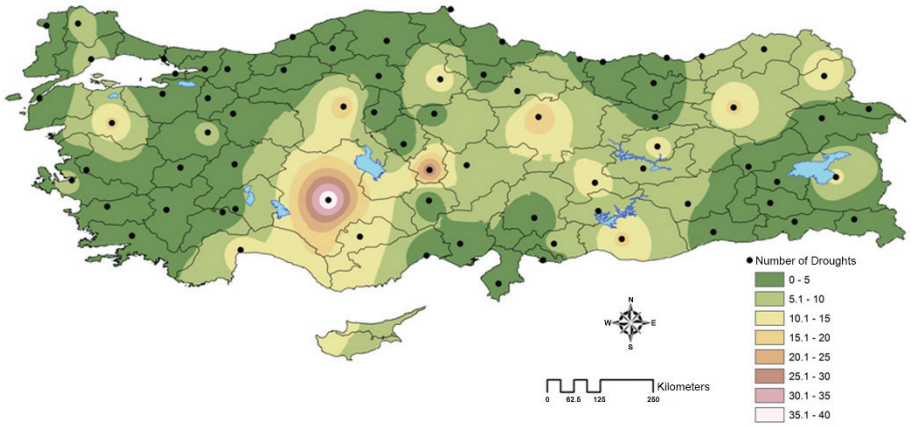

Figure 1 - Areal distribution of drought numbers in Turkey (1940-2010) [32]

1.2. The Study Area and Available Data

The Central Anatolian Region extends over an area of approximately 151.000 km^2, which is the second largest region of Turkey. It consists of four subbasins (the upper Kızılırmak, the middle Kızılırmak, the upper Sakarya and the Konya basin) (Figure 2). Steppe climate prevails in the region [27, 35, 36]. In this study, precipitation observations from 13 meteorological stations in the Central Anatolian Region listed in Table 1 were used for meteorological drought analysis.

Figure 2 - Central Anatolian Region (adapted from [37])

Table 1 - Spatial characteristics of the investigated stations [37]

Watershed	Meteorological Stations	Meteorological Station Number	Longitude	Latitude	Elevation (m)	Watershed Area (km^2)
Upper Sakarya	Eskişehir	17124	30º 35′	39º 47′	786	33.847
	Ankara	17130	32º 53′	39º 57′	891	
	Çankırı	17080	33º 37′	40º 37′	751	
Konya	Konya	17244	32º 33′	37º 59′	1031	53.850
	Aksaray	17192	34º 03′	38º 23′	961	
	Karaman	17246	33º 13′	37º 12′	1023	
Upper Kızılırmak	Sivas	17090	37º 01′	39º 45′	1285	6.607
Middle Kızılırmak	Kayseri	17196	35º 29′	38º 45′	1093	78.180
	Nevşehir	17193	34º 42′	38º 37′	1260	
	Niğde	17250	34º 41′	37º 58′	1211	
	Kırşehir	17160	34º 09′	39º 10′	1007	
	Kırıkkale	17135	33º 31′	39º 51′	751	
	Yozgat	17140	34º 48′	39º 49′	1298	

This study presents the application of the two-dimensional correlation method for determining the spatial and temporal variability of drought among the SPI series. For this aim, two-dimensional correlation analysis was performed on SPI-1, SPI-3, SPI-6, SPI-9, SPI-12 and SPI-24 series which were calculated for all stations. The following chapter provides a short background information on the calculation of the SPI and the two-dimensional correlation coefficients. Then, the application of the SPI and the two-dimensional correlation methods on available data is described. Finally, the results and conclusions are presented together with some discussion on the new approaches and viewpoints on the investigation of drought variability enabled by the use of the presented methodology.

2. METHODS

2.1. The Standardized Precipitation Index (SPI)

The SPI was introduced by McKee et. al. [12] with the purpose of determining droughts by investigating precipitation data. The SPI is a drought index which is commonly used worldwide [14]. Researchers have been routinely calculating the SPI based on monthly precipitation totals for various durations including 1, 3, 6, 12, 18, 24, 36, 48, and 60 months [15]. The SPI is calculated as follows:

$$SPI = \frac{x_i - \mu}{\sigma} \tag{1}$$

where x_i is precipitation, μ is the mean of precipitation and σ is the standard deviation. Probability distribution function for data is calculated by fitting the gamma function [38]. The data sets are organized for various periods. Later, x is presumed as the monthly total precipitation in the investigated period of time. The gamma distribution function is first fitted to the data accumulated for various time scales. The probability density function of the gamma distribution is defined as:

$$g(x) = \frac{1}{\beta^{\alpha}\Gamma(\alpha)} x^{\alpha-1} e^{x/\beta} \tag{2}$$

for $x > 0$ where, x is the amount of precipitation and $\Gamma(\alpha)$ is the Gamma function. The following equations are used for calculating α, the shape parameter, and β, the scale parameter.

$$\alpha = \frac{1}{4A}\left(1 + \sqrt{1 + \frac{4A}{3}}\right) \tag{3}$$

$$\beta = \frac{\bar{x}}{\alpha} \tag{4}$$

Here, $\bar{x}$ is the mean precipitation and A is given by:

$$A = ln(\bar{x}) - \frac{\sum ln(x)}{n} \tag{5}$$

The following equation defines the cumulative probability distribution:

$$G(x) = \int_0^x g(x)dx = \frac{1}{\beta^{\alpha}\Gamma(\alpha)} \int_0^x x^{\alpha-1} e^{-x/\beta} dx \quad (6)$$

The gamma distribution is undefined when x = 0, and, when the probability of zero precipitation q = P(x = 0) is positive, the cumulative probability is calculated as follows:

$$H(x) = q + (1 - q) \cdot G(x) \quad (7)$$

The cumulative probability distribution is then transformed into the standard normal distribution to yield the SPI [32]. The following table shows the drought classification according to the ranges of the calculated SPI values.

Table 2 - The categories of the Standardized Precipitation Index [12][39]

SPI index values	Drought Category
≥ 2	Extremely Wet (W4)
1.50 ~ 1.99	Very Wet (W3)
1.00 ~ 1.49	Moderately Wet (W2)
0.99 ~ 0	Mildly Wet (W1)
0 ~ -0.99	Mild Drought (D1)
-1.00 ~ -1.49	Moderate Drought (D2)
-1.50 ~ -1.99	Severe Drought (D3)
≤ - 2	Extreme Drought (D4)

2.2. Two-dimensional Correlation

The two-dimensional correlation method assesses associations between matrices in two directions by making use of the horizontal and the vertical covariances [34, 40]. The approach is based on the idea that the values of a variable generally have different variances in the horizontal and vertical directions when placed on a matrix. Before giving the equations for the two-dimensional correlation, two-dimensional variance and two-dimensional covariance are defined for a better understanding of the methodology.

2.2.1. Two-dimensional Variance

Variance is the measure of the spread around the average. The following equations show the calculation of the horizontal and the vertical variance:

$$Var_h(A) = \frac{\sum_m \sum_n (A_{mn} - \overline{A_m})^2}{m \times n} \quad (8)$$

$$Var_v(A) = \frac{\sum_m \sum_n (A_{mn} - \overline{A_n})^2}{m \times n} \quad (9)$$

In the above equations the averages of the m[th] row and the n[th] column of the matrix A are indicated by $\overline{A_m}$ and $\overline{A_n}$ respectively.

When the column averages in the matrices are more scattered around the overall average, the horizontal variance takes high values and when the column averages are closer to the overall average, the horizontal variance decreases in value. The same situation is valid for the row averages when calculating the vertical variance.

2.2.2. Two-dimensional Covariance

The linear dependence among variables is calculated by covariance which is a quantitative indicator of the co-variation of the variables. In the calculation of two-dimensional correlation, the horizontal covariance provides a measure of how changes in the column averages of one matrix are associated with changes in the column averages of a second matrix. Correspondingly, the vertical covariance provides a similar information among the rows of the compared matrices. The association between the compared variables is generally expected to be high when the covariance takes higher values (positive covariance indicates direct relationship and negative covariance indicates inverse relationship). The horizontal and vertical covariances between scalar matrices A and B are defined by the following equations:

$$Cov_h(A, B) = \frac{\sum_m \sum_n (A_{mn} - \overline{A_m})(B_{mn} - \overline{B_m})}{m \times n} \quad (10)$$

$$Cov_v(A, B) = \frac{\sum_m \sum_n (A_{mn} - \overline{A_n})(B_{mn} - \overline{B_n})}{m \times n} \quad (11)$$

In the above equations, $\overline{B_m}$ and $\overline{B_n}$ are the averages of the m[th] row and the n[th] column of the matrix B respectively.

2.2.3. Two-dimensional Correlation

Covariance is a scale dependent measure of the joint variability among variables. The covariance is positive when the higher values of a variable correspond to the higher values of the compared variable and the same behavior is observed between the lower values of the variables. Covariance takes negative values when the values of the variables tend to show inverse relationship (i.e., higher values of a variable correspond to the lower values of the compared variable). The value of covariance is influenced with the magnitudes of the compared variables, therefore, its value has to be normalized when there is need for comparison of associations among multiple variable pairs. For example, it would not be reasonable to make comparisons of precipitation series by only using covariance because generally there are significant differences between scales of the observed precipitation series in different basins of varied climate zones. Correlation coefficient, which should be preferred in comparisons of variables, is the scaled and normalized version of covariance and it is

dimensionless. Based on the horizontal and the vertical covariance values, the horizontal and vertical correlation coefficients are obtained with the following equations:

$$r_h = \frac{Cov_h(A,B)}{\sqrt{Var_h(A)\,Var_h(B)}} \tag{12}$$

$$r_v = \frac{Cov_v(A,B)}{\sqrt{Var_v(A)Var_v(B)}} \tag{13}$$

The horizontal and the vertical correlations might also be calculated directly as follows:

$$r_h = \frac{\sum_m \sum_n (A_{mn} - \overline{A_m})(B_{mn} - \overline{B_m})}{\sqrt{[\sum_m \sum_n (A_{mn} - \overline{A_m})^2][\sum_m \sum_n (B_{mn} - \overline{B_m})^2]}} \tag{14}$$

$$r_v = \frac{\sum_m \sum_n (A_{mn} - \overline{A_n})(B_{mn} - \overline{B_n})}{\sqrt{[\sum_m \sum_n (A_{mn} - \overline{A_n})^2][\sum_m \sum_n (B_{mn} - \overline{B_n})^2]}} \tag{15}$$

In the above equations, r_h and r_v are the horizontal and the vertical correlations between the matrices A and B.

The two-dimensional correlation coefficients provide a quantitative measure of association between rows and columns of the compared matrices. Here in this paper, the SPI values obtained for each month of year are located in rows to generate the SPI matrices for all 13 stations. Then, the two-dimensional correlation coefficients are obtained for each year for each station allowing a quantitative comparison between both the annual drought characteristics of the stations and the differences between the SPI series when different durations are considered (1, 3, 6, 9, 12 and 24 months). For example, it is expected that the SPI series will have different annual averages when the investigated duration varies and quantitative evaluation of these differences will provide information on differences in drought behavior among the stations. The two-dimensional correlation method provides tools for making this deterministic comparison. The details of this process are presented below in Section 4.

3. RESULTS AND DISCUSSION

3.1. The Standardized Precipitation Index (SPI) Analysis

SPI values were computed for the 13 stations in the Central Anatolian Region, for the periods of 1, 3, 6, 9, 12 and 24 months, covering the years 1959-2001 (43 years). As an example, the relative frequencies of the SPI values calculated for the Çankırı station for the 1, 3, 6, 9, 12 and 24 months time periods are given in Figure 3. Extreme, severe and moderate droughts were identified in the basin. Relative frequencies were also calculated. The results obtained for all stations are displayed in Table 3.

The results of the SPI analysis indicated that a significant change could not be observed according to the ratios of the dry, normal or wet periods of a single station. However, normal (mild wet) or mild droughts were more frequently encountered in shorter periods (3-6 months) whereas severe and very severe droughts were observed during longer time periods

(12-24 months) in the Central Anatolian Region. Both cases can be evaluated in a different view for various water resources problems. For instance, a drought with a 3 months duration might have more influence on soil moisture, while underground water resources might be influenced by a drought with a longer duration. The dryness ratios of the stations under investigation in the Central Anatolian Region were determined to vary between 55% and 20%, and the wetness ratios were found to vary between 19% and 13% based on their SPI indices.

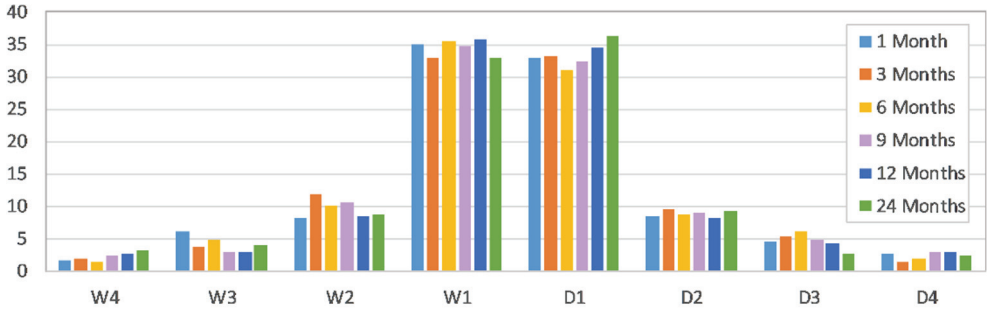

Figure 3 - Relative frequencies of SPI for the Çankırı Station

Table 3 - The dryness (D) and wetness (W) ratios (%) of the SPI values of the evaluated stations in the Central Anatolian Region for time periods of 3, 6, 9, 12 and 24 months

		3 Months		6 Months		9 Months		12 Months		24 Months	
		D	W	D	W	D	W	D	W	D	W
Upper Sakarya	Eskişehir	47	16	44	18	44	16	41	15	44	16
	Ankara	50	17	51	16	50	16	51	16	52	15
	Çankırı	50	18	48	16	49	16	50	14	51	16
Konya	Konya	45	15	46	14	48	16	50	14	46	13
	Aksaray	48	16	50	17	53	18	52	17	53	16
	Karaman	49	17	46	16	46	16	48	15	54	16
Upper Kızılırmak	Sivas	45	16	48	16	51	18	50	17	20	18
Middle Kızılırmak	Kayseri	50	16	50	17	50	16	50	16	55	18
	Nevşehir	46	16	50	16	47	16	46	16	51	16
	Niğde	45	17	44	15	46	16	48	15	47	14
	Kırşehir	46	17	48	16	49	18	52	18	47	19
	Kırıkkale	49	17	49	15	54	17	55	17	52	18
	Yozgat	48	15	46	17	48	16	48	15	20	16
	Average	48	16	48	16	49	17	49	16	46	16
	Range	45-50	15-18	44-51	14-18	44-54	16-18	41-55	14-18	20-55	13-19

It was observed that the maximum drought duration increased with the increase of the period. Moreover, when the droughts in the Central Anatolian Region are examined, it has been determined that the duration of droughts tend to increase. Three months SPI indicated a 13 months of drought duration, while 24 months SPI indicated a 72 months of drought duration. After the determination of the SPI values for each station for each period, the degree of relationship between the obtained SPI series were assessed by applying the two-dimensional correlation method. The assessment is made both in terms of the SPI values of each month for each year and in terms of the calculated durations (1-24 months) as explained below.

3.2. Two-dimensional Correlation Analysis

For calculating the horizontal and vertical correlations between each station for each year, all calculated SPI series were located on matrices for each station as shown in the heatmaps generated by using the SPI series of Ankara and Çankırı stations (Figure 4). In the heatmaps, the columns for each year start with January and end with December. Ankara and Çankırı stations were selected to introduce the application of the two-dimensional correlation analysis on SPI series. The heatmaps for the remaining 11 stations are presented in the Appendix. As far as the authors know, this representation is used for the first time in literature for the inspection of SPI series and enables a visual evaluation of drought variation both with time and with the variation of investigated period. The darker shades of red indicate the periods with a higher intensity of drought and alternatively, the darker shades of blue indicate the wet periods. Visual comparison of the SPI temporal variability heatmaps of different stations also provides clues about the existence, duration and severity of concurrent droughts. For example, the heatmaps in the Appendix show that a very wet period is observed for most of the cities in the years 1996 and 1997; while a persistent drought was observed in Eskişehir in the same years it was neither dry nor wet in Aksaray in these years.

Calculation of the two-dimensional correlations between the SPI matrices of different stations provides an opportunity to make a quantitative comparison of associations between the variation of the SPI values both with time and with the evaluated period (1, 3, 6, 9, 12 and 24 months). The two-dimensional Pearson's correlations calculated between the whole SPI matrices of all station pairs present an overall evaluation of the degrees of associations (Figure 5). For a better discrimination of higher and lower associations, this figure uses tones of red for indicating lower values and tones of green for indicating higher values. The stations in Ankara and Çankırı have the highest correlation (0.740) followed by the station pairs Çankırı-Kırıkkale (0.735) and Kayseri-Nevşehir (0.725). These relatively higher correlations point out that drought shows a similar behavior among the stations. Alternatively, the lower correlated pairs might have more significant differences in view of drought behavior. For example, the correlation values obtained for Eskişehir are all close to zero which might indicate that drought variability in Eskişehir has no significant association with the compared stations.

Another finding based on the results in Figure 5 is that there are two groups of stations highly correlated with each other but having lower correlations with the remaining stations. The first group is Ankara, Çankırı, Kırıkkale and Kırşehir stations which are located in the upper section of the region and the correlations between these stations vary between 0.531 and 0.740. The other highly correlated group includes the stations Kayseri, Nevşehir, Niğde,

Sivas and Yozgat, which are in the eastern part of the region. The correlations for the second group varies between 0.588 and 0.725.

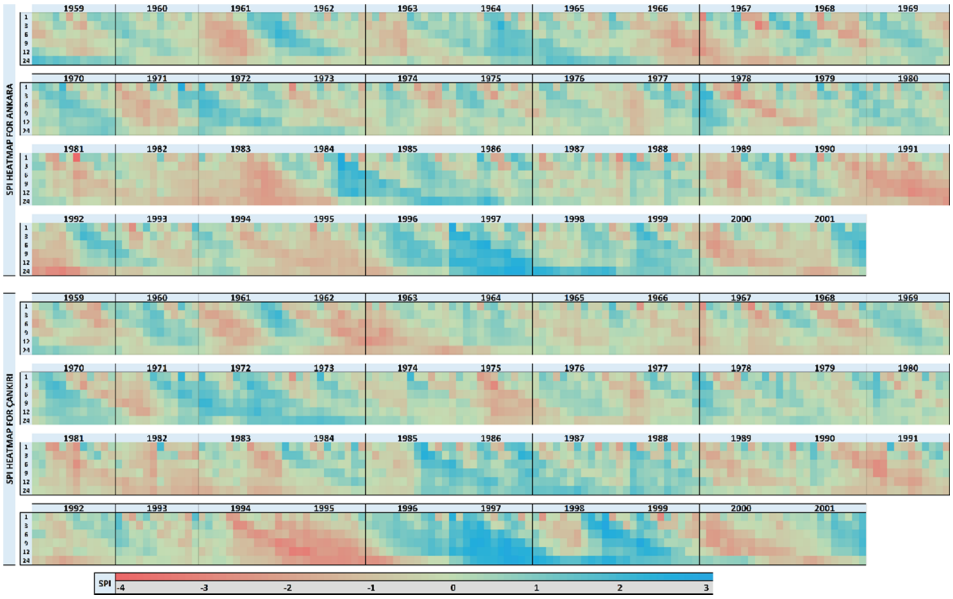

Figure 4 - SPI matrices for Ankara (top) and Çankırı (bottom) stations showing temporal variability of drought

	Ankara	Çankırı	Eskişehir	Karaman	Kayseri	Kırıkkale	Kırşehir	Konya	Nevşehir	Niğde	Sivas	Yozgat
Aksaray	0,033	0,014	0,063	0,099	0,135	-0,026	0,058	0,059	0,135	-0,003	0,049	0,023
Ankara		0,740	-0,014	0,215	0,237	0,715	0,604	0,176	0,286	0,252	0,280	0,309
Çankırı			-0,086	0,075	0,202	0,735	0,531	0,042	0,215	0,219	0,229	0,301
Eskişehir				0,113	-0,024	-0,025	-0,010	0,126	-0,115	-0,115	0,007	-0,083
Karaman					0,448	0,154	0,249	0,625	0,464	0,532	0,468	0,403
Kayseri						0,289	0,279	0,407	0,725	0,670	0,691	0,588
Kırıkkale							0,634	0,125	0,306	0,245	0,265	0,341
Kırşehir								0,160	0,368	0,302	0,287	0,341
Konya									0,468	0,600	0,463	0,474
Nevşehir										0,652	0,679	0,647
Niğde											0,667	0,627
Sivas												0,602

Figure 5 - Two-dimensional Pearson's correlations between the SPI matrices of the stations

The behavior of drought might show variations with the progress of time even though there is a relatively high correlation between the SPI values of the stations. For example, the heatmaps for Ankara and Çankırı show that drought was more severe in Ankara in 1992 while it was more severe in Çankırı in 1994-1995 period. Therefore, calculation of correlations at annual scale enables determination of the differences between the variations of drought behavior through the investigated duration for the compared stations. Figure 6 shows the two-

dimensional Pearson's correlations (r), the horizontal correlations (r_h) and the vertical correlations (r_v) between the SPI matrices of the Ankara and Çankırı stations for each year in the investigated period. This figure also uses tones of red for indicating lower values and tones of green for indicating higher values.

Year	1959	1960	1961	1962	1963	1964	1965	1966	1967	1968	1969	1970	1971	1972	1973
r	0,503	0,017	0,882	0,311	-0,097	0,681	0,640	0,452	0,616	0,602	0,474	0,397	0,666	0,538	0,142
r_h	0,549	-0,059	0,813	0,408	0,162	0,557	0,649	0,594	0,565	0,558	0,675	0,401	0,736	0,516	-0,011
r_v	0,416	0,151	0,886	0,378	-0,195	0,757	0,698	0,412	0,765	0,661	0,469	0,417	0,629	0,635	0,150

Year	1974	1975	1976	1977	1978	1979	1980	1981	1982	1983	1984	1985	1986	1987	1988
r	0,728	0,609	0,396	-0,356	0,754	0,622	0,436	0,678	0,595	0,708	0,885	0,735	0,442	0,567	0,514
r_h	0,725	0,619	0,594	-0,322	0,675	0,570	0,441	0,578	0,479	0,625	0,902	0,732	0,583	0,581	0,442
r_v	0,737	0,626	0,410	-0,324	0,792	0,579	0,512	0,752	0,708	0,709	0,854	0,695	0,390	0,645	0,570

Year	1989	1990	1991	1992	1993	1994	1995	1996	1997	1998	1999	2000	2001
r	0,863	0,328	0,743	0,898	0,712	0,279	0,609	0,844	0,849	0,841	0,790	0,599	0,752
r_h	0,846	0,348	0,751	0,917	0,737	0,234	0,693	0,846	0,865	0,876	0,753	0,756	0,762
r_v	0,860	0,487	0,733	0,834	0,736	0,321	0,462	0,803	0,769	0,754	0,771	0,424	0,669

Figure 6 - Two-dimensional Pearson's correlations (r), horizontal correlations (r_h) and vertical correlations (r_v) between the annual SPI matrices of the Ankara and Çankırı stations

An overall inspection of the heatmaps and Figure 6 reveals that the SPI matrices are generally not highly correlated except for a few years including 1961, 1984, 1989 and the 1996-1998 period. It is also seen that there is an inverse relationship between the monthly SPI series for the compared stations in 1977 (r_v = -0.324) and that the SPI-1, SPI-3, SPI-6, SPI-9, SPI-12 and SPI-24 series are also inversely related in 1977 (r_h = -0.322). This inverse relationship is also validated by the Pearson's correlation for the same year (r = -0.356).

The highest r (0.898) and r_h (0.917) values were obtained for 1992 while the highest r_v (0.886) was obtained for 1961, all of which are much higher than the correlation between the whole matrices (0.740). All correlations for 1977 are negative (and minimum) indicating an inverse relationship both in the vertical and the horizontal directions. For some years, there are significant differences between the values of r, r_h and r_v. For example, in the year 2000, r_h = 0.756 and r_v = 0.424, indicating that the row-wise relationship of SPI values are stronger and that the column-wise relationship is weaker than the association indicated by the Pearson's correlation. Alternatively, in 1982, the row-wise relationship is weaker (r_h = 0.479) and the column-wise relationship (r_v = 0.708) between the SPI values are stronger. Similar situations are observed in years like 1993, 1967 and 1995 in which a severe drought was observed in both stations as also seen in the heatmaps. The correlation values in Figure 6 provide a clear picture of the variation of the behavior of drought from 1959 to 2001 and show that there are periods where the relationship is strong and there are periods where the relationship is weak or even inverse. This situation was also observed in other stations indicating a strong temporal and spatial variation of drought behavior in the region.

The correlation calculations were made for a total of 77 station pairs, but they are not presented here because of space restrictions and can be downloaded from the following link:

https://drive.google.com/open?id=1soOtBWN5dcDQ_QPR1hyYygF_4YJPVVyU

The results for other stations point out that there are significant variations in drought behavior through the investigated period and the variations do not follow a similar trend. The obtained results show that the behavior of drought might show significant differences when investigated annually even though the compared stations are spatially close to each other and even their SPI series are highly correlated. For example, the stations in Kayseri and Nevşehir are very close to each other but through the investigated period of 43 years the correlations were higher than 0.9 for only 3 years (1976, 1996 and 1998). The average annual correlation for this pair is 0.67, and in some years (1960, 1990 and 1994) the correlations fall under 0.3. The correlations do not show a stable behavior in any of the station pairs. Under the light of the findings of this study, future works might aim at determination of drought frequency and variation of drought severity by evaluating more recent data.

3.3. The 2DCorr Software

The software used for the application of the presented methodology was developed in the Visual Studio environment with Visual Basic. The software is an adapted version of the Corr2D software and accepts SPI data matrices as input. The software will be provided freely by the authors upon request together with sample input and output files.

4. CONCLUSIONS

In this study, SPI values were calculated by using monthly precipitation values of 13 stations in the Central Anatolian Region. Two-dimensional correlations were calculated between the station pairs for investigating variability of drought according to both the annual relationships and the evaluated period (1, 3, 6, 9, 12 and 24 months). The drought periods in the region have shown a cyclic behavior as indicated by the long term observation data. Furthermore, the two-dimensional correlation results have shown that the drought behavior exhibits significant variations even for the station pairs which are highly correlated.

The two-dimensional correlation method provides an in-depth evaluation of the SPI series. The main conclusion of the study is that there are significant temporal and spatial variations in drought behavior in the investigated Central Anatolian Region which is regarded as the most vulnerable region for drought. The findings indicate that the presented approach might be reliably used in drought assessment and evaluation. Determination of regional variations in drought behavior has an important role in the planning and design of water structures. Therefore, knowledge of drought variability makes an important contribution in making decisions on drought precautions and provides possibilities for better predictions on future droughts.

Symbols

x_i : Observed precipitation

μ : Mean precipitation

σ : Standard deviation

$\Gamma(\alpha)$: Gamma function

α : Shape parameter

β : Scale parameter

$Var_h(A)$: Horizontal variance of matrix A

$Var_v(A)$: Vertical variance of matrix A

$Cov_h(A, B)$: Horizontal covariance between the matrices A and B

$Cov_v(A, B)$: Vertical covariance between the matrices A and B

r_h : Horizontal correlation

r_v : Vertical correlation

References

[1] Hansen, J., Sato, M., Ruedy, R., Lacis, A., Oinas, V., Global Warming in the Twenty-First Century: An Alternative Scenario. Proc. Natl. Acad. Sci. U. S. A., 97(18), 9875-9880, 2000.

[2] Leconte, J., Forget, F., Charnay, B., Wordsworth, R., Pottier, A., Increased Insolation Threshold for Runaway Greenhouse Processes on Earth-Like Planets. Nature, 504(7479), 268-271, 2013.

[3] Popp, M., Schmidt, H., Marotzke, J., Transition to a Moist Greenhouse with Co2 and Solar Forcing. Nat Commun, 7, 2016.

[4] Mishra, A.K., Singh, V.P., A Review of Drought Concepts. Journal of Hydrology, 391(1), 202-216, 2010.

[5] Wilhite, D.A., Glantz, M.H., Understanding: The Drought Phenomenon: The Role of Definitions. Water International, 10(3), 111-120, 1985.

[6] Van Rooy, M.P., A Rainfall Anomaly Index Independent of Time and Space. Notos, 14, 43, 1965.

[7] Palmer, W.C., Keeping Track of Crop Moisture Conditions, Nationwide: The New Crop Moisture Index. Weatherwise, 21(4), 156-161, 1968.

[8] McKee, T.B.N., J. Doeskin, N., Kleist, J., Drought Monitoring with Multiple Time Scales. 1995.

[9] Shafer, B.A., Dezman, L.E., Development of a Surface Water Supply Index (Swsi) to Assess the Severity of Drought Conditions in Snowpack Runoff Areas, in 50th Annual Western Snow Conference. 1982, Western Snow Conference: Reno, Nevada.

[10] Willeke, G., Hosking, J., Wallis, J., Guttman, N., The National Drought Atlas. Institute for water resources report, 94, 1994.

[11] Vicente-Serrano, S.M., Beguería, S., López-Moreno, J.I., A Multiscalar Drought Index Sensitive to Global Warming: The Standardized Precipitation Evapotranspiration Index. J. Clim., 23(7), 1696-1718, 2010.

[12] McKee, T.B., Doesken, N.J., Kleist, J., The Relationship of Drought Frequency and Duration to Time Scales, in 8th Conference on Applied Climatology. 1993: Anaheim, CA, . p. 179-184.

[13] Guttman, N.B., Accepting the Standardized Precipitation Index: A Calculation Algorithm. Journal of the American Water Resources Association, 35(2), 311-322, 1999.

[14] Hayes, M., Svoboda, M., Wall, N., Widhalm, M., The Lincoln Declaration on Drought Indices: Universal Meteorological Drought Index Recommended. Bulletin of the American Meteorological Society, 92(4), 485-488, 2011.

[15] Keyantash, J., Dracup, J.A., The Quantification of Drought: An Evaluation of Drought Indices. Bulletin of the American Meteorological Society, 83(8), 1167-1180, 2002.

[16] Morid, S., Smakhtin, V., Moghaddasi, M., Comparison of Seven Meteorological Indices for Drought Monitoring in Iran. Int. J. Climatol., 26(7), 971-985, 2006.

[17] Livada, I., Assimakopoulos, V.D., Spatial and Temporal Analysis of Drought in Greece Using the Standardized Precipitation Index (Spi). Theoretical and Applied Climatology, 89(3-4), 143-153, 2007.

[18] Jamshidi, H., Khalili, D., Zadeh, M.R., Hosseinipour, E.Z. Assessment and Comparison of Spi and Rdi Meteorological Drought Indices in Selected Synoptic Stations of Iran. in World Environmental and Water Resources Congress 2011: Bearing Knowledge for Sustainability - Proceedings of the 2011 World Environmental and Water Resources Congress. 2011.

[19] Jain, V.K., Pandey, R.P., Jain, M.K., Comparison of Drought Indices for Appraisal of Drought Characteristics in the Ken River Basin. Weather and Climate Extremes, (8), 1-15, 2015.

[20] Bandyopadhyay, N., Saha, A.K., A Comparative Analysis of Four Drought Indices Using Geospatial Data in Gujarat, India. Arabian Journal of Geosciences, 9(5), 2016.

[21] T.C. Tarım ve Orman Bakanlığı, Su Yönetimi Genel Müdürlüğü, Ulusal Kuraklık Yönetimi Strateji Belgesi ve Eylem Planı, 2017-2023.

[22] Şener, E., Şener, Ş., Meteorolojik Kuraklığın Coğrafi Bilgi Sistemleri Tabanlı Zamansal ve Konumsal Analizi: Çorak Gölü Havzası (Burdur-Türkiye) Örneği. Mühendislik Bilimleri ve Tasarım Dergisi, 7(3), 596-607, 2019.

[23] Önöz, B., Oğuz, B., İstanbul Su Temini Sistemi Ve Kuraklık Analizi. Teknik Dergi, 1083-1090, 1996.

[24] Kömüşcü, A.Ü., Using the Spi to Analyze Spatial and Temporal Patterns of Drought in Turkey. Vol. 11. 1999.

[25] Türkeş, M., Tatlı, H., Use of the Standardized Precipitation Index (Spi) and a Modified Spi for Shaping the Drought Probabilities over Turkey. International Journal of Climatology, 29(15), 2270-2282, 2009.

[26] Sırdaş, S., Şen, Z., Meteorolojik Kuraklık Modellemesi ve Türkiye Uygulaması. İTÜ Mühendislik Dergisi, 2(2), 95-103, 2003.

[27] Bacanli, Ü.G., Dikbaş, F., Baran, T., Meteorological Drought Analysis Case Study: Central Anatolia. Desalination and Water Treatment, 26(1-3), 14-23, 2011.

[28] Karabulut, M., Drought Analysis in Antakya-Kahramanmaraş Graben, Turkey. Journal of Arid Land, 7(6), 741-754, 2015.

[29] Bulut, B., Yilmaz, M.T., Analysis of the 2007 and 2013 Droughts in Turkey by Noah Hydrological Model. Teknik Dergi/Technical Journal of Turkish Chamber of Civil Engineers, 27(4), 7619-7634, 2016.

[30] Güner Bacanli, Ü., Trend Analysis of Precipitation and Drought in the Aegean Region, Turkey. Meteorological Applications, 24(2), 239-249, 2017.

[31] Dabanlı, İ., Mishra, A.K., Şen, Z., Long-Term Spatio-Temporal Drought Variability in Turkey. Journal of Hydrology, 552, 779-792, 2017.

[32] Sönmez, F.K., Kömüscü, A.Ü., Erkan, A., Turgu, E., An Analysis of Spatial and Temporal Dimension of Drought Vulnerability in Turkey Using the Standardized Precipitation Index. Natural Hazards, 35, 243-264, 2005.

[33] Kadıoğlu M., Türkiye'de İklim Değişikliği Risk Yönetimi, Türkiye'nin İklim Değişikliği II. Ulusal Bildiriminin Hazırlanması Projesi Yayını, 172 sf., 2012.

[34] Dikbas, F., A Novel Two-Dimensional Correlation Coefficient for Assessing Associations in Time Series Data. International Journal of Climatology, 37(11), 4065-4076, 2017.

[35] Sensoy, S., Demircan, M., Ulupınar, Y., Climate of Turkey. Turkish State Meteorological Service.

[36] Erinç, S., Applied Climatology and the Climate of Turkey (in Turkish). 1957, Istanbul Technical University, Hydrogeology Institute: Istanbul, Turkey.

[37] Bacanli, U.G., Entropy Based Assessment and Palmer Drought Severity Index of Drought Analysis. Scientific Research and Essays, 7(44), 3823-3833, 2012.

[38] Zhang, Y., Cai, W., Chen, Q., Yao, Y., Liu, K., Analysis of Changes in Precipitation and Drought in Aksu River Basin, Northwest China. Vol. 2015. 2015. 1-15.

[39] Tsakiris, G., & Vangelis, H. Towards a drought watch system based on spatial SPI. Water Resources Management, 18(1):1-12, 2004.

[40] Dikbas, F., A New Two-Dimensional Rank Correlation Coefficient. Water Resour Manage, 32(5), 1539-1553, 2018.

Appendix

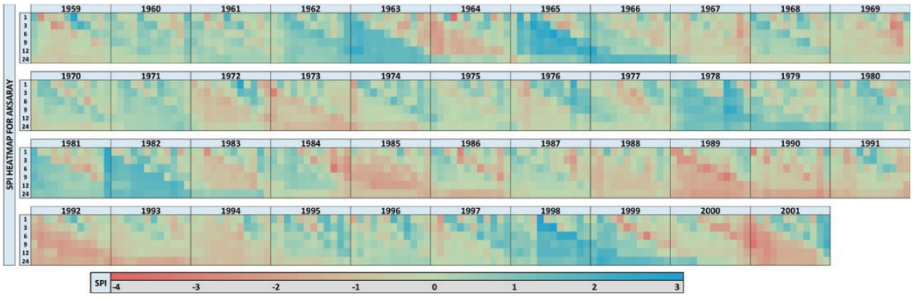

Figure A1 - Heatmap of the 1, 3, 6, 9, 12 and 24 month SPI series for the Aksaray station

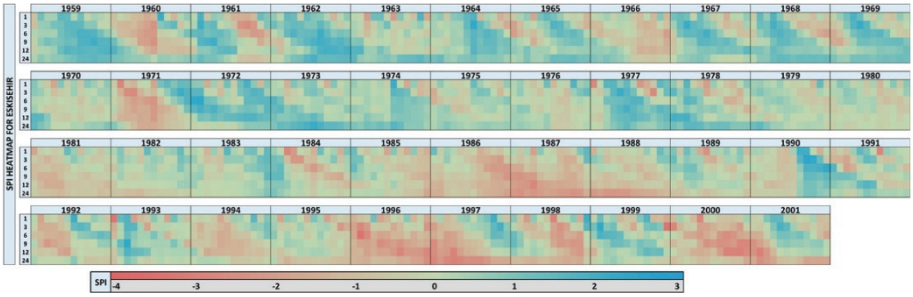

Figure A2 - Heatmap of the 1, 3, 6, 9, 12 and 24 month SPI series for the Eskişehir station

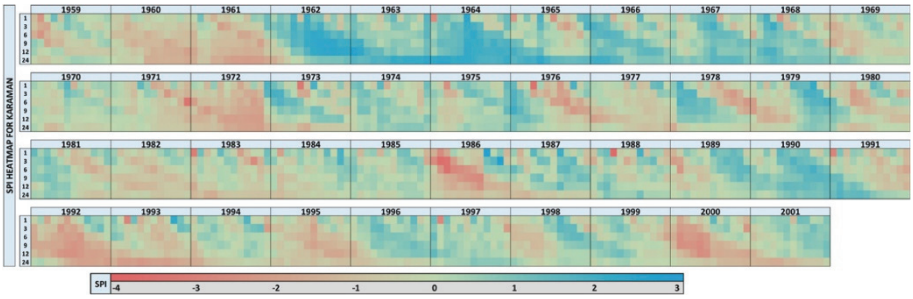

Figure A3 - Heatmap of the 1, 3, 6, 9, 12 and 24 month SPI series for the Karaman station

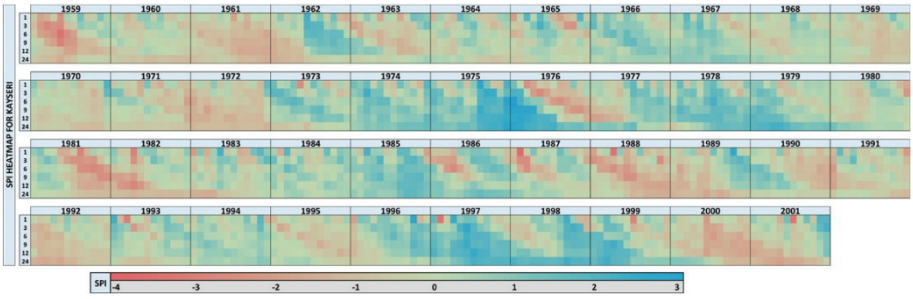

Figure A4 - Heatmap of the 1, 3, 6, 9, 12 and 24 month SPI series for the Kayseri station

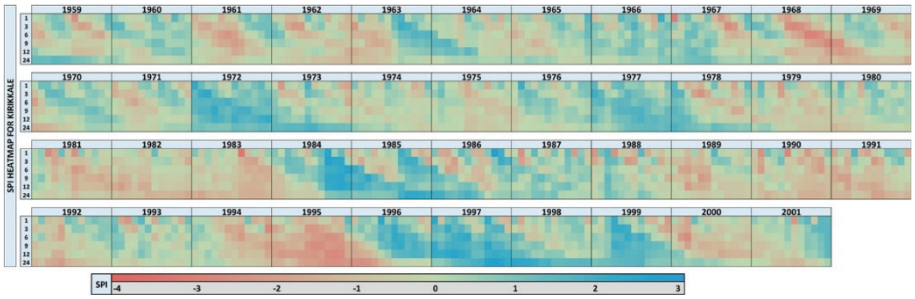

Figure A5 - Heatmap of the 1, 3, 6, 9, 12 and 24 month SPI series for the Kırıkkale station

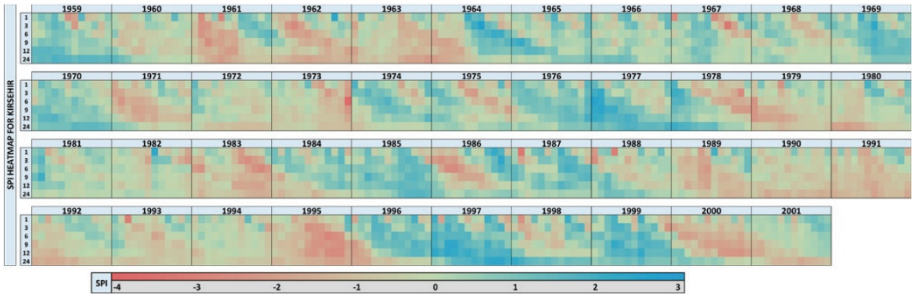

Figure A6 - Heatmap of the 1, 3, 6, 9, 12 and 24 month SPI series for the Kırşehir station

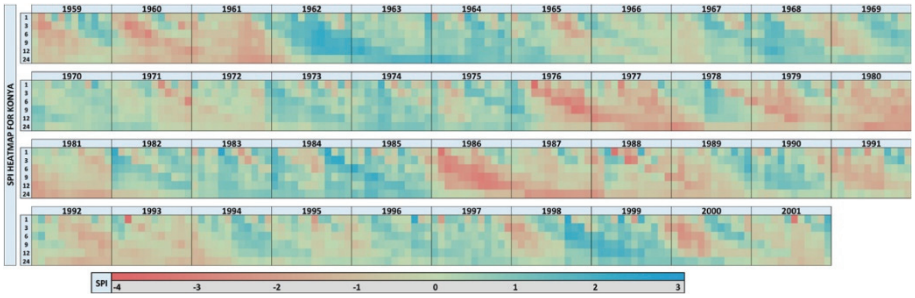

Figure A7 - Heatmap of the 1, 3, 6, 9, 12 and 24 month SPI series for the Konya station

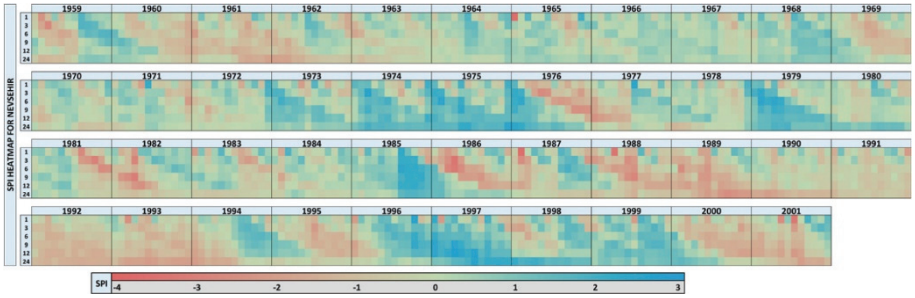

Figure A8 - Heatmap of the 1, 3, 6, 9, 12 and 24 month SPI series for the Nevşehir station

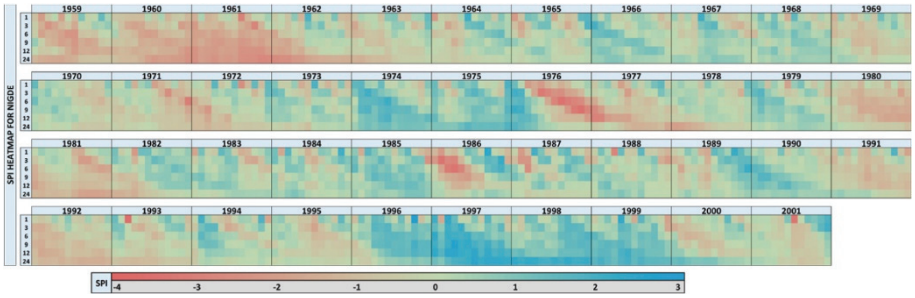

Figure A9 - Heatmap of the 1, 3, 6, 9, 12 and 24 month SPI series for the Niğde station

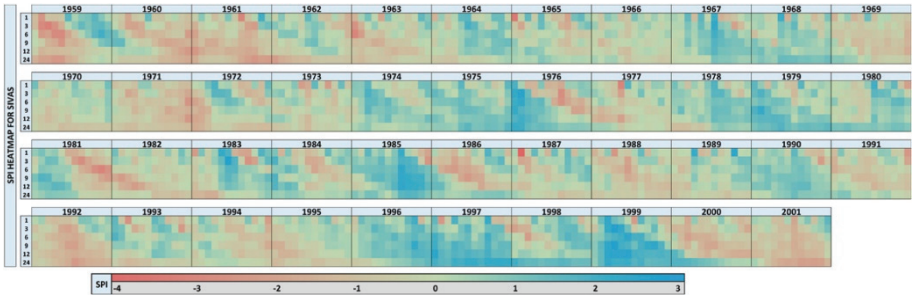

Figure A10 - Heatmap of the 1, 3, 6, 9, 12 and 24 month SPI series for the Sivas station

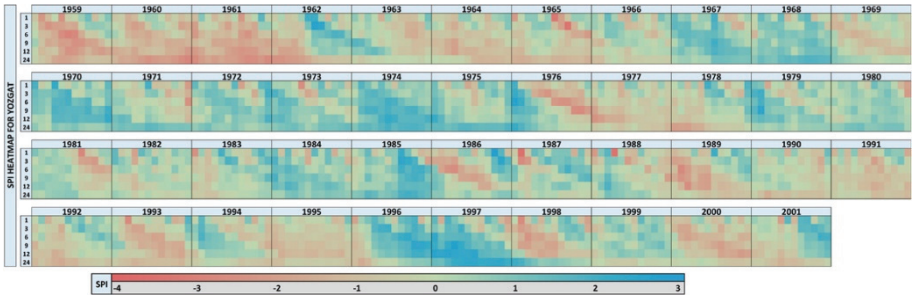

Figure A11 - Heatmap of the 1, 3, 6, 9, 12 and 24 month SPI series for the Yozgat station

Teknik Dergi, 2021 10967-10993, Paper 620

Metaheuristics-based Pre-Design Guide for Cantilever Retaining Walls

Esra URAY[1]
Özcan TAN[2]
Serdar CARBAS[3]
I. Hakkı ERKAN[4]

ABSTRACT

A pre-design guide for cantilever retaining walls and a detail parametric study of such walls is presented here. Mathematical models based on statistical methods were improved for calculating safety factors of sliding, overturning, and slope stability of those walls. The harmony search algorithm (HSA)-a metaheuristic optimization method-was employed to realize reasonable results of the pre-design guide from all distinct cases. Through the design algorithm, the optimal design was determined for varied soil types differently from suggestions of design codes. Thus, an optimal pre-design guide for safe and economic wall design was realized in a shorter time compared to the conventional method.

Keywords: Cantilever retaining wall, taguchi Method mathematical model, pre-design guide, external stability of the wall.

1. INTRODUCTION

In geotechnical engineering, the stability of two different soil levels is achieved by using retaining walls. In the absence of sufficient excavation areas at construction sites or docks, retaining walls act as a vertical connector, thus providing resistance to lateral soil forces.

Retaining wall design must satisfy external stability conditions and be economical. In traditional retaining wall design, wall dimensions to ensure stability are determined by a trial

Note:
- This paper has been received on May 9, 2019 and accepted for publication by the Editorial Board on March 2, 2020.
- Discussions on this paper will be accepted by September 30, 2021.
- https://doi.org/10.18400/tekderg.561956

1 KTO Karatay University, Department of Civil Engineering, Konya, Turkey - esra.uray@karatay.edu.tr https://orcid.org/0000-0002-1121-2880

2 Konya Technical University, Department of Civil Engineering, Konya, Turkey - ozcantan@selcuk.edu.tr https://orcid.org/0000-0002-8217-1502

3 Karamanoglu Mehmetbey University, Department. of Civil Engineering, Karaman, Turkey - scarbas@kmu.edu.tr - https://orcid.org/0000-0002-3612-0640

4 Konya Technical University, Department of Civil Engineering, Konya, Turkey - iherkan@ktun.edu.tr https://orcid.org/0000-0003-4514-4553

and error method [1]. In this method, the designer may select wall dimensions randomly until the stability of the wall is satisfied. Therefore, obtaining a safe design for selected wall dimensions is time-intensive when a large number of trials is required. Furthermore, obtained wall dimensions may not be economic among all possibilities. To consider all phenomena involved in the design, using a pre-design guide in the design of the cantilever retaining wall (CRW) becomes important for the designer.

The suggested wall dimensions according to TS 7994 and ACI 318 which are implemented in the CRW design have been demonstrated in Figure 1 [2-4]. The LRFD Bridge Design Manual [5] provides the pre-design dimensions of the base length, base thickness, and toe extension. The base length should be 60%–70% of the stem height and the base thickness should be 10%–15% of the stem height. The toe extension should be ~30% of the base length.

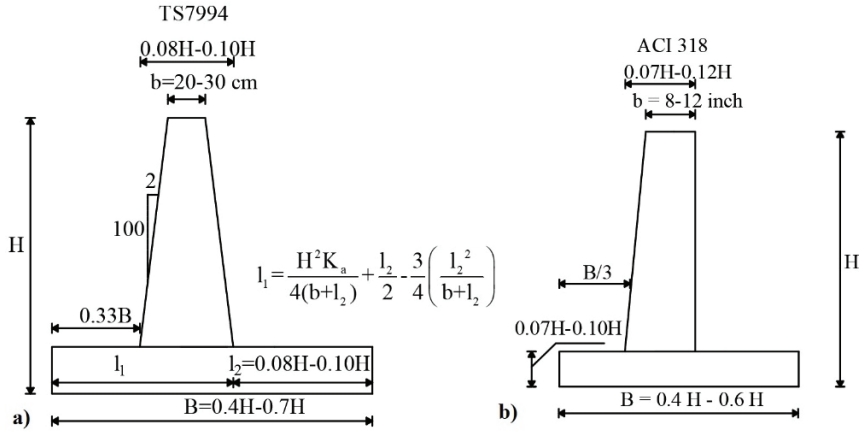

Figure 1 - Suggested dimensions of the CRW according to design codes; a) TS7994 and b) ACI 318.

Because retaining wall design is one of the complex design problems in the field of geotechnical engineering, there is a need for new design techniques. Metaheuristic optimization algorithms, which have received considerable attention in recent years, have been effectively used for solving complex optimization problems over the last two decades. Their popularity is attributed to their simplicity, compatibility to a wide range of situations, and effectiveness. Among these algorithms, harmony search algorithm (HSA) [6] was used as an optimization tool in this study. The HSA is based on the improvisation of identifying the best harmony in any piece of music; it is more advantageous than the other metaheuristics algorithms because it is easy to use, yields result in a reasonable time even with numerous iterations, utilizes both discrete and continuous variables, and reaches the global optimal without getting trapped in local optimum solutions during optimization. Moreover, many successful applications of HSA have been used, especially in the fields of structural optimization [7], hydraulics [8], vehicle routing [9], and geotechnical engineering [10]. Furthermore, to boost the accuracy and increase the rate of convergence of the standard HSA, some modified, improved, and hybrid versions of the algorithm are specifically proposed for

determining the critical sliding surface for slopes [11], optimal foundation design [12], and optimizing reinforced cantilever retaining walls [13, 14].

Parameters such as the total wall height, the angle of internal friction, and the unit volume weight play an important role in such designs. Furthermore, the design of retaining wall structures depends on several parameters such as elevation difference between soil levels, soil properties, groundwater, construction area, intended use, and cost. The effect of parameters on the optimal design of a retaining wall was investigated in a parametric study, and the results have been presented here [15, 16]. Although there are many studies on optimal retaining wall design [17–19], there has been no detailed study presenting a pre-design guide for different soil types to the best of our knowledge.

In the design procedure, the wall dimensions selected from pre-dimension sets must satisfy the external stability conditions of the wall and must be cost-efficient. Therefore, many iterations and long computational time are required to obtain wall dimensions; however, in this study, results were acquired within a short period for examining pre-design guide using the HSA. The minimum values of the safety factors of sliding (F_s), overturning (F_o), and slope stability (F_{ss}) are the objective function of HSA. These safety factors and a constraint, originating from the geometry of the wall, are considered the design constraints. The optimal dimensions of the wall corresponding to the minimum values of the safety factors and satisfying the design constraints are obtained. At the end of the analyses, economic wall designs were generated for obtaining the minimum safety factors of F_s, F_o, and F_{ss}.

The existence of certain cases such as the complex characteristics of problems with many unknowns or the numerous iterations in real-world problems has led to the need for a pre-design guide. Although there are design codes for cantilever retaining wall design, they do not have any detailed explanation in which the angle of internal friction value is valid for suggested wall dimensions. In this study, the effects of different values of angle of internal friction were investigated by using suggested wall dimensions according to design codes and pre-design guide was improved for CRW. Finally, for different wall heights and values of angle of internal friction, a pre-design guide meeting the requirements for the external stability of the CRW was developed.

2. DESIGN OF A CANTILEVER RETAINING WALL

To ensure that the stability conditions of a CRW are satisfied, the safety factors of F_s, F_o, and F_{ss} were considered when dealing with the pre-design guide for the CRW. Mathematical models based on statistics were developed for considering the safety factors of F_s, F_o, and F_{ss} using real CRW designs obtained from GEO5 geotechnical analysis computer software [20]. In this study, the wall dimensions, i.e., the base length (X_1), the toe extension (X_2), the base thickness (X_3), the front face angle (X_4, %), and a soil parameter, as well as the angle of internal friction (Ø°) are considered as the design parameters in the optimization process (Figure 2).

To statistically improve the mathematical models of safety factors, the levels of design parameters and the levels of the CRW shown in Table 1 were determined according to the related design codes [2-5].

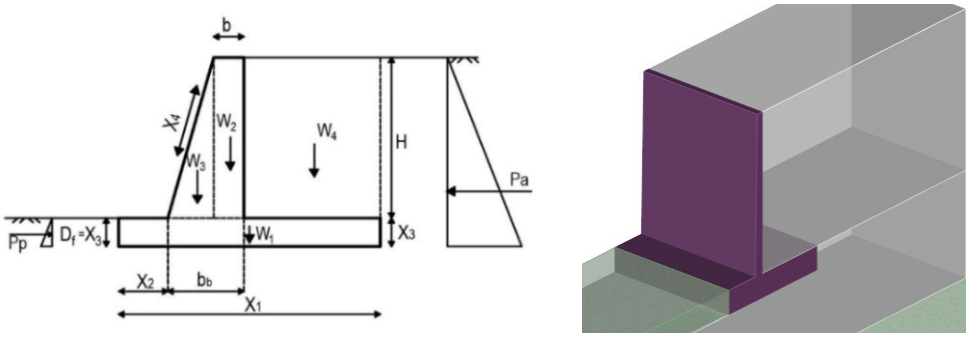

Figure 2 - Design variables and acting loads and a GEO 5 model of CRW.

Table 1 - RC retaining wall design parameters and their levels.

Design parameters	Level 1	Level 2	Level 3	Level 4
X_1: The base length	0.25H	0.50H	0.75H	1.0H
X_2: The toe extension	$0.15X_1$	$0.30X_1$	$0.45X_1$	0.60X1
X_3: The base thickness	0.06H	0.09H	0.12H	0.15H
X_4 (%): The front face angle	0	1	2	4
Ø (°): The angle of internal friction	20	27	34	41

For designing the CRWs, wall height plays an important role in calculating the acting loads on the wall. Other parameters are the soil properties such as unit volume weight and angle of internal friction. Changes in the unit volume weights during optimal design do not affect the optimal weight values significantly; thus, γ_{soil} = 18 kN/m^3 was selected as the mean value [21].Analysis parameters are the same for all CRW numerical analysis in GEO5 (Table 2). The safety factor of F_{ss} was obtained by the Bishop method [22] via numerical analysis. For numerical analysis, soil properties of the base soil and the backfill soil of the wall were the same. In the designs, only the weight of concrete was considered to identify the designs that satisfy the external stability conditions of the wall.

Table 2 - Analysis parameters for GEO5 numerical analysis.

Parameter	Value
b: The top thickness of the stem	0.25 m
δ: The friction angle between base and soil	(2/3) Ø
D_f: The depth of the base	X_3
γ_{soil}: The unit volume weight of soil	18 kN/m^3
c: The cohesion of the soil	0
$\gamma_{concrete}$: The unit volume weight of concrete	25 kN/m^3

2.1. Taguchi Method

In this study, the Taguchi method [23], which is powerful and easily applicable, was employed to develop mathematical models of safety factors. This method gives the effects of the parameters as results within a short time and minimizes the effects of uncontrollable factors and limits the number of analysis required using orthogonal arrays; moreover, it reduces research cost and allows parametric analysis with fewer trials. In general, to examine the effect of five design parameters with four levels on the safety factors of F_s, F_o, and F_{ss}, 1024 (4^5) designs must be examined. However, the Taguchi method makes it is possible to obtain the effect of parameters with only 16 designs using an orthogonal array. In this study, L_{16} orthogonal array which is given in the first column of Table 3 for five parameters with four levels was employed.

Table 3. L_{16} (4^5) orthogonal array, CRW Taguchi design table and results of numerical analyses.

	L_{16} orthogonal array parameter levels					Revised design parameters according to L_{16}					Safety factor (Fs) obtained from numerical analyzes		
Design No	P_1	P_2	P_3	P_4	P_5	X_1	X_2	X_3	X_4 (%)	Ø (°)	Fs(s)	Fs(o)	Fs(ss)
1	1	1	1	1	1	0.25H	0.15X_1	0.06H	0	20	0.22	0.35	0.75
2	1	2	2	2	2	0.25H	0.30X_1	0.09H	1	27	0.34	0.42	1.09
3	1	3	3	3	3	0.25H	0.45X_1	0.12H	2	34	0.52	0.48	1.48
4	1	4	4	4	4	0.25H	0.60X_1	0.15H	4	41	0.97	0.53	1.96
5	2	1	2	3	4	0.50H	0.15X_1	0.09H	2	41	2.48	3.11	2.18
6	2	2	1	4	3	0.50H	0.30X_1	0.06H	4	34	1.08	2.24	1.54
7	2	3	4	1	2	0.50H	0.45X_1	0.15H	0	27	0.59	1.36	1.27
8	2	4	3	2	1	0.50H	0.60X_1	0.12H	1	20	0.24	0.92	0.84
9	3	1	3	4	2	0.75H	0.15X_1	0.12H	4	27	1.15	3.68	1.51
10	3	2	4	3	1	0.75H	0.30X_1	0.15H	2	20	0.54	2.55	1.06
11	3	3	1	2	4	0.75H	0.45X_1	0.06H	1	41	2.34	6.13	2.10
12	3	4	2	1	3	0.75H	0.60X_1	0.09H	0	34	1.11	3.65	1.58
13	4	1	4	2	3	1.00H	0.15X_1	0.15H	1	34	3.04	8.31	2.26
14	4	2	3	1	4	1.00H	0.30X_1	0.12H	0	41	4.77	11.18	2.67
15	4	3	2	4	1	1.00H	0.45X_1	0.09H	4	20	0.57	4.38	1.00
16	4	4	1	3	2	1.00H	0.60X_1	0.06H	2	27	0.78	4.94	1.23

Accordingly, the L_{16} design table was revised by using the design parameters and the levels in Table 1 (the second column of Table 3). For obtaining this design table, 16 CRW designs were modeled and analyzed in the GEO5. At the end of those analyses, safety factors of

sliding, Fs(s), overturning, Fs(o), and slope stability, Fs(ss) were obtained and have been demonstrated as the results of numerical analyses in the last column of Table 3.

In the Taguchi method, the effects of the parameters on the results and the mathematical model are designated with a signal-to-noise (S/N) ratio described by Taguchi; it is used as the performance criterion in experiment design. The reduction of design parameter effects with the bigger S/N ratios can affect the result by decreasing the variance around the target value. The S/N ratios are classified into three types according to the purpose of the application: the smaller is better, the nominal is the best, and the larger is better (Equations 1 to 3, respectively).

$$S/N = -10\log(\sum(Y^2)/n) \quad (1)$$

$$S/N = -10\log(\bar{Y}/\sigma^2) \quad (2)$$

$$S/N = -10\log(\sum(1/Y^2)/n) \quad (3)$$

In these equations, Y is the response value, n is the number of repetitions, $\bar{Y}$ is the arithmetic mean, and σ is the standard deviation. For developing a mathematical model statistically with Taguchi Method, better models were obtained using S/N ratios according to the target state "the larger is better" [24]. In this study, S/N analyses were performed according to the target state "the larger is better," which maximizes the robustness. In the Statistica statistical software [25], S/N ratios were obtained using safety factors from numerical analyses in GEO5 and the change in the average S/N ratios according to parameter levels have shown in Figure 3 for each design parameters. In the CRW designs, the most effective parameter for the safety factors of Fs(s) and Fs(ss) is Ø, whereas that for the safety factor of Fs(o) is X_1.

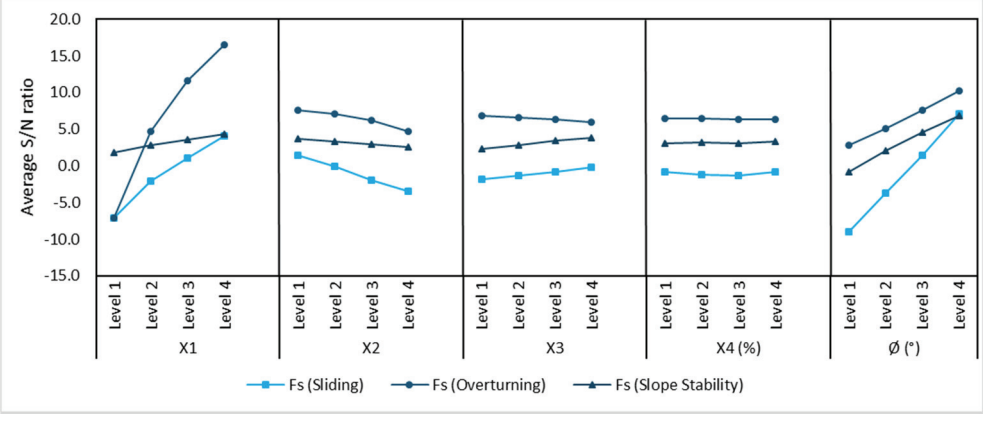

Figure 3 - Average S/N ratios for design parameters.

2.2. Mathematical Model

In this study, the average S/N ratios were employed to enhance the mathematical models for calculating the safety factors of sliding Fm(s), overturning Fm(o), and slope stability Fm(ss) and the general representation of the model for CRW height (H) of 6 m is given by Equation 4.

$$F_m = \sqrt{\frac{1}{10^{-\lambda/10}}} \tag{4}$$

where λ is the total effect coefficient, which is explained by Equation 5.

$$\lambda = \psi_B + \psi_{B_t} + \psi_d + \psi_m + \psi_f + \Delta \tag{5}$$

Table 4 - The effect coefficients of parameters of Fm(s).

The lower-upper limits of parameters	Safety factor	Mathematical Model
(B/H) = 0.25–1.0	Fm(s)	$\psi_B = 18.486(B/H)^3 - 42.672(B/H)^2 + 43.961(B/H) - 14.9016$
	Fm(o)	$\psi_B = 31.275(B/H)^3 - 86.36(B/H)^2 + 98.437(B/H) - 31.9741$
	Fm(ss)	$\psi_B = -0.9481(B/H)^3 + 1.104(B/H)^2 + 3.1679(B/H) - 1.4958$
(B_t/B) = 0.15–0.60	Fm(s)	$\psi_{B_t} = 28.534(B_t/B)^3 - 32.262(B_t/B)^2 - 0.1304(B_t/B) + 2.8788$
	Fm(o)	$\psi_{B_t} = -6.1339(B_t/B)^3 - 4.6395(B_t/B)^2 - 0.0334(B_t/B) + 2.5975$
	Fm(ss)	$\psi_{B_t} = -0.0165(B_t/B)^3 - 1.1675(B_t/B)^2 - 1.8(B_t/B) + 1.5046$
(d/H) = 0.06–0.10	Fm(s)	$\psi_d = 334.17(d/H)^3 - 39.307(d/H)^2 + 15.177(d/H) - 1.8281$
	Fm(o)	$\psi_d = -226.44(d/H)^3 + 46.681(d/H)^2 - 12.536(d/H) + 2.376$
	Fm(ss)	$\psi_d = -2336.4(d/H)^3 + 702.1(d/H)^2 - 48.723(d/H) + 0.7493$
m =0.00–0.04	Fm(s)	$\psi_m = 5415.9m^3 + 950.03m^2 - 46.71m + 0.0130$
	Fm(o)	$\psi_m = 26766m^3 - 1478m^2 + 15.336\,m + 1.3036$
	Fm(ss)	$\psi_m = 43197m^3 - 2498.5m^2 + 37.666\,m + 0.4955$
Ø = 20°–41°	Fm(s)	$\psi_\phi = 23.23(\tan\phi)^3 - 51.682(\tan\phi)^2 + 67.598(\tan\phi) - 26.9956$
	Fm(o)	$\psi_\phi = -2.4364(\tan\phi)^3 + 1.584(\tan\phi)^2 + 15.801(\tan\phi) - 8.2024$
	Fm(ss)	$\psi_\phi = 14.299(\tan\phi)^3 - 38.059(\tan\phi)^2 + 45.098(\tan\phi) - 15.4637$
ψ_B	: effect coefficient of the base length, X_1(H)	
ψ_{Bt}	: effect coefficient of the toe extension, $X_2(X_1)$	
ψ_d	: effect coefficient of the base thickness, X_3(H)	
ψ_m	: effect coefficient of the front face angle, X_4 (%)	
$\psi_Ø$	: effect coefficient of the angle of internal friction, Ø (°)	

The coefficient of Δ, which is the average S/N ratio, is considered as −1.034, 6.423, and 3.156 for Fm(s), Fm(o), and Fm(ss), respectively. Detailed mathematical explanations of all parameter-effect coefficients are provided in Table 4 for the safety factors of Fm(s), Fm(o), and Fm(ss). The values of all effect coefficients were defined between the lower and upper limits of design parameters listed in Table 1.

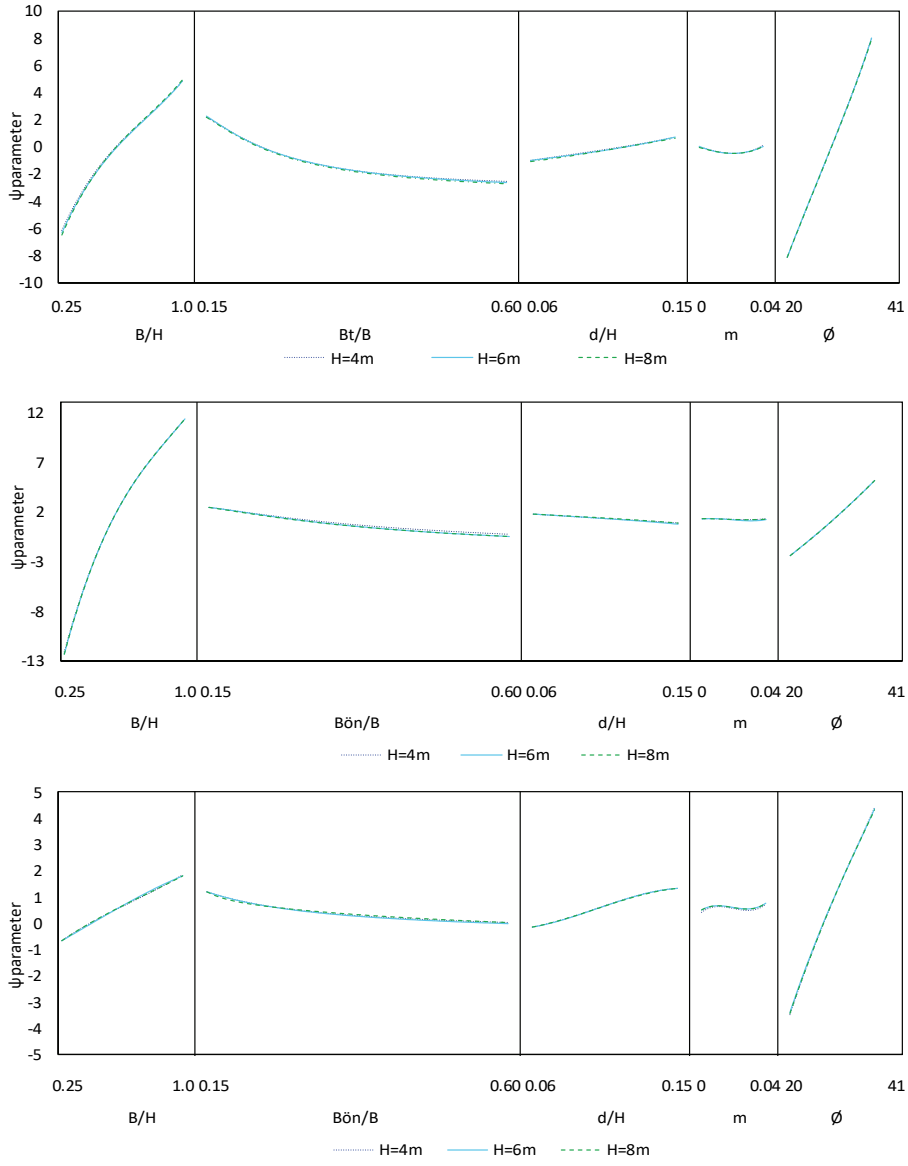

Figure 4 - The change between the effect coefficients of parameters and the different mathematical models for safety factors sliding, overturning and slope stability, respectively.

Mathematical models have statistically developed for H=4, 8 m by using the same way and the changes in the safety factor of the effect coefficient for each parameter according to wall height is shown in Figure 4. An examination of the figures clearly shows that the behavior of the effect coefficient is approximately the same for all wall heights. Thus, the mathematical model for H=6 m can be used in the CRW design with a range of H=4–8 m.

The safety factors of 1024 CRW designs, which involve all possibilities of five design parameters with four levels, were obtained by both numerical analysis and mathematical models for H = 6 m.

Relative errors (R_E) of safety factors were calculated by Equation 6 and their histograms and scatter plots for 1024 data have been constituted using relative errors (Figure 5).

$$R_E = \frac{Fm(s, o, ss) - Fs(s, o, ss)}{Fs(s, o, ss)} x100 \quad (6)$$

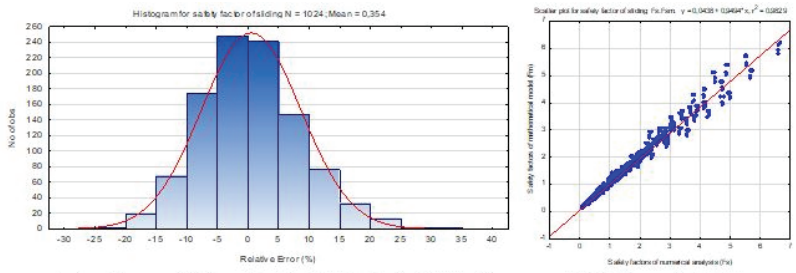

Figure 5 - Histograms and scatter plots of relative errors for the safety factors

Note that the data set should follow a normal distribution when using the obtained mathematical model, i.e., the mean, median, and mode of the dataset coincide and that the coefficients of skewness and kurtosis of the data set are equal to zero. According to the criteria of the normal distribution of relative error histograms, which are presented in Figure 5, the mean, median, and mode are approximately coincident, and the coefficients of skewness and kurtosis are almost zero. The given criteria of histograms for the safety factors show that the relative error histograms of the obtained mathematical models have approximately normal distributions.

To control the mathematical models of safety factors, design parameters that satisfy the previously mentioned lower and upper limits were randomly selected. In all, 25 models of CRW were formed; this result differs from levels of design parameters given in Table 1. Table 5 lists all safety factors obtained from the mathematical model and numerical analyses with randomly selected parameters. Figure 6 shows the relative errors of the safety factors.

Table 5 - The cantilever retaining wall design results for 25 randomly data sets.

No	Design Parameters						Mathematical Model			Numerical Analysis		
	H (m)	X_1 (m)	X_2 (m)	X_3 (m)	X_4 (%)	Ø (°)	Fm(s)	Fm(o)	Fm(ss)	Fs(s)	Fs(o)	Fs(ss)
1	4	1.20	0.24	0.28	0.011	22	0.28	0.52	0.83	0.30	0.54	0.88
2	5	1.75	0.39	0.40	0.039	39	1.42	1.36	1.77	1.31	1.40	1.81
3	6	2.70	1.35	0.78	0.022	35	0.88	1.48	1.61	0.96	1.49	1.65
4	7	4.55	1.82	0.70	0.031	40	2.12	4.37	2.03	2.24	4.32	2.10
5	8	7.20	3.96	0.88	0.012	24	0.61	3.60	1.15	0.64	3.63	1.16
6	5	4.00	1.40	0.50	0.025	25	0.73	3.58	1.19	0.83	3.66	1.27
7	7	2.80	1.23	0.98	0.034	26	0.43	0.83	1.13	0.42	0.84	1.16
8	4	2.20	0.62	0.32	0.028	37	1.54	3.03	1.71	1.64	3.07	1.85
9	6	5.70	1.37	0.78	0.036	30	1.75	6.21	1.72	1.74	6.35	1.78
10	8	4.80	1.25	0.56	0.018	33	1.17	3.12	1.49	1.28	3.10	1.63
11	4	1.76	0.74	0.44	0.026	28	0.51	1.16	1.18	0.56	1.21	1.24
12	5	1.90	0.61	0.70	0.038	21	0.32	0.68	0.92	0.30	0.69	0.93
13	6	5.10	0.87	0.78	0.035	31	1.78	5.30	1.77	1.83	5.43	1.84
14	7	3.15	1.42	0.56	0.013	38	1.12	1.90	1.65	1.16	1.89	1.73
15	8	7.36	4.12	0.56	0.024	32	1.11	5.27	1.47	1.16	5.33	1.53
16	6	1.68	0.32	0.60	0.038	23	0.32	0.45	0.93	0.29	0.46	0.95
17	4	1.48	0.64	0.44	0.025	36	0.85	1.13	1.58	0.93	1.19	1.64
18	8	3.36	1.88	0.64	0.032	29	0.43	0.98	1.09	0.42	0.98	1.17
19	7	6.72	1.88	0.98	0.022	34	2.35	7.28	2.02	2.48	7.40	2.12
20	5	1.80	0.56	0.35	0.032	21	0.26	0.66	0.77	0.28	0.69	0.83
21	6	1.68	0.64	0.84	0.014	38	0.95	0.73	1.79	1.00	0.73	1.81
22	8	6.16	3.33	0.88	0.027	23	0.47	2.57	1.03	0.51	2.58	1.06
23	4	2.24	1.19	0.40	0.034	35	0.99	2.31	1.56	1.05	2.33	1.62
24	5	4.10	2.42	0.70	0.039	22	0.49	2.53	1.06	0.48	2.58	1.05
25	7	3.01	0.84	0.49	0.024	39	1.47	2.03	1.73	1.46	2.06	1.83

According to Figure 6, the maximum absolute relative errors for the safety factors of F_s, F_o, and F_{ss} are viewed from the figure as 11.2%, 4.7%, and 8.7%, respectively. This result shows that the developed mathematical models can be used with ~10% error for controlling CRW stability for the defined lower and upper limits of the design parameters.

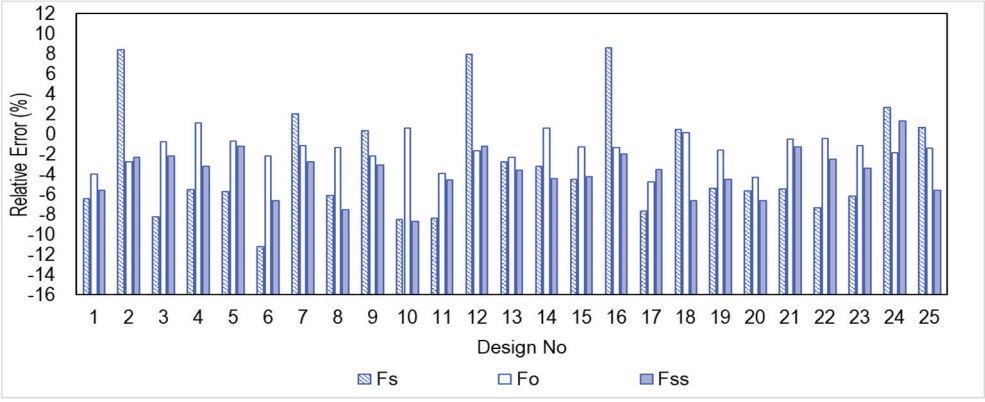

Figure 6 - The values of relative errors of all safety factor for randomly selected 25 data set.

3. HARMONY SEARCH ALGORITHM

The harmony memory size (HMS) constitutes the basis of the HSA. The best example to explain HMS is a jazz group. Any jazz group comprises three musicians: a guitarist, a pianist and a drummer. Initially, three musicians keep different notes in their minds. For example, let the musicians think of playing the following notes randomly; e.g., the guitarist [Fa, Mi, Sol, Re, Si], the pianist [Si, La, Re, Sol, Do] and the drummer [Do, Fa, Sol, Re, Mi]. From these notes, let the guitarist plays Sol, the pianist plays Si, and the drummer plays Re. Thus, three musicians form a harmony as [Sol, Si, Re], which is called G-accord in music. If the harmony they generate in this way is better than the worst harmony in their memory, they eliminate the worst harmony from their memory and record the new harmony. They repeat this process until they identify that they have the best harmony. Hence, the relationship between HSA and design of a CRW can be established as follows. While the harmony in HSA represents the optimal CRW design, the different harmonies show the different feasible CRW designs. Each instrument acts for a design variable and so each note is represented by the base length (X_1), the toe extension (X_2), the base thickness (X_3) and the front face angle (X_4) in the range given in Table 6. Finally, better harmonies correspond to local optimum designs, and the best harmony corresponds to the global optimal design for a CRW design [6,26,27].

In Figure 7, a detailed flowchart is exhibited about the steps of the HSA to minimize the safety factors of a CRW with inequality constraints containing discrete design variables.

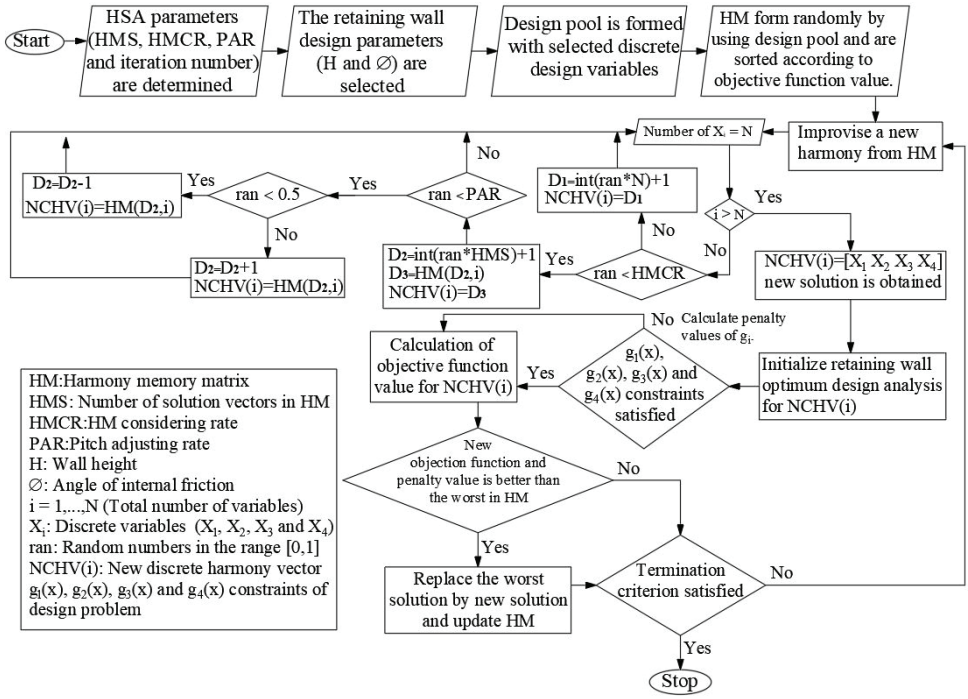

Figure 7 - Flowchart of the HSA for the optimum design of a CRW.

Moreover, the steps of the HSA can be interpreted in detail as follows:

Step 1: Initialization

The HSA parameters are initialized. The harmony search parameters can be defined as the harmony memory size (HMS), the harmony memory considering rate (HMCR), the pitch adjusting rate (PAR), and the maximum number of iterations (max_{iter}). Furthermore, in the design problem, a potential value set is determined for each design parameter. The algorithm selects these values for determining the design variables from the design pool.

First, the values of HMS, HMCR, PAR and maximum iteration number have been identified for each feasible design. In this study, the parameters of the HSA are selected as HMS = 20, HMCR = 0.95, and PAR = 0.15. These parameter values are allocated at the beginning and they stay unchanged during the optimization process. The most suitable ranges for the parameters are specified by Geem et al [6]. When performing sufficient amount of runs for the sensitivity of the predetermined parameters, abovementioned HSA parameters are determined to utilize the least values of safety factors. To ensure the optimal values, which are obtained with the algorithm, the numerous iterations have been performed and the optimal values have been found within 10,000 iterations. For processing the optimal design, the optimal result remains the same after 5,000 iterations.

Step 2: Harmony memory matrix is initialized

A harmony memory matrix (HM) is formed and randomly filled with the first values. Each row of this matrix includes possible solution vectors and values, which are selected randomly from a design pool for that particular design variable. Therefore, the number of this row corresponds to the HMS. The HM matrix, shown in Equation 7, has N columns where N is the total number of the design variables of the optimization problem. In this equation, $x_{i,j}$ is the value of the j^{th} design variable that is randomly selected in the i^{th} possible solution (i =1, 2,…., HMS and j = 1,2,…, N). In the i^{th} possible solution, $x_{i,j}$ values are determined and the objective function value corresponding to the present solution is calculated. After all harmony vectors have been calculated and are sorted in decrescent layout through their objective function value.

$$[HM]=\begin{bmatrix} x_{1,1} & x_{2,1} & \cdots & x_{N-1,1} & x_{N,1} \\ x_{1,2} & x_{2,2} & \cdots & x_{N-1,2} & x_{N,2} \\ \cdots & \cdots & \cdots & \cdots & \cdots \\ \cdots & \cdots & \cdots & \cdots & \cdots \\ x_{1,HMS-1} & x_{2,HMS-1} & \cdots & x_{N-1,HMS-1} & x_{N,HMS-1} \\ x_{1,HMS} & x_{2,HMS} & \cdots & x_{N-1,HMS} & x_{N,HMS} \end{bmatrix} \quad (7)$$

Step 3: Improvisation of a new harmony memory matrix

In the HSA, generating of a new harmony vector is realized according to three rules: (i) considering HM (HMCR), (ii) applying pitch adjustment (PAR), and (iii) using random selection (1-HMCR). For creating a new harmony matrix, the new value of the j^{th} design variable is selected from the values stored in HM with the probability of HMCR, which varies between 0 and 1. In the random selection, the new value of the j^{th} design variable is selected from the entire pool with the probability of (1-HMCR). Each design variable chosen from HM is then verified for whether it should be pitch-adjusted with the probability of PAR. HMCR and PAR are effective in determining global and local optimum designs, respectively.

Step 4: Harmony memory matrix is updated

After creating the recent solution (new harmony) vector, a new value for each design parameters have been obtained using the abovementioned three rules. So, the objective function value is calculated for the recent solution (new harmony) vector. This value is compared with the worst value of the objective function in HM. If it is better than the worst objective function, the recent solution vector is saved in HM and the worst design is eliminated. The HM is then sorted by the objective function value.

Step 5: Termination

Steps 3 and 4 are repeated until the criterion of termination (e.g., the maximum number of iterations) is satisfied. When the criterion of termination has been met, the algorithm is stopped.

4. OPTIMALLY FORMULATED CRW FOR PRE-DESIGN GUIDE

Investigation of the pre-design guide of the CRW, since calculating safety factors of F_s, F_o, and F_{ss} considering all combinations of the design parameters is tedious, the HSA is employed to obtain results faster. The HSA which is the optimum design algorithm was encoded using MATLAB [28]. The general mathematical formation for optimal CRW design is identified below.

4.1. Design Parameters

In the optimal design problem, a design pool has been formed to solve the design problem with inequality constraints including discrete variables presented in Table 6. The lower and the upper bounds of them have been arranged according to mathematical models limits for design parameters. Because of the design parameters conform to the dimensions of CRW, these values and their intervals have been selected to be discrete to achieve integer wall sizes. This design pool contains information of the changing values of the base length, X_1; toe extension, X_2; base thickness, X_3; front face angle, X_4; and constant values of the wall height, H; and the angle of internal friction, Ø. X_1, X_2, X_3 and X_4 which increase from the lower limit to the upper limit with the value of the interval have different sixteen, ten, seven and five values, respectively.

Table 6 Discrete design parameters and definition of limits.

Design parameters	Lower limit	Upper limit	Interval
X_1: The base length	0.25H	1.0H	0.05H
X_2: The toe extension	0.15X1	0.60X1	0.05X1
X_3: The base thickness	0.06H	0.15H	0.015H
X_4 (%): The front face angle	0	4	1

4.2. Objective Function

Minimum values of safety factors (F_s, F_o, and F_{ss}) were taken as the objective function with the intent of obtaining safe and economic CRW design, which is used as the maximum capacity of stability. When the safety factors of the wall are the minimum but greater than 1.3 and close each other as much as possible, the maximum capacity of F_s, F_o, and F_{ss} of the wall is employed. In the case of using the maximum capacity of wall stability, it is possible to find implicitly economic wall design with obtaining close safety factors each other. In this study, unlike other studies conducted on CRW optimum design reported in the literature, a weighted-sum model as a multi-objective function has been employed to compute minimum safety factors value. Multi-objective function based on the weighted-sum model [29, 30] has been adopted as the sum of safety factors of sliding, overturning, and slope stability of CRW as given in Equation 8.

$$f_{min} = a\,Fm(s) + b\,Fm(o) + c\,Fm(ss) \quad (8)$$

Here, Fm(s), Fm(o) and Fm(ss) are safety factors of sliding, overturning, and slope stability, respectively, and explained by Equations 4 and 5. According to the weighted-sum objective function model, the total value of coefficients a, b, and c should be 1.0. On the assumption that all safety factors have the same impact on the external stability of the wall, each of those coefficients is taken as 0.33.

4.3. Constraints

The design constraints for formulating the optimization problem are so-called safety factors of F_s, F_o, and F_{ss}, as well as the geometric constraints of the wall. The lower and upper limits of the safety factors against sliding, overturning, and slope stability are taken as 1.3 and 3.0 to yield the more economic wall design, respectively. In other words, it is intended to determine wall designs by providing the maximum capacity of stability. Maximum capacity of stability indicates that the wall design is safe (satisfy stability with safety factors greater than 1.3) and economic (with close safety factors each other and smaller than 3.0). In the optimization analyses, any designs having greater safety factors of F_s and F_{ss} value than 1.3 could not be attained for any of lower internal friction angles (Ø < 24°). Wall designs that safety factor of F_o is smaller than 3.0 could not be obtained for Ø < 30°. Consequently, wall designs could not be obtained, which satisfy both the lower and upper limits of safety factors for Ø =20°-30°. For these reasons, the lower and upper limits of safety factors for different values of Ø (°) used in the optimization process are designated in Table 7. They are also the values of limits for safety factors by which the feasible designs are obtained.

Table 7 - The lower-upper limits of safety factors of constraints.

Ø (°)	Fm(s)		Fm(o)		Fm(ss)	
	Min	Max	Min	Max	Min	Max
24	1.30	1.35	1.30	6.20	1.30	1.50
26	1.30	1.70	1.30	6.70	1.30	1.70
28	1.30	1.95	1.30	5.00	1.30	1.80
30−42	1.30	3.00	1.30	3.00	1.30	3.00

In the CRW design, the constraints are considered as normalized mathematical expressions as shown in Equation 9 and Equation 10 for the safety factor of F_s, in Equation 11 and Equation 12 for the safety factor of F_o, and in Equation 13 and Equation 14 for the safety factor of F_{ss}. Moreover, the normalized geometric constraints of the wall are given in Equation 15.

$$g_x(1) = 1 - (Fm(s)/Fm(s)_{min}) \leq 0 \quad (9)$$

$$g_x(2) = (Fm(s)/Fm(s)_{max}) - 1 \leq 0 \quad (10)$$

$$g_x(3) = 1 - (Fm(o)/Fm(o)_{min}) \leq 0 \quad (11)$$

$$g_x(4) = (Fm(o)/Fm(o)_{max}) - 1 \leq 0 \quad (12)$$

$$g_x(5) = 1 - (Fm(ss)/Fm(ss)_{min}) \leq 0 \quad (13)$$

$$g_x(6) = (Fm(ss)/Fm(ss)_{max}) - 1 \leq 0 \quad (14)$$

$$g_x(7) = \frac{X_2 + 0.25 + H*X_4}{X_1} - 1 \leq 0 \quad (15)$$

4.4. Pre-Design Guide for Cantilever Retaining Wall

In this study, the HSA is implemented to just obtain an optimal pre-design guide for CRW in a short time. For the optimization process, after the initial selection of HSA parameters (HMS, HMCR, PAR, and max_{iter}), the wall height, the angle of internal friction, and the design pool have been determined. The new wall design is obtained using values of the discrete design variables randomly selected from the design pool. In accordance to this new design, which surely satisfies the whole constraints as given in Equations 9–15, the minimum objective function (Equation 8) value and accordingly the wall dimensions have been obtained from all combinations for each case. Figure 8 shows the obtained minimum values of the CRW design parameters that the safety factors were greater than 1.3. All the safety factors of F_s, F_o, and F_{ss} exceeded 1.3 for Ø ≥ 24° and were lesser than 3.0 for Ø ≥ 30°. The CRW designs that satisfy the external stability condition of the wall were not obtained for Ø = 20° and 22°. Generally, designs with safety factors between 1.3 and 3.0 are obtained for Ø = 30°–42°. Except for Ø = 34° and Ø = 36° (X_4=%3.00), the values of X_4 were 0.00% for all values of the angle of internal friction (Ø).

For realizing a pre-design guide for the CRW, 60 different cases, including five values of H (4, 5, 6, 7, and 8 m) and twelve values of Ø (20°, 22°, 24°, 26°, 28°, 30°, 32°, 34°, 36°,38°, 40°, and 42°) were examined using HSA. Each case has been involved in 5600 (16 × 7 × 10 × 5) combinations for variable values of design parameters.

The proportional values of the design parameters (X_1/H, X_2/X_1, and X_3/H) and safety factors remained constant despite changes in the wall height and the angle of internal friction. The optimum values of X_4 and proportions of the wall dimensions for X_1, X_2, and X_3 shown with their safety factors in Figure 8 with average relative errors which were calculated using safety factors obtained from verification analysis conducted in GEO5 and safety factors of the optimum wall designs. Because changes in the design parameters exhibited similar behavior for all wall heights, the average relative errors given in Figure 8 are valid for all wall heights.

In Table 8, suggested wall dimensions according to design codes for the base length, the toe extension, and the base thickness are demonstrated. The analysis results listed in Figure 8 were compared with the proposed wall dimensions based on the design codes (Table 8). When X_1/H was examined for all wall heights, the proposed based length in design codes (0.40 H- 0.75 H) was obtained for Ø = 28°, 30°, 32°, 34°, and 36°. The proposed base length according to the design codes was not obtained for other internal friction angles. Although the toe extension was proposed as $0.30X_1$ or $0.33X_1$, it was obtained generally as $0.15X_1$ for Ø = 26°–34°. The values of the suggested design codes for the toe extension were obtained

approximately for only Ø = 40° in the analyses. Except for Ø = 38°, 40°, and 42°, the values of the base thickness were approximately 0.15H for all angles of internal friction. This value satisfies the in the proposed wall dimensions according to the design code of LRFD. Values of the base thickness for Ø = 38°, 40°, and 42° are close to those mentioned in the design code of ACI318. Because the base thickness in TS7994 is given as 80 cm, Figure 8 was used for comparison. For wall heights of 6, 7, and 8 m and angles of internal friction between 36° and 38°, the value of X_3 is ~80 cm. Consequently, it is not recommended to use the wall dimensions based on the design codes from the viewpoint of economic design of CRW in soil with Ø < 30°.

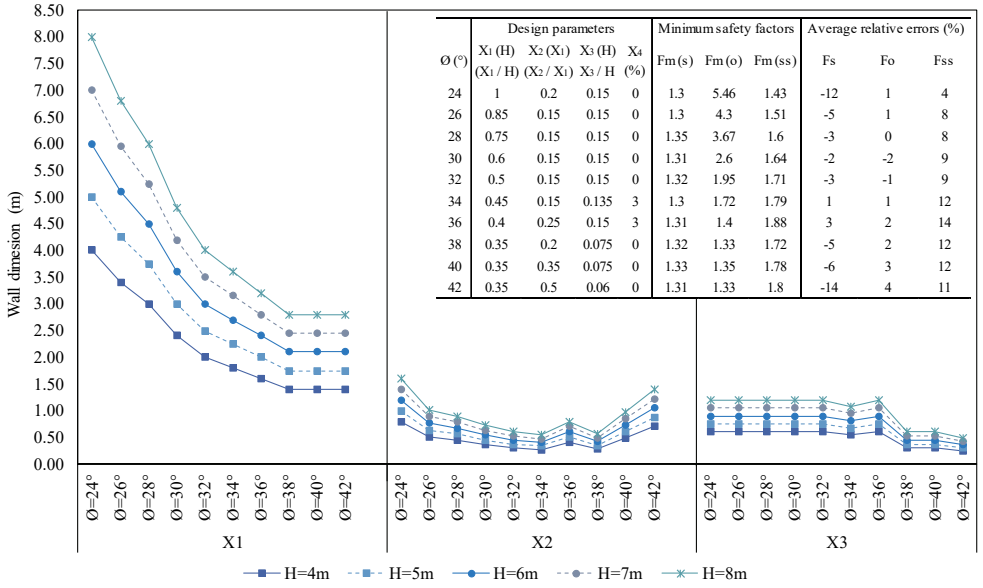

Ø (°)	Design parameters				Minimum safety factors			Average relative errors (%)		
	X_1 (H) (X_1 / H)	X_2 (X_1) (X_2 / X_1)	X_3 (H) X_3 / H	X_4 (%)	Fm (s)	Fm (o)	Fm (ss)	Fs	Fo	Fss
24	1	0.2	0.15	0	1.3	5.46	1.43	-12	1	4
26	0.85	0.15	0.15	0	1.3	4.3	1.51	-5	1	8
28	0.75	0.15	0.15	0	1.35	3.67	1.6	-3	0	8
30	0.6	0.15	0.15	0	1.31	2.6	1.64	-2	-2	9
32	0.5	0.15	0.15	0	1.32	1.95	1.71	-3	-1	9
34	0.45	0.15	0.135	3	1.3	1.72	1.79	1	1	12
36	0.4	0.25	0.15	3	1.31	1.4	1.88	3	2	14
38	0.35	0.2	0.075	0	1.32	1.33	1.72	-5	2	12
40	0.35	0.35	0.075	0	1.33	1.35	1.78	-6	3	12
42	0.35	0.5	0.06	0	1.31	1.33	1.8	-14	4	11

Figure 8 - Suggestion of pre-design guide for the CR wall.

Table 8 - Suggested wall dimensions according to design codes.

Codes	The base length	The toe extension	The base thickness
TS7994 [2]	0.40H–0.70H	$0.33X_1$	80 cm
ACI318 [3]	0.40H–0.60H	$0.33X_1$	0.07H–0.10H
LRFD [4]	0.70H*–0.75H*	$0.30X_1$	0.10H–0.15H

H: The wall height, H*: The stem height

Because feasible solutions for Ø = 20° and 22° were not obtained in the analyzes, the numerical analyses in GEO5 were repeated to obtain the wall dimensions that satisfy the external stability conditions for the minimum safety factors (Table 9). In the same table, the

proportional values of wall dimensions were obtained with the safety factors of Fs(s), Fs(o), and Fs(ss). From Table 9, it is seen that the designs that satisfied the minimum stability conditions of CRW does not have economic wall dimensions because of obtained great base length and safety factor of F_o. Moreover, despite changes in the wall heights, proportional wall dimensions stay constant. When the safety factors for Ø = 20° and 22° are examined, the value of Fs(o) is higher than the values of Fs(s) and Fs(ss). Consequently, an economic design is not possible when the internal friction angle of soil is either 20° or 22°.

Table 9 - Results for satisfied stability conditions of CRW designs in GEO5.

	H (m)	X_1 (m)	X_1/H	X_2 (m)	X_2/X_1	X_3 (m)	X_3/H	X_4(%)	Fs(s)	Fs(o)	Fs(ss)
	4	6.60	1.65	1.32	0.20	0.60	0.15	0.00	1.33	12.87	1.54
	5	8.30	1.65	1.65	0.20	0.75	0.15	0.00	1.32	12.85	1.48
Ø=20°	6	9.90	1.65	1.98	0.20	0.90	0.15	0.00	1.32	12.84	1.47
	7	11.60	1.65	2.31	0.20	1.05	0.15	0.00	1.32	12.84	1.49
	8	13.20	1.65	2.64	0.20	1.20	0.15	0.00	1.32	12.83	1.41
	4	5.60	1.40	1.12	0.20	0.60	0.15	0.03	1.35	9.98	1.53
	5	7.00	1.40	1.40	0.20	0.75	0.15	0.03	1.35	9.96	1.51
Ø=22°	6	8.40	1.40	1.68	0.20	0.90	0.15	0.03	1.34	9.95	1.52
	7	9.80	1.40	1.96	0.20	1.05	0.15	0.03	1.34	9.95	1.52
	8	11.2	1.40	2.24	0.20	1.20	0.15	0.03	1.34	9.94	1.52

The proposed wall dimensions of CRW for wall heights of 4, 5, 6, 7, and 8 m and different values of angle internal friction are shown in Figure 9, Figure 10, Figure 11, Figure 12, and Figure 13, respectively. It is possible to perform CRW design by using these figures. For example, the design of wall for H = 6 m and Ø = 30°, the obtained wall dimensions are X_1 = 3.6, X_2 = 0.54, and X_3 = 0.90 m according to Figure 11. In these figures, while the safety factors of F_s, F_o, and F_{ss} are in the range of 1.3–3.0 for Ø = 30°, 32°, 34°, 36°, 38°, 40°, and 42°, they are just greater than 1.3 for Ø =24°–30°. In other words, for wall designs in soil with Ø < 30°, a safety factor of overturning smaller than 3.0 is not obtained using these figures.

Ultimately, the obtained all CRW designs were examined in terms of soil bearing capacity using Terzaghi bearing capacity theory [31] for the strip foundation. The results show that soil bearing capacity of the obtained all CRW designs is provided except for Ø = 24°. Therefore, the proposed pre-design guide designated in Table 10 is included the CRW designs for H = 4, 5, 5, 6, 8 m and Ø = 26°, 28°, 30°, 32°, 34°, 36°, 38°, 40°, 42°. Using values of the minimum design parameters given in Table 10, some sample CRW designs have been analyzed for different conditions of soil and slope in GEO5, and they have been listed in Table 11. The ultimate bearing capacities (q_u, kN/m^3) of the base soil have been calculated for wall designs. Then, safe bearing capacities (q_s, kN/m^3) for SF= 3.0, and maximum values of base pressure distribution (σ_{max}) of the wall designs have been calculated, and the results are listed in Table 11.

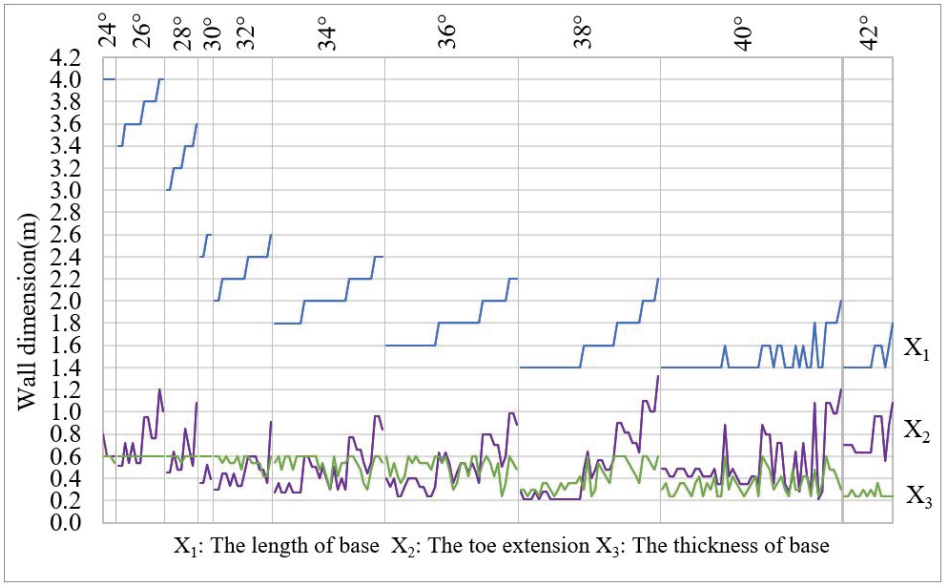

Figure 9 - Suggestions of wall dimensions for H =4 m.

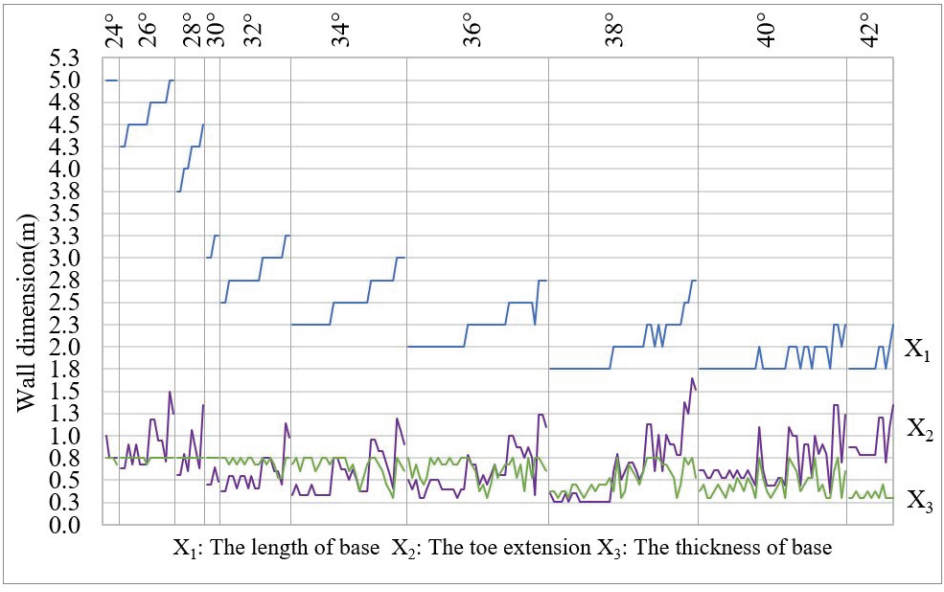

Figure 10 - Suggestions of wall dimensions for H =5 m.

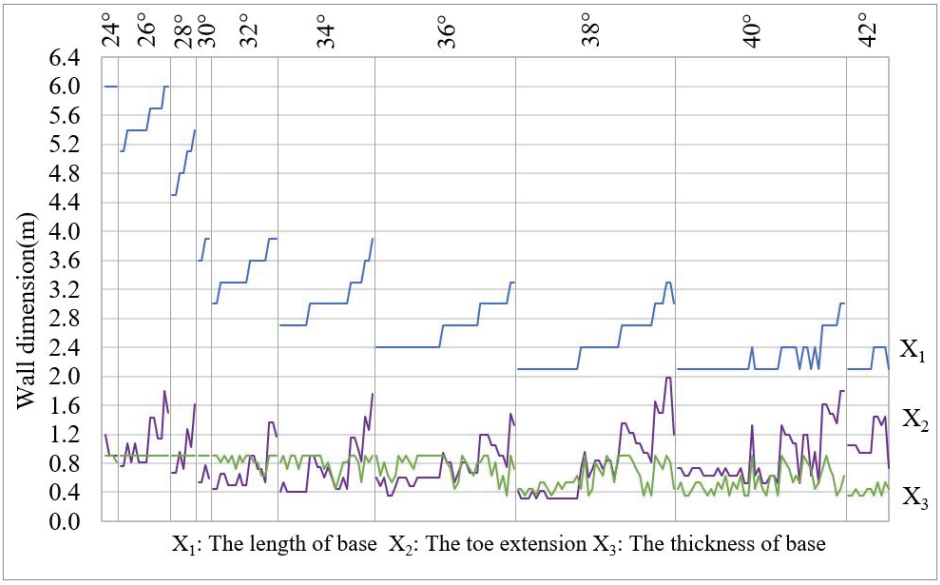

Figure 11 - Suggestions of wall dimensions for H =6 m.

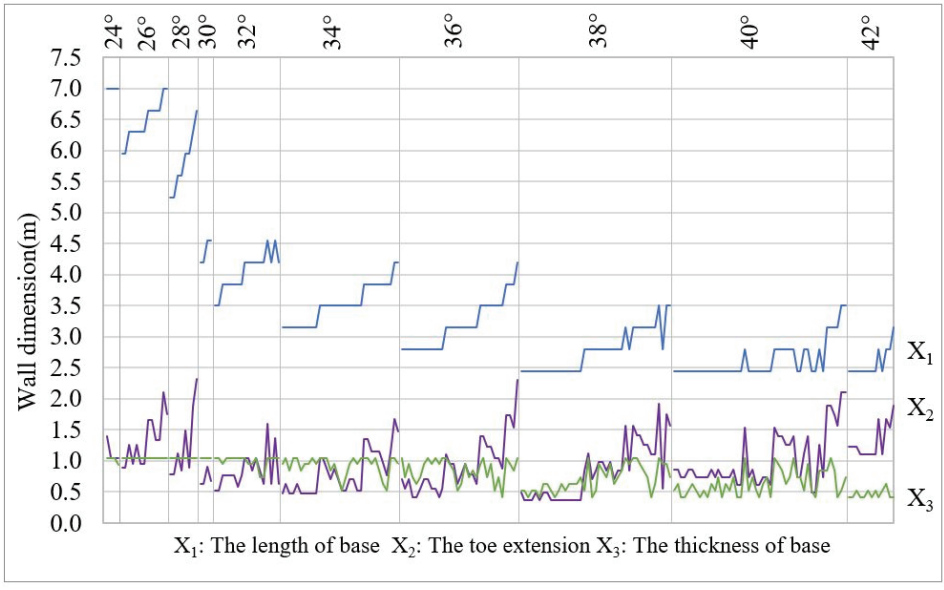

Figure 12 - Suggestions of wall dimensions for H=7 m.

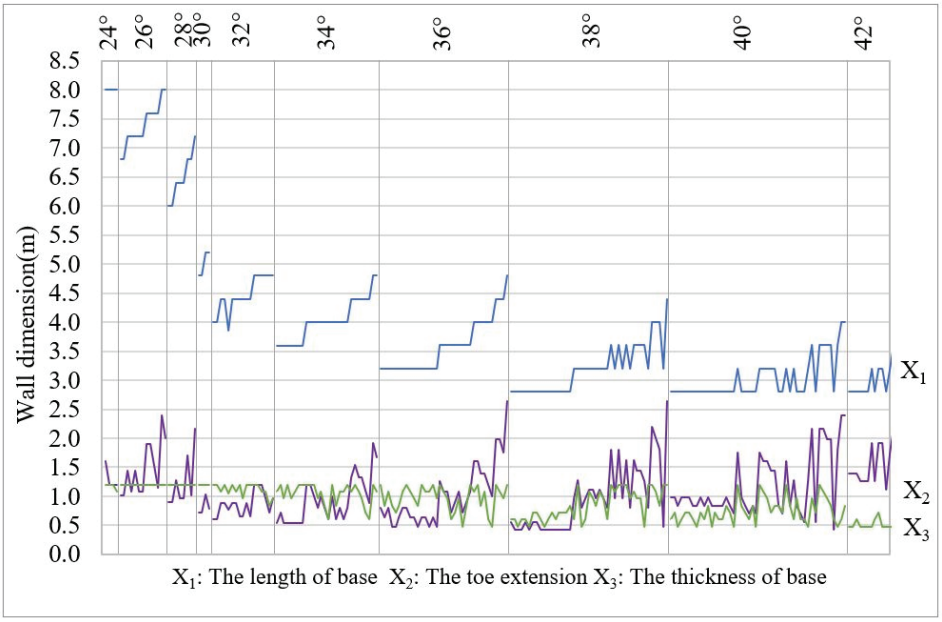

Figure. 13 Suggestions of wall dimensions for H =8 m

Table 11 shows that safe bearing capacities (q_s) of the base soil are greater than the maximum value of base pressure distribution (σ_{max}) of example wall designs. When safety factors of Fs(s), Fs(o), and Fs(ss), as well as criteria of bearing capacity of wall designs in table are examined, safety factors are greater than 1.3 and loads from the base to the soil are safely transmitted for the minimum suggested wall dimensions. The results show that the suggested design table (Table 10) can be used for designing a CRW for determined values of angle of internal friction and wall height.

5. CONCLUSIONS

In this study, a pre-design guide depending on soil properties was improved using the HSA for a CRW. The lower and upper limits of the wall dimensions were assigned following TS7994, ACI 318, and LRFD design codes such that the wall dimensions obtained from the analyses could be compared with those proposed based on the design codes. The base length, X_1; the toe extension, X_2; the base thickness, X_3; the front face angle, X_4; and the angle of internal friction, Ø were considered as the design parameters with their varied values.

To verify the external stability of the CRW, the safety factors of F_s, F_o, and F_{ss} were considered. For calculating the safety factors, mathematical models were improved by a statistical method according to the determined design parameters. In developing the mathematical model, the safety factors of sliding Fs(s), overturning Fs(o), and slope stability Fs(ss), as obtained from CRW designs, were used and analyzed in GEO5.

Table 10 - Pre-design table of cantilever retaining wall for different values of wall height and the angle of internal friction

	X_1 (m)	X_2 (m)	X_3 (m)	X_1 (m)	X_2 (m)	X_3 (m)	X_1 (m)	X_2 (m)	X_3 (m)	X_1 (m)	X_2 (m)	X_3 (m)	X_1 (m)	X_2 (m)	X_3 (m)
H(m)	Ø=26° (1.30 < Fs(sliding) < 1.50) (1.30 < Fs(overturning) < 6.00) (1.30 < Fs(slopestability) < 2.00)			Ø=28° (1.30 < Fs(sliding) < 2.00 (1.30 < Fs(overturning) < 5.50) (1.30 < Fs(slopestability) < 2.00)			Ø=30° (1.30 < Fs(sliding) < 3.00) (1.30 < Fs(overturning) < 3.00) (1.30 < Fs(slopestability) < 3.00)			Ø=32° (1.30 < Fs(sliding) < 3.00) (1.30 < Fs(overturning) < 3.00) (1.30 < Fs(slopestability) < 3.00)			Ø=34° (1.30 < Fs(sliding) < 3.00) (1.30 < Fs(overturning) < 3.00) (1.30 < Fs(slopestability) < 3.00)		
4	**3.55-4.00**	**0.55-1.00**	**0.60**	3.00-3.60	0.45-1.00	0.60	2.40–2.60	0.30–0.55	0.60	2.20–2.50	0.30–0.70	0.45–0.60	1.90–2.40	0.30–0.90	0.40–0.60
5	4.45–5.00	0.65–1.25	0.75	**3.75–4.50**	**0.55–1.35**	**0.75**	3.05–3.25	0.45–0.65	0.75	2.70–3.05	0.35–0.80	0.55–0.75	2.35–3.00	0.35–1.15	0.45–0.75
6	5.35–6.00	0.80–1.60	0.90	4.50–5.40	0.70–1.60	0.90	**3.70–3.90**	**0.55–0.80**	**0.90**	3.20–3.75	0.45–1.10	0.75–0.90	2.80–3.70	0.40–1.65	0.60–0.90
7	6.20–7.00	0.90–1.80	1.05	5.25–6.65	0.80–2.30	1.05	4.30–4.55	0.60–0.90	1.05	**3.60–4.35**	**0.55–1.25**	**1.05**	3.25–4.20	0.45–1.50	0.75–1.05
8	7.05–8.00	1.00–2.10	1.20	6.00–7.20	0.90–2.15	1.20	4.90–5.20	0.70–1.00	1.20	4.25–4.80	0.60–1.20	1.05–1.20	**3.70–4.80**	**0.55–1.80**	**0.90–1.20**
H(m)	Ø=36° (1.30 < Fs(sliding) < 3.00) (1.30 < Fs(overturning) < 3.00) (1.30 < Fs(slopestability) < 3.00)			Ø=38° (1.30 < Fs(sliding) < 3.00) (1.30 < Fs(overturning) < 3.00) (1.30 < Fs(slopestability) < 3.00)			–Ø=40° (1.30 < Fs(sliding) < 3.00) (1.30 < Fs(overturning) < 3.00) (1.30 < Fs(slopestability) < 3.00)			Ø=42° (1.30 < Fs(sliding) < 3.00) (1.30 < Fs(overturning) < 3.00) (1.30 < Fs(slopestability) < 3.00)			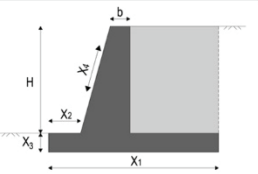		
4	**1.65–2.20**	**0.25–0.85**	**0.25–0.60**	1.50–2.20	0.25–1.10	0.25–0.60	1.40–2.00	0.25–1.05	0.25–0.60	1.40–1.80	0.55–1.00	0.25–0.40			
5	2.10–2.75	0.35–1.00	0.30–0.75	**1.85–2.75**	**0.25–1.25**	**0.30–0.75**	1.75–2.30	0.35–1.35	0.30–0.75	1.75–2.25	0.70–1.25	0.30–0.45			
6	2.50–3.30	0.35–1.20	0.35–0.90	2.20–3.30	0.30–1.40	0.40–0.90	**2.10–3.00**	**0.45–1.50**	**0.35–0.90**	2.10–2.55	0.75–1.35	0.35–0.55			
7	2.90–4.20	0.40–1.80	0.40–1.05	2.45–3.60	0.35–1.60	0.45–1.05	2.45–3.50	0.50–1.80	0.45–1.05	**2.45–3.15**	**0.95–1.65**	**0.40–0.65**			
8	3.35–4.80	0.45–2.00	0.45–1.20	2.85–4.40	0.40–2.10	0.50–1.20	2.80–4.00	0.55–2.05	0.50–1.20	2.80–4.00	1.10–2.15	0.50–0.75			

Table 11 - Examples designs of cantilever retaining wall by using the pre-design table for random values of wall height and the angle of internal friction

Analysis parameters for GEO5 wall designs	Example No	H (m)	X_1 (m)	X_2 (m)	X_3 (m)	X_4 (%)	Ø (°)	Fs (sliding)	Fs (overturning)	Fs (slope stability)	q_u (kN/m^2) (SF=3.00)	σ_{max} (kN/m^2)
b=0.25 m	1	4	3.55	0.55	0.60	0	26	1.30	4.75	1.54	186.7	106.7
δ=(2/3) Ø	2	5	3.75	0.55	0.75	0	28	1.33	3.68	1.64	262.0	154.9
γ_{soil}=18kN/m^3	3	6	3.70	0.55	0.90	0	30	1.31	2.69	1.65	352.1	222.8
$\gamma_{concrete}$=25kN/m^3	4	7	3.60	0.55	1.05	0	32	1.31	2.03	1.68	1354.2	317.6
c=0	5	8	3.70	0.55	0.90	0	34	1.31	1.89	1.66	1404.2	376.58
Slope stability: Bishop method	6	4	1.65	0.25	0.25	0	36	1.31	1.79	1.69	609.1	196.7
Calculation of coefficients of active and passive earth pressure: Mazindrani (Rankine)	7	5	1.85	0.25	0.30	0	38	1.34	1.57	1.77	714.4	301.4
	8	6	2.10	0.45	0.35	0	40	1.37	1.50	1.80	855.8	322.6
	9	7	2.45	0.95	0.40	0	42	1.33	1.51	1.87	1060.3	272.97

As the wall designs did not satisfied stability conditions such as sliding, overturning, slope stability, and bearing capacity for Ø = 20°, 22°, and 24°, the results were not added in the pre-design guide. For all combinations of variable values of design parameters, it needs to be checked whether the constraints have been satisfied and which one has the minimum objective function value. For this case, the formulations of safety factors derived from mathematical models were used as design constraints and objective function to obtain safe and economic CRW designs, the lower constraint limit was set as 1.3 and the upper constraint limit as 3.0. HSA provides the optimal result in a short time for obtaining the minimum value of the objective function in the analyses. The wall height (H) and the angle of internal friction (Ø) were considered as a constant parameter in each HSA-based optimization analyses. Analyses were performed for each value of H and Ø, and the wall dimensions (X_1, X_2, X_3, X_4) satisfying the upper and lower limits were determined. The obtained results and suggestions are as follows:

Finding absolute average relative errors of improved mathematical models for safety factors of F_s, F_o, and F_{ss} as 6.4%, 1.0%, and 2.8%, respectively, shows that these models may be reliably used for determining safety factors. Coefficients of determination (r^2) have been found as ~0.99 for the abovementioned mathematical models from scatter plots.

While feasible solutions with safety factors greater than 1.3 were not obtained for Ø = 20° and 22°, the criteria of bearing capacity of proposed wall designs were not satisfied for Ø = 24°. Because soils with Ø < 24° are not sufficient to provide the safety factors of F_s and F_{ss} for the CRW, reasonable wall designs that satisfied the lower limit (1.3) of the constraints were not obtained for these values of Ø. Hence, when the angle of internal friction of backfill and foundation soil was lesser than 26°, it is recommended that the soil be improved or a different type of retaining structure such as CRW with keys or steps or counterfort wall be used.

CRW designs were not obtained for the safety factor of F_o smaller than 3.0 for Ø < 30°. Consequently, safe and economic CRW designs may be obtained for soil with Ø > 30° such that the lower limit (1.3) and upper limit (3.0) are satisfied.

The proposed wall dimensions for the aforementioned design codes were not achieved for loose sand soil (Ø < 30°). According to the results, the use of the designs codes of T7994, ACI 318, and LRFD for the design of CRW is not recommended in soils with Ø < 30°.

Soil properties have not been considered in the proposed wall dimensions according to the current design codes [2, 3, 4]. Safe and economic wall designs can be obtained using the proposed pre-design guide for CRW that incorporates varied values of angles of internal friction and wall heights are presented in this paper.

Eventually, a pre-design guide for CRW design was realized for conditions such as H = 4, 5, 6, 7, and 8 m; Ø = 30°, 32°, 34°, 36°, 38°, 40°, and 42°; and γ_{soil} = 18 kN/m^3.

In future, the scope of this study may be extended by considering different types of retaining walls and soil and slope properties.

Symbols

b	The top thickness of the stem
b_b	The bottom thickness of the stem
B	The base length
c	Cohesion of soil
CRW	Cantilever retaining wall
D_f	Depth of base
f_{min}	Objective function
F_s	General representation for sliding safety factor
F_o	General representation for sliding safety factor overturning
F_{ss}	General representation for sliding safety factor slope stability
Fs (s)	Sliding safety factor of numerical analysis
Fs (o)	Overturning safety factor of numerical analysis
Fs (ss)	Slope stability safety factor of numerical analysis
Fm (s)	Sliding safety factor mathematical model
Fm (o)	Overturning safety factor mathematical model
Fm (ss)	Slope stability safety factor mathematical model
$g_x(1)$	The constraint of the minimum sliding safety factor
$g_x(2)$	The constraint of the maximum sliding safety factor
$g_x(3)$	The constraint of the minimum overturning safety factor
$g_x(4)$	The constraint of the maximum overturning safety factor
$g_x(5)$	The constraint of minimum slope stability safety factor
$g_x(6)$	The constraint of maximum slope stability safety factor
$g_x(7)$	Geometric constraints of the wall
H	Wall height
HM	Harmony memory matrix
HMCR	Harmony memory considering the rate
HMS	Harmony memory size
HSA	Harmony search algorithm
i	The row number of HM
j	Column number of HM
L_{16}	Orthogonal array
max_{iter}	Maximum number of iterations
N	Total number of the design variables
n	Number of repetitions
$P_{1,2,3,4,5}$	Number of parameters

PAR	Pitch adjusting rate
R_E	Relative Error
r^2	Coefficients of determination
S/N	Signal/Noise ratio
Y	Response value
$\bar{Y}$	Arithmetic mean
X_1	Base length
X_2	Toe extension
X_3	Base thickness
X_4	Front face angle
Δ	Coefficient of the average S/N ratio
δ	Friction angle between base and soil
Ø	The angle of internal friction
γ_{soil}	Unit volume weight of soil
$\gamma_{concrete}$	Unit volume weight of concrete
ψB	Effect coefficient of the base length, X_1(H)
ψBt	Effect coefficient of the toe extension, X_2(X1)
ψd	Effect coefficient of the base thickness, X_3(H)
ψm	Effect coefficient of the front face angle, X_4 (%)
ψØ	Effect coefficient of the angle of internal friction, Ø (°)
λ	Total effect coefficient
σ	Standard deviation

Acknowledgements

In this study, results of a part of the continuing doctoral thesis have been submitted and also it is supported by Scientific Research Projects Coordination Units of Selcuk University Research Funding (BAP- 17401107) which are gratefully acknowledged.

References

[1] Coduto, D., Geotechnical Engineering: Principles and PracticesPrentice-Hall, New Jersey, pp. 528–552. 1999.

[2] Turkish Standards Institute, Soil Retaining Structures; Properties and Guidelines for Design (TS 7994), Turkish Standard, 1990.

[3] American Concrete Institute, ACI Committee, and International Organization for Standardization, Building Code Requirements for Structural Concrete (ACI 318-14), 2014.

[4] McCormac, J. C., Brown, R. H., Design of Reinforced Concrete, John Wiley and Sons, 2015.

[5] Minnesota Department of Transportation Bridge Office, LRFD Bridge Design Manual, 5-392, 11-52, 2016.

[6] Geem, Z. W., Kim, J. H., Loganathan, G.V., A New Heuristic Optimization Algorithm: Harmony Search, Simulation, 76, 2, 60-68, 2001.

[7] Saka, M., Çarbaş, S., Optimum Design of Single Layer Network Domes Using Harmony Search Method, Asian Journal of Civil Engineering (Building and Housing), 10, 1, 97-112, 2009.

[8] Geem, Z. W., Optimal Cost Design of Water Distribution Networks Using Harmony Search, Engineering Optimization, 38, 3, 259-277, 2006.

[9] Geem, Z. W., Lee, K. S., Park, Y., Application of Harmony Search to Vehicle Routing, American Journal of Applied Sciences, 2, 12, 1552-1557, 2005.

[10] Cheng, Y. M., Li, L., Fang, S. S., Improved Harmony Search Methods to Replace Variational Principle in Geotechnical Problems, Journal of Mechanics, 27, 1, 107-119, 2011.

[11] Fattahi, H., Prediction of Slope Stability State for Circular Failure: A Hybrid Support Vector Machine with Harmony Search Algorithm, International Journal of Optimization in Civil Engineering, 5, 1, 103-115, 2015.

[12] Khajehzadeh, M.; Taha, M.R.; El-Shafie, A., Eslami, M., Economic Design of Foundation Using Harmony Search Algorithm, Australian Journal of Basic and Applied Sciences, 5, 6, 936-943, 2011.

[13] Akın, A., Saka, M. P., Optimum Design of Concrete Cantilever Retaining Walls Using the Harmony Search Algorithm, Proceeding of 9th International Congress on Advances in Civil Engineering Civil-Comp Press, 27-30, 2010.

[14] Uray, E., Çarbaş, S., Erkan, İ.H., Tan, Ö., Optimum Design of Concrete Cantilever Retaining Walls with the Harmony Search Algorithm, 6th Geotechnical Symposium, Turkey, 2015.

[15] Yepes, V., Alcala, J., Perea, C., González-Vidosa, F., A Parametric Study of Optimum Earth-Retaining Walls by Simulated Annealing, Engineering Structures, 30, 3, 821–830, 2008.

[16] Molina-Moreno, F., García-Segura, T., Martí, J. V., Yepes, V., Optimization of Buttressed Earth-Retaining Walls Using Hybrid Harmony Search Algorithms, Engineering Structures, 134, 205-216, 2017.

[17] Rhomberg, E. J., Street, W. M., Optimal Design of Retaining Walls, Journal of the Structural Division, 107, 5, 992-1002, 1981.

[18] Keskar, A. V., Adidam, S. R., Minimum Cost Design of a Cantilever Retaining Wall, Indian Concrete Journal, 63, 8, 401-405, 1989.

[19] Saribas, A., Erbatur, F., Optimization and Sensitivity of Retaining Structures, Journal of Geotechnical Engineering, 122, 8, 649-656, 1996.

[20] GEO5, Geotechnical Design Computer Program, Fine Software, https://www.finesoftware.eu.

[21] Uray, E., Çarbaş, S., Erkan, İ. H., Tan, Ö., Parametric Investigation for Discrete Optimal Design of a Cantilever Retaining Wall, Challenge Journal of Structural Mechanics, 5, 3, 108-120, 2019.

[22] Bishop, A. W., The Use of the Slip Circle in the Stability Analysis of Slopes, Geotechnique, 5, 1, 7-17, 1955.

[23] Taguchi, G., Elsayed, E. A., Hsiang, T. C., Quality Engineering in Production Systems, McGraw-Hill, New York. 173, 1989.

[24] Tan, Ö., Investigation of Soil Parameters Affecting the Stability of Homogeneous Slopes Using the Taguchi Method. Eurasian Soil Science, 39, 11, 1248-1254, 2006.

[25] Statistica, Statistical Analyses Computer Program, TIBCO Software Inc., https://www.tibco.com/products/tibco-statistica.

[26] Çarbaş, S., Saka, M. P, Optimum Topology Design of Various Geometrically Nonlinear Latticed Domes Using Improved Harmony Search Method, Structural and Multidisciplinary Optimization. 45, 3, 377-399, 2012.

[27] Lee, K. S., Geem, Z. W., A New Structural Optimization Method Based on the Harmony Search Algorithm, Computers and Structures, 82, 9, 781-798, 2004.

[28] Matlab R2017b, a programing language, MathWorks.

[29] Fishburn, P.C., Additive Utilities with Incomplete Product Set: Applications to Priorities and Assignments. ORSA Publication, Baltimore, 1967.

[30] Triantaphyllou, E., Multi-Criteria Decision-Making Methods. In Multi-Criteria Decision-Making Methods: A Comparative Study. Springer, Boston, MA, 5-21, 2000.

[31] Terzaghi, K., Theoretical Soil Mechanics, 4th ed., John Wiley & Sons, Inc., New York, 1947.

Teknik Dergi, 2021 10995-11011, Paper 621

Evaluation of Two Vegetation Indices (NDVI and VCI) Over Asi Basin in Turkey

Mehmet DIKICI[1]
Murat AKSEL[2]

ABSTRACT

Climate change and global warming are among the issues that humanity is most concerned about the future. The growing drought and flood risks that increase despite the taken measures have led to the adoption of an integrated understanding on the topic of water management in recent years. To manage the increased risk of drought and to make sustainable planning, the dimensions of drought should be known first. For this purpose, many drought indices have been developed. The Normalized Difference Vegetation Index (NDVI) and Vegetation Condition Index (VCI), which determined by remote sensing, are two of these. In this study, in which the agricultural drought was analyzed with vegetation indices by taking into consideration the historical drought archive, the Asi Basin was addressed. The data of the Asi Basin, which covers an area of 7800 km^2 and was obtained from the Moderate Resolution Imaging Spectroradiometer (MODIS) and Advanced Very High-Resolution Radiometer (AVHRR) satellites, was used in this study. With the satellites benefited in remote sensing and with the Coordination of Information on the Environment (CORINE), where the layers of vegetation were determined, agricultural and forest areas were evaluated separately. The vegetation indices, which change with the increase in temperature, have revealed the necessity of a long-term drought management for the Asi Basin. Result of the work pointed that NDVI index is more appropriated to the Asi Basin than the VCI index to monitor drought.

Keywords: Remote sensing, drought index, NDVI, VCI.

1. INTRODUCTION

Within the context of the planning, development and management of water resources, which are adversely affected by climate change, the subject of mitigation of expected impacts of drought has gained considerable importance. Management of the increased drought risk and

Note:
- This paper has been received on July 10, 2019 and accepted for publication by the Editorial Board on January 7, 2020.
- Discussions on this paper will be accepted by September 30, 2021.

• https://doi.org/10.18400/tekderg.590356

1 Alanya Alaaddin Keykubat University, Department of Civil Engineering, Antalya, Turkey
mehmet.dikici@alanya.edu.tr - https://orcid.org/0000-0001-5955-3425

2 Alanya Alaaddin Keykubat University, Department of Civil Engineering, Antalya, Turkey
murat.aksel@alanya.edu.tr - https://orcid.org/0000-0002-6456-4396

adaptation to it are only achieved through the development of sustainable and effective drought risk management strategies that adopt holistic approaches. The drought management is part of the disaster management [1]. Drought risk management is the concept and study of prevention and mitigation of the negative consequences of drought hazard and potential disaster through activities and measures aimed at prevention, harm reduction and preparedness [2]. Drought risk management is an important part of water resources management policies and strategies. National drought policies play a major role in managing drought risk [3]. In order to reduce the impacts caused by drought, drought management plans need to be prepared based on country legislation and taking into account the specific drought characteristics and impacts of the basin [4]. It is very important that these plans should be prepared as part of the basin management plan in order to create integrity. In addition, the involvement of all stakeholders, affected sectors, decision makers and experts in the process of creating plans contributes greatly to the success of drought management plans. Elements of drought management plan include knowledge of the characteristics of the river basin, investigation of historical drought incidents in the basin, evaluation of the risk that may occur, determination of indicators and threshold values for drought analysis, establishment of a precautionary program to reduce the effects of drought, instillation of early warning system and establishment of the organizational structure [5]. Drought risk management covers the early warning system including hazard, exposure, impact assessment and vulnerability, drought monitoring and forecasting; it also covers the stages of preparation and harm reduction [1]. Early warning systems, one of the most important elements of drought management plans, are used within the framework of two targets, drought monitoring and drought forecasting. Drought early warning systems typically aim to monitor, assess and present information about climate, hydrological properties, water supply conditions and trends. The objective here is to take action within a drought risk management plan to reduce potential impacts and to provide early information before or during the onset of drought. Since drought is a hydrological phenomenon that begins slowly and progresses monitoring and analysis of drought are of great importance [6]. Monitoring and analysis of drought is done through various indicators and indices. These indicators and indices enable the characterization of drought by providing information about the severity, location, duration and timing of drought in order to determine, classify, and monitor drought conditions. Some indicators and indices can also be used to validate drought indicators that are modeled, remotely detected or assimilated to the model of remote sensing data [6].

Thanks to the geographic information systems and the power of developing computing and imaging systems, it has been possible to overlap, map and compare different indicators and indices [6]. Location of the Asi Basin is shown in Figure 1. Drought analysis study for the Asi Basin, which is addressed in this study, has been investigated by various researchers for different indices. The Asi Basin is one of Turkey's 25 basins and covers all and/or part of Hatay, Kilis, Gaziantep, Adana and Osmaniye provinces.

Studies focusing on the Asi Basin are usually related to the recent past, however, there are some studies by historians and researchers that evaluate the records of a few centuries ago. It is known that in the Ottoman Empire in the 16th century and later (the period of 1564, 1565-67, 1586, 1588 and 1560), some drought and famine events occurred. Also in the following periods, droughts lasting two years were experienced (seven times in the Mediterranean region, five times in the Black Sea region). The years of drought in both regions were 1676, 1679, 1696, 1715, 1725, 1746, 1757, 1797, 1815, 1887 [7]. Two great disasters processed in

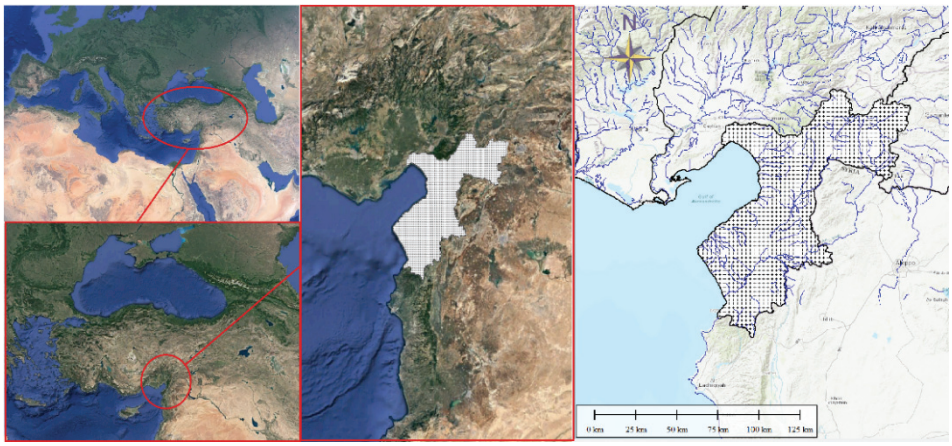

Figure 1 - Asi Basin

the Ottoman Empire in 19th century were identified by Sariköse [8]. The first was the famine caused by a severe drought in 1845, and the other was the famine experienced in 1874-1875. In the study, it was stated that the drought was effective throughout the Ottoman geography in the 19th century. In the study carried out by Akbas, arid years affecting the basin were determined by the analysis conducted based on the study called "*Significant drought years in Turkey*", and by focusing on Turkey according to Palmer drought severity index [9]. As a result of that study, it was determined that drought conditions were observed in 1972-1974, 1989, 1991, 2001, and 2007 - 2008 periods in the Asi Basin. According to the study carried out by Simsek et al. [10], it was observed that the drought conditions prevailed throughout all the basin during the 2013-2014 years, especially during the summer months when the drought was experienced throughout Turkey and throughout the agricultural year. According to the hydrological drought analysis results conducted by using the Streamflow Drought Index (SDI) [11] method to identify the total annual natural stream flows of the Asi Basin between 1981 and 2010, "moderate drought" was observed in 1991, 2001 and 2007-2008 periods [12]. In the study conducted by Gumus, hydrological drought analysis was performed by using 52-year flow data (1954-2005) obtained from four streamflow observation stations (1905, 1906, 1907, 1908) in Asi Basin [13]. SDI method was used to determine the drought. Using monthly flow data, the intensity, size and distribution of the dry and humid periods of the Asi Basin were determined by 3, 6 and 12 month SDI values. As a result of the study, based on the average SDI values of all time scales, it was observed that the number of year lasting dry between 1980 and 2005 was much higher than the number of year lasting dry between 1954 and 1979. In addition, excessive dry years on the basis of the basin were determined as 2000 and 2001. According to the SDI-12 values calculated to monitor the annual drought and humidity, it was observed that the rate of drought occurrence in all stations, except Station 1907, was more than the rate of humidity occurrence. The rate of being Excessive Dry (ED) of all stations was around 3%, Severe Dry (SD) was around 5%, and Moderate Dry (MD) was around 10%. It was determined that the highest drought calculated by SDI-12 was at the stations 1905, 1907 and 1908 with 34.6%, and the highest humidity was at the station 1907 with 38.0%. When all values are examined together, it is

seen that the dry and humid periods are close to each other. The occurrence percentage of dry/humid periods are given in Figure 2.

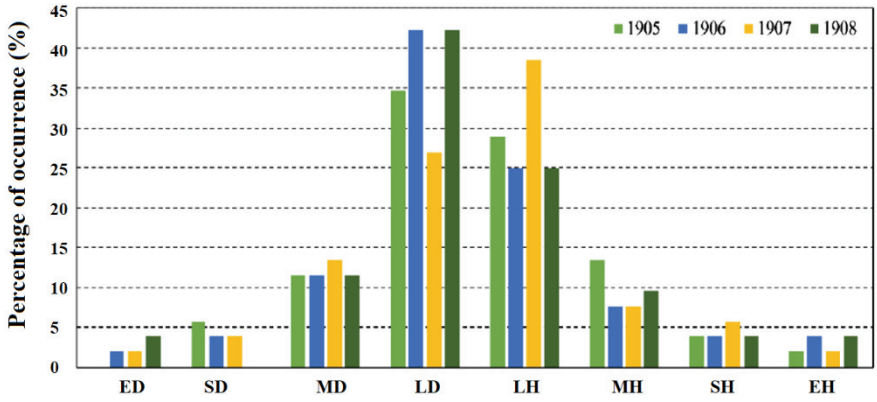

Figure 2 - Rates of being dry/humid of the stations

NDVI and VCI indices have been widely used in monitoring of vegetation for the analysis of agricultural productivity by remote sensing methods. [14]. In this study, the application of NDVI and VCI indices, which have gained importance in recent years, to the Asi Basin by using remote sensing method is emphasized.

2. MATERIALS AND METHOD

2.1. Remotely Sensed Data

By the development of space technology, Remote Sensing (RS) applications have rapidly increased as integrated with powerful software-hardware opportunities and Geographic Information Systems (GIS). The ability to easily transfer spatial data from space via satellite and various ground data to GIS environment has increased the possibilities of analysis on natural resource management, land cover and land use, environmental and ecological analysis, disaster and risk assessment, meteorological, hydrological and agricultural applications, etc. Remote sensing data is used effectively and intensively in various hydrological applications. Drought studies are among these practices. The vegetation and soil moisture that can be obtained by remote sensing are the data sources commonly used in drought studies. High resolution vegetation change information provided by vegetation indices (such as NDVI) temporally and spatially can contribute to drought information. Vegetation indices are preferred because they are both easy to use and do not require any assumptions and/or additional information except for themselves [15]. Plant indices are parameters which can be determined by remote sensing methods and which have very wide application area. The reason for this is that the green vegetation gives high reflection values in the near-infrared region of the electromagnetic spectrum [16]. Certain pigments in plant leaves absorb strongly the rays on the visible wavelengths (390 nm-700 nm wavelength range). From these rays, especially red (620 nm– 750 nm wavelength range) wavelength rays

are absorbed by the plant to use during photosynthesis. On the other hand, it strongly reflects the near-infrared rays (760 nm- 900 nm wavelength range) that are invisible to the human eye. Vegetation indices use this information to make inference about the greenery of the plant. The vegetation spectrum is given in Figure 3 [17]. Changing reflection properties of vegetation in its maturation period from the early spring period to the late maturity season and harvest time causes plant indices to change. Most of the satellite sensors measure red and close infrared light waves reflected from the earth. By using mathematical formulas, raw satellite data on these light waves are converted into vegetation indices. Vegetation indices are indicators that define the greenness of the plant (that is, its relative density) and health status for each cell in the satellite image. Not all of the vegetation indices obtain the greenness of the vegetation by directly measuring visible and near-infrared wavelengths; some indirectly perceive the change in the vegetation. For example, some vegetation indices can obtain information about plant changes on the surface by using temperature change information on the earth surface. In other words, the water content in the plant enables the plant to release less heat in the day compared to the soil, and the information on the vegetation change is obtained by using the information about the temperature change during the day. These indices have the potential to provide important information about the drought experienced in the basin because they are sensitive to vegetation. For this purpose, there are various indices that are widely used in the literature such as Enhanced Vegetation Index (EVI), Evaporative Stress Index (ESI), Normalized Difference Vegetation Index (NDVI), Temperature Condition Index (TCI), Vegetation Condition Index (VCI), Vegetation Drought Response Index (VegDRI), Vegetation Health Index (VHI), Water Requirement Satisfaction Index (WRSI), Normalized Difference Water Index (NDWI), Land Surface Water Index (LSWI) and Soil Adjusted Vegetation Index (SAVI).

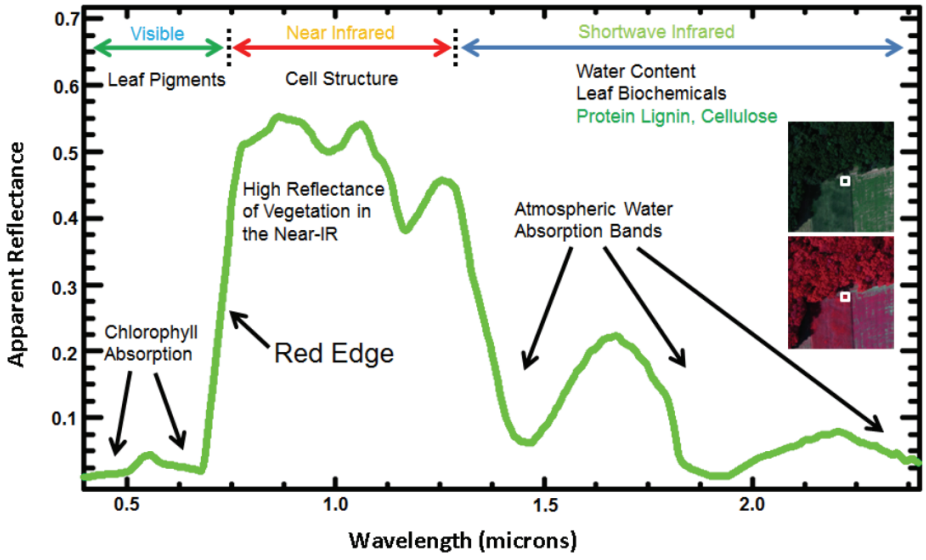

Figure 3 - Vegetation spectrum [17]

Within the scope of the Asi Basin drought analysis study, the use of vegetation indices which provide information about the change in plant green were preferred. In this direction, NDVI and VCI were analyzed as temporal and spatial within the Asi Basin boundaries.

2.1. Normalized Difference Vegetation Index (NDVI)

Normalized Difference Vegetation Index (NDVI) is one of the most widely used tools for monitoring green vegetation by using remote sensing data. NDVI is also one of the most widely used vegetation indices in forest classification and agricultural studies as well as the identification of the change in land cover. Certain pigments in plant leaves absorb strongly the rays in visible wavelengths (390 nm - 700 nm wavelength), especially the rays in red wavelengths (620 nm – 700nm wavelength), in order to use during photosynthesis. On the other hand, rays that are in the near-infrared wavelengths (760 nm – 900 nm wavelength) and invisible to human eye are strongly reflected through spongy mesophyll in the plant. NDVI makes inference about the greenery of the plant by normalizing this difference information. Different ranges of red and near-infrared wavelengths are measured using sensors by different satellites. Based on observations of satellite images on near-infrared (NIR) and red (RED) wavelengths, NDVI is calculated as in Equation 1.

$$NDVI = \frac{(NIR-RED)}{(NIR+RED)} \quad (1)$$

Theoretically, NDVI values range from (-1) to (+1), and more rays are reflected in the near-infrared wavelengths compared to the red wavelength. In areas where green vegetation is more, the index value approaches to (+ 1) (NIR-RED difference increases and approaches to NIR + RED). Clouds, water and snow cover have low NDVI index values (-). Bare soil and weak vegetation shows near-zero or (-) NDVI value. On an NDVI map showing areas where agriculture is intensive, areas with low NDVI values point to weak plant development due to a variety of reasons such as drought, extreme humidity, disease and pests. On the other hand, high NDVI values show the healthy areas of plant development [18]. For example, in areas consisting of barren rock, sand, or generally snowy areas, NDVI values are 0.1 or smaller. In shrubs and grazing areas, or in areas covered with sparse vegetation such as crops at the harvest period, NDVI values are observed in the range of 0.2 – 0.5. The highest NDVI values range from about 0.6 – 0.9 in temperate and tropical forests or in the maximum growth stage of crops. NDVI is considered as the main indicator of the biomass amount of plants and the index value of leaf area and is used for monitoring plant growth and estimating the yield during the growth period. NDVI is particularly useful for monitoring plant status on a global scale because the normalization phase used during its calculation can compensate some factors such as varying brightness conditions, surface slope and angle of view. The average of NDVI values can be taken in order to determine the normal growth conditions for a given year in a region. In this way, the health of the plant can be assessed by characterizing according to normal. When the NDVI values are analyzed as temporal, it can give information about the plant's development, whether it is under water stress, and the changes that occur as a result of human activities such as deforestation or fire. NDVI data of NOAA, AVHRR and MODIS satellites are widely used satellite images to monitor vegetation changes in large areas. MODIS data was used to detect drought from vegetation in the Seyhan Basin[19]. AVHRR and MODIS satellites provide NDVI data as ready for use; therefor, no

atmospheric correction is required in these satellite data, and thus, no additional data is needed for Atmospheric correction. The data on NIR and RED wavelengths obtained from Landsat satellite need atmospheric correction before the NDVI is calculated. Although the normalization phase reduces the effect of these atmospheric components on the NDVI, the study used the NDVI data obtained from AVRR and MODIS satellites that did not require atmospheric correction. The time interval, resolution and repeat time of the NDVI values obtained from these two satellites are given in Table 1.

Table 1 - Data Properties of AVHRR and MODIS Satellites

Satellite	Data Name	Time Interval	Resolution	Repetition Period
AVHRR-The Advanced Very High Resolution Radiometer	AVHRR NDVI	1981 –2016	3.6 km	16 days
AVHRR-The Advanced Very High Resolution Radiometer	AVHRR NDVI3gc	1981 –2015	8.0 km	16 days
MODIS-The Moderate Resolution Imaging Spectroradiometer	MODIS MOD13Q1 NDVI	2000 –2016	250 m	16 days

2.2. Advanced Very High Resolution Radiometer (*AVHRR)*

The Advanced Very High Resolution Radiometer (AVHRR) first began its observations on the TYROS-N that was sent to space in 1978 and then on the NOAA satellite. The basic properties of AVHRR have not changed and AVHRR has been continuously utilized in Earth Observation. AVHRR provides approximately 3.6 km of spatial resolution and the band area is 2,399 km wide. Whereas NOAA gets around the world 14 times a day, AVHRR observes the same area twice a day. Wide-band images measured by AVHRR are suitable for a variety of purposes, such as cloud cover area, vegetation index and surface temperature.

There are several studies in the literature which show that the NDVI values calculated by using AVHRR satellite data are different from the NDVI values obtained from other satellite data [20-26] The main reasons for the fact that AVHRR NDVI values are problematic are inadequate atmospheric correction, orbital drift and bidirectional reflectance distribution function, correction deficiencies, and scanning and solar angle effects [25, 26] The AVHRR NDVI3G product was obtained as a result of the study conducted to partially correct the time series of AVHRR NDVI [26]. In addition to the AVHRR NDVI product, the time series of AVHRR NDVI3g products were also used in the scope of this study.

2.3. MODIS

The National Aeronautics and Space Administration (NASA) blasted off the MODIS sensor on the Terra platform on December 18, 1999 and on the Aqua platform on May 4, 2002 to

space within the framework of the Earth Observing System (EOS) program [27]. The MODIS sensor on Terra and Aqua satellites is used to obtain comprehensive data on ground, ocean and atmospheric processes. The design of MODIS goes back to previous sensors (such as the AVHRR sensor used in NOAA satellite). However, the difference of it from the previous sensors is that both the temporal and positional resolution of it is high, and it can collect data from 36 separate spectral bands from 0.4 µm to 14 µm [28]. The MODIS sensor has a positional resolution of 250 m between 1-2 bands, 500 m between 3-7 bands and 1 km between 8 - 36 bands [29]. MODIS observations, used in the ocean and atmosphere studies in the first place, today provide important facilities in vegetation, land use, and drought and Agriculture studies. Although MODIS images are taken twice a day, NDVI products are published in 8-day composites [30]. MODIS NDVI images consisting of 4800 rows and 4800 columns allow analyzing the changes in vegetation activity in a wide range of areas [31, 32]. In many studies, the NDVI data obtained from different satellites have been compared. While some studies argue that MODIS NDVI values are better than AVHRR NDVI and AVHRR NDVI3g product [33], some studies indicate that long-term trends show high consistency with each other [34]. In this study, AVHRR NDVI, AVHRR NDVI3g and MODIS NDVI values were used and NDVI time series were compared among themselves. The comparative graph is presented in Figure 4.

In drought studies, since the definitions of the drought period are generally made as deviations from the normal values obtained for long periods, the mean seasonality of NDVI values and the anomaly values obtained by subtracting these seasonal data from the original data were compared. When calculating the anomaly time series of the data series, the period of 2001-2015 when all three data were observed was selected. When the anomaly and seasonal values are compared, it is observed that the actual change between the data is due to the seasonal time series and the difference among the anomaly values is less on the average. This shows that the differences between NDVI datasets can be minimized by calculating as an anomaly in drought studies. Normal, seasonal and anomaly NDVI data charts are given in Figure 5 As a result of the large turbulence and evaluation of the spatial distribution in AVHRR data, the data set was found to contain too much error. Therefore, in the study, the AVHRR NDVI-3G version whose quality control was done was used in conjunction with MODIS NDVI in the calculations carried out with drought indices.

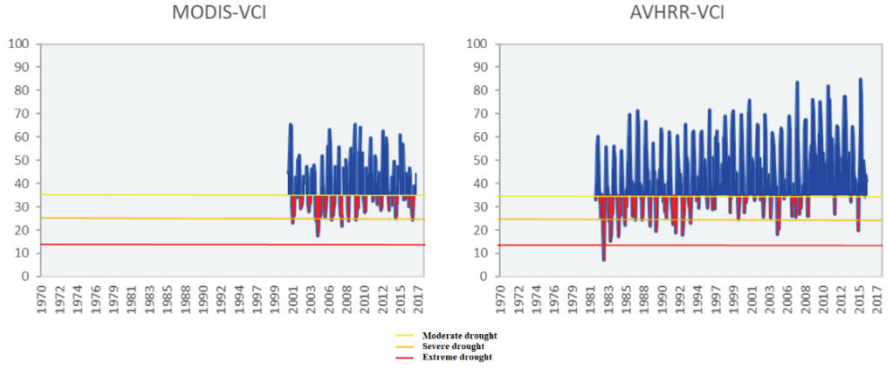

Figure 4 - Time series of the field average of MODIS (2001-2016) and AVHRR (1982-2015) VCI values for Asi Basin

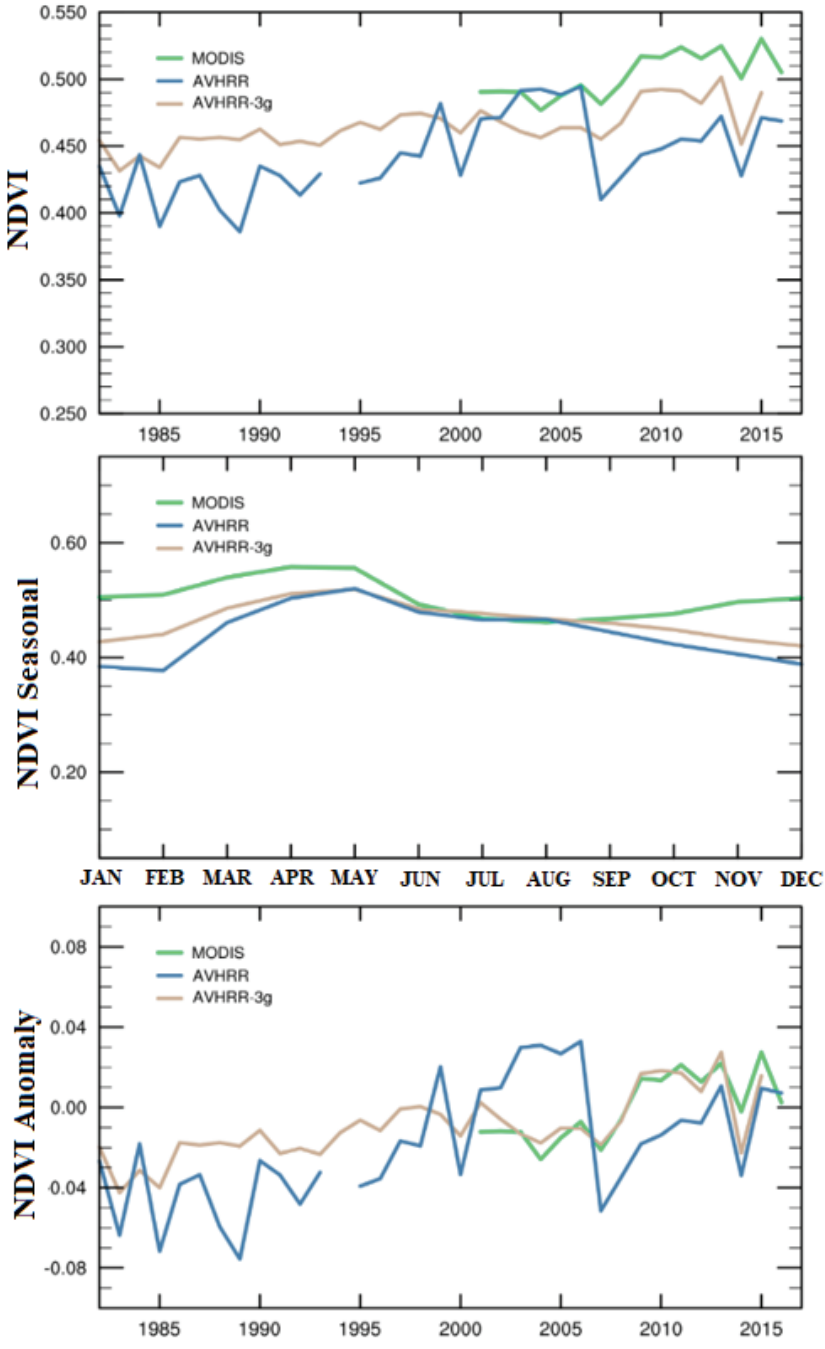

Figure 5 - NDVI time series obtained from different satellites for the Asi Basin

2.4. Vegetation Condition Index (VCI)

VCI can provide information about the start, duration and severity of drought by taking into account the effect of drought on vegetation. Together with NDVI, it is used for the evaluation of vegetation in drought conditions affecting agriculture [35]. VCI compares the NDVI data for a given period with the highest and lowest values of the NDVI data for the whole period [36]. VCI is expressed as a percentage (%) and provides information about when the highest and lowest values of the observed value occurred in previous years. While the low VCI values indicate that the vegetation is in bad condition, the high VCI values indicate that the vegetation was in good condition [37]. Considering that the data derived from satellite data are obtained from many cells in the spatial sense, the VCI_i for any cell (i) is calculated as in Equation 2.

$$VCI_i = \frac{(NDVI_i - NDVI_{min})}{(NDVI_{max} - NDVI_{min})} x100 \quad (2)$$

VCI can be considered as the normalized state of NDVI. In this study, in addition to NDVI, the VCI index was also evaluated because VCI is a more appropriate index for assessing the amount of deviation of vegetation from normal condition. Therefore, VCI allows an opportunity for comparison of the simultaneously measured NDVI values for different ecosystems (that is for different vegetation in different geographies). Since VCI can distinguish short-term climate signal from long-term ecological signal, it is a better indicator of soil moisture deficit than NDVI. The importance of VCI is related to the vitality of the vegetation examined by the vegetation index [38]. VCI data, like NDVI, has high resolution and good field coverage. There are various studies in literature on the use of VCI for drought analysis [35, 39, 40].

3. RESULTS AND DISCUSSION

3.1. Drought Intensity Analysis for Vegetation Condition Index

For this study, the Vegetation Condition Index (VCI) was calculated to compare the drought determined as a result of the drought analysis for the Asi Basin by using the NDVI values obtained from MODIS and AVHRR satellite data. In this direction, for each 250 m satellite cell within the basin area, the VCI time series obtained using satellite data for the years 2001-2016 are presented in Figure 4. While VCI values shown in red in time series indicate drought in plant condition, the values shown by blue can be interpreted as the plant condition in the seasonal and climatic conditions.

The graphic in which the comparison of MODIS VCI and AVHRR-3G VCI of the Asi Basin is shown is given in Figure 6. It is seen that the index values are frequently overlapping but calculated magnitudes are different. Root mean square error between two data was calculated as 20. The main reason is MODIS spatial resolution is higher than the AVHRR and MODIS data are more accurate than the AVHRR for VCI[41].

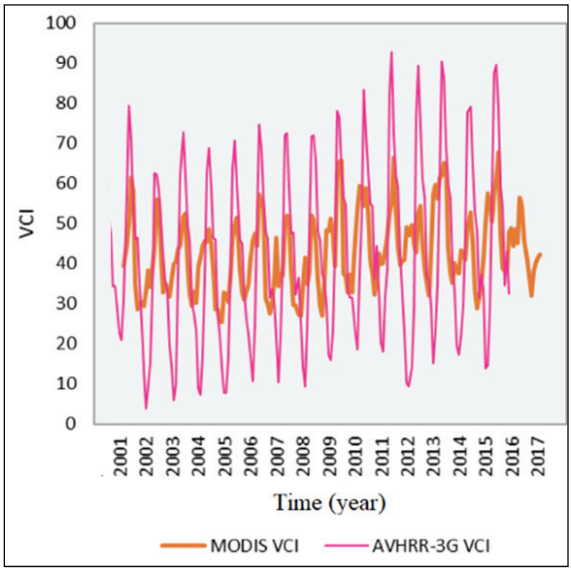

Figure 6 - Comparison of MODIS VCI and AVHRR-3G VCI of the Asi Basin

3.2. Agricultural Drought Analysis

Within the scope of drought index studies, climate change responses of the unregularly irrigated or non-irrigated agricultural fields and vegetation areas in Asi Basin should be analyzed. The CORINE (Coordination of Information on the Environment) layers to be used for these analyses were determined and the changes of the NDVI time series were calculated on these layers. While selecting classes, the areas where vegetation was not subjected to human interventions such as irrigation, fertilization and changes were mostly due to natural processes were targeted. The distribution of these determined CORINE layers on the basin is given in Figure 7.

The fact that the AVHRR-3G and MODIS NDVI data used in the analysis were at different resolutions led to the differentiation of the classified areas. Reason of this was that the majority value (that is, dominant class) was used when the category-based high-resolution data was moved to a coarser resolution. The 8-km resolution pixel in AVHRR-3G data corresponds to 250-m resolution 1024 pixels in MODIS data. Therefore, some pixels consist of the mosaic of classes of very different properties, as well as the class that is designated as the dominant class. Another problem caused by the resolution difference is that some classes in the minority, which can be detected at high resolution, cannot be expressed at a coarse resolution and disappear. This can be seen in the graphs below. Some classes that can be detected in MODIS data cannot be expressed in AVHRR-3G resolution: The fact that the determined classes can be found in geographically discrete areas in both data can sometimes lead to the layers take very discrete values. Another issue to be considered during the evaluation is that land use may change over time. This change is inevitable, especially given a long period of time, such as 1982-2016. With the increase in population, it should be taken into consideration that forest areas can become agricultural areas and agricultural areas can

become artificial lands and that the opposite situation may sometimes arise due to the reasons such as migration from the village to the city and this may result in artificial tendencies.

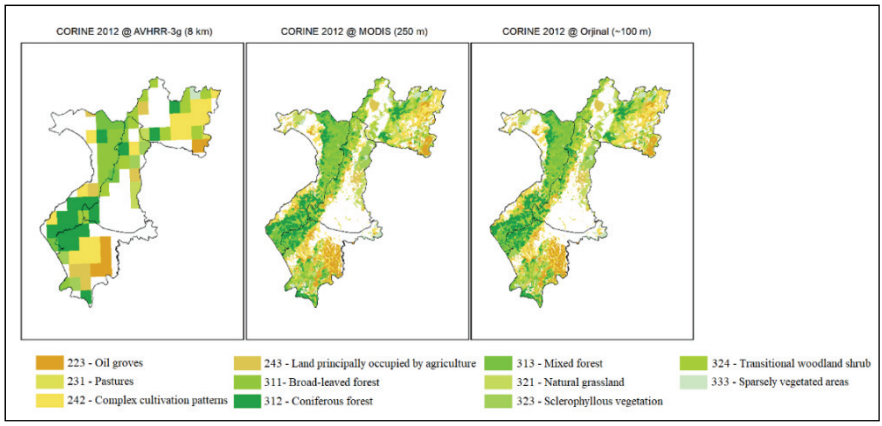

Figure 7 - The layers examined for the CORINE NDVI comparison in the Asi Basin

In CORINE 2012 land use data, the NDVI temporal variation series for agricultural areas starting with code 2 are given as annual and seasonal in Figure 8. AOS (December-January-February) refers to winter months, MNM (March-April-May) spring months, HTA (June-July-August) summer months, and EEK (September-October-November) autumn months.

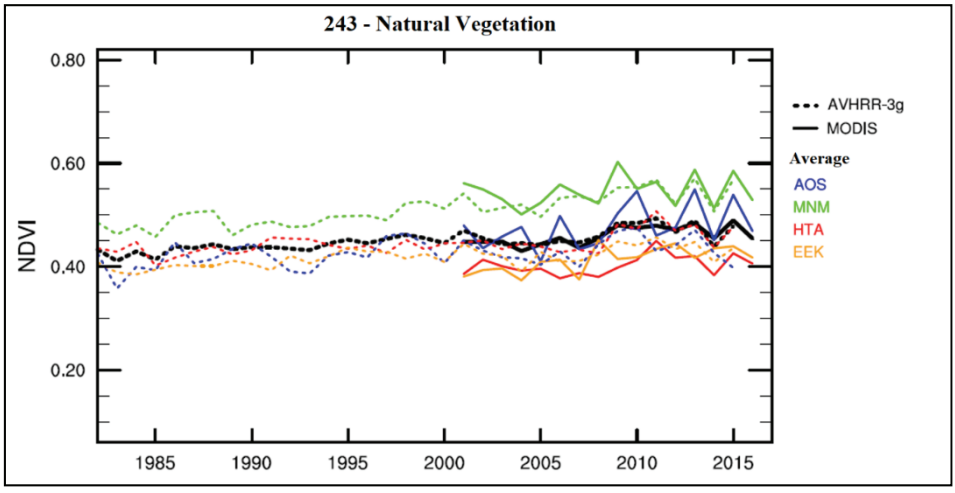

Figure 8 - ASI Basin CORINE 243 - Natural vegetation NDVI temporal change

When the examined time series of the layers is evaluated in general, it is observed that NDVI values were relatively low in 2002 and 2004 and were significantly increased between 2007 and 2013. Except the fluctuations in the data, it was observed that NDVI values were higher

in the spring months and lower in the summer months. Because the pasture class had too small areas to be represented at the AVHRR-3G resolution, it was not included in the figure instead of graphics. In the olive groves, which are resistant to cold, do not shed leaves, and are also known as the everlasting tree, values above average were observed in winter months, unlike other classes. It was considered that the olive groves was not well represented in indices. Since the class of natural vegetation was in large areas, it was well represented in both data and it was observed that it received close values to each other. This layer, where human influence is limited, is one of the classes where the effects of drought on plants can be better observed and it showed significant decreases in 1982, 1989, 2004, 2007, 2014. The highest values were observed in 2011 and 2015. The series of annual and seasonal temporal changes of NDVI that belongs to sparse plant areas and that start with code 3 of CORINE classification is presented in Figure 9.

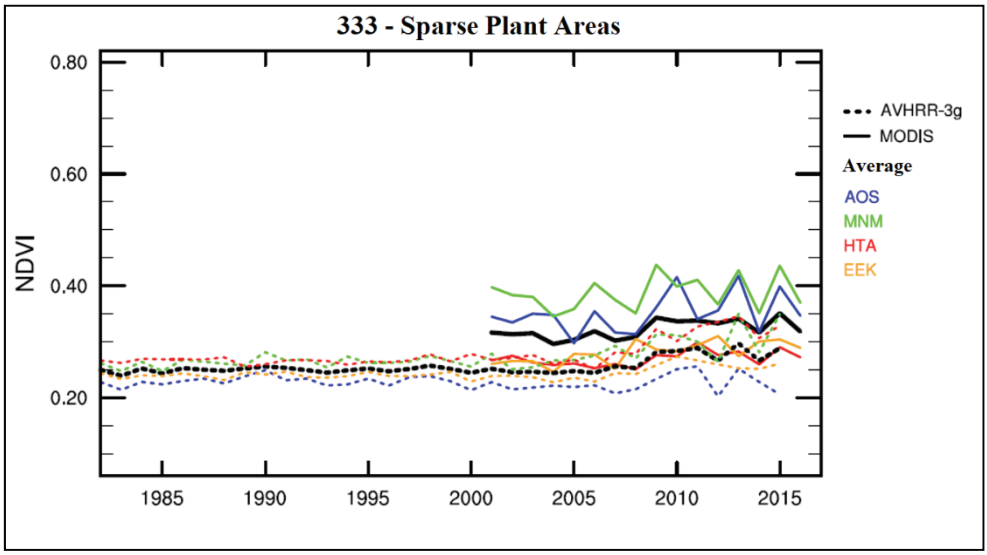

Figure 9 - Asi Basin CORINE 333 –NDVI Time series of sparse plant areas

The difference between the calculated NDVI of two data increases due to dilution in vegetation.

4. CONCLUSION

This study set out to assess NDVI and VCI vegetation indices over Asi Basin by using MODIS and AVHRR-3G data. In the examined forest layers, annual changes in agricultural areas was seen in a similar way and in NDVI calculations, while the lowest values were determined in winter and the highest values were determined in summer and spring. Whereas the cold-resistant and non-deciduous needle-leaved trees (conifers) got the highest values in MODIS data during the winter months, they got the lowest values in AVHRR-3G data. Therefore, it was assessed that as a result of the lack of vegetation class separation at 8 km resolution, the needle-leaved forests were mixed with other classes. It was also evaluated that

because the deciduous (non-evergreen) trees were in the same pixels with the needle-leaved trees, they got much lower values in winter than expected. In general, since 2000, there has been an increase in NDVI values. This may be a result of the decrease in the snow cover, which reduces NDVI values due to the result of climate change, in terms of process and area. It is thought that the positive contribution of increasing temperature values to the photosynthesis process may have consequences on NDVI values. Changes in land use may also cause differences in NDVI values. For the Asi Basin, the periods when indices and historical data jointly point to drought were identified as 1973-1974, 1989-1991, 1993-1994, 2000-2001, 2004-2005, 2014 and 2016. For the Asi Basin, a process in which droughts management becomes more and more important. Precipitation based hydrological drought analysis which is mentioned in Figure 2 shows parallelism with vegetation based drought indices results.

Basin based water resources planning studies have an important place in civil engineering. Current and future status of the watershed are always examined in investment planning, water resources management, structural and administrative solutions. In terms of water resources and irrigation planning, this study is important for the Asi Basin. As can be seen from the NDVI and VCI indices, it is beneficial to develop water resources and take additional precautions due to climate change and population growth for the Asi Basin. In addition, this study showed that the NDVI index is better appropriated to the Asi Basin than the VCI index.

Acknowledgement

We would like to thank General Directorate of Water Management of The Ministry of Forest and Water Management for their contribution to providing the data in this study.

References

[1] D.A. Wilhite, Drought : A Global Assessment, 2000. doi:10.4324/9781315830896.

[2] UNDP, DROUGHT RISK MANAGEMENT, 2016.

[3] D.A. Wilhite, M.V.K. Sivakumar, R. Pulwarty, Managing drought risk in a changing climate: The role of national drought policy, Weather Clim. Extrem. 3 (2014) 4–13. doi:10.1016/j.wace.2014.01.002.

[4] Water Scarcity and Droughts Expert Network, Drought Management Plan Report Including Agricultural, Drought Indicators and Climate Change Aspects European Commission Directorate of Environment, 2008.

[5] G.W.P.C. and E. Europe, Guidelines for preparation of the Drought Management Plans Guidelines for preparation of the Drought Management Plans, 2015.

[6] M.D. Svoboda, B.A. Fuchs, Handbook of drought indicators and indices, 2017. doi:10.1201/b22009.

[7] S. Tekin, 19.Yüzyılın Sonu 20.Yüzyılın Başlarında Batı Anadolu'da Yaşanan Kuraklık Olayları, He J. Acad. Soc. Sci. Stud. Int. (2015) 329–341.

[8] S.T. Sarıköse, XIX. Yüzyilda Çukurova'da Doğal Afetler Ve Salgin Hastaliklar, 2013.

[9] A. Akbaş, Türkiye Üzerindeki Önemli Kurak Yıllar, Coğrafi Bilim. Derg. 12 (2014) 101–118. doi:10.1501/Cogbil_0000000155.

[10] O. Şimşek, M. Yildirim, N. Gördebil, 2013 – 2014 Tarim Yili Kurakli Analizi, (2014).

[11] I. Nalbantis, Evaluation of a Hydrological Drought Index, Eur. Water. 2324 (2008) 67–77.

[12] A.D. Özdemir, M.K. Erkuş, Havza Bazında Hidrolojik Kuraklık Analizi, in: IX Natl. Hydrol. Congr., 2017.

[13] V. Gümüş, Akım Kuraklık İndeksi ile Asi Havzasının Hidrolojik Kuraklık Analizi, 5 (2017) 65–73.

[14] F.B. Sanli, A. Delen, Assessment of vegetation indices for the determination of agricultural crop types, J. Environ. Prot. Ecol. 19 (2018) 417–425.

[15] B. Bulut, M.T. Yılmaz, Türkiye'deki 2007 ve 2013 Yılı Kuraklıklarının NOAH Hidrolojik Modeli ile İncelenmesi, Teknik Dergi. 27 (2016) 7619–7634. http://dergipark.gov.tr/tekderg/issue/28142/299116.

[16] O. Gökdemir, A. Arikan, NOAA-AVHRR Uydu Girintileri ile Bölgesel Buharlaşma-Terlemenin Belirlenmesi, (1999) 187–198.

[17] M.R. Elowitz, What is Imaging Spectroscopy (Hyperspectral Imaging), (2018). http://www.markelowitz.com/Hyperspectral.html (accessed May 28, 2019).

[18] H. Yıldız, A. Mermer, E. Ünal, F. Akbaş, Türkiye Bitki Örtüsünün NDVI Verileri ile Zamansal ve Mekansal Analizi, Tarla Bitk. Merk. Araştırma Enstitüsü Derg. 21 (2012) 50–56. doi:10.21566/tbmaed.43176.

[19] M.A. ÇELIK, Investigation the Effect of the Drought Year of 2014 on the Vegetation in the Seyhan Basin, J. Int. Soc. Res. 10 (2017) 424–432. doi:10.17719/jisr.20175434606.

[20] A.P.. Cracknel, Advanced very high resolution radiometer, CRC Press, 1997.

[21] C.J. Tucker, J.E. Pinzon, M.E. Brown, D.A. Slayback, E.W. Pak, R. Mahoney, E.F. Vermote, N. El Saleous, An extended AVHRR 8-km NDVI dataset compatible with MODIS and SPOT vegetation NDVI data, Int. J. Remote Sens. 26 (2005) 4485–4498. doi:10.1080/01431160500168686.

[22] J.E. Pinzón, M.E. Brown, C.J. Tucker, EMD Correction of Orbital Drift Artifacts in Satellite Data Stream, in: Hilbert?Huang Transform Its Appl., WORLD SCIENTIFIC, 2013: pp. 241–260. doi:10.1142/9789814508247_0011.

[23] H. Yin, T. Udelhoven, R. Fensholt, D. Pflugmacher, P. Hostert, How normalized difference vegetation index (NDVI) trends from advanced very high resolution radiometer (AVHRR) and système probatoire d'observation de la terre vegetation (SPOT VGT) time series differ in agricultural areas: An inner mongolian case study, Remote Sens. 4 (2012) 3364–3389. doi:10.5829/idosi.mejsr.2012.12.3.64113.

[24] E. Lee, Analysis of MODIS 250 m NDVI Using Different Time-Series Data for Crop Type Separability, 2014.

[25] J.R. Nagol, E.F. Vermote, S.D. Prince, Quantification of impact of orbital drift on inter-annual trends in AVHRR NDVI data, Remote Sens. 6 (2014) 6680–6687. doi:10.3390/rs6076680.

[26] J.E. Pinzon, C.J. Tucker, A non-stationary 1981-2012 AVHRR NDVI3g time series, Remote Sens. 6 (2014) 6929–6960. doi:10.3390/rs6086929.

[27] D.K. Hall, G.A. Riggs, N.E. Digirolamo, K.J. Bayr, MODIS Snow-Cover Products, Remote Sens. Environ. 83 (2002) 181–194. doi:10.1016/S0034-4257(02)00095-0.

[28] J.W. Pomeroy, D.M. Gray, T. Brown, N.R. Hedstrom, W.L. Quinton, R.J. Granger, S.K. Carey, The cold regions hydrological model: a platform for basing process representation and model structure on physical evidence, Hydrol. Process. 21 (2007) 1534–1547. doi:10.1002/hyp.6787.

[29] T. Lillesand, R.W. Kiefer, J. Chipman, Remote Sensing and Image Interpretation, 7th ed., Wiley, 2015.

[30] NASA, NDVI Nasa Data, (n.d.). https://gimms.gsfc.nasa.gov/MODIS/std/GMOD09Q1/tif/NDVI/ (accessed April 25, 2019).

[31] M.A. Celik, M. Karabulut, Ahir Dağı (Kahramanmaraş) ve Çevresinde Bitki Örtüsü ile Yağış Koşullari Arasindaki İlişkilerin MODIS Verileri Kullanilarak İncelenmesi, Havacılık VE Uzay Teknol. Derg. 6 (2013) 123–133.

[32] S. Aksoy, O. Gorucu, E. Sertel, Drought monitoring using MODIS derived indices and google earth engine platform, 2019 8th Int. Conf. Agro-Geoinformatics, Agro-Geoinformatics 2019. (2019) 1–6. doi:10.1109/Agro-Geoinformatics.2019.8820209.

[33] H.E. Beck, T.R. McVicar, A.I.J.M. van Dijk, J. Schellekens, R.A.M. de Jeu, L.A. Bruijnzeel, Global evaluation of four AVHRR-NDVI data sets: Intercomparison and assessment against Landsat imagery, Remote Sens. Environ. 115 (2011) 2547–2563. doi:10.1016/j.rse.2011.05.012.

[34] R.K. Nayak, N. Mishra, V.K. Dadhwal, N.R. Patel, M. Salim, K.H. Rao, C.B.S. Dutt, Assessing the consistency between AVHRR and MODIS NDVI datasets for estimating terrestrial net primary productivity over India, J. Earth Syst. Sci. 125 (2016) 1189–1204. doi:10.1007/s12040-016-0723-9.

[35] F.N. Kogan, Application of vegetation index and brightness temperature for drought detection, Adv. Sp. Res. 15 (1995) 91–100. doi:10.1016/0273-1177(95)00079-T.

[36] S.M. Quiring, S. Ganesh, Evaluating the utility of the Vegetation Condition Index (VCI) for monitoring meteorological drought in Texas, Agric. For. Meteorol. 150 (2010) 330–339. doi:10.1016/j.agrformet.2009.11.015.

[37] W.T. Liu, F.N. Kogan, Monitoring regional drought using the Vegetation Condition Index, Int. J. Remote Sens. 17 (1996) 2761–2782. doi:10.1080/01431169608949106.

[38] S.K. Jain, R. Keshri, A. Goswami, A. Sarkar, Application of meteorological and vegetation indices for evaluation of drought impact: A case study for Rajasthan, India, Nat. Hazards. 54 (2010) 643–656. doi:10.1007/s11069-009-9493-x.

[39] O. Orhan, S. Ekercin, Konya Kapalı Havzasında Uzaktan Algılama ve CBS Teknolojileri, in: TUFUAB VIII. Tek. Sempozyumu, Konya, 2015: pp. 202–208.

[40] M.A. Çelik, M. Karabulut, Farklı Bitki İndeks Modelleri (Evi, Ndvi, Vci) Kullanılarak Resulosman Dağı Kilis Bitki Örtüsünü İncelenmesi, in: Coğrafyacılar Derneği Uluslararası Kongresi, Coğrafyacılar Derneği, Muğla, 2014: pp. 372–379.

[41] R. Fensholt, I. Sandholt, Evaluation of MODIS and NOAA AVHRR vegetation indices with in situ measurements in a semi-arid environment, Int. J. Remote Sens. 26 (2005) 2561–2594. doi:10.1080/01431160500033724.

Teknik Dergi, 2021 11013-11027, Paper 622

Flow Rate along the Length of the Swirling Vortex Axis at an Intake

Kerem TAŞTAN[1]
Nevzat YILDIRIM[2]

ABSTRACT

In this study, the characteristics of the flow in the region of swirling vortex are examined. The potential flow model based on the summing infinite number of spherical sinks along the vortex core is introduced to predict the flow field and the flow rate along the vortex axis. The flow towards the swirling vortex core has considerable effects on the radial velocity distribution within the ambient fluid flow region near the intake. The agreement between available test data relating to the radial velocity and the method introduced in this study is found to be satisfactory.

Keywords: Intake, submergence, swirling flow, vortex.

1. INTRODUCTION

Hydraulic problems attributed to the swirling vortex flow occurring at intakes are frequently encountered in practice (such as discharge reduction, loss of efficiency in pumps and turbines, vibration, air-entrainment, erosion in water-conveying structures etc). The previous studies on this issue may briefly be summarized in three categories that are as follows. i) Studies considering the critical submergence: Fully developed air-entraining vortices occur at intakes that have no sufficient submergence, S (the vertical distance of the intake center to the fluid surface). There are several studies about the critical submergence [$S = S_c$ at which the lower end (tip) of the air-core vortex just reaches the intake] include those by Denny [1], Anwar et al. [2], Hecker [3], Taştan and Yıldırım [4], Kocabaş and Yıldırım [5], Yang et al. [6], Yıldırım et al. [7], Sun and Liu [8]. ii) Studies relating to the modelling of main characteristics of air-core vortices are: Odgaard [9]; Suerich-Gulick et al. [10]; and Vatistas et al. [11]. iii) Studies relating to profile of the air-core vortex: Typical example works on this issue are by Anwar [12]; Vatistas et al. [13]; and Sun and Liu [8].

Note:
- This paper has been received on July 18, 2019 and accepted for publication by the Editorial Board on January 7, 2020.
- Discussions on this paper will be accepted by September 30, 2021.
- https://doi.org/10.18400/tekderg.593595

1 Gazi University, Department of Civil Engineering, Ankara, Turkey
ktastan@gazi.edu.tr - https://orcid.org/0000-0003-1747-2496

2 Çankaya University, Department of Civil Engineering, Ankara, Turkey
nevzaty@cankaya.edu.tr - https://orcid.org/0000-0002-0985-8084

So far, in the available literature mentioned earlier, the following two classical points are considered for the potential flow region of the vortex. **i)** The circulatory velocity vectors are tangential to completely closed co-centric circular streamlines in a horizontal plane and varying in magnitude inversely with the radial distance from the vertical axis of the vortex (the center of the circular streamlines). The pressure distribution is hydrostatic. The entire ambient circulatory flow is in the form of an infinite number of concurrently rotating co-axial vertical cylindrical sink surfaces extending from the free surface to the bottom boundary and having the same vertical axis as the air-entraining vortex. **ii)** The path of each particle is a completely closed circular streamline with no swirling, and the entire profile of the air-core vortex is of a single closed-ended "hyperbolic paraboloid of revolution of circular cross-section" with constant flux of magnitude of vorticity (the net circulation is identical at all levels along the entire length of the air-core vortex).

The flow visualization in the study by Kocabaş and Yıldırım [5] indicated that the path lines of the particles are in the form of descending and converging unclosed lines that appear as a swirling-vortex filament. This indicates that in reality, the streamlines are not completely closed circular lines in the horizontal plane and they also have curvatures in the vertical plane. Therefore, the pressure distribution is not exactly hydrostatic. The circulatory ambient fluid is not in the form of rotating co-centric cylindrical sink surfaces and the circulation along the pathway axis of the vortex is not an identical constant. The circulation along the axis of the vortex increases from its minimum magnitude at the free surface to its maximum magnitude at the intake.

The air-core vortex has to be attributed to the submerged swirling vortex flow developed under the surface extending from the free-surface (air-boundary) to the intake. The exact nature of the swirling vortex flow developing under the water surface is still unknown. Especially the discharge towards any point along the axis of the swirling vortex flow-filament is needed to be known in order to predict the variation of the magnitude of the vorticity or circulation (along the axis of the swirling vortex) that is the main reason for the occurrence of the swirling vortex or air-core vortex. The available studies have not given any information or explanations relating to the flow rate along the axis of swirling vortex or air-core vortex. Taştan and Yıldırım [14] have found that the vortex core consists of hydraulically developed coaxial subsurface depressions (SSDs) towards which the flows are of coaxial spherical sink surface sectors (SSSSs) with centers changing along the axis of the vortex core towards the intake. They have presented an analytical analysis for the profile of the air-core vortex and SSSSs, and verified it by using available test data relating to the air-core vortex. However, they have not considered the flow rate along the axis of the vortex core. Note that, if an SSSS is in the form of a hemisphere then the SSSS is denoted by HSSS (hemispherical sink surfaces) in the present study.

This paper continues the work presented in the study by Taştan and Yıldırım [14]. The main difference is that the present study introduces a potential flow model based on the summing infinite number of SSSSs along the swirling vortex core (not necessarily the air-core vortex) to predict the flow field and the flow rate along the axis of the swirling vortex occurring at an intake. The flow towards the SSDs relating to the swirling vortex-filament has considerable effects on the radial velocity distribution within the ambient fluid flow region near the intake. The agreement between available test data and the method introduced in this study is found to be satisfactory.

2. THEORETICAL CONSIDERATION

Whenever there exists an intake in an ambient fluid with net circulation; an unavoidable swirling vortex flow filament develops within the ambient fluid at the intake (Fig. 1a).

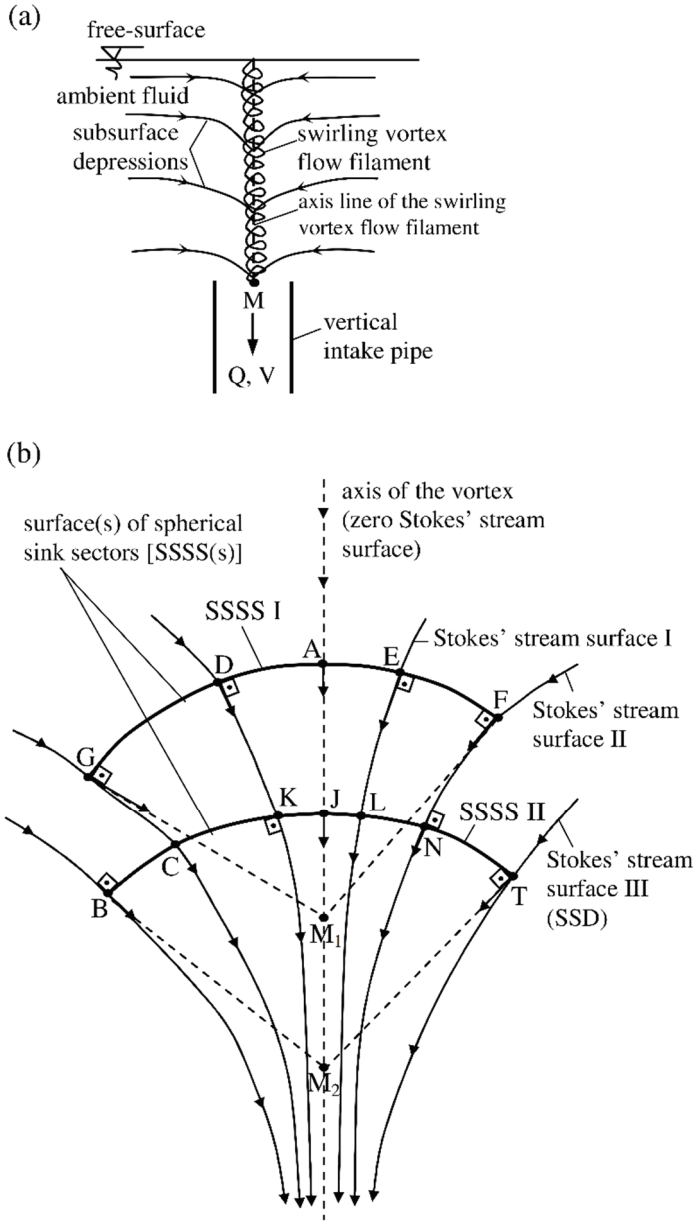

Figure 1- (a) SSDs and the swirling vortex filament, (b) SSSS(s), and Stokes' stream surfaces or SSD(s) [14]

The swirling motion of the fluid particles or swirling characteristic of the vortex-path line is due to the circulation attributed to that may be either self-developed due to the Coriolis effect or disturbances and rotations present within the ambient fluid flow towards the intake or induced, imposed, or loaded circulation on the ambient fluid flow field. Circulation is the essential and main reason for the development of a swirling vortex flow or air-core vortex in an ambient fluid with an intake. If there is no net circulation, a swirling vortex flow cannot develop. In the study by Taştan and Yıldırım [14] relating to the air-core vortex at an intake, it is proven that regardless of the flow and geometrical conditions the fluid flow towards the swirling vortex consists of hydraulically developed coaxial SSSSs of varying centers along the axis of hydraulically developed coaxial SSDs of point (spherical) sink character for the ambient fluid (Fig. 1b). The SSDs are a kind of depression intakes (DIs) whose boundaries are of Stokes' stream surfaces. In reality, all SSDs or DIs are open-ended through which the ambient fluid flow filling in the SSDs reaches and enters the intake.

In the study by Taştan and Yıldırım [14] it is stated that :

"The geometrical location of whole fluid particles that have an identical magnitude of radial velocity towards any chosen center point on the axis of the vortex depression (vortex path line) is an SSSS. Note that these particles belong to an infinite number of coaxial Stokes' stream surfaces (Figs. 1b and 2). For example, in Fig. 1b, the particles G, D, A, E, and F of different Stokes' stream surfaces [DI(s)] are on the same SSSS I and have identical radial velocity towards the center M_1 of the SSSS I. Similarly, the particles B, C, K, J, L, N, and T of different Stokes' stream surfaces [DI(s)] are on the same SSSS II and have identical radial velocity towards the center M_2 of the SSSS II."

The potential flow model is based on the summation of infinite number of SSSSs along the length of the vortex axis. The potential lines representing radial velocity are perpendicular to the stream surfaces of SSSSs. For this purpose, firstly it is necessary to prove that for each SSD there exist HSSSs or SSSSs in general. This is achieved in the following way.

Considering an air-core vortex depression and the coordinate system as indicated in Fig. 2 (basing on the formula developed by Vatistas et al. [13]; Sun and Liu, [8]) for the profile of an air-core vortex, Taştan and Yıldırım [14] have written as

$$\frac{H_r - H_0}{h} = \frac{2}{\pi}\arctan(\beta R^2) \tag{1}$$

where $R = r/r_m$ = dimensionless horizontal radial distance from the vertical centerline of the depression (vortex) or intake entrance; r = horizontal radial distance from the vertical centerline of the air-core vortex depression (or intake entrance); r_m = air-core vortex depression core radius (outer limit radius of the viscous region); H_r = water surface elevation at R; H_0 = elevation of the lower end or tip of the depression (air-core vortex); h = total depth of the depression (air-core vortex); and β = a coefficient relating to the flow conditions. In reality, the lower end (tip) of the air-core vortex depression should have a tiny opening but the surface tension (capillary) forces overcome the small inertia and gravity forces at the lower end of the air-core vortex. Therefore the lower end (tip) of the air-core vortex depression is seen as closed and slightly curved [14].

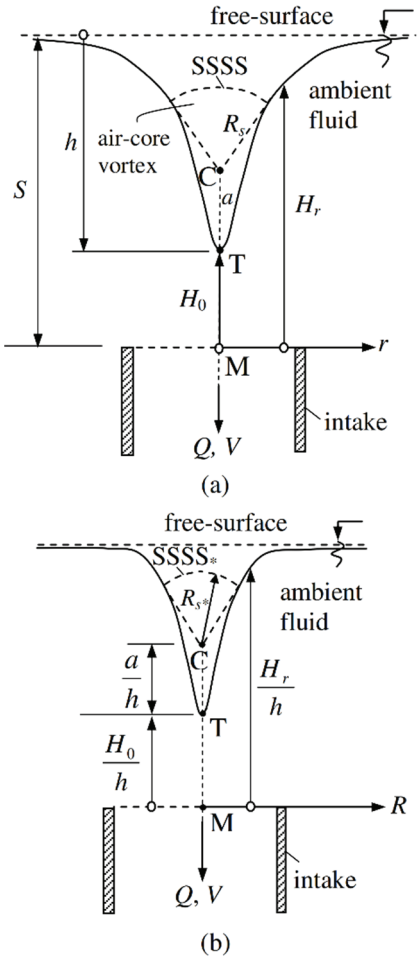

Figure 2 - Geometric variable definitions [14]

Consider an SSSS whose center C on the axis of symmetry of the intake entrance or air-core vortex is above the lower end (tip) of the air-core vortex for an amount of a or a/h, as shown in Fig. 2a and b. The SSSS can be described by the equation of a circle in which the horizontal dimension is R and the vertical dimension is the radius of the circle expressed in terms of the geometry of the air-core vortex. For the circular arch, one can write [14],

$$R^2 + \left(\frac{H_r - H_0}{h} - \frac{a}{h} \right)^2 = R_{s*}^2 \tag{2}$$

where R_{s*} is the dimensionless radius of a different kind of SSSS that is indicated as SSSS$_*$ (in the dimensionless coordinate system of H_r/h and R) in Fig. 2b.

Taştan and Yıldırım [14] have shown that SSSS$_*$ and air-core vortex depression profile normally intersect (for example at intersection point A in Fig. 1) for which one can write

$$R^2 = \left[\frac{1}{\pi\left(\frac{H_r - H_0}{h} - \frac{a}{h}\right)} + \sqrt{\frac{1}{\pi^2\left(\frac{H_r - H_0}{h} - \frac{a}{h}\right)^2} - 0.25} \right] \frac{2}{\beta} \tag{3}$$

Substituting Eq. (3) in Eq. (1) (for the intersection point of SSSS and air-core vortex profile) it yields

$$\left(\frac{H_r - H_0}{h}\right) = \frac{2}{\pi}\arctan\left\{ 2\left[\frac{1}{\pi\left(\frac{H_r - H_0}{h} - \frac{a}{h}\right)} + \sqrt{\frac{1}{\pi^2\left(\frac{H_r - H_0}{h} - \frac{a}{h}\right)^2} - 0.25} \right] \right\} \tag{4}$$

Note that Eq. (4) is independent of β.

To prove that there exist HSSSs or SSSSs for each SSD; consider any ith SSD (call it SSD$_i$) as indicated in Fig. 3. For simplicity let the origin of the coordinate system (r, H_{ri}) or (R_i, H_{ri}/h_i) is located at the lower end (tip) point T$_i$ of the SSD$_i$ (Fig. 3). Herein, $R_i = r/r_{mi}$; r_{mi} = core radius (outer limit radius of the viscous region) of the SSD$_i$; H_{ri} = elevation of the SSD$_i$ profile with respect to the lower end (tip) of the SSD$_i$ at R_i ; h_i = the vertical distance of the top level of the SSD$_i$ at sufficiently large horizontal radial distance from the vertical central axis line of the SSD$_i$ or the intake centre. In reality an air-core vortex depression is also an SSD for which the depth of ambient fluid above it is not sufficient to fill out the SSD alone (SSD is filled out by both the ambient fluid and air as explained in the study by Taştan and Yıldırım [14]. Therefore; Eq. (1) can be adopted for any ith SSD (call it SSD$_i$) provided that H_{ri} , h_i, β_i, and R_i are used in lieu of their corresponding ($H_r - H_0$) , h, β, and R respectively as indicated in Fig. 3. For the profile of SSD$_i$ Eqs. (1) and (2) may be rewritten as;

$$\frac{H_{ri}}{h_i} = \frac{2}{\pi}\arctan\left(\beta_i R_i^2\right) \tag{5}$$

$$R_i^2 + \left(\frac{H_{ri}}{h_i} - \frac{a_i}{h_i}\right)^2 = {R_{si*}}^2 \tag{6}$$

Herein, R_{si*} = dimensionless radius of a different kind of SSSS$_i$ that is indicated as SSSS$_{i*}$ (in the dimensionless coordinate system of H_{ri}/h_i and R_i); and a_i = vertical distance of the center point of the SSSS$_i$ to the lower end (tip) of the SSD$_i$ (Fig. 3b). Note that H_{ri} ; h_i ; β_i ; R_i ; and R_{si*} may change for all SSDs. Considering Eqs. (3) and (4); for the normal-intersection of the profiles of the SSD$_i$ and the SSSS$_i$ one may write

$$R_i^2 = \left[\frac{1}{\pi\left(\frac{H_{ri}}{h_i} - \frac{a_i}{h_i}\right)} + \sqrt{\frac{1}{\pi^2\left(\frac{H_{ri}}{h_i} - \frac{a_i}{h_i}\right)^2} - 0.25} \right] \frac{2}{\beta_i} \tag{7}$$

$$\frac{H_{ri}}{h_i} = \frac{2}{\pi} \arctan\left\{ 2 \left[\frac{1}{\pi\left(\frac{H_{ri}}{h_i} - \frac{a_i}{h_i}\right)} + \sqrt{\frac{1}{\pi^2\left(\frac{H_{ri}}{h_i} - \frac{a_i}{h_i}\right)^2} - 0.25} \right] \right\} \tag{8}$$

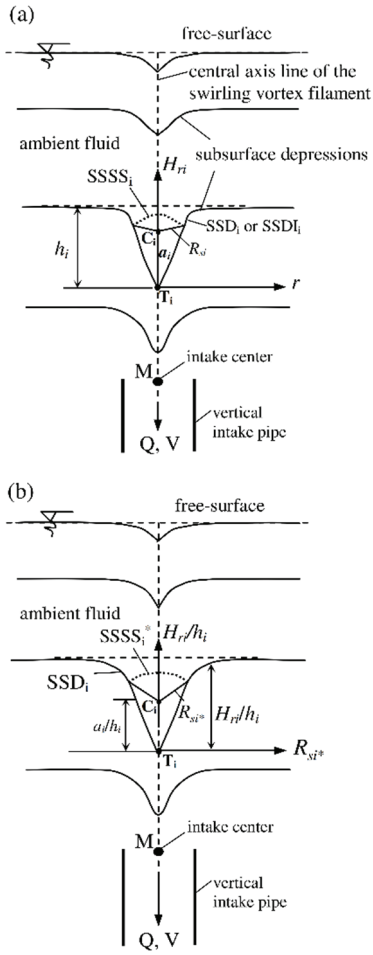

Figure 3 - SSD(s) and relating geometric parameters

Eq. (8) can be solved for H_{ri}/h_i by a trial and error procedure for a chosen magnitude of a_i/h_i indicating that for every point on the axis of the vortex there corresponds an SSSS. It can be shown that Eq. (8) has only one real root within the domain of solution by constructing a graph of assumed values of H_{ri}/h_i with respect to computed values of H_{ri}/h_i for all possible a_i's.

For simplicity it may be advised to study the case of $a_i = 0$ first. For $a_i = 0$ the $SSSS_i$ has the same center as the lower end (tip) for which Eqs. (5)-(8) give

$$H_{ri}/h_i = 0.6033; \text{ or } H_{ri} = 0.6033h_i; \text{ and } R_i = 0.8343; \text{ or } r = 0.8343r_{mi} \tag{9}$$

Now, one can go to Fig. 4a (with $a_i = 0$; $H_{ri} = 0.6033h_i$; and $r = 0.8343r_{mi}$ that correspond the point B in Fig. 4a) and write the equation for a circle (whose revolution gives an SSS_i) of radius of R_{si} as follows:

$$r^2 + H_{ri}^2 = R_{si}^2 \tag{10a}$$

$$\left(0.8343r_{mi}\right)^2 + \left(0.6033h_i\right)^2 = R_{si}^2 = \text{constant} \tag{10b}$$

$$h_i^2 = \text{constant} - 1.912r_{mi}^2 \tag{10c}$$

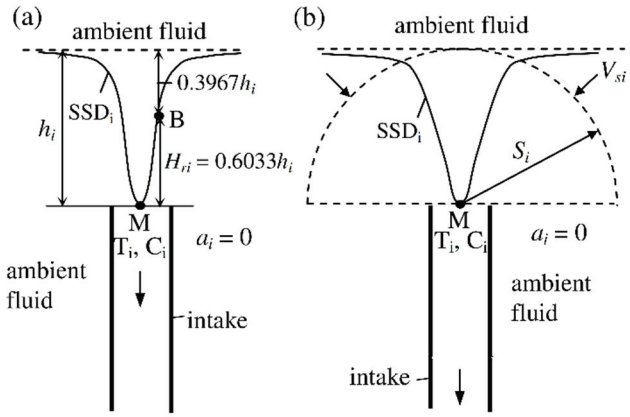

Figure 4 - SSD_i for the case of $a_i = 0$

Considering the air-core vortex depression, the test results of Sun and Liu [8] indicate that r_m is a constant for the vertical distance from the top level of SSD_i less than or equal to $0.7S_c$ (or $H_r/S_c = 1 - 0.7 = 0.3$).

Noting that the air-core vortex depression is also one of the SSDs; for an SSD_i Eq. (9) indicates that for $a_i = 0$, the vertical distance of the point B (Fig. 4a) from the top level of SSD_i is $(h_i - H_{ri})_{\text{at B}}$ or, $(h_i - 0.6033h_i) = 0.3967h_i < 0.7h_i$, this infers that r_{mi} in Eq. (10c) can also be taken as a constant. Thus, Eq. (10c) can be rewritten as

h_i^2 = a constant (11)

One can multiply both sides of Eq. (11) by 2π and get

$2\pi h_i^2$ = constant (12)

Equation (12) indicates that regardless of flow and geometrical conditions (including the profile of the intake-entrance) there exists an $HSSS_i$ of radius of h_i (on upstream side of the tip point T_i) that has the same centre as the point T_i, and with the base normal to the central axis of the swirling vortex filament at point T_i as indicated in Fig. 4.

Considering Eq. (12), the discharge, q_i, towards the centre T_i of the $HSSS_i$ can be written as

$$q_i = \left(2\pi h_i^2\right) V_{si} \tag{13}$$

where V_{si} = radial velocity at the $HSSS_i$ whose magnitude depends on the flow and geometrical conditions. V_{si} may be measured.

Equation (13) infers that the discharge towards any point under consideration on the centerline of the swirling vortex filament is equal to that through the $HSSS_i$ (on upstream side of the point T_i) that has the same center as T_i, and the base normal to the central axis of the swirling vortex filament at T_i (Fig. 4). This discharge is valid for the flow on the upstream side of the point T_i. Note that the above conclusion is reached for $a_i = 0$. If similar analysis is done for a given $a_i \neq 0$ the same conclusion is to be obtained. Existence of HSSSs within the flow field along the path of the swirling vortex does not depend on the value of a_i.

Physically the lower ends (tips) of whole SSDs at upstream of a point on the axis of the swirling vortex flow-filament must one after another reach (and pass from) that point. Because these SSDs have their own respective HSSSs, one can draw infinite number of concentric HSSSs with different radii at that point as indicated in Fig. 5. This means that at every point along the axis of the swirling vortex flow infinite number of concentric HSSSs having identical discharge can be drawn. Not to make the figure crowded HSSSs at only a few points are presented in Fig. 5.

As for the practice, Eq. (13) indicates that if V_{si} at a given radial distance of h_i to the point under consideration on the axis of the swirling vortex filament is measured, then the discharge (q_i) towards that point (center of the HSSS) can be calculated. To measure the radial velocities, a point on the path of the swirling vortex should be chosen. Then a velocity meter (i.e., a pitot tube) should be radially aligned at the point that has required radial distance (radius of SSS) to the point under consideration.

By means of this method one can know the magnitude of the discharge participating in the vortex filament (vorticity feeding-discharge) at any level along the axis of the swirling vortex flow-filament.

Figure 5 indicates that HSSSs radially shrink towards their center. As HSSSs radially shrink they must simultaneously rotate [due to the forces caused by non-uniformities in the ambient flow media, the Coriolis force, and imposed or induced circulation] about their axis (axis of

the SSDs). This may be the reason why the swirling vortex flow is observed to be a swirling filament (Fig. 1a).

Physically it is seen that HSSSs having centers on the central axis line of the swirling vortex filament at upstream of the intake center M (Fig. 5) have open bases through which the fluid flows or escapes (evacuation of the fluid within the HSSSs occurs). The base of the HSSS or SSSS having the same center and discharge as the intake has the opening of the intake entrance. Similar to the swirling vortex filament above the intake as indicated in Figs. 1-4, in reality another swirling vortex filament also exists below the intake that is not visible (not indicated in Figs. 1-4) since it is blocked by the vertically downward flowing intake pipe. Therefore, similar to the HSSSs above the intake level, one can also draw HSSSs below the intake level as indicated Fig. 5c. Note that spatial growth of the swirling vortex from free-surface to the intake is not considered in this study.

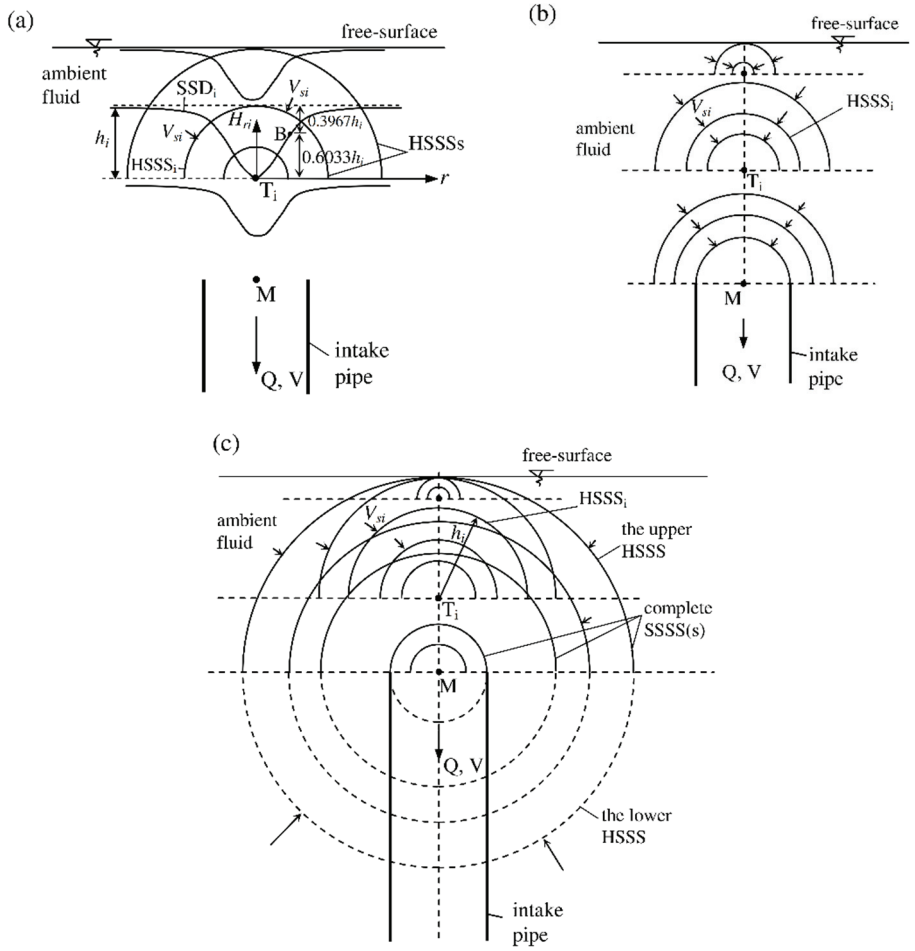

Figure 5 - HSSSs at different levels along the swirling vortex flow filament in case of a vertically flowing downward intake

In the above analysis a vertically downward perfect straight vortex flow-filament on which there exist no boundary blockages is considered [profiles of the SSDs are perfectly symmetric about their vertical axis due to which HSSSs are perfect and complete, there cannot be velocity vectors below the horizontal plane (on which T_i takes place) pointing T_i].

In practice the position, orientation and configuration of the intake-entrance, flow and geometrical conditions may be different, and there may exist boundary blockages on the profile of the SSDs due to which HSSSs may not be complete or HSSSs may be in any forms of SSSSs [because, there can be velocity vectors below the horizontal plane (on which T_i takes place) pointing T_i] as indicated for an inclined intake in Fig. 6.

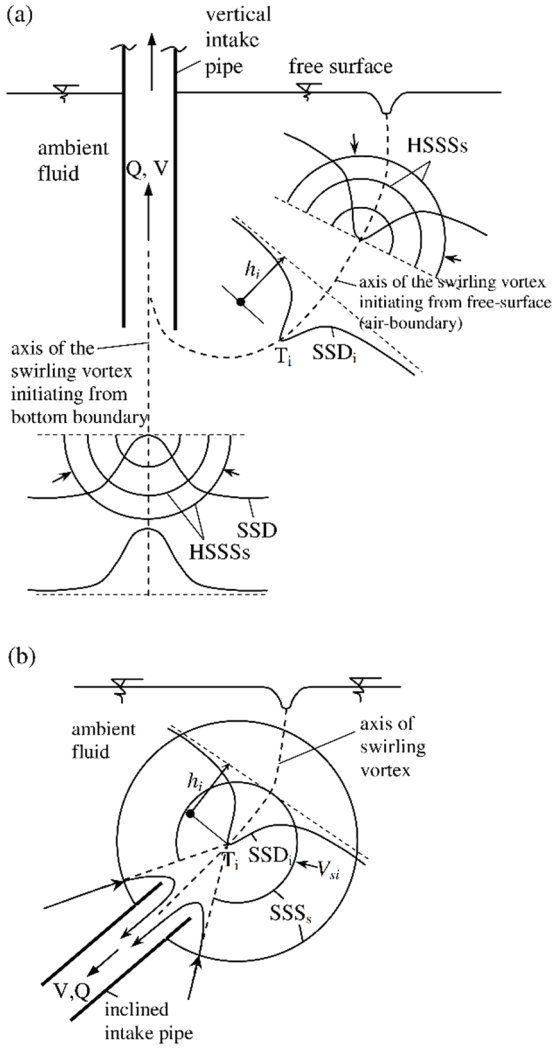

Figure 6 - HSSSs and SSDs along the swirling vortex flow filament in case of inclined intake(s)

Basing on this fact, for general purposes it may be appropriate to rewrite Eqs. (12), and (13) as in Eqs. (14) and (15), respectively.

$$A_{si} = k\pi h_i^2 = \text{constant} \tag{14}$$

$$q_i = A_{si} V_{si} \tag{15}$$

where A_{si} = the effective surface area of the ith SSSS (or SSSS$_i$); and k = coefficient for the ith SSSS (or SSSS$_i$) under consideration.

3. VERIFICATION OF EXISTENCE OF HSSSs OR SSSSs

The test data in the study by Suerich-Gulick et al. [15] relating to the constant velocity contours (isovels) on upstream side of a pipe intake issuing from a dead-end wall is replicated in Fig. 7.

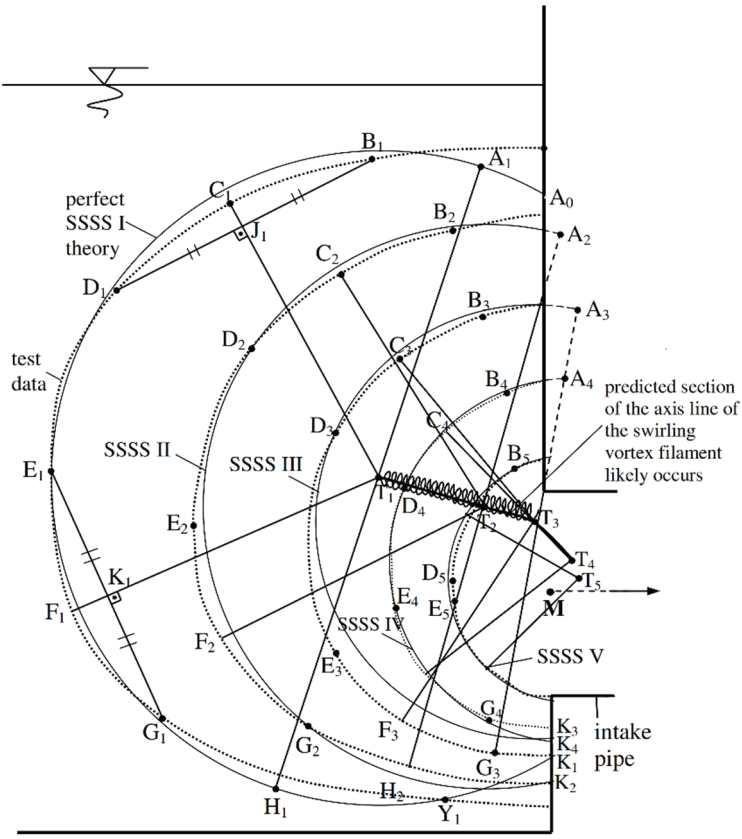

Figure 7 - Comparison of the theory and the available data in the study by Suerich-Gulick et al. [15]

The clearances of the center of the intake to the dead-end wall and the bottom boundary are zero, and relatively small, respectively. In addition, there are two symmetric flow-disturbing vertical piers (with small clearance to the intake entrance) mounted on each side of the intake-entrance. Therefore, the velocity distribution in the ambient fluid region close to the intake should be under large boundary-effects that are clearly observable in the measured velocity contours in Fig. 7. It is a typical challenging case to test the method introduced in the present study. In Fig. 7 there are five isovels (HSSSs or SSSSs) that are denoted by SSSS I, II, III, IV, and V. By choosing arbitrarily chords (applied to the test data) and their locations the centers of SSSSs are geometrically located. For example, two arbitrarily chosen chords of $D_1J_1B_1$ and $E_1K_1G_1$ are used and thereby the center T_1 for SSSS I is found as indicated in Fig. 7. By following the same geometrical procedure the centers T_2, T_3, T_4, and T_5 for SSSSs II, III, IV, and V, respectively are found. Not to make the figure crowded the chords for SSSSs II, III, IV, and V are not indicated in Fig. 7.

The line connecting the centers T_1, T_2, T_3, T_4, and T_5 (Fig. 7) is the approximate profile of the axis line of the swirling vortex flow-filament that is very similar to the one observed by several researchers (i.e., Quick [16], Figs. 2-7; Anwar et al. [2], Figs. 2-3). In practice the centers of HSSSs or SSSSs on downstream side of the intake-entrance center M are observed to be on the straight extension of the swirling vortex filament-line parallel to the axis of the intake pipe. But, Fig. 7 indicates that the predicted centers T_4 and T_5 are on downstream side of the intake center M, and they are not exactly on the straight extension of the swirling vortex filament-line parallel to the inside-axis of the intake pipe. The reasons for this are as follows.

(1) The method may not give good results for the sections of SSDs whose centers remain within the intake since the approximations and assumptions under which the equations derived earlier (basing on those by Vatistas et al. [13]; Sun and Liu [8]) may not be acceptable in the fluid flow section within the intake pipe.

(2) The centers of the SSSs in Fig. 7 are found by applying geometry to the test data relating to the radial velocity on which boundary effects are obviously present and more pronounced in the flow region close to the boundaries (Fig. 7). Radial iso-velocity contours deviate from being perfect spheres for the flow regions close to the solid boundaries (especially very confined intakes, i.e., intakes completely surrounded by very close solid boundaries).

(3) Arbitrarily chosen chords (applied to the test data-set) and their locations to predict the centers of SSSSs.

Figure 7 indicates that the agreement between method introduced in present study and the test data is satisfactory. The difference between the test data and the method is more pronounced in the flow regions close to the flow boundaries that is attributable to the effects of the boundaries as expected. In addition to visual comparison, to quantify the error between suggested method and the theory, the values of SSSS I, which has the maximum deviation with respect to the experimental data among the other SSSSs in Fig. 7, are used. The mean error is found as 4.2%. Maximum error, which is obtained at close to the solid boundaries is about 12%. Similar analysis can be done for other SSSSs in Fig. 7.

Figures 5-7 indicate that if an SSSS or HSSS cuts whole flow boundaries and thereby the SSSS along with boundaries completely encloses entire intake-entrance, q_i through the net

effective surface of the SSSS is the same as the intake discharge Q ($q_i = Q$). Otherwise, $q_i < Q$.

4. CONCLUSIONS

From this study, the following conclusions may be drawn.

- The discharge towards any point on the axis of the swirling vortex flow-filament from the free-surface to the intake can be calculated if the radial velocity at a given radius is measured.
- The flow towards the SSDs relating to the swirling vortex-filament has considerable effects on the radial velocity distribution within the ambient fluid flow region near the intake-entrance.
- The swirling vortex flow-filament consists of infinite number of coaxial SSSSs at every point along the axis of the swirling vortex flow-filament. Swirling vortex flow-filament is the result of the concurrently shrinking of the SSSSs along the axis of the swirling vortex.

Symbols

A_{si} : the net (effective) surface area of the i^{th} SSSS [m^2]

a : distance between the tip of the air-core vortex and center of the SSSS [m]

H_r : water surface elevation at R [m]

H_0 : elevation of the lower end or tip of the air-core vortex [m]

h : total depth of the air core [m]

k : coefficient for the i^{th} SSSS (or $SSSS_i$) under consideration

q_i : discharge towards the centre point T [m^3/s]

Q : intake discharge [m^3/s]

R : dimensionless radius

R_{s*} : dimensionless radius of the $SSSS_*$

r : horizontal radial distance from the vertical centerline of the vortex or intake entrance [m]

r_m : vortex core radius (outer limit radius of the viscous region) [m]

S : submergence [m]

S_c : critical submergence [m]

V : average intake-entrance velocity [m/s]

V_{si} : radial (normal) velocity at the $SSSS_i$ [m/s]

β : a coefficient

β_i : magnitude of β for SSD_i

References

[1] Denny, D.F., An experimental study of air-entraining vortices in pump sumps. Proceedings of Institution of Mechanical Engineering, 170(2), 106–116, 1956.

[2] Anwar, H.O., Weller, J.A., Amphlett, M.B., Similarity of free vortex at horizontal intake. J. Hydraul. Res. 16(2), 95–106, 1978.

[3] Hecker, G.E., Fundamentals of vortex intake flow. In: Knauss, J (ed) Swirling Flow Problems at Intakes, pp. 13-38. A.A. Balkema, Rotterdam, 1987.

[4] Taştan, K., Yıldırım, N., Effects of Froude, Reynolds and Weber numbers on an air-entraining vortex. J. Hydraul. Res. 52(3), 421-425, 2014.

[5] Kocabaş, F., Yıldırım, N., Effect of circulation on critical submergence of an intake pipe. J. Hydraul. Res. 40(6), 741-752, 2002.

[6] Yang, J., Liu, T., Bottacin-Busolin, A, Lin C., Effects of intake-entrance profiles on free-surface vortices. J. Hydraul. Res. 52(4), 523-531, 2014.

[7] Yıldırım, N., Eroğlu, N., Taştan, K., Occurrences of vortices at an intake of point sink character. Teknik Dergi, 23(1), 5799-5812, 2012.

[8] Sun, H., Liu, Y., Theoretical and experimental study on the vortex at hydraulic intakes. J. Hydraul. Res. 53(6), 787-796, 2015.

[9] Odgaard, A.J., Free-surface air-core vortex. J. Hydraul. Eng. 112(7), 610-620, 1986.

[10] Suerich-Gulick, F., Gaskin, S.J., Villeneuve, M., Parkinson, E., Characteristics of free surface vortices at low-head hydropower intakes. J. Hydraul. Eng. 140(3), 291-299, 2014.

[11] Vatistas, G.H., Lin, S., Li, P.M., A similar profile for the tangential velocity in vortex chambers. Exp. Fluids, 6 135-137, 1988.

[12] Anwar, H.O., Flow in a free vortex. Water Power, 4, 153-161, 1965.

[13] Vatistas, G.H., Kozel, V., Mih, W.C., A simpler model for concentrated vortices. Exp. Fluids, 11(1), 73-76, 1991.

[14] Taştan, K., Yıldırım, N., Effects of intake geometry on the occurrence of a free-surface vortex. J. Hydraul. Eng. 144(4), 04018009-1-04018009-11, 2018.

[15] Suerich-Gulick, F., Gaskin, S J., Villeneuve, M., Parkinson, E., Free surface intake vortices: Theoretical model and measurements J. Hydraul. Res. 52(4), 502-512, 2014.

[16] Quick, M.C., Efficiency of air-entraining vortex formation of water intake. Journal of the Hydraulics Division, 96(7), 1403-1415, 1970.

Teknik Dergi, 2021 11029-11050, Paper 623

Wavelet Packet-Genetic Programming: A New Model for Meteorological Drought Hindcasting

Ali DANANDEH MEHR[1]
Mir Jafar Sadegh SAFARI[2]
Vahid NOURANI[3]

ABSTRACT

This study presents developing procedures and verification of a new hybrid model, namely wavelet packet-genetic programming (WPGP) for short-term meteorological drought forecast. To this end, the multi-temporal standardized precipitation evapotranspiration index (SPEI) has been used as the drought quantifying parameter at two meteorological stations at Ankara province, Turkey. The new WPGP model comprises two main steps. In the first step, the wavelet packet, which is a generalization of the well-known wavelet transform, is used to decompose the SPEI series into deterministic and stochastic sub-signals. Then, classic genetic programming (GP) is applied to formulate the deterministic sub-signal considering its effective lags. To characterize the stochastic component, different theoretical probability distribution functions were assessed, and the best one was selected to integrate with the GP-evolved function. The efficiency of the new model was cross-validated with the first order autoregressive (AR1), GP, and random forest (RF) models developed as the benchmarks in the present study. The results showed that the WPGP is a robust model, superior to AR1 and RF, and significantly increases the predictive accuracy of the standalone GP model.

Keywords: Drought, SPEI, wavelet packet, genetic programming, stochastic modelling.

1. INTRODUCTION

Drought is a hydrological extreme condition that can bring serious problems to the human life. It makes significant impacts on water quantity and quality, of land and soil degradation, agricultural productivity, desertification, famine, etc. Drought conditions are usually

Note:
- This paper has been received on August 15, 2019 and accepted for publication by the Editorial Board on January 7, 2020.
- Discussions on this paper will be accepted by September 30, 2021.
- https://doi.org/10.18400/tekderg.605453

1 Antalya Bilim University, Department of Civil Engineering, Antalya, Turkey
ali.danandeh@antalya.edu.tr - https://orcid.org/0000-0003-2769-106X

2 Yaşar University, Department of Civil Engineering, Izmir, Turkey
jafar.safari@yasar.edu.tr - https://orcid.org/0000-0003-0559-5261

3 Center of Excellence in Hydroinformatics and Faculty of Civil Engineering, Uni. of Tabriz, Tabriz, Iran
Near East University, Faculty of Civil and Environmental Engineering, Nicosia, North Cyprus
vnourani@yahoo.com - https://orcid.org/0000-0002-6931-7060

classified under four categories of meteorological, hydrological, agricultural, and socioeconomic droughts. Each of these groups indicates how long a dry period lasts and effects the human life/environment. To monitor/forecast meteorological drought, deviation of meteorological variables such as precipitation, evaporation, and transportation from their long-term mean are investigated using variety of existing drought indices. There are various meteorological drought indices including (but not limited to) the well-known Standardized Precipitation Index (SPI, [1]), Drought Area Index (DAI, [2]), Palmer Drought Severity Index (PDSI, [3]), and the most recently developed Standardized Precipitation Evapotranspiration Index (SPEI; [4]). While SPI and DAI are calculated using historical precipitation data, calculation of PDSI and SPEI is based on both precipitation and temperature data series.

To date, a large number of research articles have been conducted to forecast drought indices using classical regression or data-driven techniques [5-14]. For example, the Artificial Neural Network (ANN) based forecast models of 1 to 12 months lead time were developed taking the advantage of SPI and Effective Drought Index [15]. The suitability of the Adaptive Neuro-Fuzzy Inference System (ANFIS) for SPI-based drought forecasting at different time scales was tested and compared to that of feed-forward neural networks [6]. Nonlinear Aggregated Drought Index-based drought conditions were forecast using the ANN approach [16]. The SPI was forecast at Bojnurd synoptic station using ANN, ANFIS, and Support Vector Regression (SVM) [17]. The results showed that the SVM model is superior to ANFIS and ANN models. A recent study demonstrated that M5-tree and multivariate adaptive regression splines (MARS) models outperform the least square support vector machine (LSSVM) model in the forecasting of the SPI in Australia [13].

With specific attention to hydrology, Labat (2005) noted that the hybridization of data-driven models using wavelets may lead to several improvements in the analysis of global hydrological fluctuations and their natural time-varying relationships [18]. Successful applications of wavelet-based hydrological models have also been reported in [19]. In drought forecasting community, wavelets were applied to decompose/denoise different drought indices or its predictors [9-10, 20-23]. The conjunction of wavelet transform and ANNs was used to forecast PDSI and the results showed that wavelet-based models can significantly increase the accuracy of forecasts [20]. Long-term SPI was forecast using ARIMA, ANN, SVM, W-ANN, and WSVM models [21]. Among the models, the W-ANN was more accurate. A gene-wavelet model was used to forecast Palmer Modified Drought Index (PMDI) in which previous PMDI series and NINO 3.4 index were employed as the inputs [10]. The results demonstrated that the standalone genetic programming (GP) model was unable to learn non-linearity of drought series in 3-month ahead forecasts. However, the gene-wavelet model could effectively forecast 3-, 6-, and 12-month lead times. More recently, wavelet-ARIMA-ANN and wavelet-ANFIS hybrid models were used to forecast SPEI drought index in a tropical climate in Malaysia [24]. The results suggested that wavelet-ARIMA-ANN forecast SPEI-3 and SPEI-6 accurately.

In this study, we tackle the problem of hindcasting drought index through GP coupled with a wavelet-packet. Besides, autoregressive (AR), non-coupled GP, and random forest (RF) methods were used as the benchmarks. We considered two case studies from Ankara, Turkey. For this purpose, we used a 46-year long time series of monthly SPEI at each case with no additional predictors such as large scale oceanic or atmospheric variables. Two time-scales,

SPEI-3 and SPEI-6, were analyzed separately. GP setup, RF modeling, and wavelet packet denoising are fully described in a step by step procedure. Besides, the impact of different decomposition depths (3, 6, and 9) on the improvement of standalone GP was investigated. Although a number of earlier studies have assessed the impact of wavelets in drought forecasting [10], to the best of the authors' knowledge, this is the first study that uses wavelet packet to improve GP-based predictions of drought indices.

2. STUDY AREA AND DATA

2.1. Overview of the SPEI Drought Index

The *SPEI* is rather a new meteorological drought index which combines the variability of precipitation and temperature to derive drought condition. It has been offered to be more consistent for drought studies under climate change projections [25, 26]. The index method first developed by [4] where local temperature and precipitation (*P*) are used to estimate monthly potential evapotranspiration (*PET*) and deficit (*D*), i.e., water balance of the month *i*.

$$D_i = P_i - PET_i \tag{1}$$

Once D_i is estimated, its standardized time series is fitted to a given probability distribution function (e.g., log-logistic function as suggested by 4) and then, the SPEI time series is calculated as the standardized values of cumulative probability of deficit using Equation (2).

$$\begin{aligned} SPEI_i &= W_i - \frac{2.515517 + 0.802853\, W_i + 0.010328\, W_i^2}{1 + 1.432788\, W_i + 0.189269\, W_i^2 + 0.001308\, W_i^3} \\ W_i &= \sqrt{-2\ln p} \qquad for \quad p \le 0.5 \\ W_i &= \sqrt{-2\ln(1-p)} \qquad for \quad p > 0.5 \end{aligned} \tag{2}$$

Where *p* is the probability of exceeding a given deficit. It is important to note that the sign of the calculated SPEI must be reversed for the cases of p>0.5.

Table 1 - Classifications of drought events using SPI and SPEI indices

Classification	SPI threshold	SPEI threshold
Moderate drought	-1.49 <SPI< -1.0	-1.42 <SPEI< -1.0
Severe drought	-2.0 <SPI< -1.5	-1.82 <SPEI< -1.43
Extreme drought (ED)	SPI≤ -2.0	SPEI ≤ -1.83

Returning to the study of [4], there is no drought classification thresholds for the SPEI values. In some studies, the well-documented standardized precipitation index (SPI) thresholds have been used regardless of the difference in cumulative density functions (CDFs) of the SPI and

SPEI indices [e.g., 27]. Considering the inconsistency caused by different CDFs, we used the drought classes suggested by Danandeh Mehr et al. (2019) in which SPEI thresholds were attained for a set of given probability of exceeding the deficit (see Table 1). For more details about the SPEI and its classification procedure, the interested reader is referred to [26].

2.2. Observed Data and Hindcasting Scenarios

Historical precipitation and temperature measurements in the period 1971-2016 from two meteorological stations (Beypazari and Nallihan; see Figure 1) were used in this study to calculate SPEI time series at each station. The stations with a rough distance of 55 km represent the climatology of north-western Ankara, Turkey. To obtain the SPEI time series in 3-month and 6-month time resolutions, the SPEI package available in R library (http://sac.csic.es/spei/tools.html) is used. The package uses Thornthwaite method to calculate PET by default, and we followed this initial setup. For more details about the climatology of the study area, the reader is referred to [26].

Figure 1 - Location of meteorological stations used in this study

Drought forecasting using data-driven methods can be divided into two categories of univariate hindcasting and multivariate forecasting models. In the univariate hindcasting models, the desired SPEI index is modelled using lagged values of the index, i.e., past events. This is a fast methodology, particularly useful in the station-scale studies. In the multivariate forecasting models, one may use exogenous predictors (inputs) or ensemble precipitation and PET forecasts from meteorological authorities like European Centre for Medium-Range Weather Forecasts (ECMWF).

One important step in drought hindcasting is to determine the optimum number of lags (m) which plays a significant role on the accuracy and complexity of forecasts. Despite the fact that the optimal set of lags leads to the reliable forecasts, inadequate or even more than required lags may result in weak or complex solutions, respectively. It might be identified

either via trial and error method [28] or through the autocorrelation function (ACF) analysis of drought index [21]. However, it is a linear method and the values achieved are often too large. To prevent the presence of spurious lags that tend to confuse the training process, the optimum lags can be judged via partial autocorrelation function (PACF).

In this study, SPEI-3 (i.e., precipitation and temperature conditions over 3 months) and SPEI-6 were forecast for both meteorology stations over the lead time of 1 month. The 3-month SPEI (SPEI-3) and 6-month SPEI (SPEI-6) forecasts with a 1-month lead time are desirable for early warning and taking action against meteorological drought. The relevant forecasting scenarios can be mathematically expressed as below:

$$SPEI\text{-}3(t) = f(SPEI\text{-}3_{t\text{-}i}, \ldots, SPEI\text{-}3_{t\text{-}m}, \varepsilon_t) \quad (3)$$

$$SPEI\text{-}6(t) = f(SPEI\text{-}6_{t\text{-}i}, \ldots, SPEI\text{-}6_{t\text{-}m}, \varepsilon_t) \quad (4)$$

where the time index i (=1, …, m), the lag indicating the number of past months (i.e., lags), must be considered in the scenarios.

3. METHODS

3.1. The Benchmark Random Forest and Autoregressive Models

Random forest (RF) is constructed through the combination of several numbers of decision trees (DT). RF is an ensemble machine learning technique that has been widely used for classification and regression analysis [29]. Recently, RF has been applied in verity of water resources problems [30-32]. Poor performance on testing data set, i.e., overfitting is the primary problem in the application of conventional DT. The RF works out the deficiency of DT through its randomness feature [33]. Randomness elements have been introduced in a growing process by the partial selection of variables in the tree structure. Created trees are combined to generate a robust predictor based on a given dataset. The predicted values are the results of averaging the individual outputs. RF differs from the conventional DT in which the bootstrap sample is used instead of using all training data for each tree creation. The decision tree separates the data into portions by using the best splitter variable at a time. While RF changes the split selection procedure by randomly choosing the predictors. The robustness of RF comes from the combination of several trees. As basic futures of RF, there is no need to rescale the data like other data-driven techniques, and it can determine the best predictor, automatically. As it uses several trees at its structure, RF provides more accurate results and prevents overfitting. The regression tree generates a non-linear model via a collection of some linear portions of training data. The RF regression model is generated through a random vector that grows the trees. The results of such tree predictors are numerical values. RF provides numerical outputs and the training set is independently drawn from the random vector distribution [29].

Assuming a regression problem having training data of Z with N records and P variables, it is aimed to obtain prediction $\hat{f}_{rf}^{B}(x)$ in input x. Through bootstrap aggregation or bagging averages, variance in predication is reduced. The model is fitted for each bootstrap samples of b = 1, 2, 3, . . ., B. RF is created firstly by random selection of m variables from set of P

variables, then best variable is picked from *m* variables and finally, the node is split into two daughter nodes. This process is repeated until the minimum node size n_{min} is achieved at each terminal node to grow a random forest tree T_b on the bootstrapped data. In order to make prediction at point *x*, it is defined as

$$\hat{f}_{rf}^{B}(x) = \frac{1}{B}\sum_{b=1}^{B} T_b(x) \tag{5}$$

Through modeling of the random forest, it is required to set the number of trees. To this end, various number of trees should be evaluated by trial and error process.

The first order autoregressive AR1 model which is a standard linear difference equation is also used as another benchmark. It is a well-documented model that directly relates the parameter *x* at time *k* to the value of *x* at a previous time period, plus another variable ε dependent on time *k*.

3.2. Canonical GP

GP is one of the modern soft computing methods emerged in the last three decades. Similar to the well-known genetic algorithm, GP uses Darwinian evolutionary process to find the best solution but unlike GA, it simultaneously optimizes both the solution structure (function) and its coefficients. In other words, the functional form of the best model (solution) has not been chosen in advance. The three main evolutionary operations that map a population of random functions, aka GP, trees to a set of potential solutions include reproduction, crossover, and mutation. An example of randomly produced GP tree and its associated functional expression are illustrated in Figure 2. As shown in the figure, the function has three levels (tree depth =4) constructed from a root node level (plus function at the top), three inner nodes, and five terminal nodes comprising two variables x_1 and x_2 and two random constants linked via branches.

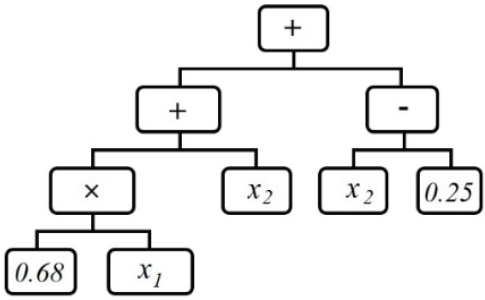

Figure 2 - Structure of GP tree representing the function $y = 0.68x_1+x_2+(x_2-0.25)$

During the training process, the three that shows the fittest function to the given problem is transferred to the next population without any alteration which is called reproduction. Crossover is the interchange of tree materials between two high performance trees called

parents. Mutation is the last evolutionary operation in which a randomly selected node (inner or terminal) is replaced with another node from the initial population that has not necessarily the same functionality with the selected node. These three operations are iterated on the GP trees till the fittest function is generated for the given problem or a function satisfies the modeler's goal. GP and its variants were successfully applied to solve variety of engineering problems [34-35]. This is more or less the whole processes in canonical GP as well as its different variants. For details its applications in hydrological studies, the reader is referred to [35].

3.3. Wavelet Packet Transform

The conventional Fourier transform was extended as wavelet transform that provides a multi-resolution analysis of signals. Wavelet packets (WP) are the generalization of wavelet transform capable of providing better frequency localization of signals [36]. The WP provides extensive decomposition over classic wavelet transform. The foremost difference between wavelet transform and WP transform is the way of the decomposition of a signal. Whereas classic wavelet transform decomposes only the low pass (approximation subspace) signals, the WP transform effectively decomposes both the low pass and high pass (detail subspace) components for the production of high-frequency resolution. Indeed, WPs are ways of mixing and matching wavelet filter banks in tree-like structures to create arbitrary time-frequency tiling. Recently WP has been compared with discrete wavelet transform [36].

3.4. Structure of the Proposed WPGP Model

The proposed WPGP model is a hybrid evolutionary model (Figure 3) that intends for the fine-tuning of the denoised SPEI signals attained from WP decomposition. As illustrated in Figure 4, the model includes three phases of data pre-processing (denoising), modeling (GP mapping and random noise creation), and data post-processing phase (noise injecting). In the first phase, SPEI time series at desired time horizons (here SPEI-3 and SPEI-6) are decomposed using WP transformation procedure. The result is a denoised SPEI time series plus a noise signal. The WPs can be used for various expansions of the original SPEI time series. Thus, an important task in this phase is to determine the most appropriate level of decomposition for the given signal. Either an entropy-based criterion [37] or Brute-force search method can be used to optimal decomposition selection.

In the modeling phase, the denoised SPEI time series and an optimum number of its lags are used respectively as target and predictor vectors to construct a predictive model. To create an explicit model, the GP could be an ideal option. As it is also capable of identifying the best predictors (among a set of input vectors), the well-established ACF analysis can be used to select required lags, i.e., input vectors. Since the GP deals with deterministic time series in this phase, a range of precise predictive models/solutions may be evolved. However, such solutions need to be modified using the stochastic component (noise) of the original SPEI time series. To this end, an appropriate probability distribution function (PDF) that perfectly represents the noise signal pattern is added to the evolved deterministic model. The identification of the best PDF for the noise signals is an important issue in this phase. In the present study, different unbounded distribution models were fitted to the noise signals, and

Kolmogorov–Smirnov (K-S) goodness-of-fit test was utilized in order to obtain the PDF so that it perfectly describes the likelihood of the behavior of the noise at each decomposition level. The assessed distribution models include Four-parameter Johnson SB, Beta, Wakeby, and Burr distributions, three-parameter Weibull, Log-Logistic, generalized extreme value, and two-parameter Normal distributions. The distribution parameters were estimated by the maximum likelihood estimation method in all the models.

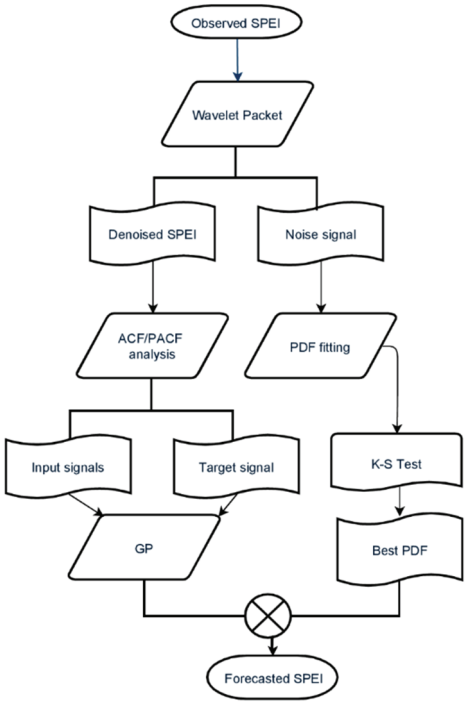

Figure 3 - The proposed WPGP model for SPEI hindcasting

It is worth mentioning that GP solutions need to control in terms of program size (so-called complexity), as the evolved models could be of illogical complexity that may result in over-fitting problem [35]. To avoid such a problem, we selected the best solution at potential validation data sets instead of the best in the training data set that guarantees both parsimony and generalizability of the best solutions. The idea was taken from the distinctive feature of GP that produces a population of solutions (potential models) instead of improving a single solution at each iteration for a given problem.

As previously mentioned, the last phase is the reconstruction of the forecasted SPEI through the accumulation of the GP-evolved model and the perfect PDF. For stochastic processes, it's logistic to provide a range of future forecasts instead of a deterministic value. To this end, maximum and minimum values of a set of random numbers (noises) that follow the distribution of the obtained perfect PDF generated at each forecasting scenario can be considered as the lower and upper bounds of SPEI forecasts.

4. PERFORMANCE EVALUATION METRICS

Nash-Sutcliffe efficiency (NSE) and root mean squared error (RMSE) measures were used in the present study.

$$\mathrm{NSE} = 1 - \frac{\sum_{i=1}^{n}(X_i^{obs} - X_i^{pre})^2}{\sum_{i=1}^{n}(X_i^{obs} - X_{mean}^{obs})^2} \tag{6}$$

$$\mathrm{RMSE} = \sqrt{\frac{\sum_{i=1}^{n}(X_i^{obs} - X_i^{pre})^2}{n}} \tag{7}$$

where X_i^{obs} = observed value of X (here SPEI), X_i^{pre} = predicted value X_{mean}^{obs} = mean value of observed data, and n is the number of observed data.

5. RESULTS AND DISCUSSION

5.1. RF and Baseline GP results

To develop the benchmark of RF and GP models at each station, the best input vectors were determined using the ACF and PACF analysis in each scenario (Figure 4). The figure shows more or less the same autocorrelation pattern for a given index at both stations. Thus, the forecasting scenarios were structured as below:

$$SPEI\text{-}3(t) = f(SPEI\text{-}3_{t-1}, SPEI\text{-}3_{t-2}, SPEI\text{-}3_{t-4}, SPEI\text{-}3_{t-7}, SPEI\text{-}3_{t-10}, \varepsilon_t) \tag{8}$$

$$SPEI\text{-}6(t) = f(SPEI\text{-}6_{t-1}, SPEI\text{-}6_{t-2}, SPEI\text{-}6_{t-3}, SPEI\text{-}6_{t-4}, SPEI\text{-}6_{t-7}, SPEI\text{-}6_{t-13}, \varepsilon_t) \tag{9}$$

The RF and GP structures were trained to minimize the *MSE* between the outputs from the model and the targets in the data set. Determination of the optimum number of trees in RF structure is of importance to construct the best RF model. Therefore, several number of trees are examined through trial and error procedure. To this end, RF models are constructed adjusting the maximum 200 number of trees. Results for two meteorological stations of Beypazari and Nallihan for both indexes of SPEI-3 and SPEI-6 are shown in Figure 5 at training stage. It is seen from Figure 6 that there is noticeable reduction in *MSE* until 20 number of trees for all cases, however, for higher number of trees no significant changes are seen. The optimum number of trees are shown in Figure 5 by red vertical lines where for SPEI-3 and SPEI-6 at both stations, they are found to be 60 and 70, respectively.

As useful feature of RF technique, it examines the importance of input variables on computing the output. Results of four RF models for two meteorological stations of Beypazari and Nallihan and for SPEI-3 and SPEI-6 indexes are given as pie charts in Figure 6. It is seen in Figure 6 that RF provides similar results for Beypazari and Nallihan stations

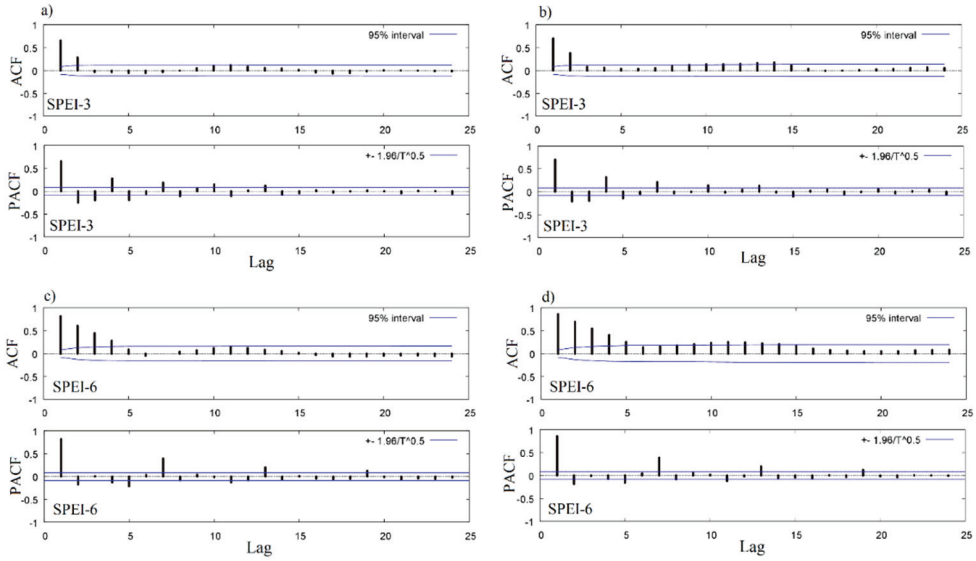

Figure 4 - Autocorrelation function (ACF) and Partial autocorrelation function (PACF) of original SPEI-3 (a and b) and SPEI-6 (c and d) time series at Beypazari (left column) and Nallihan (right column) meteorology stations

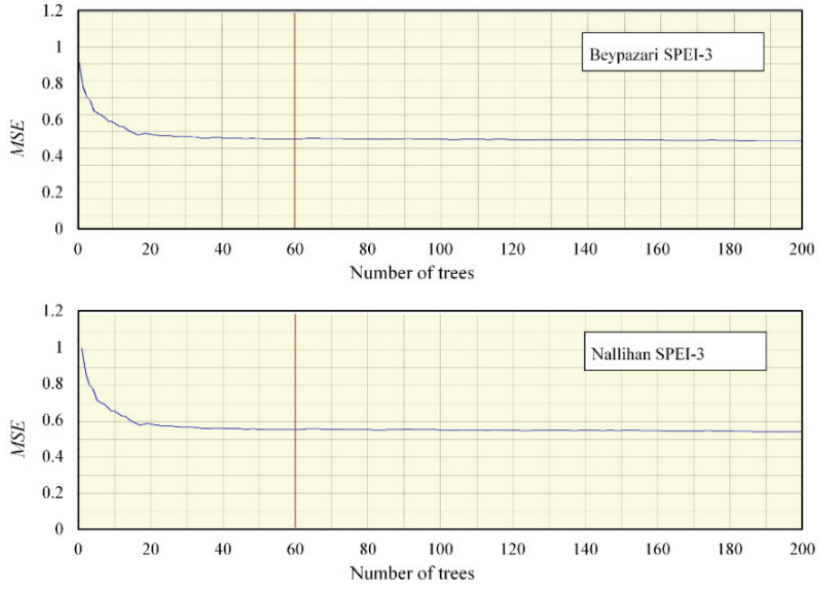

Figure 5 - Performance of RF models with different number of tress

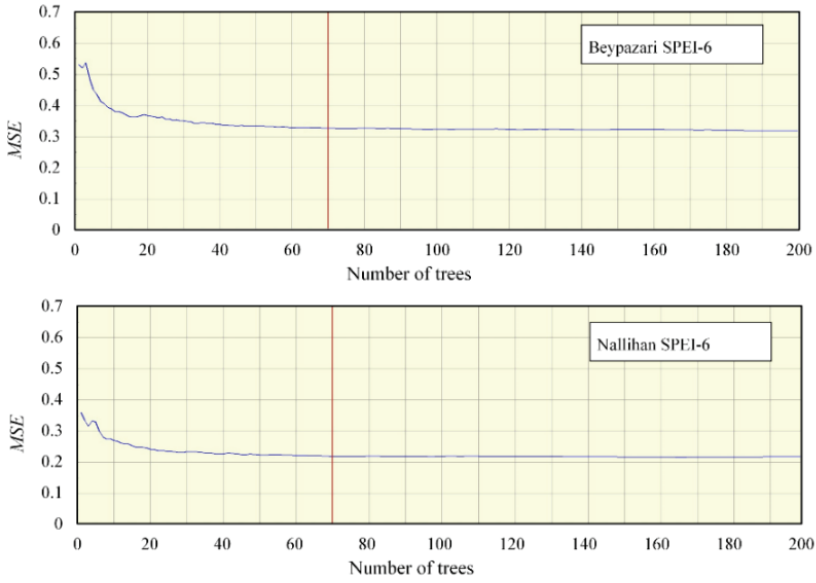

Figure 5 - Performance of RF models with different number of tress (continue)

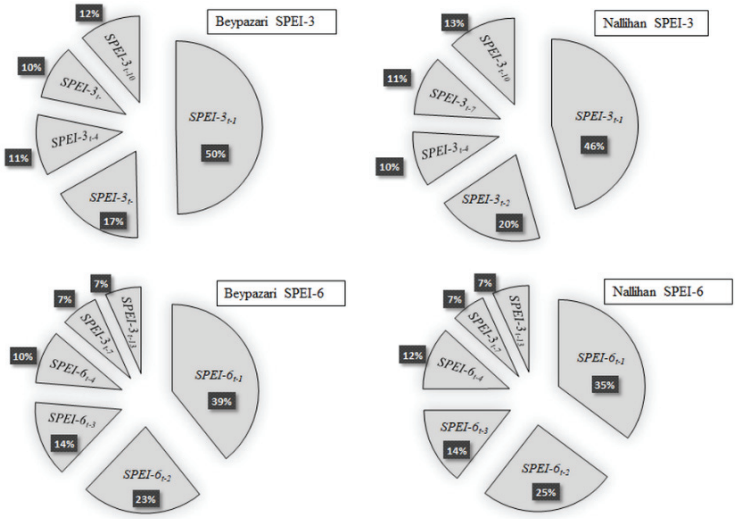

Figure 6. Variable importance at the RF models

considering two different SPEI-3 and SPEI-6 indexes. It is found that SPEI-3_{t-1} and SPEI-3_{t-2} have greatest effect while, SPEI-3_{t-4}, SPEI-3_{t-7} and SPEI-3_{t-10} are less important in RF models output. Similar results are achieved for SPEI-6 where, SPEI-6_{t-1} and SPEI-6_{t-2} are found as most important variables and SPEI-6_{t-7} and SPEI-6_{t-13} have the lower contribution in model

output. It is worthy to mention that the degree of importance of input variables is also related to selected SPEI index. It is seen in Figure 6 that t-1 lag in SPEI-3 is more important than SPEI-6. On the other hand, the degree of importance of t-2 lag is increased in SPEI-6 in comparison with SPEI-3 index results.

Table 2 - Parameter setting for standalone GP runs

Parameter	**Value**
Functions	+,-, *, /
Maximum generation	250
Initialization	Half and Half
Initial Population	500
Mutation rate	5 %
Crossover rate	90 %
Reproduction rate	20 %
Maximum depth	6

Table 3 - Performance metrics of the best RF and GP models

Model	Station	index	RMSE		NSE	
			Train	Test	Train	Test
AR1	Beypazari	SPEI-3	0.712	0.837	0.448	0.362
		SPEI-6	0.575	0.664	0.642	0.576
	Nallihan	SPEI-3	0.727	0.880	0.391	0.322
		SPEI-6	0.682	0.864	0.457	0.333
RF	Beypazari	SPEI-3	0.737	0.839	0.409	0.359
		SPEI-6	0.564	0.658	0.656	0.582
	Nallihan	SPEI-3	0.669	0.821	0.486	0.409
		SPEI-6	0.469	0.618	0.745	0.652
GP	Beypazari	SPEI-3	0.670	0.831	0.511	0.371
		SPEI-6	0.529	0.637	0.697	0.610
	Nallihan	SPEI-3	0.628	0.806	0.547	0.430
		SPEI-6	0.449	0.576	0.765	0.700

GPdotNetV5.0, the open source software frame work [38], was used in this study to develop standalone GP-based SPEI forecasting models. The software has been successfully applied in variety of hydrological modelling tasks in the recent studies [e.g., 39-40]. The evolutionary parameters adopted for GPdotNetV5.0 setup were tabulated in Table 2. Among the hundreds

of standalone GP models evolved at each scenario, the best models were selected with respect to both accuracy and complexity of the potential solution at validation period. The complexity of each model is calculated after finding and eliminating the introns in GP trees.

It is worth to mention that a set of random floating-point numbers in the range [0, 1] were used in terminal set given that the noise term is not separated in standalone GP models. Table 3 presents the performance metrics of the best RF and GP models at each station. The table also includes performance of the AR1 models developed for each index. The results show that GP models produce better forecasts than both RF and AR1 in terms of all error measures. However, they are not accurate enough, particularly during testing period.

Table 3 clearly shows that the models trained for SPEI-6 achieved higher accuracy than the models trained for SPEI-3. The reason behind it may be due to the smoother time series in SPEI-6 as a result of averaging of temperature and precipitation over six months period.

5.2. The WPGP Results

To forecast drought in a regional- or even catchment-scale, modelers typically deal with drought time series from several meteorology stations. It is not a good plan to denoise each of them individually. Thus in the first step, we create a matrix of such time series (here two dimensional real data) before using WP decomposition. In each hindcasting scenario, first a concatenated signal was made and then, the denoised signal in concatenated form was created. Now, the modeler can subtract denoised signal from original SPEI series to obtain the remaining noise signal. Figure 7 exhibits the concatenated SPEI-3 and SPEI-6 signals decomposed at depths 3, 6, and 9 with Debauches (db4) wavelet packets. Bearing in mind that db4 is commonly used to decompose hydrological time series [41], one may use any other type of WPs to this end. As previously mentioned, the optimal subtree of an initial wavelet packet tree can be obtained with respect to an entropy type criterion. In this study, the optimal subtree at each depth was computed considering Shannon entropy criterion that perhaps yields to a smaller tree than the initial one. Figure 8 provided an example of the initial and best WP trees at depth 3.

To select the best WP tree depth (i.e., deterministic part of SPEI series) at each meteorology station, the noise signals were suppressed and the denoised versions of SPEI series were modeled using GP. As illustrated in Figure 7, the inputs are the optimum number of lagged denoised signals having the highest correlation with the denoised SPEI at current time (i.e., 1-month ahead hindcasting scheme). Table 4 presented accuracy of the WPGP models at different depths.

The modeling results showed that different decomposition depths had different impacts on the original SPEI signal. The best deterministic model was found at depth 6. Therefore, the associated noise signals (see Figure 9 left column) were used to determine the perfect noise PDF at each station/time horizon. The results of goodness-of-fit tests applied to identify the PDF of the noise signals were given in Table 5 and the best distribution model was compared to normal distribution in Figure 9 (right column). Out of 8 empirical models, the K-S test showed that the Johnson SB distribution is the best representor for noise signal in SPEI-3.Therefore, the relevant forecasting scenarios can be mathematically expressed as Equations 10-12.

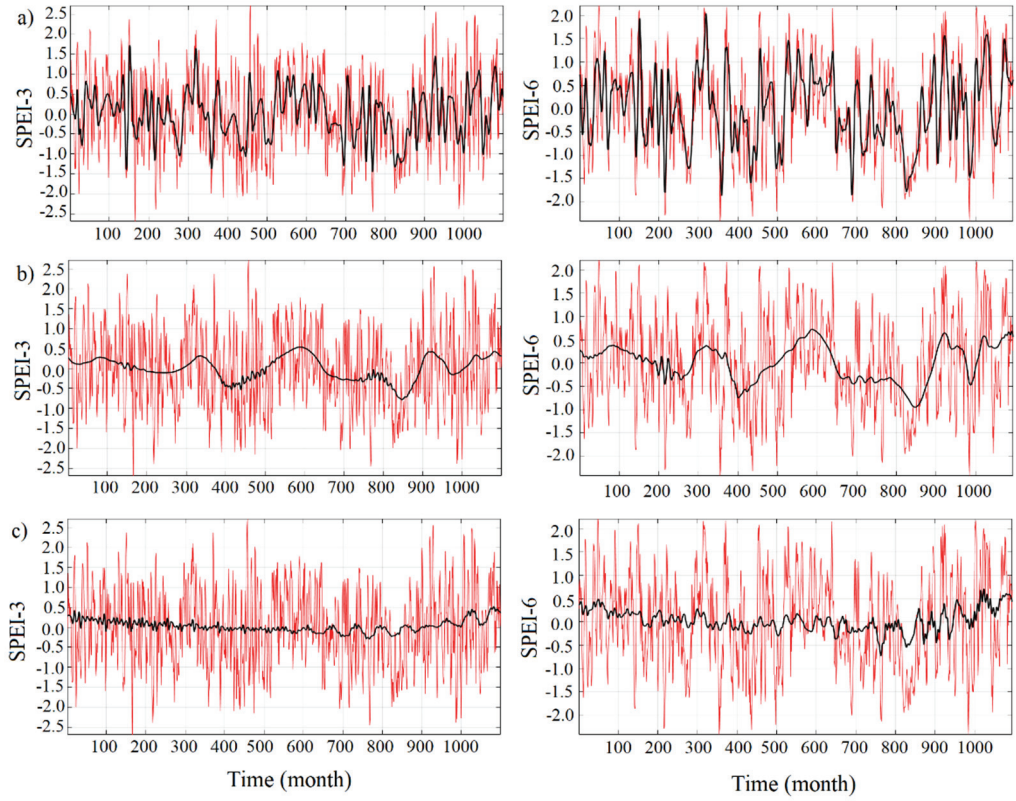

Figure 7 - Concatenated original SPEI and denoised SPEI signals at decomposition depth of (a) 3, (b) 6, and (c) 9.

Table 4 - Efficiency results of one-month a head WPGP models at different depth

Station	Drought index	WP Depth	Best model	Training		Testing	
				NSE	RMSE	NSE	RMSE
Beypazari	SPEI-3	3	$x_4+0.927(x_4-x_3)+e$	0.983	0.072	0.993	0.044
		6	$x_4-(((((x_1\times x_2)/(x_3+x_2))\times 0.84)+0.84)\times(x_3-x_4))+e$	**0.999**	**0.004**	**0.992**	**0.023**
		9	$(x_4/0.777)-((x_2-x_1)+(0.225\times((x_2-0.025)\times 0.854)))+e$	0.844	0.04	0.731	0.021

Table 4 - Efficiency results of one-month ahead WPGP models at different depths (continue)

Beypazari	SPEI-6	3	x_4 -0.9016(x_3 -x_4) + e	0.987	0.086	0.992	0.067
		6	((0.8776(x_4 -x_3))+x_4)-((((x_3 × (x_2 - x1)) ×x_4)/(x_2 /x_4)) + e	**0.997**	**0.011**	**1.00**	**0.006**
		9	x_4 -((((((x_3 -0.3157)+(x_3 -0.9395)) × ((x_2 /0.9395)-x_4))+0.785) × (x_3 -x_4)) + e	0.987	0.017	0.990	0.011
Nallihan	SPEI-3	3	2x_4 -x_3 - 0.0447(2x_4 -x_3) +e	0.991	0.059	0.989	0.062
		6	x_4 -(0.817(x_3 -x_4)) + e	**0.999**	**0.013**	**1.00**	**0.003**
		9	((1.367-x_4×x_1) (x_1-x_2)) (0.8085-x_4))+((((x_4 -x_1) ((0.559 -x_4)/(1.118 -x_2)))+x_4+e	0.982	0.012	0.989	0.016
	SPEI-6	3	x_4-(0.8357((x_3/0.966)-x_4)) + e	0.995	0.054	0.994	0.0962
		6	x_4+((x_4 /(x_2 ×x_4))(x_2(x_4 -x_3))) + e	**1.000**	**0.003**	**0.999**	**0.009**
		9	x_4-(0.745 ((x_3 -x_4))) + e	0.975	0.031	0.974	0.041

x_1=$SPEI_{t-4}$, x_2=$SPEI_{t-3}$, x_3=$SPEI_{t-2}$, and x_4=$SPEI_{t-1}$

$SPEI\text{-}3(t) = SPEI\text{-}3_{t-1}$ - (((((*SPEI*-3_{t-4} × *SPEI*-3_{t-3})/ (*SPEI*-3_{t-2} + *SPEI*-3_{t-3})) ×0.84) +0.84) × (*SPEI*-3_{t-2} - *SPEI*-3_{t-1})) + *SPEI*-3_N *for Beypazari station* (10)

$SPEI\text{-}3(t) = SPEI\text{-}3_{t-1}$ – (0.817(*SPEI*-3_{t-2} -*SPEI*-3_{t-1})) + *SPEI*-3_N *for Nallihan station* (11)

Where *SPEI*-3_N represents the noise value extracted from Johnson SB distribution with shape parameters of γ=0.32655 and δ=1.9162, the scale parameter of λ=7.852, and the location parameter of ξ=-3.6218 at Beypazari station and γ=0.08172, δ=1.8022, λ=7.002, and ξ=-

3.4173 at Nallihan station. Considering these parameters the Johnson SB distribution is expressed as below:

$$f(x) = \frac{\delta}{\lambda\sqrt{2\pi}z(1-z)}\exp(-\frac{1}{2}(\gamma + \delta.\ln(\frac{z}{1-z}))^2) \quad \text{and } z = (SPEI\text{-}3_{(t-1)} - \xi)/\lambda \qquad (12)$$

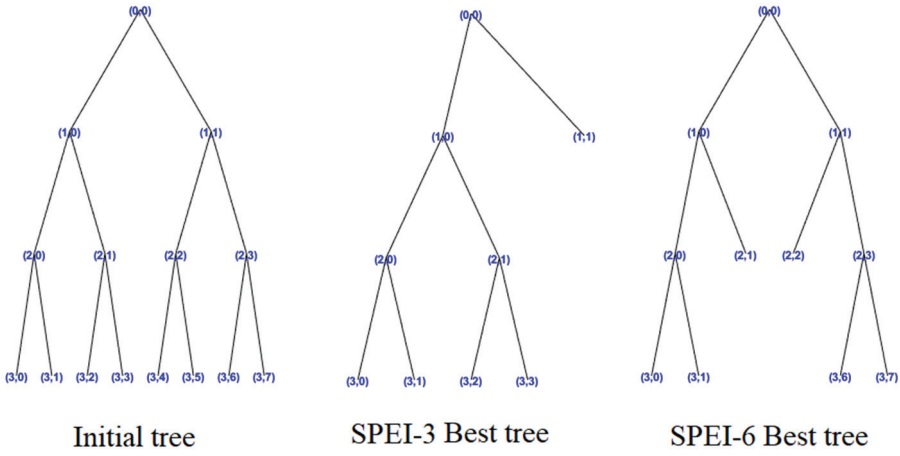

Figure 8 - Example of initial and best wavelet packet tree at depth 3

Table 5 - Summary of Kolmogorov-Smirnov Goodness of Fit test

Distribution	SPEI-3				SPEI-6			
	Beypazari		Nallihan		Beypazari		Nallihan	
	Statistic	Rank	Statistic	Rank	Statistic	Rank	Statistic	Rank
Johnson SB	**0.023**	**1**	**0.015**	**1**	0.022	3	0.022	3
Beta	0.025	2	0.016	3	0.022	4	0.022	2
Wakeby	0.025	3	0.021	6	0.022	5	0.026	5
Burr (4P)	0.026	4	0.018	4	0.021	2	0.023	4
Weibull (3P)	0.026	5	0.018	5	**0.021**	**1**	**0.022**	**1**
Gen. Extreme Value	0.026	6	0.015	2	0.024	7	0.024	6
Normal	0.031	7	0.024	7	0.028	9	0.026	7
Log-Logistic (3P)	0.045	8	0.034	8	0.036	11	0.033	8

Considering the SPEI-6, Weibull probability function is the best distribution model. Therefore, the relevant forecasting scenarios can be mathematically expressed as Equations 13-15.

$$SPEI\text{-}6(t) = ((0.8776(SPEI\text{-}6_{t-1} - SPEI\text{-}6_{t-2})) + SPEI\text{-}6_{t-1}) - (((SPEI\text{-}6_{t-2} \times ((SPEI\text{-}6_{t-3} - SPEI\text{-}6_{t-4}) \times SPEI\text{-}6_{t-1}) / (SPEI\text{-}6_{t-3} / SPEI\text{-}6_{t-1})) + SPEI\text{-}6_N \quad \textit{for Beypazari station} \quad (13)$$

$$SPEI\text{-}6(t) = SPEI\text{-}6_{t-1} + ((SPEI\text{-}6_{t-1} / (SPEI\text{-}6_{t-3} \times SPEI\text{-}6_{t-1})) \times (SPEI\text{-}6_{t-3} \times (SPEI\text{-}6_{t-1} - SPEI\text{-}6_{t-2}))) + SPEI\text{-}6_N \quad \textit{for Nallihan station} \quad (14)$$

Where $SPEI\text{-}6_N$ represents the noise value extracted from Weibull distribution with the shape parameter of α=3.5324, the scale parameter of β=3.2345, and the location parameter of γ= -2.9211 at Beypazari station as well as α =3.4774, β=2.8798, and γ =-2.5827 at Nallihan station. Considering these parameters, Weibull distribution is expressed as below:

$$f(x) = \frac{\alpha}{\beta}\left(\frac{SPEI-6_{(t-1)} - \gamma}{\beta}\right)^{\alpha-1} \exp\left(-\left(\frac{SPEI-6_{(t-1)} - \gamma}{\beta}\right)^{\alpha}\right) \quad (15)$$

It is also evident from the table that the best distribution model varies among both stations and time scales. This means that if a distribution model is superior for a station, it is not necessarily an effective model for the adjacent station. Therefore, instead of using a single distribution model, a comparative analysis among different models is crucial when using WPGP at multi-station studies.

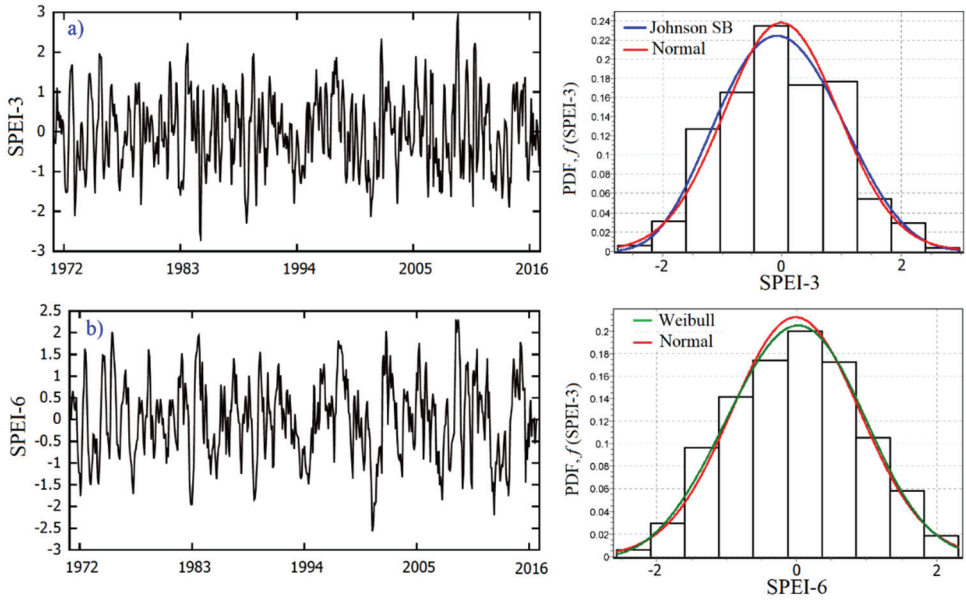

Figure 9 - Noise signals (left) and histogram with theoretical PDFs for noise signals of SPEI at Beypazari (a and b) and Nallihan (c and d) stations

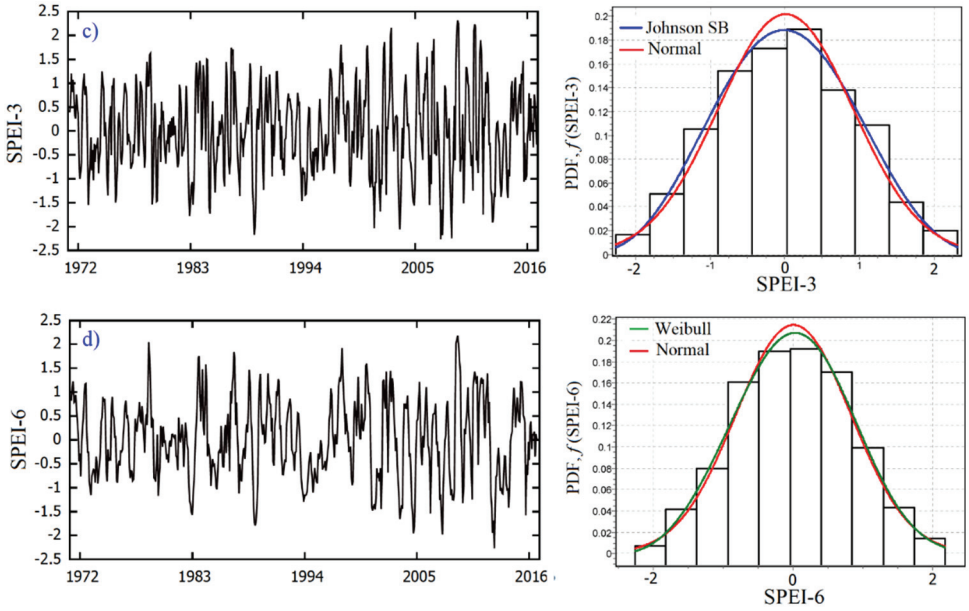

Figure 9 - Noise signals (left) and histogram with theoretical PDFs for noise signals of SPEI at Beypazari (a and b) and Nallihan (c and d) stations (continue)

6. CONCLUSIONS

In this study, a novel hybrid data-driven model, namely WPGP, has been introduced for 1-month ahead hindcasting of meteorological drought. The model integrates WP denoising technique with symbolic regression ability of GP to model SPEI time series. Using historical SPEI series from two meteorological stations, efficiency of the proposed WPGP model was compared to those of three benchmarks: the standalone GP, RF, and AR1 models. The WPGP uses antecedent denoised SPEI signal instead of their original time series and provides explicit predictive models under parsimony pressure. To use the model for future forecasts, a PDF with the similar pattern of noise signals is added to the evolved models. Indeed, the WPGP is an evolutionary model that assimilates the capabilities of standalone GP and WP to yield a better solution through the elimination of noise and reconstruction of predictive signals and good noises. Based on the forecasting results, the proposed WPGP model was found to have a higher ability than its baseline GP as well as the benchmark RF and AR1. The proposed methodology resulted in the acquisition of a more robust model that yields significant improvement in terms of RMSE and NSE metrics. From a model developing view, it is worthy to remind that the WPGP is a hybrid but explicit approach which means a mathematical expression is provided for future predictions in each scenario. It must be noted that the methodology presented is general and can be applied to similar problems dealing with other drought indices. The present study was confined to 1-month ahead hindcasting scenarios which use past SPEI series as the only input information. For many implementations in water resources management, the future studies can comprise improving the offered model so that it is able to do forecasts with longer lead-times such as seasonal, or

even longer. To this end, implementation of exogenous inputs or ensemble precipitation and PET forecasts from ECMWF would be informative. Another suggestion for the future studies may be the use of frequency-based estimations to predict chaotic features of drought time series as those studies accomplished for streamflow series [42].

Symbols

γ : shape parameters 0

ξ : location parameter

λ : scale parameter

ACF : autocorrelation function

ANN : artificial neural network

ANFIS : adaptive neuro-fuzzy inference system

db : Debauches

DAI : drought area index

DT : decision trees

GP : genetic programming

LSSVM : least square support vector machine

MARS : multivariate adaptive regression splines

PACF : partial autocorrelation function

PDF : probability distribution function

PDSI : Palmer drought severity index

RF : random forest

SPEI : standardized precipitation evapotranspiration index

SPI : standardized precipitation index

SVR : support regression vector

WP : wavelet packets

WPGP : wavelet packet-genetic programming

References

[1] McKee, T.B., Doesken, N.J., and Kleist, J., (1993). The relationship of drought frequency and duration to time scales. In Proceedings of the International 8th Conference on Applied Climatology. American Meteorological Society, Anaheim, CA, USA, 17–22 January. pp. 179–184.

[2] Bhalme, H.N., and Mooley, D. A. (1980). Large-scale droughts/floods and monsoon circulation. Monthly Weather Review, 108(8), 1197-1211.

[3] Palmer, W.C. (1965). Meteorological Drought, Weather Bureau Research Paper No. 45, U.S. Department of Commerce, Washington, D.C.

[4] Vicente-Serrano, S.M., Beguería, S., and López-Moreno, J.I. (2010). A multiscalar drought index sensitive to global warming: the standardized precipitation evapotranspiration index. Journal of climate, 23(7), 1696-1718.

[5] Mishra, A. K., & Desai, V. R. (2005). Drought forecasting using stochastic models. Stochastic Environmental Research and Risk Assessment, 19(5), 326-339.

[6] Bacanli, U. G., Firat, M., & Dikbas, F. (2009). Adaptive neuro-fuzzy inference system for drought forecasting. Stochastic Environmental Research and Risk Assessment, 23(8), 1143-1154.

[7] Keskin, M. E., Terzi, O., Taylan, E. D., & Küçükyaman, D. (2009). Meteorological drought analysis using data-driven models for the Lakes District, Turkey. Hydrological sciences journal, 54(6), 1114-1124.

[8] Durdu, Ö. F. (2010). Application of linear stochastic models for drought forecasting in the Büyük Menderes river basin, western Turkey. Stochastic Environmental Research and Risk Assessment, 24(8), 1145-1162.

[9] Özger, M., Mishra, A. K., & Singh, V. P. (2012). Long lead time drought forecasting using a wavelet and fuzzy logic combination model: A case study in Texas. Journal of Hydrometeorology, 13(1), 284-297.

[10] Danandeh Mehr, A., Kahya, E., & Özger, M. (2014). A gene–wavelet model for long lead time drought forecasting. Journal of Hydrology, 517, 691-699.

[11] Bazrafshan, O., Salajegheh, A., Bazrafshan, J., Mahdavi, M., & Fatehi Maraj, A. (2015). Hydrological drought forecasting using ARIMA models (case study: Karkheh Basin). Ecopersia, 3(3), 1099-1117.

[12] Karavitis, C. A., Vasilakou, C. G., Tsesmelis, D. E., Oikonomou, P. D., Skondras, N. A., Stamatakos, D., ... & Alexandris, S. (2015). Short-term drought forecasting combining stochastic and geo-statistical approaches. European Water, 49, 43-63.

[13] Deo, R. C., Tiwari, M. K., Adamowski, J. F., & Quilty, J. M. (2017). Forecasting effective drought index using a wavelet extreme learning machine (W-ELM) model. Stochastic environmental research and risk assessment, 31(5), 1211-1240.

[14] Katip, A. (2018). Meteorological Drought Analysis Using Artificial Neural Networks for Bursa City, Turkey. Applied Ecology and Environmental Research, 16(3), 3315-3332.

[15] Morid, S., Smakhtin, V., & Bagherzadeh, K. (2007). Drought forecasting using artificial neural networks and time series of drought indices. International Journal of Climatology: A Journal of the Royal Meteorological Society, 27(15), 2103-2111.

[16] Barua, S., Ng, A. W. M., & Perera, B. J. C. (2012). Artificial neural network–based drought forecasting using a nonlinear aggregated drought index. Journal of Hydrologic Engineering, 17(12), 1408-1413.

[17] Mokhtarzad, M., Eskandari, F., Vanjani, N. J., & Arabasadi, A. (2017). Drought forecasting by ANN, ANFIS, and SVM and comparison of the models. Environmental earth sciences, 76(21), 729.

[18] Labat, D. (2005). Recent advances in wavelet analyses: Part 1. A review of concepts. Journal of Hydrology, 314(1-4), 275-288.

[19] Nourani, V., Baghanam, A. H., Adamowski, J., & Kisi, O. (2014). Applications of hybrid wavelet–artificial intelligence models in hydrology: a review. Journal of Hydrology, 514, 358-377.

[20] Kim, T. W., & Valdés, J. B. (2003). Nonlinear model for drought forecasting based on a conjunction of wavelet transforms and neural networks. Journal of Hydrologic Engineering, 8(6), 319-328.

[21] Belayneh, A., Adamowski, J., Khalil, B., & Ozga-Zielinski, B. (2014). Long-term SPI drought forecasting in the Awash River Basin in Ethiopia using wavelet neural network and wavelet support vector regression models. Journal of Hydrology, 508, 418-429.

[22] Maity, R., & Suman, M. (2019). Predictability of Hydrological Systems Using the Wavelet Transformation: Application to Drought Prediction. In Hydrology in a Changing World (pp. 109-137). Springer, Cham.

[23] Gyamfi, C., Amaning-Adjei, K., Anornu, G. K., Ndambuki, J. M., & Odai, S. N. (2019). Evolutional characteristics of hydro-meteorological drought studied using standardized indices and wavelet analysis. Modeling Earth Systems and Environment, 5(2), 455-469.

[24] Soh, Y. W., Koo, C. H., Huang, Y. F., & Fung, K. F. (2018). Application of artificial intelligence models for the prediction of standardized precipitation evapotranspiration index (SPEI) at Langat River Basin, Malaysia. Computers and electronics in agriculture, 144, 164-173.

[25] Ahmadalipour, A., Moradkhani, H., and Demirel, M.C. (2017). A comparative assessment of projected meteorological and hydrological droughts: Elucidating the role of temperature. Journal of Hydrology, 553, 785-797.

[26] Danandeh Mehr, A., Sorman, A. U., Kahya, E., & Hesami Afshar, M. (2019). Climate change impacts on meteorological drought using SPI and SPEI: case study of Ankara, Turkey. Hydrological Sciences Journal, DOI: 10.1080/02626667.2019.1691218

[27] Meresa, H. K., Osuch, M., and Romanowicz, R. (2016). Hydro-meteorological drought projections into the 21-st century for selected Polish catchments. Water, 8(5), 206.

[28] Khan, M., Muhammad, N., & El-Shafie, A. (2018). Wavelet-ANN versus ANN-based model for hydrometeorological drought forecasting. Water, 10(8), 998.

[29] Breiman, L., 2001. Random forests. Mach. Learn. 45 (1), 5–32.

[30] Chen, J., Li, M., & Wang, W. (2012). Statistical uncertainty estimation using random forests and its application to drought forecast. Mathematical Problems in Engineering, 2012.

[31] Yu, P.S., Yang, T.C., Chen, S.Y., Kuo, C.M., Tseng, H.W., 2017. Comparison of random forests and support vector machine for real-time radar-derived rainfall forecasting. Journal of hydrology 552, 92-104.

[32] Zhao, W., Sánchez, N., Lu, H., Li, A., (2018). A spatial downscaling approach for the SMAP passive surface soil moisture product using random forest regression. Journal of hydrology 563, 1009-1024.

[33] Sadler, J.M., Goodall, J.L., Morsy, M.M., Spencer, K., (2018). Modeling urban coastal flood severity from crowd-sourced flood reports using Poisson regression and Random Forest. Journal of hydrology 559, 43-55.

[34] Şarlak, N., & Güven, A. (2016). Global güneş radyasyon tahmini: Gaziantep uygulaması. Teknik Dergi, 27(3), 7561-7568.

[35] Danandeh Mehr, A., Nourani, V., Kahya, E., Hrnjica, B., Sattar, A. M., & Yaseen, Z. M. (2018). Genetic programming in water resources engineering: A state-of-the-art review. Journal of hydrology 566, 643-667.

[36] Hu, J., Liu, B., & Peng, S. (2019). Forecasting salinity time series using RF and ELM approaches coupled with decomposition techniques. Stochastic Environmental Research and Risk Assessment, 1-19.

[37] Coifman, R.R.; M.V. Wickerhauser, (1992), "Entropy-based algorithms for best basis selection," IEEE Trans. on Inf. Theory, vol. 38, 2, pp. 713–718

[38] Hrnjica, B., & Danandeh Mehr, A. (2018). Optimized Genetic Programming Applications: Emerging Research and Opportunities: Emerging Research and Opportunities. IGI Global. DOI: 10.4018/978-1-5225-6005-0

[39] Rahmani-Rezaeieh, A., Mohammadi, M., & Danandeh Mehr, A. (2019). Ensemble gene expression programming: a new approach for evolution of parsimonious streamflow forecasting model. Theoretical and Applied Climatology, 1-16.

[40] Danandeh Mehr, A., & Safari, M. J. S. (2020). Multiple genetic programming: a new approach to improve genetic-based month ahead rainfall forecasts. Environmental Monitoring and Assessment, 192(1), 25.

[41] Danandeh Mehr, A., Kahya, E., & Olyaie, E. (2013). Streamflow prediction using linear genetic programming in comparison with a neuro-wavelet technique. Journal of Hydrology, 505, 240-249.

[42] Dikbaş, F. (2016). Büyük Menderes Akımlarının Frekans Tabanlı Tahmini. Teknik Dergi, 27(1), 7325-7343.

Teknik Dergi, 2021 11051-11068, Paper 624

An Experimental Study on Unit Side Resistance of Gaziantep Limestone

Volkan KALPAKCI[1]
Islam TABUR[2]

ABSTRACT

In this study, the correlation between the uniaxial compressive strength and unit side resistance of Gaziantep limestone was investigated experimentally for dry and fully saturated conditions. The results were compared with the methods given in the literature which correlate these two parameters. The linear correlations significantly overestimated the measured side resistance values for all tests while the non-linear methods generally overestimated the unit side resistance under fully saturated conditions but provided a reasonable estimation for dry samples. As a result, a linear correlation and non-linear correlation ranges for estimating the unit side resistance of such limestones were also suggested.

Keywords: Limestone, side resistance, rock, strength, correlation.

1. INTRODUCTION

Construction of rock-socketed piles is a preferable method in geotechnical engineering especially in case of an available rock layer at a reasonable depth below foundation. Generally, a higher bearing capacity is provided by such piles besides significantly smaller settlements as compared to those of floating piles. The magnitude of bond strength between concrete and rock surface, namely the unit side resistance of rock (q_s), is a key factor in determining the bearing capacity of such piles. For this reason, there are various studies conducted for estimating the unit side resistance of rocks. Generally, the unit side resistance of rocks was correlated with their uniaxial compressive strength (σ_c) in these studies. The correlations are generally classified in two groups as linear and non-linear correlations.

Note:
- This paper has been received on August 22, 2019 and accepted for publication by the Editorial Board on March 2, 2020.
- Discussions on this paper will be accepted by September 30, 2021.

• https://doi.org/10.18400/tekderg.608631

1 Hasan Kalyoncu University, Civil Engineering Department, Gaziantep, Turkey - volkan.kalpakci@hku.edu.tr - https://orcid.org/0000-0002-5277-795X

2 Hasan Kalyoncu University, Civil Engineering Department, Gaziantep, Turkey - islam.tabur@std.hku.edu.tr - https://orcid.org/0000-0003-0752-4205

The linear correlations are in the general form of Eq. (1) where "A" is the linear correlation coefficient and dependent on the rock type. The equations suggested by [1], [2], [3] and [4] may be given as examples of such linear correlations.

$$q_s = Ax\sigma_c \quad (1)$$

On the other hand, the non-linear correlations are in the general form of Eq. (2) where "C" and "b" are coefficients dependent on the rock type. The relationships provided by [5], [6], [7], [8], [9], [10], [11] and [12] may be listed as examples of such non-linear correlations.

$$q_s = Cx\sigma_c^b \quad (2)$$

Alternatively; in some studies such as [13] and [14], the rock mass parameters and socket roughness were also included in these correlations. However, these methods were not considered during assessment of the results of this study since the experiments of this research were performed on intact samples with smooth socket interfaces. Additionally, in a recent study by [15], the bearing capacity of rock-socketed piles in 4 different cities of Turkey was investigated through pile load tests.

Gaziantep, the eighth biggest city with leading trade capacity and highest population growth rate in its region, is located in the south-eastern part of Turkey. Generally, the soil profile of the city is composed of a surficial loose soil layer underlied by Gaziantep limestone. As a result, the use of rock socketed piles has become a popular solution for most of the recently built structures during the rapid construction of the city in the past decade. However, Gaziantep limestone is a chalky and clayey, porous soft rock as it was explained in detail in [16]. As a result of this fact, Gaziantep limestone becomes saturated easily which results in significant reduction of the uniaxial compressive strength (σ_c) of Gaziantep limestone upon saturation which was also verified by [17]. The possible reasons of strength reduction observed in similar porous soft rocks upon water interaction were discussed by [18] and it was concluded that water saturation reduced the yield stress and failure strength of equivalent solid matrix due to a decrease in the capillary force of the liquid contact and the softening of the general rock structure.

Based on this fact; in this research it was aimed to investigate the relation between the unit side resistance and uniaxial compressive strength of Gaziantep limestone under dry and fully saturated conditions through an experimental study. For this purpose, firstly an unconfined compression testing machine was modified to perform these tests in laboratory scale. Then, 24 limestone blocks were taken from a quarry site in Gaziantep. Each block was separated into two adjacent parts and one part was tested under dry conditions while the other part was tested under fully saturated conditions. As a result of this study, a linear correlation and upper bound and lower bound curves as a non-linear correlation range were suggested for estimating the unit side resistance of Gaziantep limestone. Moreover, the test results were compared with the selected methods from the literature. These evaluations have revealed that especially the linear correlations were significantly overestimating the test data while the non-linear methods generally provided a reasonable estimation for dry samples but overestimated the unit side resistance under fully saturated conditions.

2. EXPERIMENTAL STUDY

The experiments of this study were conducted in the soil mechanics laboratory of Hasan Kalyoncu University. As the first step of the experimental study, 24 limestone blocks having dimensions of 300x300x150mm (WidthxLengthxHeight) were taken from different places of a quarry site in Gaziantep. After assigning a number to each block; the blocks were cut into two adjacent parts having equal dimensions of 150x300x150mm (WidthxLengthxHeight) making a total of 48 limestone blocks. In this way, it was aimed to have a dry and a fully saturated test result for each block. Then, a NX size cylindrical sample (D = 54.7mm) was extracted from the middle of each of the 48 blocks (Figure 1). All the tests conducted on limestone samples were done in accordance with the suggested methods in ISRM [19]. The cylindrical samples were first weighed and then oven-dried at least for 24 hours (until constant weight) at 105 ± 3^0C. After the drying procedure, uniaxial compression tests were done for the dry samples of each block. The height/diameter ratio of the samples were H/D = 150/54.7 = 2.74 and the loading rate was selected as 0.7 MPa/s from the range given in [19] as 0.5 – 1.0 MPa/s. As a result, the uniaxial compressive strength of each dry sample from each block was determined.

The rest of the samples were soaked under water and weighed each day until constant weight (to nearest 0.01g), to ensure the fully saturation of the samples. A representative set of measurements is presented in Table 1. As it can be seen from this table, all the samples had become fully saturated in a week. After full saturation, the uniaxial compressive strengths of these samples were determined experimentally applying the same testing procedure described for dry samples. As a result, the uniaxial compressive strength of each sample from each block was determined for fully saturated condition. Additionally, some basic properties of the tested samples like porosity, water absorption capacity, dry and fully saturated unit weights were also determined during these tests in accordance with the testing procedures suggested in [19].

Upon completion of the uniaxial compression tests, the holes at the middle of the blocks which were drilled during the extraction of the cylindrical samples were filled with a concrete having 28 days characteristic compressive strength of 30MPa. CEM I 42.5 cement class was used for concrete production and the characteristic compressive strength was determined according to ASTM C39 [20] standard. All the rock blocks were soaked under water for 28 days to obtain the target compressive strength of the infilled concrete. The upper and lower ends of the cylindrical concrete core was levelled with a suitable cutter before testing in order to obtain a plane loading surface. After soaking procedure, the unit side resistance tests were executed for samples under fully saturated conditions while the remaining blocks were tested after completely dried in the oven. Here it should be mentioned that the soaking procedure followed for these tests may not fully simulate the situation for dry condition at site. Nevertheless, same procedure was applied for both dry and saturated samples to ensure having similar compressive strengths for infilled concrete to be able to obtain comparable side resistance values. The infilled concrete was intentionally selected to have a higher compressive strength than the highest uniaxial compressive strength value obtained for the tested limestone samples in order to ensure the failure of the surface between concrete and rock to be controlled by the side resistance of rock but not by the side cohesion of the concrete as it was also discussed in [21], [22] and [23].

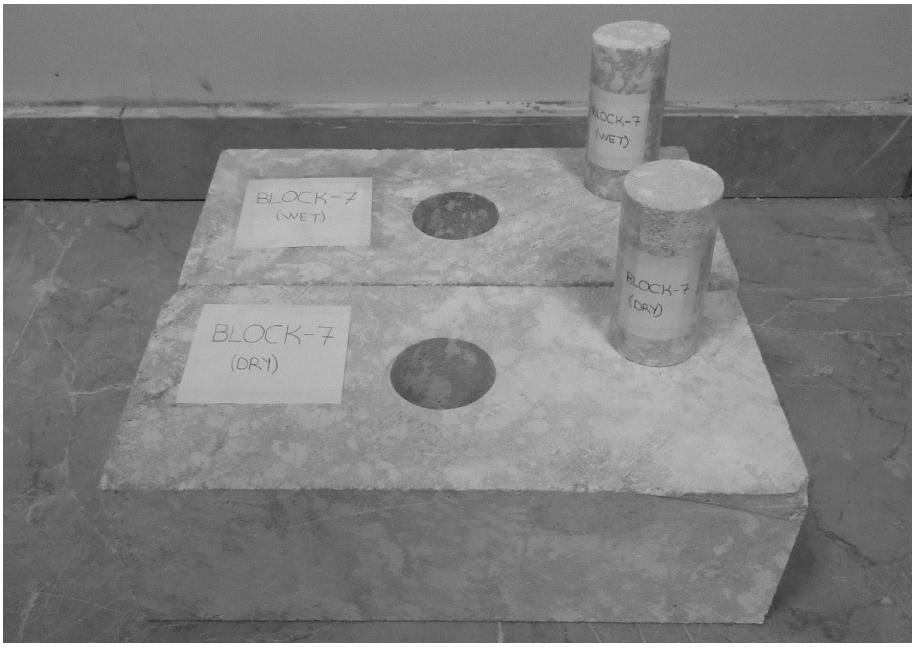

Figure 1 - Adjacent parts of Block-7 and NX size samples taken from the middle

Table 1 - Representative set of measurements for saturation

	1st day	2nd day	3rd day	4th day	5th day	6th day	7th day	8th day
Block	Completely Dry	Saturated Weight (g)						
Block 1	613,87	737,78	740,68	742,51	744,03	744,82	744,82	744,82
Block 2	608,67	730,95	734,42	734,45	734,50	736,56	737,32	737,33
Block 3	752,61	838,65	840,52	840,98	841,57	842,13	842,17	842,18
Block 4	755,25	836,45	838,06	838,82	840,45	840,79	840,87	840,87
Block 5	602,08	726,61	730,10	731,73	732,18	733,96	734,16	734,17
Block 6	597,27	721,57	725,33	726,73	728,08	729,84	730,00	730,00

Since the cylindrical sampler had a side wall thickness of 3.00mm, the diameter of the holes opened to take NX size samples and later infilled with concrete were D_{IC} = 60.7 mm while the heights of the holes were equal to the heights of the blocks (H = 150mm). An unconfined compression testing machine was modified for determination of the unit side resistance of limestone blocks. A circular loading piston having a slightly smaller diameter (D_{LP} = 60mm) than that of the infilled concrete core (D_{IC} = 60.7 mm) was mounted to the loading system to load the concrete core in the rock block axially without any friction. Also, a stiff steel box with a hole in the middle having a diameter slightly wider than that of the concrete core (D_h = 65mm) was put under the block to allow the slip displacement of the concrete cylinder in

the rock block (as illustrated in Figure 2). The steel box had a slightly larger surface (WidthxLength = 170x340mm) than the base of the rock block (WidthxLength = 150x300mm) to prevent any motion of the rock block during testing. The axial loads were recorded by a 100kN capacity load cell with a sensitivity of 0.001%. A displacement-controlled testing procedure was applied during the experiments. In order to determine the suitable displacement rate, tests were conducted on control blocks for both dry and fully saturated conditions for displacement rates changing between 0.001 – 0.1 mm/s. Since the obtained side resistance values were changing within a very narrow band (≈±5%) for the tested displacement rate range, the displacement rate was selected as 0.01 mm/s. This rate was both slow enough to observe the experiment and fast enough to complete it in a reasonable duration. The displacement of the rock block was also measured by a LVDT having 25mm axial displacement capacity. The test setup is presented schematically in Figure 2 and a sample view of the test is given in Figure 3. All experiments were continued after failure, to ensure that the sliding had occurred along the contact surface between limestone and concrete. An example of the observed slip surfaces is given in Figure 4 in which the slipped concrete core from rock block can be clearly seen.

The unit side resistance of each block was determined by dividing the ultimate failure load to the inner surface contact area of each hole at the time of failure. A sample test data is given in Figure 5. As it can be observed from this figure, the applied axial load (F) was recorded with the corresponding slip displacement (Δ) and the unit side resistance was calculated by dividing ultimate load "F" to the inner surface contact area which is defined as the inner surface area of the cylinder in contact with concrete core at the time of failure. For instance, the ultimate load was recorded as F = 13199 N for Δ = 8.635mm slip displacement for the test data presented in Figure 5. For this test, the unit side resistance was calculated in Eq. (3) as:

$$q_s = \frac{F}{\pi x D_{IC} x (H-\Delta)} = \frac{13199}{\pi x 60.7 x (150-8.635)} = 0.49\ MPa \quad (3)$$

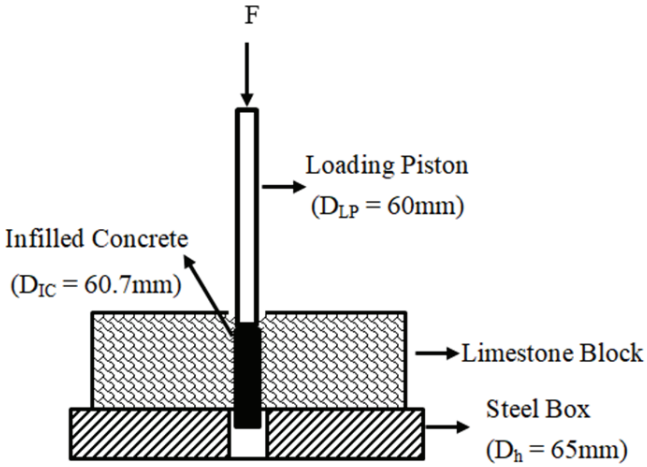

Figure 2 - Schematic cross-sectional view of test setup

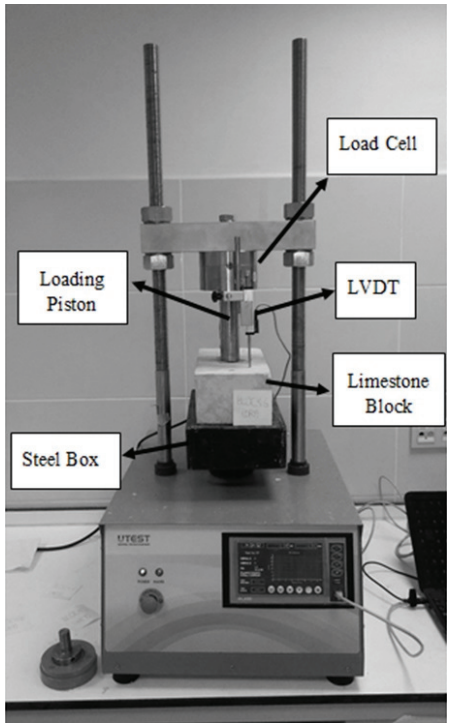

Figure 3 - A sample view of test setup

Figure 4 - A sample view from sliding failure of concrete core

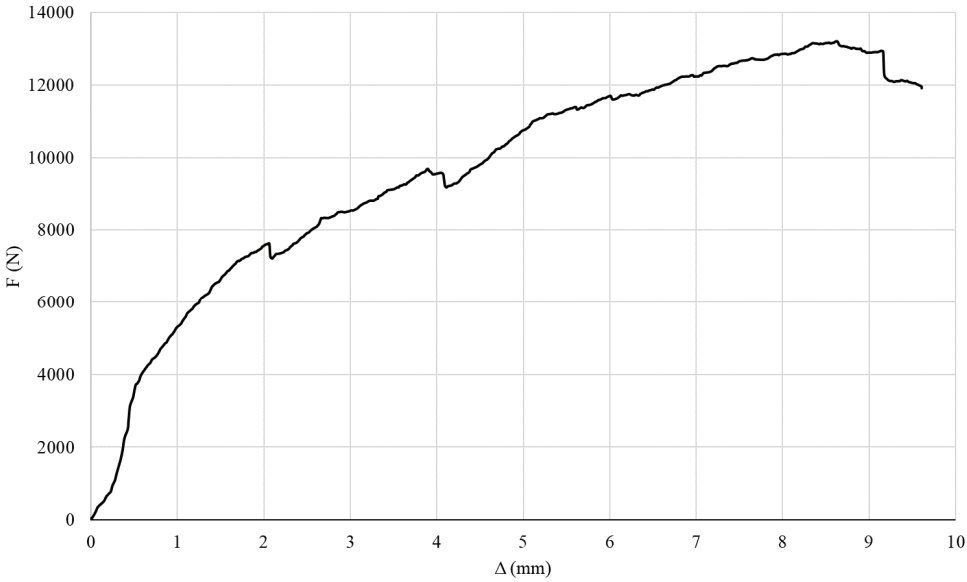

Figure 5 - Sample test data for Block 6 (Fully saturated condition)

3. RESULTS AND DISCUSSIONS

3.1. General Evaluation of the Test Results

The experiments conducted within this study have revealed that the dry unit weights of the samples were changing between γ_{dry} = 16.62 – 21.02 kN/m^3, while the saturated unit weights of the samples were between γ_{sat} = 20.32 – 23.40 kN/m^3. The porosity of the tested samples was in the range of n = 24 – 38% while the water absorption capacity was between w = 11 – 22% by weight. The uniaxial compressive strengths of the dry samples were within the range of σ_c = 15.65 – 22.07 MPa while those of the fully saturated samples were between σ_c = 10.00 – 12.97 MPa. The reduction in the uniaxial compressive strength of Gaziantep limestone between dry and fully saturated conditions was in the range of 36.10 – 42.86%. These results were within a comparable range with the results presented in [17].

The experimental results have revealed that the unit side resistances of the completely dry samples were in between q_s = 0.78 – 1.45 MPa for a rock uniaxial compressive strength range of σ_c = 15.65 – 22.07 MPa. As expected, the unit side resistances of the fully saturated samples were seen to decrease significantly as compared to those of dry samples similar to the behaviour observed for uniaxial compressive strength values. The unit side resistances of the fully saturated samples were varying in the range of q_s = 0.36 – 0.80 MPa for a uniaxial compressive strength interval of σ_c = 10.00 – 12.97 MPa.

While the percent reduction in the uniaxial compressive strength of Gaziantep limestone under fully saturated condition as compared to dry condition was in a narrow band of 36.10

– 42.86%, the percent reduction in the unit side resistance was changing in a wider range (23.96 – 64.23%). This fact was attributed to the variability in the inner surface structure of each tested block. Although all of the holes had a smooth and intact contact surface with concrete core, each had a different inner surface structure due to the chalky, clayey and porous composition of Gaziantep limestone as discussed previously. Hence, the observed side resistance reduction due to saturation was not directly comparable with the approximate 40% reduction in the uniaxial compressive strength of Gaziantep limestone upon saturation, as expected. The results of the uniaxial compression and unit side resistance experiments were summarized in Table 2.

3.2. Discussion of the Results

As explained before, the main aim in this study was to investigate the correlation between the unit side resistance and uniaxial compressive strength of Gaziantep limestone under dry and fully saturated conditions. The relationships given in the literature which correlate the uniaxial compressive strength of rocks (σ_c) with their unit side resistance (q_s) may be divided into two main groups as linear and non-linear relationships as it was briefly discussed in the introduction. In this part of the study, the experimental results were compared with selected linear and non-linear correlations and discussions were made based on these comparisons.

3.2.1. Comparison of Experimental Results with Linear Correlations

The linear correlations suggested by [1-4] were in the general form given in Eq. (1) and the coefficient "A" changed between 0.15 – 0.30 (Table 3). The linear correlations suggested by [1], [2] and [4] were obtained by site measurements on different local rocks (limestone and/or weak rock) while the correlation given by [3] was developed for a design regulation based on a larger database of measurements from different rock sites. It should here be stated that, some of these listed methods may not be originally suggested directly to estimate the unit side resistance of the limestones similar to the ones tested in this study but nevertheless they were included in the evaluations to reveal the overestimation of these linear methods for the studied limestone samples. These linear relationships were plotted on Figure 6, together with the results obtained from this study. As it can be seen on this figure, even the method with the least coefficient [3] significantly overestimated unit side resistance of Gaziantep limestone both for dry and fully saturated conditions. This fact was also reported by [12] for a large database of unit side resistance values obtained from different types of limestones. As an alternative to the proposed methods, a new linear correlation was suggested in this study for estimating the unit side resistance of Gaziantep limestone from its uniaxial compressive strength as given in Eq. (4). As it was also plotted on Figure 6, the proposed correlation yields to an almost unbiased estimation with a correlation coefficient of $R^2 = 0.77$. Additionally, a f-test was conducted to compare measured q_s values with the predicted ones from the suggested regression equation. The test result had revealed that the predicted q_s values had a meaningful correlation with the measured results within 95% confidence interval.

$$q_s = 0.056 x \sigma_c \quad (4)$$

Table 2 - Results of the experimental study

		σ_c (Mpa)	q_s (Mpa)	Reduction in σ_c (%)	Reduction in q_s (%)
Block 1	Dry	18.32	1.45	39.08	44.83
	Saturated	11.16	0.80		
Block 2	Dry	19.29	0.88	39.92	48.86
	Saturated	11.59	0.45		
Block 3	Dry	16.95	1.16	38.05	46.55
	Saturated	10.50	0.62		
Block 4	Dry	16.19	0.78	37.74	53.85
	Saturated	10.08	0.36		
Block 5	Dry	18.12	1.00	38.58	52.00
	Saturated	11.13	0.48		
Block 6	Dry	22.07	1.23	41.23	60.16
	Saturated	12.97	0.49		
Block 7	Dry	20.12	1.01	40.61	38.61
	Saturated	11.95	0.62		
Block 8	Dry	16.55	0.95	39.27	50.53
	Saturated	10.05	0.47		
Block 9	Dry	17.34	0.83	38.58	54.22
	Saturated	10.65	0.38		
Block 10	Dry	18.62	1.03	37.97	36.89
	Saturated	11.55	0.65		
Block 11	Dry	21.78	1.33	41.14	41.35
	Saturated	12.82	0.78		
Block 12	Dry	15.65	0.82	36.10	29.27
	Saturated	10.00	0.58		
Block 13	Dry	17.93	0.96	38.76	23.96
	Saturated	10.98	0.73		
Block 14	Dry	17.33	1.02	38.37	36.27
	Saturated	10.68	0.65		
Block 15	Dry	19.19	1.28	40.28	56.25
	Saturated	11.46	0.56		
Block 16	Dry	16.56	1.03	38.71	61.17
	Saturated	10.15	0.40		
Block 17	Dry	21.21	1.24	42.86	54.84
	Saturated	12.12	0.56		
Block 18	Dry	19.89	1.28	38.01	51.56
	Saturated	12.33	0.62		
Block 19	Dry	17.49	1.10	40.25	56.36
	Saturated	10.45	0.48		
Block 20	Dry	16.71	1.28	37.88	56.25
	Saturated	10.38	0.56		
Block 21	Dry	19.71	1.10	37.95	36.36
	Saturated	12.23	0.70		
Block 22	Dry	18.28	0.92	40.65	43.48
	Saturated	10.85	0.52		
Block 23	Dry	20.25	1.40	39.26	63.57
	Saturated	12.30	0.51		
Block 24	Dry	18,11	1,23	38.10	64.23
	Saturated	11.21	0.44		

Table 3 - Summary of the linear correlations discussed in this study

Correlation	Reference
$q_s = 0.15x\sigma_c$	[3]
$q_s = 0.20x\sigma_c$	[2]
$q_s = 0.25x\sigma_c$	[4]
$q_s = 0.30x\sigma_c$	[1]
$q_s = 0.056x\sigma_c$	This Study

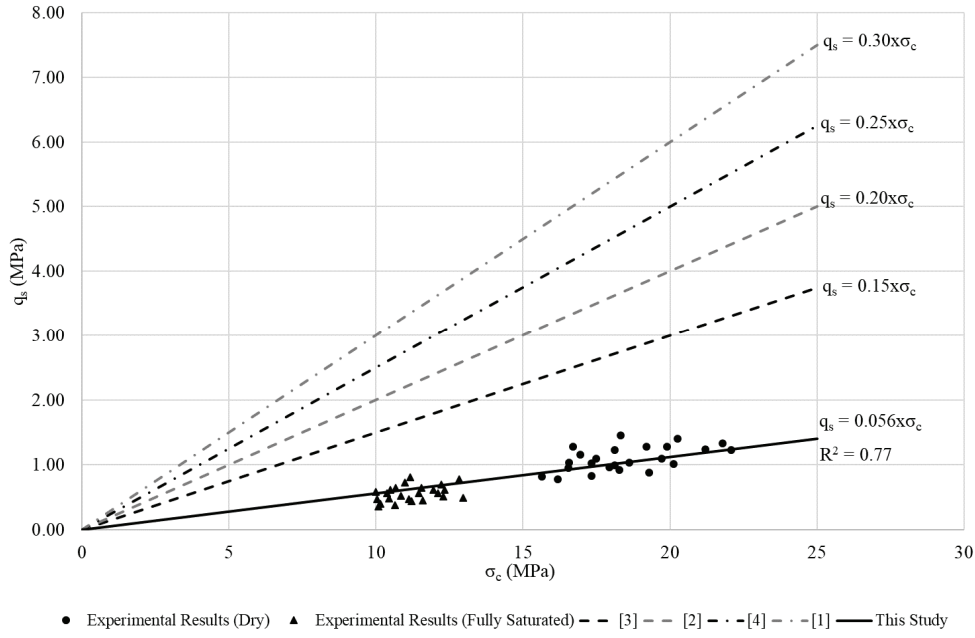

Figure 6 - Comparison of Test Results with Linear Correlations

3.2.2. Comparison of Experimental Results with Non-Linear Correlations

Among the non-linear correlations that may be found in the literature, the results of this study were compared with the methods either suggested by generally accepted standards or with the selected suitable ones during development of which a database containing data from different limestone measurements was utilized. These correlations are summarized in Table 4.

Among the selected correlations, [7] may be evaluated as an early example of such studies based on site experiments. Later, a more sophisticated non-linear correlation was developed by [9] especially for weak rocks by compiling the available literature information for shaft

resistance of rock-socketed piles including the databases collected by [24], [25] and [8]. The correlation suggested by [10] was based on 25 load tests on drilled shafts. In the study of [11], the database which was once compiled by [13] was incorporated by the results of 47 load tests from 13 different limestone sites given by [26] and [27]. The non-linear correlation suggested by [12] was developed based on load test results of 63 rock-socketed piles almost half of which were obtained from limestone sockets.

Table 4 - Summary of the non-linear correlations discussed in this study

Correlation	Reference
$q_s = 0.21x\sqrt{\sigma_c}$ for $\sigma_c > 1.9$ MPa	[28] (After [7])
$\frac{q_s}{Pa} = b(\frac{\sigma_c}{Pa})^{0.5}$ b = 0.63, Pa = Reference Pressure (100 kPa)	[29] Lower bound (After [10])
$\frac{q_s}{Pa} = b(\frac{\sigma_c}{Pa})^{0.5}$ b = 1.41, Pa = Reference Pressure (100 kPa)	[29] Upper bound (After [9])
$\frac{q_s}{Pa} = c(\frac{\sigma_c}{2Pa})^{0.5}$ c = 1 (lower bound), c = 2 (mean), c = 3 (upper bound)	[11]
$q_s = 0.4014x{\sigma_c}^{0.3411}$ (For limestones) $q_s = 0.36x{\sigma_c}^{0.36}$ (For general)	[12]
$q_s = 0.10x\sqrt{\sigma_c}$ (Lower bound) $q_s = 0.25x\sqrt{\sigma_c}$ (Upper bound)	This Study (Fully Saturated)
$q_s = 0.19x\sqrt{\sigma_c}$ (Lower bound) $q_s = 0.35x\sqrt{\sigma_c}$ (Upper bound)	This Study (Dry)

In this manner, the results were firstly compared with the methods suggested in [28] and [29]. For rocks with a uniaxial compressive strength greater than $\sigma_c > 1{,}9$ MPa, the correlation suggested by [7] was recommended by [28] for estimation of unit side resistance from uniaxial compressive strength of rock. On the other hand, the correlations suggested by [10] and [9] were recommended as lower and upper bound values respectively for estimation of unit side resistance in [29]. The test results were compared with these correlations in Figure 7. As it can be seen this figure, the suggestion of [28] and lower bound solution of [29] have given very close solutions. Both methods provided a reasonable lower bound estimation for dry samples. However, the unit side resistances of fully saturated samples were mostly overestimated by these methods.

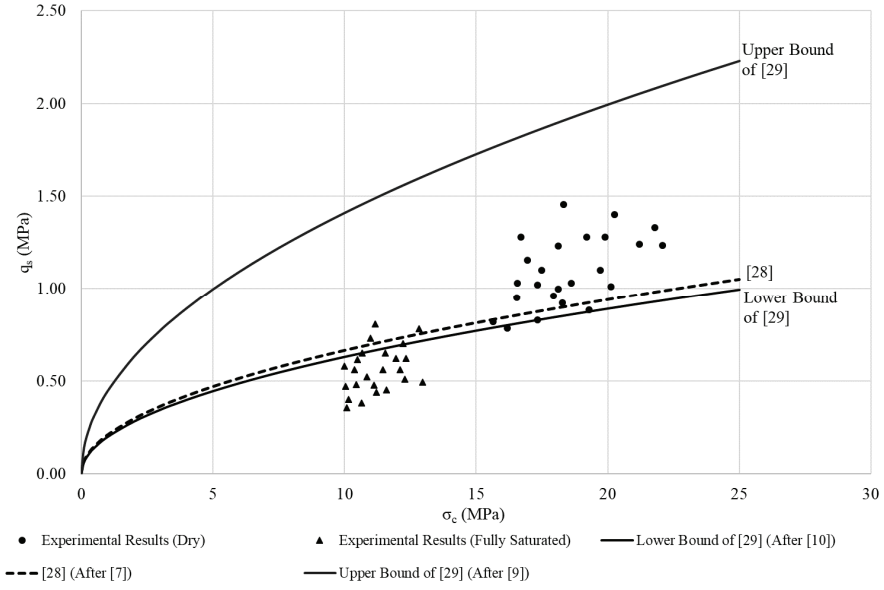

Figure 7 - Comparison of Test Results with [28] and [29]

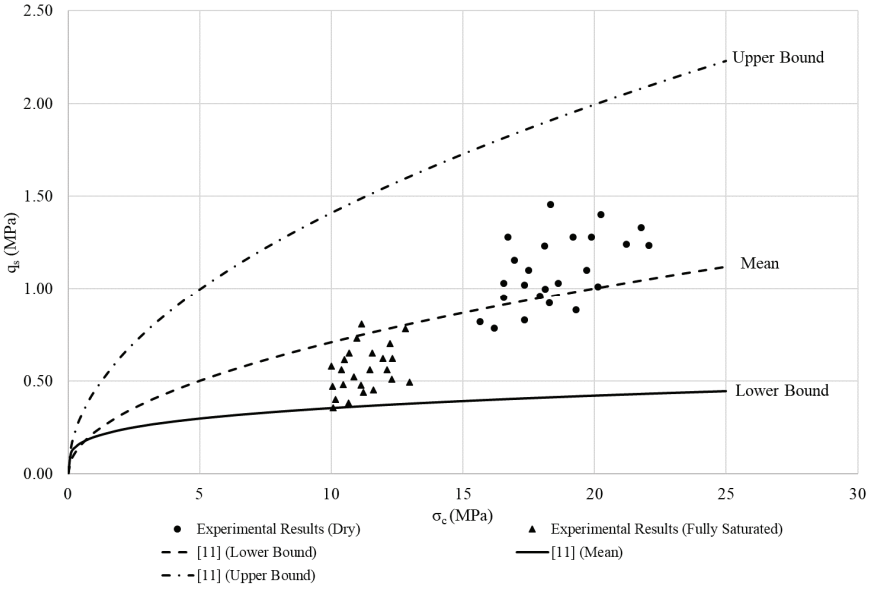

Figure 8 - Comparison of Test Results with [11]

In a more recent correlation suggested by [11] lower bound, mean and upper bound solutions were suggested for estimation of unit side resistance. It should here be noted that the database utilized in the study of [11] contained a significant amount of data obtained from limestones. As it can be observed from Figure 8, the lower bound solution of the method suggested by [11] successfully covered even the lowest data obtained for fully saturated samples of this study. On the other hand, the curve for mean (c = 2) had seemed to provide a more realistic estimation for unit side resistance of dry samples.

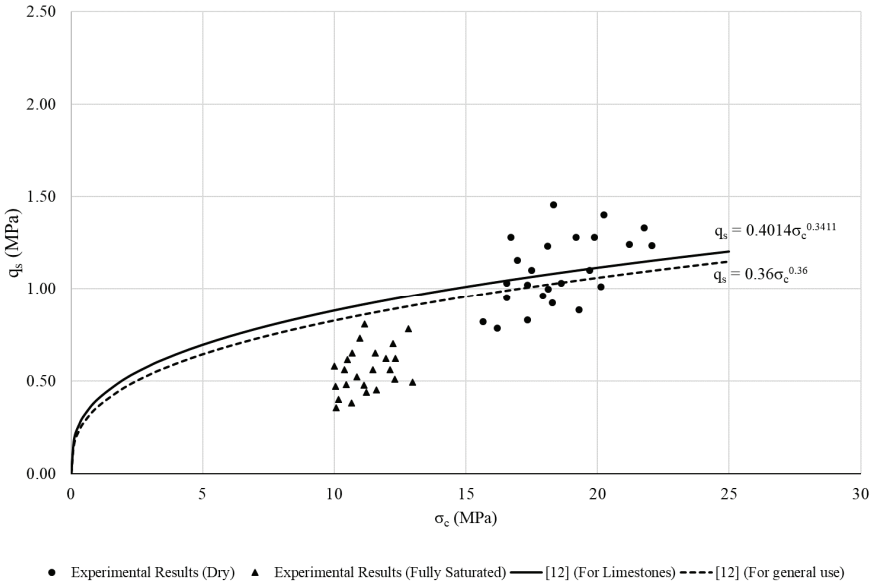

Figure 9 - Comparison of Test Results with [12]

In the study of [12], the side resistance data for various types of rocks obtained from the previous studies of various researchers were analysed in a combined manner and best-fit curves were suggested for different rock types. Among these correlations; the ones suggested for limestones and for general use which were obtained by generating a best-fit to the data only for limestones and to the combined data respectively were utilized for evaluation. Both curves have given a reasonable estimation for unit side resistance under dry conditions as it can be seen in Figure 9. However, the unit side resistance of Gaziantep limestone for fully saturated samples was overestimated by the suggested correlations.

Finally, lower bound and upper bound solutions were suggested as non-linear correlations in this study for fully saturated (Figure 10) and dry conditions (Figure 11), for estimation of the unit side resistance of Gaziantep limestone from its uniaxial compressive strength (see Eq. (5), Eq. (6), Eq. (7) and Eq. (8)).

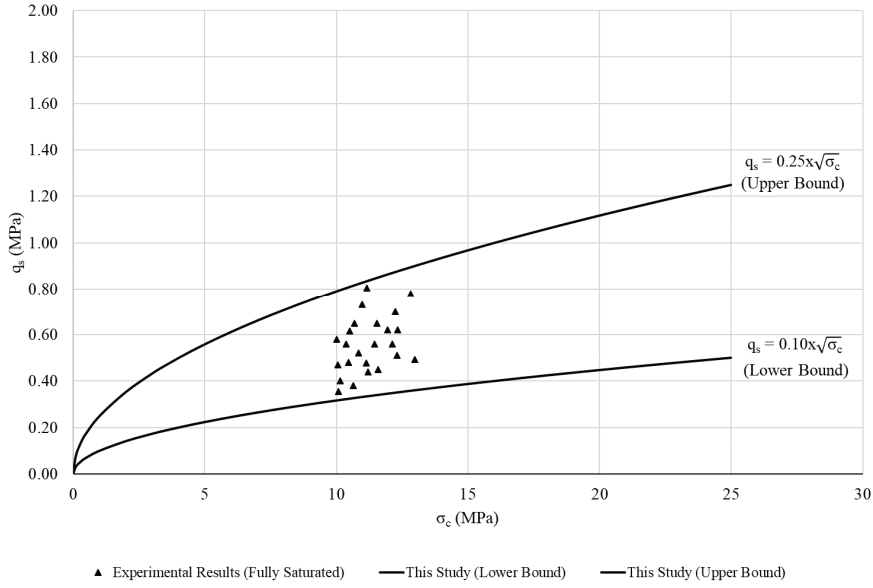

Figure 10 - Lower bound and upper bound curves for Gaziantep Limestone (Fully Saturated)

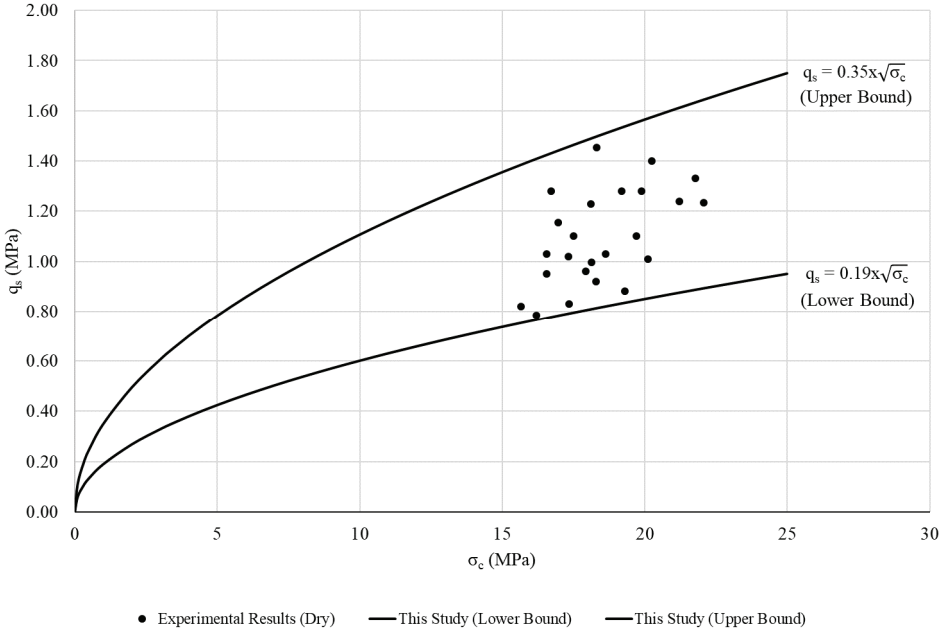

Figure 11 - Lower bound and upper bound curves for Gaziantep Limestone (Dry)

$q_s = 0.10x\sqrt{\sigma_c}$ (Lower bound solution for Gaziantep Limestone, fully saturated condition) (5)

$q_s = 0.25x\sqrt{\sigma_c}$ (Upper bound solution for Gaziantep Limestone, fully saturated condition) (6)

$q_s = 0.19x\sqrt{\sigma_c}$ (Lower bound solution for Gaziantep Limestone, dry condition) (7)

$q_s = 0.35x\sqrt{\sigma_c}$ (Upper bound solution for Gaziantep Limestone, dry condition) (8)

4. CONCLUSIONS

In this study, the unit side resistance of Gaziantep limestone was investigated experimentally under dry and fully saturated conditions and the results were correlated with the unconfined compressive strength of the corresponding test block. In order to conduct the test program, 24 rock blocks were collected from a rock quarry site in Gaziantep. Each block was divided into two adjacent parts to have a fully saturated and dry sample from each block. As a result, 48 uniaxial compression tests and 48 side resistance tests were performed at the soil mechanics laboratory of Hasan Kalyoncu University. The results have revealed that the reduction of the uniaxial compressive strength of Gaziantep limestone upon full saturation was on the order of 36.10 – 42.86 % (≈40%) with respect to the completely dry case. The reduction was also observed for the unit side resistance of Gaziantep limestone upon saturation in a wider range (23.96 – 64.23%).

The unit side resistance value was generally correlated with the uniaxial compressive strength of the corresponding rock in the literature. The methods which recommend a correlation between the unit side resistance and uniaxial compressive strength may be grouped in two broad categories as linear and non-linear correlations. The results of this study were compared with selected linear and non-linear correlations.

The comparison with the linear relationships has revealed that the unit side resistance of Gaziantep limestone was significantly overestimated by the linear correlations for both dry and fully saturated conditions. This fact was also mentioned by other studies conducted on similar rock types. Alternatively, a new linear correlation was suggested for Gaziantep limestone.

The non-linear methods used in the evaluation of the test results of this study have generally provided a reasonable estimation for dry conditions. But these methods, in general, overestimated the unit side resistance values for fully saturated conditions except for the lower bound solution of [11]. Alternatively, non-linear lower and upper bound solutions were suggested in this study as a range for estimating the unit side resistance of Gaziantep limestone for fully saturated and dry conditions.

Based on the findings of this study it may be concluded that the non-linear correlations mentioned in this study were noticeably better in estimating the unit side resistance of Gaziantep limestone as compared to considered linear correlations especially for dry conditions. It should also be emphasized that, since both the uniaxial compressive strength and the unit side resistance of Gaziantep limestone was observed to be significantly reduced

upon saturation and the measured unit side resistance values were generally overestimated even by the non-linear correlations studied in this research for fully saturated conditions, care should be taken while using these correlations for rock socket design in Gaziantep limestone for places prone to saturation. Alternatively; the lower bound solution of [11] may be utilized for design purposes in such cases. Otherwise, the unit side resistance values may be significantly overestimated resulting in an inadequate design.

It should also be noted that, the unit side resistance of rocks is generally measured by large scale load tests. In this study, an unconfined compression testing machine was modified to measure unit side resistance values in laboratory scale. So, the results presented within this study may be regarded as a primary evaluation for the utilized testing equipment and method. Although the test procedure needs to be improved by further studies, the results are evaluated to be promising since the obtained results and trends were comparable by the previous researches. Future studies should be concentrated on improving the testing method which is expected to significantly facilitate measurement of the unit side resistance as compared to large scale load tests since the test is executed in laboratory scale. Although the scale effects are thought to be negligible since the unit side resistance is investigated and neither concrete nor rock is expected to be affected from the utilized sample dimensions, the results may be compared by large scale load tests on the same rock in future studies.

Symbols

A	Linear correlation coefficient
b	Non-linear correlation coefficient
C	Non-linear correlation constant
D	Sample diameter
D_h	Hole diameter
D_{IC}	Infilled concrete core diameter
D_{LP}	Loading piston diameter
F	Axial load
H	Sample height
n	Porosity
q_s	Unit side resistance of rock
w	Water absorption capacity
γ_{dry}	Dry unit weight
γ_{sat}	Saturated unit weight
σ_c	Uniaxial compressive strength of rock
Δ	Slip displacement

References

[1] Kaderabek, T.J., Reynolds, R.T., Miami limestone foundation design and construction. Journal of Geotechnical and Geoenvironmental Engineering, 107, 1981.

[2] Gupton, C., Logan, T., Design guidelines for drilled shafts in weak rocks of south Florida. South Florida Annual ASCE Meeting, Florida, 1984.

[3] Reese, L.C., O'Neill, M.W., Drilled shafts: Construction and design. FHWA, Publication No. HI-88, 42, 1988.

[4] Toh, C.T., Ooi, T.A., Chiu, H.K., Chee, S.K., Ting, W.H., Design parameters for bored piles in a weathered sedimentary formation. Proc. 12th Int. Conf. Soil Mech. Found. Engng 2, Rio de Janeiro, 1989.

[5] Rosenberg, P., Journeaux, N.L., Friction and end bearing tests on bedrock for high capacity socket design. Canadian Geotechnical Journal, 13(3), 324-333, 1976.

[6] Meigh, A.C., Wolski, W., Design parameters for weak rocks. 7th European Conference on Soil Mechanics and Foundation Engineering, Mexico, 1969.

[7] Horvath, R.G., Kenney, T.C., Shaft resistance of rock-socketed drilled piers. Symposium on Deep Foundations, Atlanta, 1979.

[8] Horvath, R.G., Kenney. T.C., Kozicki, P., Methods of improving the performance of drilled piers in weak rock. Canadian Geotechnical Journal 20(4), 758-772, 1983.

[9] Rowe, R.K., Armitage, H.H., The design of piles socketed into weak rock. University of Western Ontario Faculty of Engineering Science, 1984.

[10] Carter, J.P., Kulhawy, F.H., Analysis and design of drilled shaft foundations socketed into rock (No. EPRI-EL-5918). Electric Power Research Inst., Palo Alto, CA (USA); Cornell Univ., Ithaca, NY (USA). Geotechnical Engineering Group, 1988.

[11] Kulhawy, F.H., Phoon, K.K., Drilled shaft side resistance in clay soil to rock. Design and performance of deep foundations: Piles and piers in soil and soft rock, Texas, 1993.

[12] Rezazadeh, S., Eslami, A., Empirical methods for determining shaft bearing capacity of semi-deep foundations socketed in rocks. Journal of Rock Mechanics and Geotechnical Engineering, 9(6), 1140-1151, 2017.

[13] Rowe, R.K., Armitage, H.H., A design method for drilled piers in soft rock. Canadian Geotechnical Journal, 24(1), 126-142, 1987.

[14] O'Neill, M.W., Reese, L.C., Drilled Shafts: Construction Procedures and Design. Report FHWA-IF-99-025, Federal Highway Administration, Virginia, 1999.

[15] Akgüner, C., Kirkit, M., Kayaya Soketli Kazıkların Yükleme Deneyi ve Ampirik Yöntemlerle Belirlenen Kapasitelerinin Karşılaştırılması. Teknik Dergi, 22(109), 5713-5723, 2011.

[16] Marangoz, L., Correlation of geotechnical properties of limestone with ultrasonic pulse velocity in Gaziantep region. M.Sc. thesis submitted to School of Natural and Applied Science, University of Gaziantep, 2005.

[17] Canakci, H., Collapse of caves at shallow depth in Gaziantep city center, Turkey: a case study. Environmental geology, 53(4), 915-922, 2007.

[18] Xie, S. Y., Shao, J. F., Elastoplastic deformation of a porous rock and water interaction. International Journal of Plasticity, 22(12), 2195-2225, 2006.

[19] International Society for Rock Mechanics, The complete ISRM suggested methods for rock characterization, testing and monitoring: 1974-2006. International Soc. for Rock Mechanics, Commission on Testing Methods, 2007.

[20] ASTM C39 / C39M-18, Standard Test Method for Compressive Strength of Cylindrical Concrete Specimens. ASTM International, West Conshohocken, PA, 2018.

[21] Carter, J.P., Kulhawy, F.H., Analysis of laterally loaded shafts in rock. Journal of Geotechnical Engineering, 118(6), 839-855, 1992.

[22] Kulhawy, F.H., Akbas, S.O., Prakoso, W.A., Evaluation of capacity of rock foundation sockets, the 40th US Symposium on Rock Mechanics (USRMS) of American Rock Mechanics Association, Alaska, 2005.

[23] Salgado, R., The engineering of foundations, New York. McGraw-Hill, 2008.

[24] Williams, A.F., Johnston, J.W., Donald, I.B., Design of socketed piled in weak rock. In: Proceedings of international conference on structural foundations on rock, 327-347, 1980.

[25] Williams, A., Pells, P. J. N., Side resistance rock sockets in sandstone, mudstone, and shale. Canadian Geotechnical Journal, 18(4), 502-513, 1981.

[26] Bloomquist, D., Townsend, F. C., Development of insitu equipment for capacity determinations of deep foundations in Florida limestone. University of Florida, Department of Civil Engineering, 1991.

[27] McVay, M. C., Townsend, F. C., Williams, R. C., Design of socketed drilled shafts in limestone. Journal of geotechnical engineering, 118(10), 1626-1637, 1992.

[28] AASHTO, AASHTO LRFD bridge design specifications. Transportation (Amst). American Association of State Highway and Transportation Officials, Inc., Washington, DC, 2007.

[29] CFEM, Canadian foundation engineering manual 4th edition. Canadian Geotechnical Society, 2006.

TECHNICAL NOTE

Teknik Dergi, 2021 11069-11080, Paper 625, ***Technical Note***

Stress Fluctuations in Triaxial Testing of Angular Grains

Aydin OZBAY[1]
Ali Firat CABALAR[2]

ABSTRACT

Stress fluctuations caused by stick-slip instabilities are frequently encountered in laboratory shear testings of granular materials. It is not common to observe stick-slips in angular-shaped granular assemblies, although rounded particles are more prone to this type of behaviour. This paper specifically concerns the deviatoric stress fluctuations in the shearing of coarse angular glass granules. A systematic experimental program comprising triaxial compression tests was realized to investigate the effects of particle size, confining pressure, and strain rate on the stick-slip mechanism. Particle size effect was examined by adopting three separate size distributions. In order to understand the influences of testing conditions on the stress fluctuations, the specimens were tested under four different confining pressures and by applying two distinct strain rates. The results showed that both the particle size and confining pressure greatly affected the stress fluctuations whereas the influence of strain rate was unclear.

Keywords: Stick-slip, stress fluctuation, coarse angular grains, triaxial compression.

1. INTRODUCTION

Unlike many solid materials which exhibit continuum properties, the mechanical response of granular matters depends greatly on the particle characteristics of their constituents. In addition to the gross mass features (e.g., void ratio, relative density), the own properties of the individual particles also affect the behaviour of granular materials. In this respect, influences of the characteristic features of particles such as shape, size, surface roughness, mineralogy, etc. on the global behaviour of the assembly should be well understood to be able to predict the mechanical response of the granular medium. Mechanical behaviour of granular assemblies are also affected by the characteristics of inter-particle load distribution. Actually, the internal force transfer is not homogeneous throughout the granular medium.

Note:
- This paper has been received on June 3, 2019 and accepted for publication by the Editorial Board on January 7, 2020.
- Discussions on this paper will be accepted by September 30, 2021.

• https://doi.org/10.18400/tekderg.573637

1 University of Gaziantep, Civil Engineering Department, Gaziantep, Turkey
aozbay@gantep.edu.tr - https://orcid.org/0000-0002-4376-8330

2 University of Gaziantep, Civil Engineering Department, Gaziantep, Turkey
cabalar@gantep.edu.tr - https://orcid.org/0000-0002-0390-5652

The forces are concentrated around load-bearing contact networks called force chains [1]. There are some strong force chains as well as the weak ones. The alignment of the strong force chains are approximately parallel to the major principal stress direction, whereas the weaker chains are generally diagonal or orthogonal [2]. While the strong force chains dominate the mechanical behaviour of granular medium, the weak force chains usually contribute to the stability of strong ones [3]. In the case of continued loading and insufficient lateral support, the strong force chains may become unstable and be prone to buckling [4]. Domination of the internal forces is shifted between the force chains. As some strong force chains fail as a result of buckling, the load distribution is rearranged among the existing and/or new force chains. At this stage, two types of deformation can be observed within force chain networks depending on the slip mechanism of particles. When the buckling of force chains occurs suddenly, the deformation is defined as stick-slip type. On the contrary, it is said to be a gradual (steady-state) deformation provided that the evolution of force chains is progressive. On the other hand, since the particles are distinct elements and there is no or little cohesion between them, granular materials may exhibit fluid-like behaviour and thus their global stability depends also on the boundary conditions to a large extent. Therefore, the effect of confinement needs to be explored carefully. In brief, the mechanism that governs the response of granular materials under various loading conditions could be defined to have a three-phase structure: (1) particle characteristics, (2) inter-particle force distribution, and (3) boundary conditions. A similar description was made by Sun et al. [3]. They proposed that granular materials are multiscale intrinsically, i.e. microscale (particle size scale), mesoscale (force chains) and macroscale (bulk matter). Actually, both the particle characteristics and the boundary conditions are relatively easy to understand, and also can be controlled. On the other hand, the internal force distribution through the evolution of force chains needs to be observed and analysed thoroughly.

In practice, some assemblages of granular materials such as cohesionless soils are frequently modelled by using the finite element method (FEM) which depends on the continuum mechanical theory. In this method, the granular medium is divided into a finite number of elements (meshes) whose dimensions are obviously different from the actual particle size. On the other hand, the FEM cannot truly model the inter-particle contact mechanics at grain-scale and the evolution of force chain networks [3]. Actually, it can only simulate the boundary conditions to a limited extent. Thus, the FEM is far from describing the mechanical behaviour of granular materials. As an alternative, Cundall [5] introduced a numerical solution called as discrete element method (DEM). Although this method was developed firstly for describing the mechanical behaviour of rock blocks, Cundall and Strack [6] extended the technique to the analysis of granular soils. Over decades, the DEM has been a powerful tool to simulate the mechanics of distinct particles due to its compatibility [7-12]. Fortunately, due to the fast processing capabilities of today's computers, model simulations can be performed more effectively. However, those DEM simulations need to be verified by physical experiments. In the literature, there are numerous experimental studies conducted to have a better understanding on the mechanical behaviour of granular materials [1,13-16]. More specifically, the stick-slip phenomenon has also been studied by many researchers [13,17-19]. Actually, the stick-slip phenomenon occurs in granular materials when particles slide, slip with respect to each other. In some cases, sudden releases of stress followed by gradual increase may be observed during the deformation of granular materials [20]. Stick slip behaviour in granular materials has been investigated by other researchers in many

different disciplines, such as; Thompson and Grest [21], Feder and Feder [22], Demirel and Granick [23], Miller et al., [24], Nasuno et al. [25], Albert et al. [26], Cain et al. [27], Gourdon and Israelachvili [28]. Earlier attempts on the geotechnical engineering were made by Kim [29] and Duchesne [30]. In those studies, some stick-slip type fluctuations in the mechanical response of granular materials were reported. Later on, Adjemian [31] conducted a number of axisymmetric uniaxial compression tests on dry spherical glass beads and also on Huston sand. The stick-slip mechanism was clearly observed in those tests. The results of that study were presented in the paper of Adjemian and Evesque [32]. Stick-slip behaviour of spherical glass beads were also investigated by Alshibli and Roussel [20] and Roussel [33]. They drew some remarkable conclusions on stick-slip load oscillations. In a recent study, Cabalar and Clayton [34] performed undrained triaxial tests on Leighton Buzzard sand and observed instabilities in the stress-strain behaviour in the form of deviatoric stress, axial strain and pore water pressure jumps. Doanh et al. [35] presented the results of another comprehensive testing facility on water-saturated specimens of glass beads. They observed similar fluctuations in deviatoric stress, volumetric strain and excess pore pressure. More recently, Ozbay and Cabalar [36] performed a series of triaxial compression tests on dry spherical glass beads under various loading conditions. They derived some robust conclusions from their experimental investigations.

In the present study, the authors would like to introduce a new experimental work performed on coarse angular granular materials. The paper is mainly focused on stick-slip deformations of dry angular glass granules. A series of triaxial compression tests were realized to investigate the effects of particle size, confining pressure and strain rate on stick-slip behaviour. Three separate particle size distributions were used in the experiments. The specimens of glass granules were tested under four different confining pressures by applying two distinct strain rates.

2. EXPERIMENTAL WORK

2.1. Materials

Coarse angular glass granules having various size distributions were used in the experimental study. The materials were supplied from the glass recycling company Akcihan, Istanbul, Turkey. The glass granules were arranged according to the supplier's designation. Three groups of materials were included in the tests. Some properties and coefficients are presented in Table 1 and Figure 1.

Table 1 - Some physical properties of the glass granules

Material Name	Specific Gravity	D_{10} (mm)	D_{30} (mm)	D_{50} (mm)	D_{60} (mm)	C_U	C_C	USCS Class.	e_{min}	e_{max}
GG1	2.50	0.32	0.50	0.60	0.65	2.03	1.20	SP	0.32	0.51
GG2	2.50	0.76	1.04	1.26	1.36	1.79	1.05	SP	0.56	0.71
GG3	2.50	0.88	1.42	1.79	1.92	2.18	1.19	SP	0.79	0.86

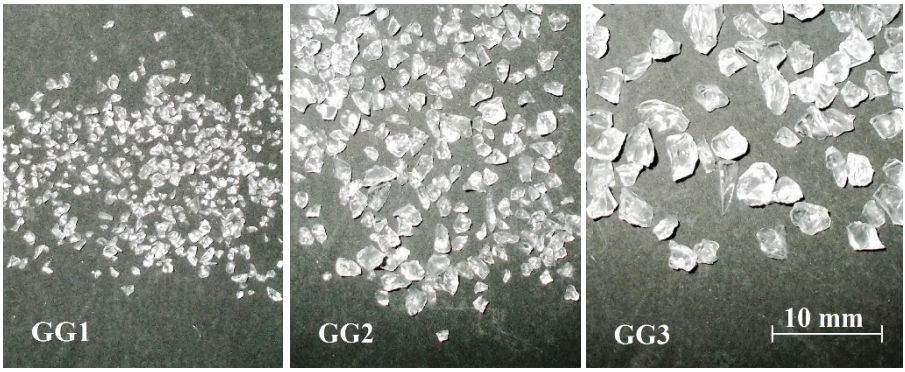

Fig. 1 - Photos of the coarse glass granules

2.2. Preparation of the Specimens

The preparation of the glass granule specimens were made by using a cylindrical split mould originally designed for cohesionless soil materials. The angular glass granules were enclosed by 0.3-mm thick latex membranes at periphery and porous stones at the top and at the bottom. The initial diameter and the height of the cylindrical specimens were 38.2 mm and 77.8 mm, respectively. The specimens were prepared according to the a relative density of about 40%. Dry glass granules within the membrane were sealed by using four O-rings. A small vacuum of nearly -20 kPa was applied to the inside material in order to hold the glass particles together. The negative pressure was maintained by closing the drainage valves. The split mould was removed gently and a plexiglass pressure chamber was placed around the specimen. Then the chamber was filled with de-aired water and subsequently pressurized to a small confining pressure (≈20 kPa). The drainage valves were opened again. The confining pressure was increased to its target value and kept constant during the shearing stage. No saturation was made and the glass granules were left dry throughout the experiments.

2.3. Testing

Stick-slip behaviour of the angular glass granules was investigated by using a conventional triaxial loading device. The specimens of glass granules were sheared under axial compression. The axial load and deformation were acquired by means of linear variable differential transformers (LVDTs) connected to a data logger. The drainage valves were open during the tests. Since the glass granule samples were dry, neither volume change nor pore water pressure measurement was done. Thus, in the calculation of deviatoric stress, the correction of the specimen's cross-sectional area was performed by measuring volume change in the cell water.

Twenty four experiments were performed on the angular glass granules (Table 2). In fact, three particle size distributions (labelled as GG1, GG2 and GG3) were utilized to investigate the effect of particle size. Those materials were tested by applying four different confining pressures (30 kPa, 50 kPa, 70 kPa and 100 kPa) and two distinct loading rates (2 mm/min and 0.2 mm/min). The glass granule specimens were loaded until an axial strain of about 20% was reached.

Table 2 - The details of the tests

Test No	Test ID	Material Type	Confining Pressure	Loading Rate
1	GG1-30F	GG1	30 kPa	2 mm/min
2	GG1-50F	GG1	50 kPa	2 mm/min
3	GG1-70F	GG1	70 kPa	2 mm/min
4	GG1-100F	GG1	100 kPa	2 mm/min
5	GG1-30S	GG1	30 kPa	0.2 mm/min
6	GG1-50S	GG1	50 kPa	0.2 mm/min
7	GG1-70S	GG1	70 kPa	0.2 mm/min
8	GG1-100S	GG1	100 kPa	0.2 mm/min
9	GG2-30F	GG2	30 kPa	2 mm/min
10	GG2-50F	GG2	50 kPa	2 mm/min
11	GG2-70F	GG2	70 kPa	2 mm/min
12	GG2-100F	GG2	100 kPa	2 mm/min
13	GG2-30S	GG2	30 kPa	0.2 mm/min
14	GG2-50S	GG2	50 kPa	0.2 mm/min
15	GG2-70S	GG2	70 kPa	0.2 mm/min
16	GG2-100S	GG2	100 kPa	0.2 mm/min
17	GG3-30F	GG3	30 kPa	2 mm/min
18	GG3-50F	GG3	50 kPa	2 mm/min
19	GG3-70F	GG3	70 kPa	2 mm/min
20	GG3-100F	GG3	100 kPa	2 mm/min
21	GG3-30S	GG3	30 kPa	0.2 mm/min
22	GG3-50S	GG3	50 kPa	0.2 mm/min
23	GG3-70S	GG3	70 kPa	0.2 mm/min
24	GG3-100S	GG3	100 kPa	0.2 mm/min

3. RESULTS AND DISCUSSION

For the purpose of presenting results in a convenient and compact manner, it was preferred to give the graphical outcomes of the experimental study with respect to two of the input parameters namely particle size and loading rate (Figs. 2-7). The figures also include the photos of the failed samples taken at the end of the tests in order to provide a direct inspection of the test results and comparison with the modes of failure. When taking each photo, the most suitable point of view reflecting the details of specimen failure as much as possible was selected.

It is clear from the stress-strain plots that there are a number of load (or stress) fluctuations observed during the axial compression of glass granule specimens. Some of these oscillations were caused by stick-slip failures which exhibit a dynamic character but some others are due to the gradual deformation of the samples. It is postulated that the mechanism observed in the specimens tested could be because of two main reasons, which are (i) the specimens' own material properties, and (ii) any compliance in the apparatus. In the light of the study by Gajo [37], it has been seen that the influence of system compliance on collapse of sand samples needs to be taken into account. Gajo [37] revealed that the compliance of the loading apparatus can deeply affect the onset of dynamic instability. One of the reasons of the fluctuations observed could be the stiffness of the apparatus itself. However, the present specifically focuses on the material properties of the specimens tested, since the apparatus used during the testing of specimens was the same apparatus, which was not thought to produce a series of fluctuations in some tests, while producing a pretty smooth curves in others. It is possible to distinguish the stick-slip deformations from the gradual ones especially in the tests of GG1 granules which have the smallest particle size among the tested materials (Figs. 2 and 3). Because of having a dynamic nature, the stick-slips result in sharp decreases in deviatoric stress [1,23-28]. Actually, fluctuation mechanism observed during the tests may be attributed to the structure of the specimens. It is postulated that the mechanism observed in the specimens tested could be because of (i) higher number of contact points, and (ii) number of open fabric structure in the specimens. The higher number of contact points may be due to the higher confining pressure values in the specimens. It seems to be possible that the grains in the specimen may be held in by interlocking asperities in a tighter packing leading to a mechanism having higher internal friction between the soil particles. Hence, from the study by Luding [38], the authors considered that, during the increase in deviatoric stress, the particles in the shear band of the specimens tested under high confining pressure values do not move (steady-state) as easy as those of the specimens tested at low confining pressure values, where the motion of the particles is allowed more easily (fluctuation), because it is assumed that the applied force exceeds easily a critical threshold force, although, the specimens tested under higher confining pressure do not exhibit any fluctuation in deviatoric stress during testing of the specimen. Just after a slip phase, the deviatoric stress increases again but the increment is decelerating as the stress approaches its previous level [5]. The stick-slip instabilities may be attributed to simultaneous buckling of all strong force chains at a section. It refers to concurrent collapse of a row of particles. However, in the steady-state deformations, the failure of strong force chains are compensated by the formation of some other force chains which are previously weak or not existing. In fact, there is a realignment or rearrangement of force chains without any sudden collapse in a gradual (non-stick-slip) deformation. As observed from the experiments given in this study, the amplitudes of the stick-slip failures are always greater than those of the steady-state deformations (see the photos) [7].

When the effect of particle size distribution is considered, similar trends are seen in the overall stress-strain behaviours of the glass granules having different sizes. Besides, it is shown that, as the particle size increases, the amplitudes of stick-slip deformations decrease generally. However, the amplitudes of stress fluctuations corresponding to gradual deformations increase in this case. As for the frequency of stick-slip jumps, it is observed that the number of stick-slips are greater in larger particles. No consistent relation was found to be between the strain ratio and characteristic of the stick-slip behaviour (amplitude,

frequency) observed in the specimens, although deviatoric stress fluctuations were observed to initiate slightly earlier in the specimens with coarser grains than those in the specimens with finer grains.

As expected, the confining pressure is very effective on the general stress-strain behaviour. Increasing the confining pressure results in higher deviatoric stresses. As a consequence, amplitudes of the stick-slip stress fluctuations increase similarly. However, in some tests, there is no stick-slip failure especially at high confining pressures. For instance, no stick-slip deformation is observed in GG1 glass granules tested under a confining pressure of 100 kPa regardless of the strain rate (Figs. 2 and 3). On the other hand, the confining pressure seems ineffective on the amplitudes of gradual deformations. It is hard to talk about the effect of strain rate on the stress fluctuations since the results are very scattered. However, a limited deduction may be possible for the tests conducted under the confining pressure of 30 kPa. In those tests, the number of stick-slip jumps decreases as the strain rate increases.

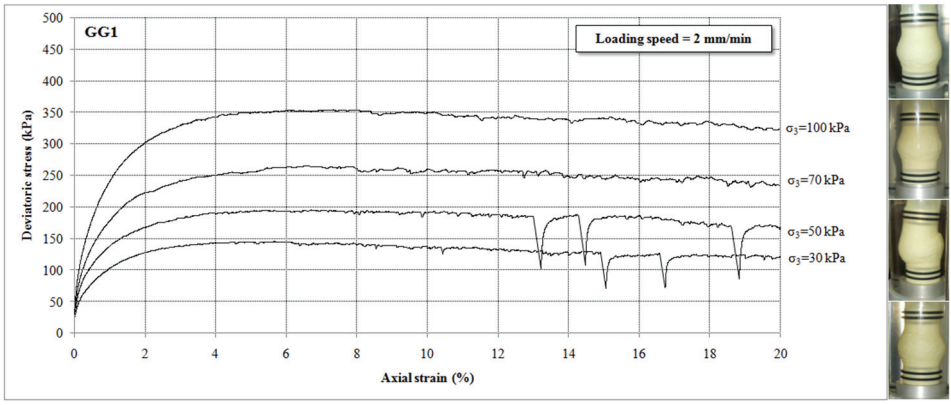

Fig. 2 - GG1 test results for the fast (2 mm/min) loading condition

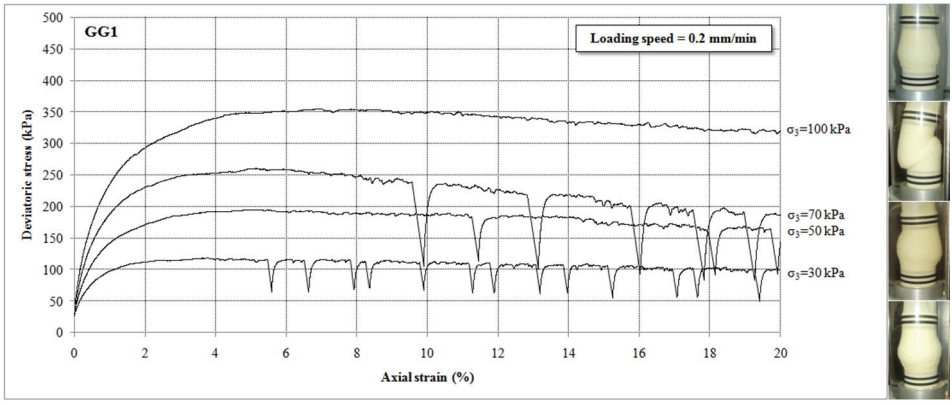

Fig. 3 - GG1 test results for the slow (0.2 mm/min) loading condition

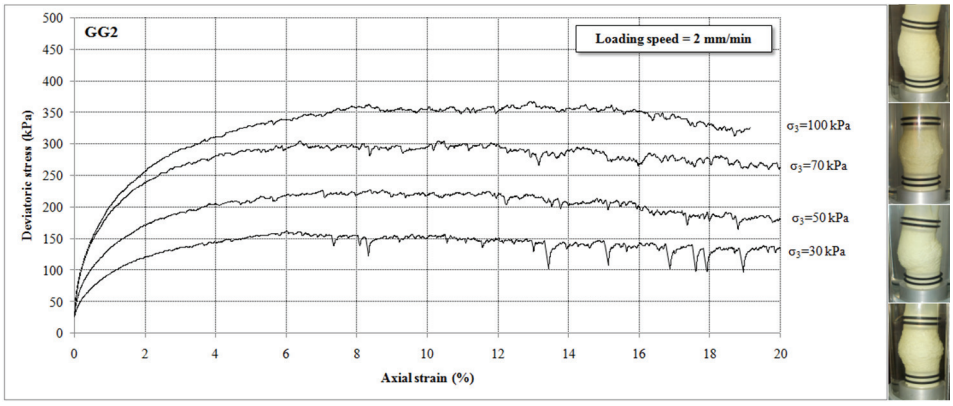

Fig. 4 - GG2 test results for the fast (2 mm/min) loading condition

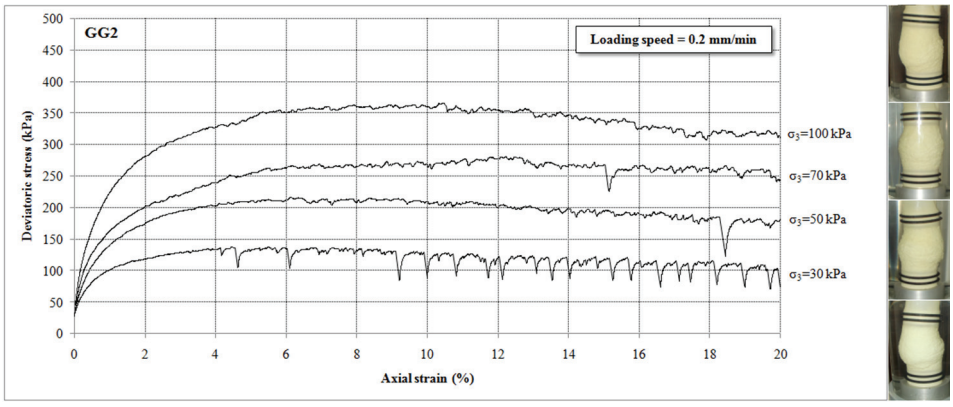

Fig. 5 - GG2 test results for the slow (0.2 mm/min) loading condition

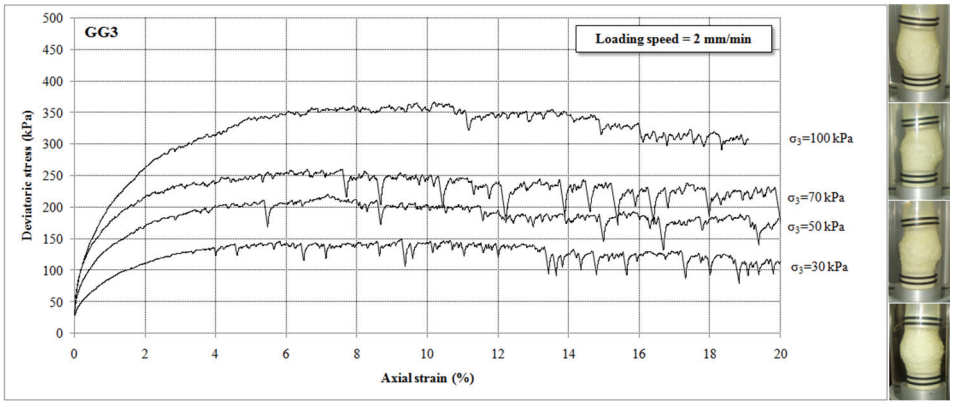

Fig. 6 - GG3 test results for the fast (2 mm/min) loading condition

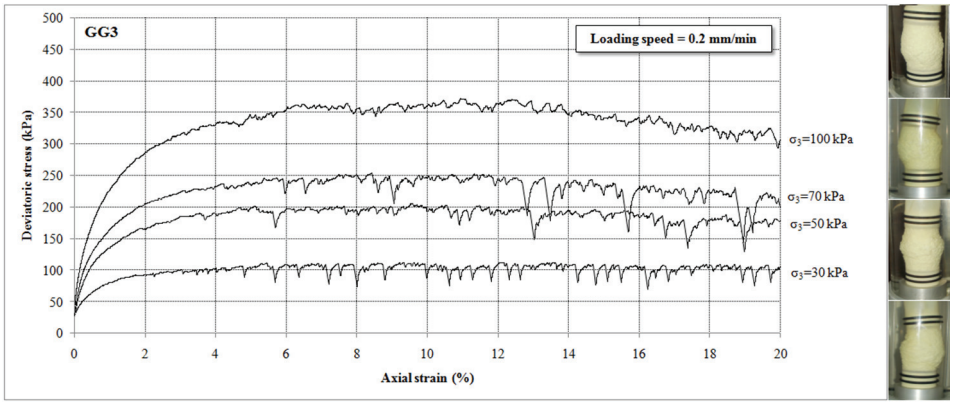

Fig. 7 - GG3 test results for the slow (0.2 mm/min) loading condition

Another factor affecting the amplitudes of stick-slip stress fluctuations is the failure mode of the specimens. In some of the tests, the failure planes developed about horizontally (symmetrical bulging). However, there are also some other tests in which the failure planes are diagonal. It is clear from the photos of the failed specimens that greater fluctuation amplitudes are observed when a diagonal shear band formation is apparent. For example, it is very remarkable in the test GG1-70S (i.e., Material: GG1, Confining pressure: 70 kPa, Loading speed: 0.2 mm/min) (Fig. 2). This could be explained by the redistribution of stresses on the inclined failure plane [12-17]. Diagonal failure causes a variation in the direction of the shear stress, and the axial normal stress contributes to the shear failure. It implies that, as the inclination angle of the failure plane increases, the extent of the slip in a stick-slip type deformation also increases. This led the authors to consider that type of failure (symmetrical bulging, diagonal plane) was governed by either steady-state or stick-slip deformation during testing the specimens, while yielding might be governed by a different criterion (Mises, Tresca).

4. CONCLUSIONS

A number of triaxial compression tests were performed on cylindrical specimens of dry glass granules which contain highly angular particles. The effects of particle size, confining pressure and strain rate on stress fluctuations were investigated. Also failure modes of the specimens were explored in order to relate with the stick-slip amplitudes. The findings of the experimental study are given as follows.

- In all the tests, a number of deviatoric stress fluctuations were observed to some extent. Some of those oscillations were caused by the stick-slip failures and some others by gradual (steady-state) deformations of the glass granule particles. Stress fluctuations corresponding to gradual deformations are existing in all the tests but stick-slip type fluctuations are missing in some cases. The amplitudes of the stick-slip fluctuations in the available tests are greater than those of the gradual fluctuations.

- Particle size distribution of the granular samples were investigated by using three different sizes. It is found that the amplitudes of stick-slip fluctuations decrease with increasing particle size. However, the fluctuation amplitudes caused by the gradual deformations become greater as the particle size increases. In other words, provided that the stick-slips are ignored, the smaller the particles, the smoother the general stress-strain curve. In addition, finer particles have a less frequency of stick-slip jumps.
- It is also concluded that increasing the confining pressure causes the stick-slip fluctuation amplitudes to increase in most samples. It may be attributed to the variation of deviatoric stress. Besides, there is probably no effect of confining pressure on the steady-state deformation amplitudes.
- Since the results are highly scattered, no such correlation could be established between the strain rate and stress fluctuations.
- The results show that the failure mode of the tested specimens is effective on the stick-slip stress oscillations. Although there are horizontal failure planes which are characterized by a symmetric bulging, some of the specimens failed diagonally. Greater stick-slip fluctuation amplitudes were observed in the samples having inclined failure surfaces. It brings about a conclusion that any increase in the inclination angle of the failure plane results in a proportional increase in the value of fluctuation amplitudes.

This suggests that, for the specimen formation in the way employed in the present study, both the particle size and the confining pressure have significant effect on the overall stress-strain behaviour of coarse angular granular materials while the influence of strain rate is unclear.

References

[1] Cabalar, A.F. Stress fluctuations in granular material response during cyclic direct shear test. *Granular Matter*, 17(4), 439-446, 2015.

[2] Hanley, K.J., O'Sullivan, C, Wadee, M.A., and Huang, X. Use of elastic stability analysis to explain the stress-dependent nature of soil strength. *Royal Society Open Science*, 2, 150038, 2015.

[3] Sun, Q., Wang, G., Hu, K. Some open problems in granular matter mechanics. *Progress in Natural Science*, 19, 523-529, 2009.

[4] Tordesillas, A., Walker, D.M., Lin, Q. Force cycles and force chains. *Physical Review E*, 81, 011302, 2010.

[5] Cundall, P.A. A computer model for simulating progressive large-scale movements in blocky rock systems. *Proc. Symp. Int. Soc. Rock Mech.*, Nancy, France, 2 (8), 132-150, 1971.

[6] Cundall, P.A., Strack, O.D.L. A discrete numerical model for granular assemblies. *Geotechnique*, 29 (1), 47-65, 1979.

[7] Antony, S.J., Kuhn, M.R., Barton, D.C., Bland, R. Strength and signature of force networks in axially compacted sphere and non-sphere granular media: micromechanical investigations. *J. Phys. D: Appl. Phys.* 38, 3944-3952, 2005.

[8] Salot, C. Gotteland, P., Villard, P. Influence of relative density on granular materials behavior: DEM simulations of triaxial tests. *Granular Matter*, 11, 221-236, 2009.

[9] Barreto, D., O'Sullivan, C. The influence of inter-particle friction and the intermediate stress ratio on soil response under generalised stress conditions. *Granular Matter,* 14, 505-521, 2012.

[10] Kozicki, J., Tejchman, J., Mühlhaus, H.-B. Discrete simulations of a triaxial compression test for sand by DEM. *Int. J. Numer. Anal. Meth. Geomech.*, 38, 1923-1952, 2014.

[11] Huang, W.-C., Sung, C.-Y., Liao, H.-Y., Chu, S.-S. Micromechanical behavior of granular materials in direct shear modeling. *Journal of the Chinese Institute of Engineers*, 38 (4), 469-480, 2015.

[12] Wang, W., Gu, W., Liu, K. Force chain evolution and force characteristics of shearing granular media in Taylor-Couette geometry by DEM. *Tribology Transactions*, 58, 197-206, 2015.

[13] Rathbun, A.P., Marone, C. Effect of strain localization on frictional behavior of sheared granular materials. *Journal of Geophysical Research*, 115, B01204, 2010.

[14] Cabalar, A.F. The effects of fines on the behaviour of a sand mixture. *Geotech. Geol. Eng.*, 29, 91-100, 2011.

[15] Cabalar, A.F., Dulundu, K., Tuncay, K. Strength of various sands in triaxial and cyclic direct shear tests. *Engineering Geology,* 156, 92-102, 2013.

[16] Benahmed, N., Nguyen, T.K., Hicher, P.Y., Nicolas, M. An experimental investigation into the effects of low plastic fines content on the behaviour of sand/silt mixtures. *European Journal of Environmental and Civil Engineering*, 19 (1), 109-128, 2015.

[17] Brace, W.F., Byerlee, J.D. Stick-slip as a mechanism for earthquakes, *Science*, 153, 990-992, 1966.

[18] Aharonov, E., Sparks, D. Stick-slip motion in simulated granular layers. *J. Geophys. Res.,* 109, B09306, 2004.

[19] Savage, H.M., Marone, C. Effects of shear velocity oscillations on stick-slip behavior in laboratory experiments. *J. Geophys. Res.*, 112, B02301, 2007.

[20] Alshibli, K.A., Roussel, L.E. Experimental investigation of slip-stick behaviour in granular materials. Int. J. Numer. Anal. Meth. Geomech., 30, 1391-1407, 2006.

[21] Thompson, P.A. and Grest, G.S. (1991). Granular flow: Friction and Dilatancy Transition. Physical Review Letters, Vol. 67, No. 13, 1751- 1754.

[22] Feder, H.J., and Feder, J. (1991). Self-organized critically in a stick-slip process. Physical Review Letters, Vol. 66, No. 20, 2669-2672.

[23] Demirel, A.L. and Granick, S. (1996). Friction fluctuations and friction memory in stick-slip motion. Physical Review Letters, Vol. 77, No. 21, 4330- 4333.

[24] Miller, B., O'Hern, C., and Behringer, R.P. (1996). Stress fluctuations for continuously sheared granular materials. Physical Review Letters, Vol. 77, No. 15, 3110- 3113.

[25] Nasuno, S., Kudrolli, A., Bak, A., and Gollub, J.P. (1998). Time-resolved studies of stick-slip friction in sheared granular layers. Physical Review E, Vol. 58, No. 2. 2161-2171.

[26] Albert, I., Tegzes, P., Kahng, B., Albert, R., Sample, J.G., and Pfeifer, M. (2000). Jamming and fluctuations in granular drag. Physical Review Letters, Vol. 84, No. 22, 5122-5125.

[27] Cain, R.G., Page, N.W., and Biggs, S. (2001). Microscopic and macroscopic aspects of stick-slip motion in granular shear. Physical Review E, Vol. 64, 016413.

[28] Gourdon, D. and Israelachvili, J.N. (2003). Transitions between smooth and complex stick-slip sliding of surfaces. Physical Review E, Vol. 68, No. 021602.

[29] Kim, M.S. Etude expérimentale du comportement mécanique des matériaux granulaires sous forte contrainte, Thèse de doctorat, Ecole Centrale Paris, 1995.

[30] Duchesne, A. Etude du comportement mécanique d'un combustible granulaire soumis a des sollicitations d'origine thermique dans un propulseur thermonucléaire spatial. Thèse de doctorat, Ecole Centrale Paris, 1998.

[31] Adjemian, F. Stick-slip et transition de broutage dans les essais triaxiaux sur billes de verre. Thèse de doctorat, Ecole Centrale Paris, 2003.

[32] Adjemian, F., Evesque, P. Experimental study of stick-slip behaviour. *Int. J. Numer. Anal. Meth. Geomech*., 28, 501-530, 2004.

[33] Roussel, L.E. Experimental investigation of stick-slip behavior in granular materials. Master thesis, Louisiana State University, 2005.

[34] Cabalar, A.F., Clayton, C.R.I. Some observations of the effects of pore fluids on the triaxial behaviour of a sand. *Granular Matter*, 12, 87-95, 2010.

[35] Doanh, T., Hoang, M.T., Roux, J.-N., Dequeker, C. Stick-slip behaviour of model granular materials in drained triaxial compression. *Granular Matter*, 15, 1-23, 2013.

[36] Ozbay, A., Cabalar, A.F. Effects of triaxial confining pressure and strain rate on stick-slip behavior of a dry granular material. *Granular Matter*, 18 (3), 60, 2016.

[37] Gajo, A. (2004). The influence of system compliance on collapse of triaxial sand samples. Canadian Geotechnical Journal, Vol. 41, 257- 273.

[38] Luding, S. (2003). The micro-macro mechanics of granular materials. GACM report 2, 22-28.

Teknik Dergi, 2021 11081-11096, Paper 626, ***Technical Note***

Effect of Different Channels on Discharge Coefficient of Labyrinth Weirs

Amir GHADERI[1]
Rasoul DANESHFARAZ[2]
John ABRAHAM[3]
Mohammadamin TORABI[4]

ABSTRACT

In this study, the effect of channel-bed slope and non-prismatic converging channel on the discharge coefficient of labyrinth weirs is numerically investigated utilizing FLOW-3D model. Numerical simulation results show that modifying the labyrinth weir channel through both methods improves the discharge coefficient. Among the selected bed slopes and converging channel wall, the slope of β=4% and angle of θ=10° yielded the highest discharge coefficient. For a ratio H_T/P=0.1, (H_T: flow height, P: weir height) the discharge coefficient and discharge rate for bed slope and convergence angle case were 19.22%, 23.9% and 22.28%, 25.91% higher than for a conventional labyrinth weir in prismatic channel, respectively. Simultaneous application of a bed slope and convergence angle significantly increases the discharge coefficient and discharge value case were 28.64% and 30.42% higher than compared to the conventional case. Therefore, changing the bed slope and wall angle of the weir channel increases the discharge coefficient and in this type of weir and these design alterations should be considered in weir design.

Keywords: Labyrinth weirs, channel bottom slope, converging channel, discharge coefficient, FLOW-3D.

Note:
- This paper has been received on October 3, 2019 and accepted for publication by the Editorial Board on March 2, 2020.
- Discussions on this paper will be accepted by September 30, 2021.
- https://doi.org/10.18400/tekderg.629128

1 University of Zanjan, Department of Civil Engineering, Zanjan, Iran - amir_ghaderi@znu.ac.ir https://orcid.org/0000-0002-8661-6302

2 University of Maragheh, Department of Civil Engineering, Maragheh, Iran - daneshfaraz@yahoo.com https://orcid.org/0000-0003-1012-8342

3 University of St. Thomas, School of Engineering, St Paul, USA - jpabraham@stthomas.edu https://orcid.org/0000-0003-4509-9641

4 Idaho State University, Department of Civil and Environmental Engineering, Pocatello, USA - toramoha@isu.edu - https://orcid.org/0000-0002-5696-4939

1. INTRODUCTION

Most failures in dams occur by water flow passing over the crest. Consequently, the most important factor is the insufficiency of the weir capacity. By increasing the weir crest length or the flow depth, it is possible to control large floods. Since the volume of flow passing through the weir is a function of length and shape of the crest, extensive research has been conducted on the impact of hydraulic and geometric parameters on the discharge coefficient of weirs. One of the most effective ways to increase the weir length is with non-linear designs (such as triangular, trapezoidal, and circular) which are called labyrinth weirs. These types of weirs increase capacity of passive-control spillways and reduce the required upstream head compared to linear weirs.

The majority of studies on labyrinth weirs have been conducted on the triangular and trapezoidal shapes. One of the first study on labyrinth weirs was conducted by Taylor [1]. Hay and Taylor [2] provided a method to calculate the discharge and design labyrinth weirs. Other technical research institutes like the University of Georgia and the Utah Water Research Laboratory (UWRL) conducted more comprehensive studies after 1980. Early empirical studies on these weirs were also conducted by Magalhaes and Lorena [3], Lux and Hinchliff [4] and Tullis, et al. [5]. Melo et al. [6] developed the method of Magalhaes and Lorena (1989) for labyrinth weirs located in a channel with converging walls (Figure 1). They believed that this method could be used to improve the orientation of inlet flow to the weir.

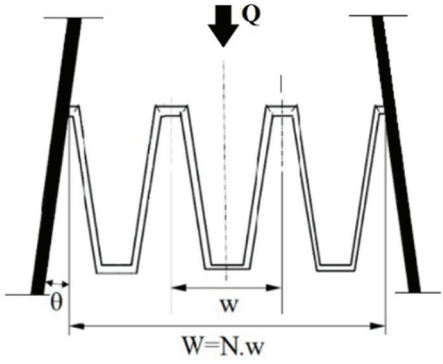

Figure 1 - Labyrinth weir in a channel with converging walls Melo, et al. [6]

In the figure, W is the channel width, N is a number of cycles of the weir, w is the width of each cycle, and θ° is the divergence angle or angle of the channel wall.

The results of Tullis, et al. [7] showed that the angle of weir labyrinth with respect to the main direction of flow affects the discharge of a submerged weir. They also provided relationships for calculating the discharge over submerged labyrinth weirs. Anderson and Tullis [8] used laboratory-scale physical models to compare the hydraulic efficiency of a piano key weir design with that of a geometrically comparable rectangular labyrinth weir. Carollo, et al. [9] provided a relationship using dimensional analysis for the discharge over a triangular labyrinth weir with a sharp edge crest. Khode, et al. [10] provided another family of curves for a wider range of weir sidewall angle, the relationships can be used for designing

labyrinth weirs. Bilhan, et al. [11] experimentally investigated the discharge capacity of labyrinth weirs with and without nappe breakers. They indicated that nappe breakers placed on the trapezoidal labyrinth weirs and circular labyrinth weirs reduced the discharge coefficient by up to 4% compared to an un-amended weir. Numerical methods have been used by various researchers in recent decades [12-17]. Shaghaghian and Sharifi [18] investigated the characteristics of flow in triangular labyrinth weirs using FLUENT. The software was able to accurately simulate flow characteristics in labyrinth weirs. Norouzi et al. [19] Investigation of Discharge Coefficient of Labyrinth Weirs with Quarter-Round Crests using Artificial Neural Networks and Support Vector Machines. The results showed that both artificial intelligent models had better accuracy in estimating C_d.

Despite the above studies, there is still a strong need for fundamental studies on the Geometry and approaching flow field on the hydraulic capacity of Labyrinth weirs and corresponding discharge coefficients. The principal aim of this study is to enhance the understanding of the effect of different channels on the discharge coefficient and discharge rate flow dynamics passing over the labyrinth weirs in a specified width using high-resolution, 3D free surface computational fluid dynamics. The paper starts with theoretical background of the labyrinth weirs, followed by governing equations and description of the numerical modeling. Then, details of the verification of the numerical modeling are presented against the experimental results reported by Crookston [28]. Finally and after ensuring a good agreement between experimental and numerical data, flow characteristics over the labyrinth weirs are described and effects of the effect of channel bed slope and converging channel wall on the hydrodynamics of the labyrinth weir will be analyzed.

2. MATERIALS AND METHODS

2.1. Hydraulic of flow over labyrinth weirs

The general equation for linear weirs, which was adopted by Tullis, et al. [5] for labyrinth weirs, is as follows:

$$Q=\frac{2}{3}\sqrt{2g}\,C_d\,L_c\,H_T^{\frac{3}{2}} \tag{1}$$

Where Q is the discharge over the weir, g is the acceleration due to gravity, and C_d is a dimensionless discharge coefficient. Figure 2 is presented which displays annotations of relevant parameters for a weir.

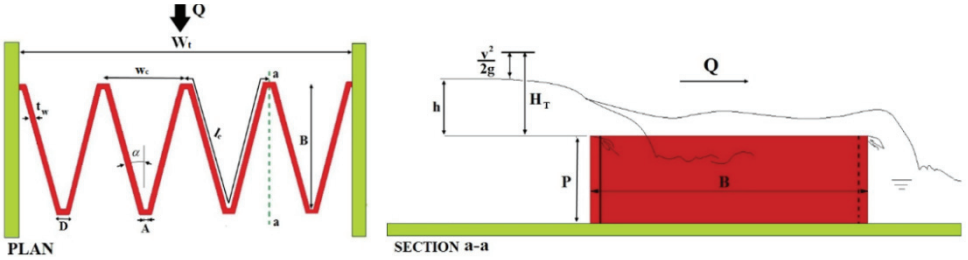

Figure 2 - Parameters effective on hydraulic performance of labyrinth weir

Aided by Figure 2, important parameters for discharge coefficient include the total head on the crest (H_T), the characteristics length of weir (L_c=N×l_c), height of weir (P), width of weir (w), the angle between weir walls (α), the thickness of weir wall (t_w) and depth of flow (y=P+h). After dimensional analysis, discharge coefficient will be obtained as a function of dimensionless parameters.

$$C_d = f\,(H_T, L_c, P, W, \alpha, t_w, y) \tag{2}$$

$$C_d = f\,(\frac{H_T}{p}, \frac{L_c}{P}, \frac{H_T}{W}, \frac{t_w}{W}, \alpha, \frac{y}{P}, \frac{y}{W}, \frac{L_c}{W}) \tag{3}$$

Several researchers have recommended an upper limit of H_T/P for labyrinth weirs based on declining hydraulic efficiency noted in their experimental results [2].

2.2. Governing Equations

FLOW-3D® is a general purpose computational fluid dynamics (CFD) program for modeling a wide variety of fluid flow fluid flow problems [13,20]. It uses the finite volume method to solve the RANS equations (Reynolds Average Navier-Stokes) in a Cartesian, staggered grid. FLOW-3D® uses an advanced algorithm for tracking free-surface flows, TruVOF developed by Hirt and Nichols [22], in which fluid configurations are defined in terms of a VOF function F (x; y; z; t). In one-fluid problems, the air is not treated as a fluid but rather as a void, a region without fluid mass with a uniform reference pressure assigned to it. In this case, F (Fluid Fraction) represents the volume fraction occupied by the fluid: F = 1 in cells completely filled with fluid, and F = 0 in cells with no fluid (void regions) [22, 23-27]. The free surface is located at a position pertaining to intermediate values of F (usually, where F=0.5, but another intermediate value may be defined by the user). The following equations describe the unsteady continuity and momentum equations in the Cartesian coordinates:

$$\frac{\partial U_i}{\partial x_i} = 0 \tag{4}$$

$$\rho\frac{\partial U_i}{\partial t_i} + \rho U_j \frac{\partial U_i}{\partial x_i} = -\frac{\partial P}{\partial x_i} + \frac{\partial}{\partial x_j}(\mu\frac{\partial U_i}{\partial x_j} - \rho u_i' u_j') + \rho g_i \tag{5}$$

In which U_i and are average velocity and fluctuating velocities in the xi direction respectively, x_i = (x,y,z), U_i = (U,V,W), and u_i' =(u′, v′, w′). The symbols ρ, μ, P and g_i are density, dynamic viscosity, pressure, and gravitational acceleration, respectively. Instantaneous velocity is defined as u_i=U_i+u'_i for the three directions.

A turbulence model is necessary in order to account for the nonlinear Reynolds stress terms. In this study, the chosen turbulence model was (RNG)† k-ε, because in Flow Science, Inc. [22] is mentioned that RNG k-ε model has wider applicability than the standard k-ε, and is usually the best choice. In particular, the mentioned turbulence model has been utilized successfully in some similar numerical studies in which the flow over a weir or under a sluice gate is simulated [24-25-26-28-29]. The k-ε (RNG) turbulence model equations are referenced to Yakhot et al. studies [30].

†Re-Normalization Group

2.3. Numerical and Experimental Model

The results of the numerical solution were validated with experimental data of Crookstone [31]. In Table 1, the geometric characteristics of the labyrinth weir are presented.

Table 1 - Geometric characteristics of labyrinth weir, Crookston [31]

Model	α (°)	P(mm)	$L_{c\text{-}cycle}$ (cm)	w/P	N	Crest	Type
Labyrinth weir	15	152.4	99.567	2.008	4	QR	Trap

In this study, the effect of bed slope and converging channel wall on discharge coefficient and discharge rate of labyrinth weir investigated. For this purpose, the slopes of β= 0%, 1%, 2%, 3%, and 4% for the channel bed, and wall converging angles of θ= 0°, 5°, 7.5°, and 10° were used. Figures 3 and 4 shows how the slopes and convergence angles were applied to the labyrinth weir channel.

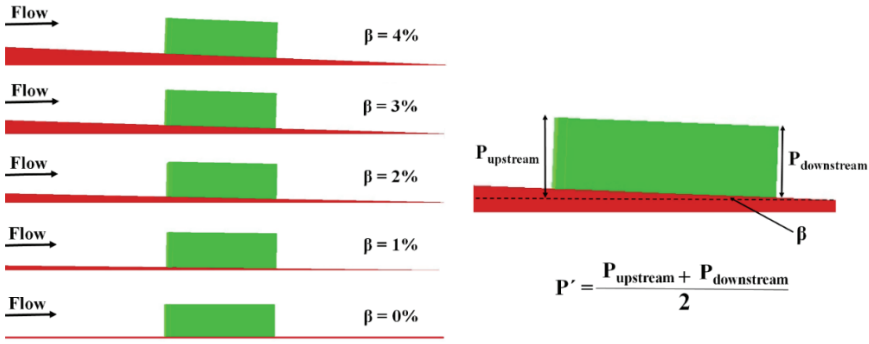

Figure 3 - Application of channel bed slope in the labyrinth weir, β=1%, 2%, 3%, 4%

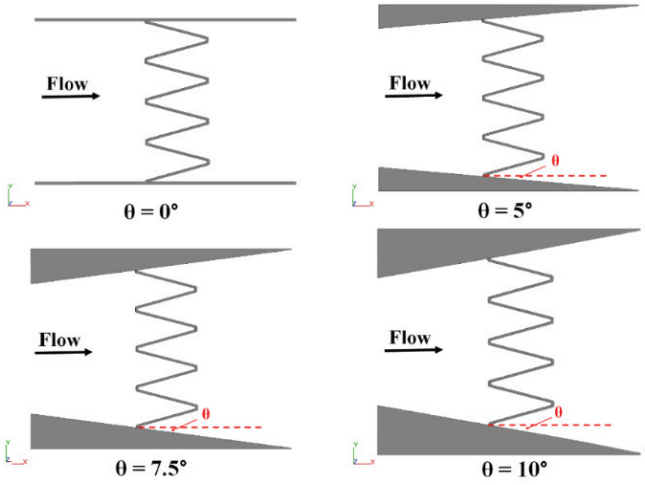

Figure 4 - Application of converging channel wall in the labyrinth weir θ= 0°, 5°, 7.5°, 10°

2.4. Computational Mesh and Boundary Conditions

The weir setup was performed by inserting an STL (sterolithography) file. The computational domain including boundary conditions is shown in Fig. 5. The domain was discretized using one non-uniform mesh block (see figure 6). Considering the geometry dimensions and the estimated values of y+, Several computational meshes were utilized to select the appropriate mesh. According to the sensitivity mesh results, listed in Table 2, and by comparing the discharge coefficients obtained from the numerical solutions with experimental results, four different mesh sizes were used at the vicinity of labyrinth weir.

Table 2 - Mesh Sensitivity analysis

Test NO.	Int. mesh (cm)	Ext. mesh (cm)	Total number of cells	C_d- H_T/P=0.2 in FLOW-3D	C_d- H_T/P=0.2 in Experimental result	*RMSE(-) $\sqrt{\frac{1}{n}\sum_{1}^{n}(X_{exp}-X_{num})^2}$	**MAPE (%) $100\times\frac{1}{n}\sum_{1}^{n}\left\|\frac{X_{exp}-X_{num}}{X_{exp}}\right\|$
T1	2.73	1.64	812547	0.775	0.679	0.096	12.38
T2	2.46	1.24	1465871	0.719	0.679	0.040	5.56
T3	2.12	0.83	1945395	0.686	0.679	0.007	1.02
T4	2.01	0.76	2378594	0.683	0.679	0.004	0.59
Finer meshes				The solution needed higher computational storage.			

*Root Mean Square Error, **Mean Absolute Percentage Error (MAPE)

X_{exp}:The experimental value of X, X_{num}: The numerical value of X, n: Count of data

Based on this mesh-refinement study, the dimensions of the larger elements are 2.12 cm with a count of 547,853 cells. The size of the smaller elements are 0.83 cm with a count of 1,397,542. So in total, 1,945,395 cells were utilized to model the channel. With the selected the appropriate mesh resulting in a relative error and RMSE of 1.02%, 0.007 and maximum aspect ratio 1.23, respectively. In this software maximum aspect ratios in X/Y, X/Z and Y/Z should be less than 4 to simulate flow pattern more precisely. This principle was considered in all runs subsequently [22]. To reduce the effect of computational mesh on simulation results the same mesh was utilized to all models of this research (Figure 5).

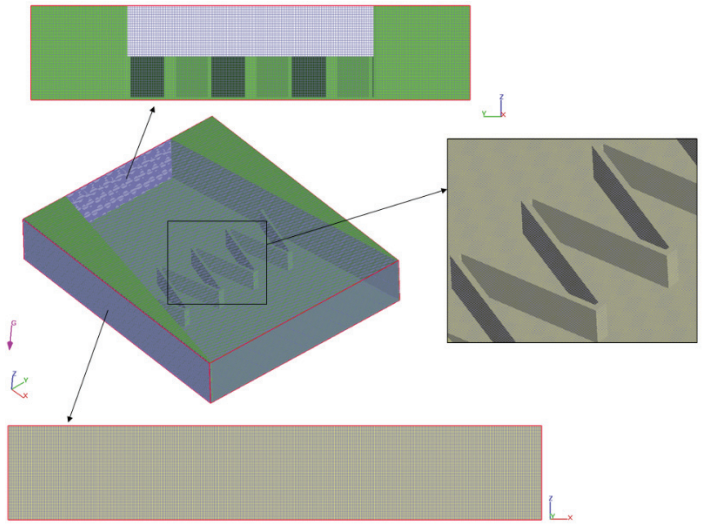

Figure 5 - Meshing in three directions X, Y, Z

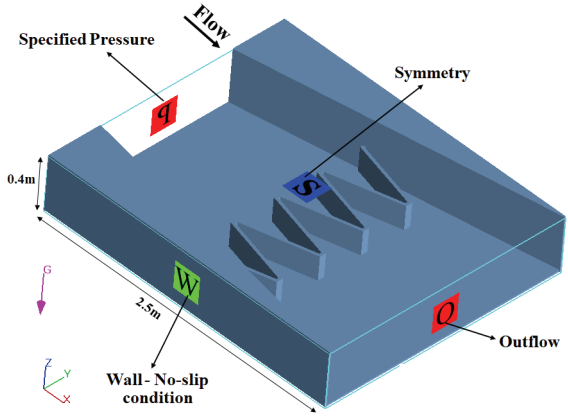

Figure 6 - Applied boundary conditions

The lower Z (Z_{min}) and both of the side boundaries were treated as rigid wall. No-slip conditions were applied at the wall boundaries, and they were treated as non-penetrative boundaries. A law-of-the-wall velocity profile was assumed near the wall, which modifies the wall shear stress magnitude. Symmetry boundary condition is used for the Z_{max} plane, which implies that identical flows occur on the other side of the boundary. In the X_{min} plane, the boundary condition was specified stagnation pressure. With this algorithm, FLOW-3D® is able to model various flow heights beginning at a stagnation pressure state corresponding to the various H_T/P values. The upstream boundary length from the weir was 1.2 m (L~8P) and monitoring of the temporal variations of the water surface elevation at various stations downstream of the inlet boundary showed that this length is sufficient enough for an undisturbed approach flow to be established. The X_{max} boundary which is located adequately far from the weir location has been considered as outflow boundary. The computed steadystate flow rate at this boundary equals the overflow capacity of the weir. Figure 6 are also included; they present the boundary conditions used for the weirs models.

3. RESULTS AND DISCUSSIONS

3.1. Data Verification

A stability criterion similar to the Courant number is used to calculate the allowed time-step size. During the iteration, the time-step size has been controlled by both of the stability and convergence criterion, which leads to time steps between 0.0001 and 0.0013 s. The evolution in time was used as a relaxation to the final steady state. The steady-state condition was checked through monitoring the flow kinetic energy. Furthermore, the flow rate at the outlet boundary and also the free surface elevation at the inlet boundary were monitored during the simulation process. It was found that with 12-s simulation of the flow, the solution becomes fully converged and the steady-state condition is achieved for all of the H_T/P values. The flow over the labyrinth weir is simulated as a steady-state of flow (Figure. 7(A)), and the discharge coefficient of flow is validated with experimental data of Crookston [31]. To ensure a good agreement between the numerical and experimental data, the error was determined and is presented in Figure. 7(B).

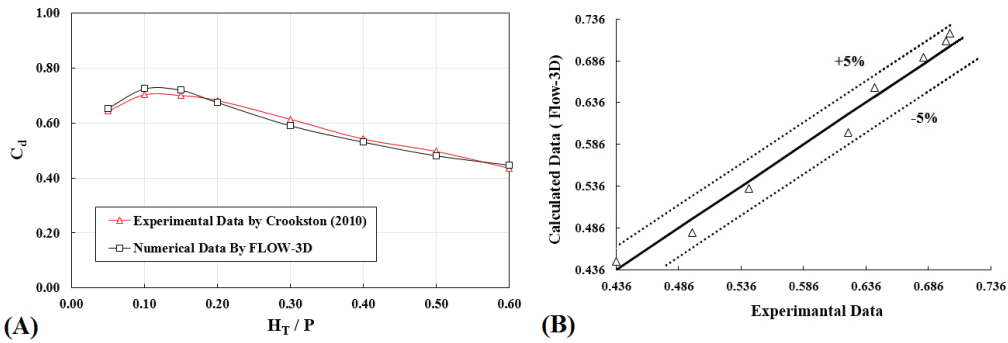

Figure 7 - (A) Comparison of discharge coefficient obtained from numerical solution with experimental data (B) Determination of the percentage of error

It can be observed that changes in discharge coefficient obtained by software are similar to the experimental data with different H_T/P ratio. The discharge coefficient increases for low H_T/P ratio and decreases for high ratios. To compare the results of the discharge coefficient obtained from the FLOW-3D Software with the experimental data, the discharge coefficient error is calculated for different H_T/P ratios according to Eq. 6.

$$E = \frac{(Cd_N - Cd_E)}{Cd_N} \times 100 \tag{6}$$

In Eq. 6, E is the relative error percentage, Cd_N is the discharge coefficient of the weir obtained by numerical solution, and Cd_E is the measured discharge coefficient. The maximum percentage of error for H_T/P=0.6 is 4.6% and the minimum value for H_T/P=0.4 is 3.1%. It can be observed that the relative error is ±5% which indicates a good agreement between the numerical and experimental data.

3.2. Discharge Coefficient of Labyrinth Weir

Flow simulations were performed on the modified weirs using the same turbulence model, boundary conditions, and mesh. Figure 8 shows the water flow profiles over the labyrinth weir by applying bed slope and convergence angle ratio of H_T/P =0.3.

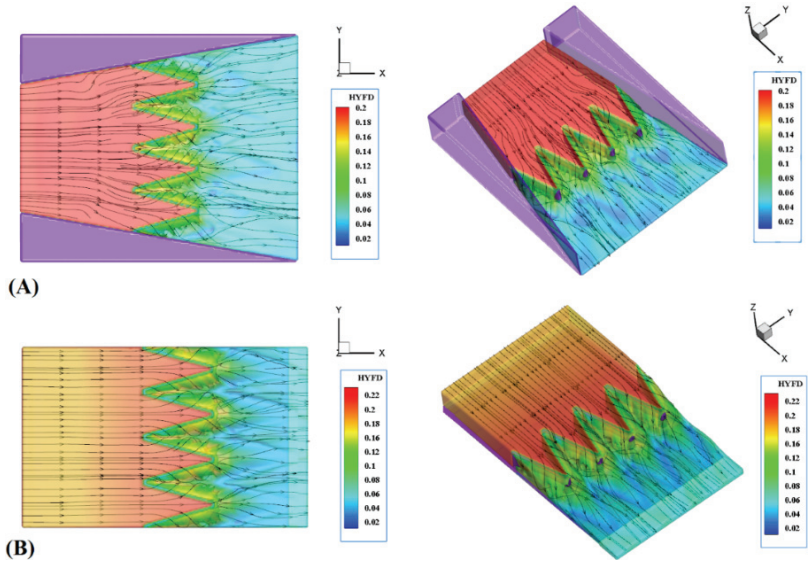

Figure 8 - Water flow profile over adjusted weirs for H_T/P=0.3
(A) Adjusting convergence angle θ=10° (B) Adjusting bed slope β=4%

It is observed that the flow over the weir with the bed slope of β=4% was higher than the one with a converging channel wall of θ=10°, which is due to increased flow velocity through applying bed slope. The discharge coefficients for labyrinth weirs were also calculated after

modifying the channel bed slope and converging channel wall. Figure 9 shows the resulting values.

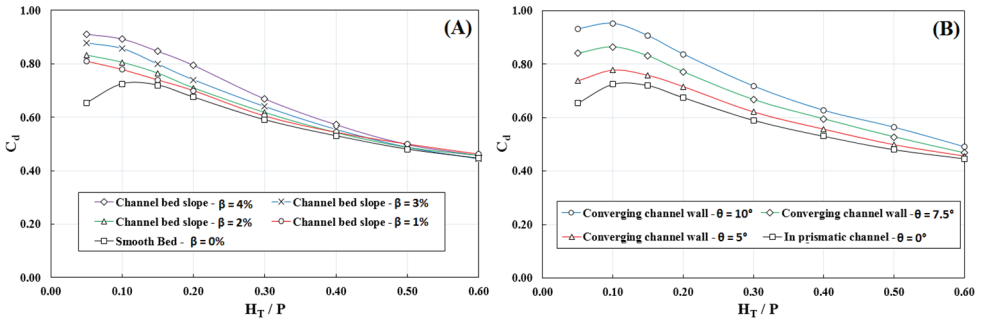

Figure 9 - (A) Discharge coefficient values after modifying channel bed slope, (B) Discharge coefficient values after modifying converging channel wall

Figure 9 indicates that, for a fixed H_T/P ratio, increasing the channel bed slope increases the discharge coefficient values and the difference is significant at low H_T/P ratios. Also for low H_T/P ratios, the discharge coefficients for converging channels exceeds that of prismatic channels. In addition, the discharge increases as the convergence angle increases. The effect is most pronounced at low H_T/P ratios. It should be noted that with an increase in H_T/P ratio, the discharge coefficient values have a decreasing trend which is due to submergence of the weir at higher ratios and increased flow interference. In Figure 10, a subset of results are brought together to show the effects of convergence angle and bed slope in a single figure.

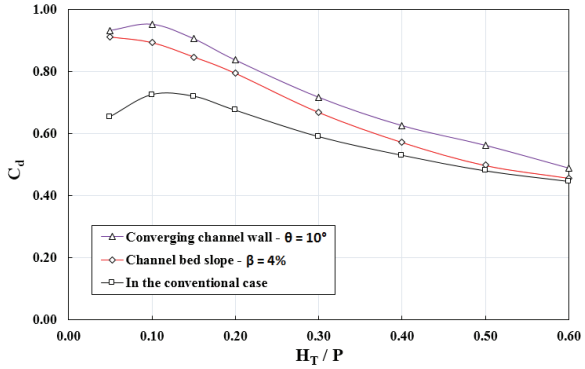

Figure 10 - Comparison of discharge coefficient values in cases with modified geometry and the conventional case

It was observed that, if bed slope and converging channel wall are modified, the discharge coefficient will be greater than the conventional case for all H_T/P ratios. Note that the increases in C_d values are due to the improved the orientation of the flow lines to the labyrinth weir sidewall. This reduces the interference in the flow over the weir especially closer to

perpendicular. Modifying the convergence angle was found to be more effective than the channel bed slope. In $H_T/P = 0.1$, discharge coefficient values for the wall with an angle of $\theta=10°$and bed slope of $\beta=4\%$ were 23.9% and 19.22% higher than the discharge coefficient in the conventional case in prismatic channel, respectively. This difference is reduced by increasing the H_T/P ratio. Figure 11 compares the discharge coefficients for a labyrinth weir with a bed slope of $\beta=4\%$ and convergence angle of $\theta=10°$ with the conventional case.

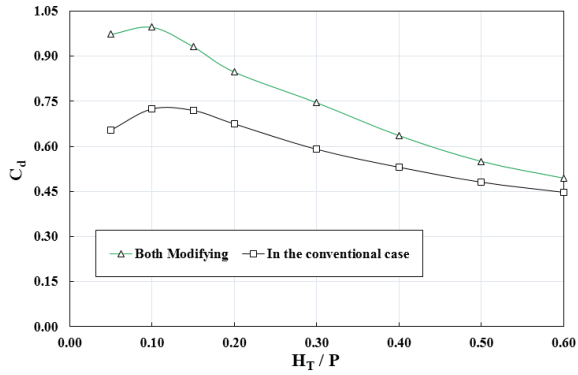

Figure 11 - Comparison of the discharge coefficient values in a case with combined bed slope and converging channel wall and the conventional weir in prismatic channel

It was observed that, for low H_T/P ratios, discharge coefficient values with a bed slope of $\beta=4\%$ and convergence angle of $\theta=10°$ were quite different from the conventional case. In $H_T/P=0.1$, use of both bed-sloping and converging channel wall increased the discharge coefficient by 28.64%.

3.3. Discharge Value of Labyrinth Weir

In labyrinth weirs, unlike linear weirs, streamlines are not perpendicular to the crest and pass the weir in various directions to reduce flow resistance [32]. A weakness of labyrinth weirs is the interference of streamlines due to flow passage over the weir, which decreases the discharge coefficient. Applying convergence angles to the labyrinth weir channel wall improves the flow lines orientation. Figure 12 presents that the flow magnification ratio for labyrinth weirs after modifying the channel bed slope and convergence angle as compared to conventional labyrinth weirs in prismatic channel.

Figure 12 shows that for a fixed H_T/P ratio, increasing the channel bed slope and convergence angle increases the flow magnification ratio as a reagent the discharge rate values. The effect is most pronounced at low H_T/P ratios. Note that a bed slope of $\beta=4\%$ and convergence angle of $\theta=10°$ create the maximum discharge rate for all H_T/P ratios. This figure also shows the submerged weir decreases flow magnification for high H_T/P ratios. Figure 13 shows the flow magnification ratio by applying both modifying bed slope and converging channel wall, $\beta=4\%$ and $\theta=10°$, compared to the conventional labyrinth weir in prismatic channel.

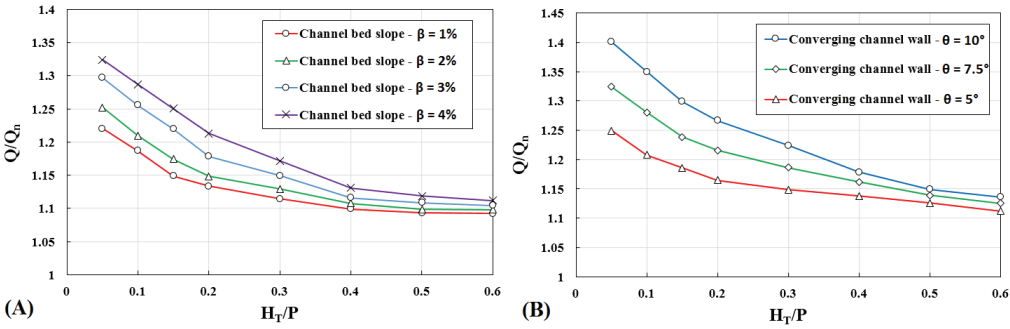

Figure 12 - The flow magnification ratio for H_T/P (A) After modifying the channel bed slope; (B) After modifying converging channel wall

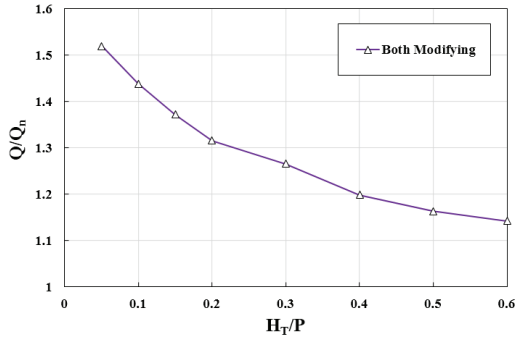

Figure 13 - The flow magnification ratio for H_T/P by simultaneous application of both modifying

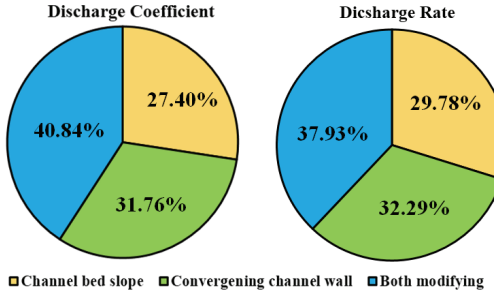

Figure 14 - Averaged contribution percentage of different components in discharge coefficient and discharge rates

The greatest difference between the discharge rates is evident at low H_T/P ratios, so that for example in $H_T/P=0.1$ if both the bed slope and the convergence angle are modified at a same

time, discharge rate can increases 30.42% compared to the conventional case. This can be due to improved flow orientation and, consequently, reduce flow interference while increasing velocity over the weir. According to Figure 14 and by considering all H_T/P ratios in different Channels, averaging the contribution percentage of converging channel wall is greater than the bed slope. There is approximately 4% difference between the two states. Simultaneous application of a bed slope and convergence angle increase the contribution of up to 40.84% and 37.93% in discharge coefficient values and the discharge rates of the flow passing over the labyrinth weir, respectively.

Therefore, the effective role of channel bed slope and converging channel wall for improving the hydraulic performance of labyrinth weirs through increasing the discharge coefficient and discharge rate should be considered in labyrinth weir design.

4. CONCLUSION

This study aimed to the effect of channel-bed slope and non-prismatic converging channel wall on the discharge coefficient of labyrinth weirs. The results of simulating of labyrinth weir adjusted geometry can be summarized as follows:

- The numerical and experimental data were validated; the range of relative error of discharge coefficient was ±5%. This finding indicates a good agreement between the numerical and experimental data.
- For a fixed H_T/P ratio, a bed slope or convergence angle increases the discharge coefficient and discharge value. The increase in discharge coefficient and discharge rate values is more pronounced at higher slopes and convergence angles.
- For = $H_T/P = 0.1$, the discharge coefficient and discharge rate values was 19.22%, 23.9% and 22.28%, 25.91% higher than for the conventional labyrinth weirs in prismatic channel, respectively. The increase is due to improved flow orientation and, consequently, reduced flow interference caused by increased flow velocity over the weir. The effect is smaller for larger H_T/P ratios, this observation is believed to be a consequence of weir submergence.
- Simultaneous application of both modifying significantly increases the discharge coefficient and discharge value compared to the conventional case. This increase, similar to the cases with only one modification, is more evident for low H_T/P ratios for the discharge coefficient and discharge rate. Discharge coefficients and discharge rate increased by 28.64% and 30.42% for $H_T/P = 0.1$, compared to conventional labyrinth weir in prismatic channel, respectively.
- Averaging the contribution percentage of show that converging channel wall is greater than the bed slope. Simultaneous application of a bed slope and convergence angle increase the contribution of up to 40.84% and 37.93% in discharge coefficient values and the discharge rates of the flow passing over the labyrinth weir, respectively.
- Results obtained by adjustment of the channel bed slope and convergence angles and through increasing discharge coefficients of the labyrinth weir agreed with those of Melo, et al. [6]. Placement of weirs inside channels with converging channel walls was one way of improving flow orientation and of increasing discharge passing over the weir.

References

[1] Taylor, G., The performance of labyrinth weirs, PhD thesis. Univ. of Nottingham, U.K.J. 1968.

[2] Hay, N., Taylor, G., Performance and design of labyrinth weirs. ASCE, Journal of Hydraulic Engineering, Vol 96, No 11, 2337-2357, 1970.

[3] Magalhães, A., Lorena, M., Hydraulic design of labyrinth weirs. Report No. 736, National Laboratory of Civil Engineering, Lisbon, Portugal. 1989.

[4] Lux, F., and Hinchliff, D., Design and construction of labyrinth spillways. 15thCongress ICOLD, Vol. IV, Q59-R15, Lausanne, Switzerland, 249-274, 1985.

[5] Tullis, J.P., Nosratollah, A., Waldron, D., Design of labyrinth weirs, ASCE, Journal of Hydraulic Engineering, Vol 121, No 3, 247-255, 1995.

[6] Melo, J., Ramos, C., Magalhaes, A., Descarregadores com soleira em labirinto de um ciclo em canais convergentes. Determinação da capacidad de vazão, Proc. 6° Congresso da Água, Porto, Portugal, in Portuguese. 2002.

[7] Tullis, B., Young, J., Chandler, M., Head-discharge relationships for submerged labyrinth weirs. Journal of Hydraulic Engineering, Vol 133, No 3, 248-254. 2007.

[8] Anderson, R.M., Tullis, B.P., Comparison of piano key and rectangular labyrinth weir hydraulics. ASCE, Journal of Hydraulic Engineering, Vol 138, No 4, 358-361, 2011.

[9] Carollo, G.F, Ferro V., Pampalone, V., Experimental Investigation of the Outflow Process over a Triangular Labyrinth-Weir. ASCE, Journal of Irrigation and Drainage Engineering, Vol 138, No 1, 73-79. 2012.

[10] Khode, BV., Tembhurkar, AR., Porey, PD., Ingle, RN., Experimental Studies on Flow over Labyrinth Weir, Journal of Irrigation and Drainage Engineering, Vol 138, No 6, 548-552, 2012.

[11] Bilhan, O., Emiroglu, M. E., Miller, C.J., Experimental Investigation of Discharge Capacity of Labyrinth Weirs with and without Nappe Breakers. World Journal of Mechanics, Vol 6, 207-221, 2016.

[12] Daneshfaraz, R., Ghahramanzadeh, A., Ghaderi, A., Joudi, A. R., Abraham, J., Investigation of the Effect of Edge Shape on Characteristics of Flow under Vertical Gates, Journal-American Water Works Association, Vol 108, No 8, 425-432, 2016.

[13] Ghaderi, A., Dasineh, M., Abbasi, S., Abraham, J., Investigation of trapezoidal sharp-crested side weir discharge coefficients under subcritical flow regimes using CFD, Applied Water Science, Vol 10, No 1, 31, 2020

[14] Savage, B., Frizell, K., Crowder, J., Brian versus brawn: The changing world of hydraulic model studies. Proc. of the ASDSO Annual Conference, Phoenix, Ariz., CD-ROM, 2004.

[15] Daneshfaraz, R., Joudi, A. R., Ghahramanzadeh, A., Ghaderi, A., Investigation of flow pressure distribution over a stepped weir, Advances and Applications in Fluid Mechanics, Vol 19, No 4, 811, 2016.

[16] Daneshfaraz, R., Minaei, O., Abraham, J., Dadashi, S., Ghaderi, A., 3-D Numerical simulation of water flow over a broad-crested weir with openings, ISH Journal of Hydraulic Engineering, 1-9, 2019.

[17] Dabling, M.R., Tullis, B.P., Modifying the downstream hydrograph with staged labyrinth weirs. Journal of Applied Water Engineering and Research, Vol 6, No3, 183-190. 2018).

[18] Shaghaghian, M.R., Sharifi, M.T., Numerical modeling of sharp-crested triangular plan form weirs using FLUENT. Indian Journal of Science and Technology, Vol 8, No, 34, 1-7. 2015.

[19] Norouzi, R., Daneshfaraz, R., Ghaderi, A., Investigation of discharge coefficient of trapezoidal labyrinth weirs using artificial neural networks and support vector machines. Applied Water Science, Vol 9, No 7, 148. 2019.

[20] Daneshfaraz, R., Ghaderi, A., Ghahremanzadeh, A. An analysis of flowing pattern around T-shaped Spur Dike at 90 Arc, based on Fluent and Flow-3D Models. International Bulletin of Water Resources and Development, Vol 3, No 3, 1-9. 2015.

[21] Hirt, C. W. and Nichols, B. D., Volume of Fluid (VOF) method for the dynamics of free boundaries. Journal of Computational Physics, 39:201–225, 1981.

[22] Flow Science, Inc. FLOW-3D User Manual. Version 11.0.3, Santa Fe, New Mexico, USA, 2014.

[23] Ghaderi, A., Abbasi, S. CFD simulation of local scouring around airfoil-shaped bridge piers with and without collar. Sādhanā, Vol 44, No, 10, 216, 2019.

[24] Zahabi, H., Torabi, M., Alamatian, E., Bahiraei, M., Goodarzi, M. Effects of Geometry and Hydraulic Characteristics of Shallow Reservoirs on Sediment Entrapment. Water, Vol 10, No 12, 1725, 2018.

[25] Seo, I.W., Do Kim Y., Park Y.S., Song C.G., Weir discharges by modification of weir shapes and overflow surroundings, Environmental Earth Sciences, Vol 75, No 6, 496, 2016.

[26] Daneshfaraz, R., Ghaderi, A., Numerical Investigation of Inverse Curvature Ogee Weir, Civil Engineering Journal, Vol 3, No 11, 1146-1156, 2017.

[27] Daneshfaraz, R., Sadeghfam, S., Ghahramanzadeh, A., Three-dimensional numerical investigation of flow through screens as energy dissipators. Canadian Journal of Civil Engineering, Vol 44, No 10, 850-859, 2017.

[28] Ghaderi, A., Dasineh, M., Daneshfaraz, R., Abraham, J., Reply to the discussion on paper: 3-D numerical simulation of water flow over a broad-crested weir with openings by Daneshfaraz et al., 2019, in ISH journal of hydraulic engineering, DOI: 10.1080/09715010.2019. 1581098. ISH Journal of Hydraulic Engineering, 1-3, 2020.

[29] Ghaderi, A., Abbasi, S., Abraham, J., Azamathulla, H.M., Efficiency of trapezoidal labyrinth shaped stepped spillways. Flow Measurement and Instrumentation, 101711, 2020.

[30] Yakhot, V., Orszag, S.A., Thangam, S., Gatski, T.B., Speziale, C.G., Development of turbulence models for shear flows by a double expansion technique, Physics of Fluids A: Fluid Dynamics, Vol 4, No 7, 1510-1520, 1992.

[31] Crookston, BM., Labyrinth Weirs. PhD thesis, Utah State University, Logan, Utah, 2010.

[32] Indlekofer, H., Rouve, G., Discharge over polygonal weirs. ASCE, Journal of Hydraulic Engineering, Vol 101, No 3, 385- 401, 1995.

TEKNİK DERGİ MANUSCRIPT DRAFTING RULES

1. The whole manuscript (text, charts, equations, drawings etc.) should be arranged in Word and submitted in ready to print format. The article should be typed on A4 (210 x 297 mm) size paper using 10 pt (main title 15 pt) Times New Roman font, single spacing. Margins should be 40 mm on the left and right sides and 52.5 mm at the top and bottom of the page.
2. Including drawings and tables, articles should not exceed 25 pages, technical notes 10 pages.
3. Your contributed manuscript must be sent over the DergiPark system. (http://dergipark.gov.tr/tekderg)
4. The text must be written in a clear and understandable language, conform to the grammar rules. Third singular person and passive tense must be used, and no inverted sentences should be contained.
5. Title must be short (10 words maximum) and clear, and reflect the content of the paper.
6. Sections should be arranged as: (i) abstract and keywords, (ii) title, abstract and keywords in the other language, (iii) main text, (iv) symbols, (v) acknowledgements (if required) and (vi) references.
7. Both abstracts should briefly describe the object, scope, method and conclusions of the work and should not exceed 100 words. If necessary, abstracts may be re-written without consulting the author. At least three keywords must be given. Titles, abstracts and keywords must be fitted in the first page leaving ten line space at the bottom of the first page and the main text must start in the second page.
8. Section and sub-section titles must be numbered complying with the standard TS1212.
9. Symbols must conform to the international rules; each symbol must be defined where it appears first, additionally, a list of symbols must be given in alphabetic order (first Latin, then Greek alphabets) at the end of the text (before References).
10. Equations must be numbered and these numbers must be shown in brackets at the end of the line.
11. Tables, drawings and photographs must be placed inside the text, each one should have a number and title and titles should be written above the tables and below the drawings and photographs.
12. Only SI units must be used in the manuscripts.
13. Quotes must be given in inverted commas and the source must be indicated with a reference number.
14. Acknowledgement must be short and mention the people/ institutions contributed or assisted the study.
15. References must be numbered (in brackets) in the text referring to the reference list arranged in the order of appearance in the text. References must include the following information:

    If the reference is an article: Author's surname, his/her initials, other authors, full title of the article, name of the journal, volume, issue, starting and ending pages, year of publication.

    Example : Naghdi, P. M., Kalnins, A., On Vibrations of Elastic Spherical Shells. J. Appl. Mech., 29, 65-72, 1962.

    If the reference is a book: Author's surname, his/her initials, other authors, title of the book, volume number, editor if available, place of publication, year of publication.

    Example : Kraus. H., Thin Elastic Shells, New York. Wiley, 1967.

    If the reference is a conference paper: Author's surname, his/her initials, other authors, title of the paper, title of the conference, location and year.

    If the source is a thesis: Author's surname, his/her initials, thesis title, level, university, year.

    If the source is a report: Author's surname, his/her initials, other authors, title of the report, type, number, institution it is submitted to, publication place, year.
16. Discussions to an article published in Teknik Dergi should not exceed two pages, must briefly express the addressed points, must criticize the content, not the author and must be written in a polite language. Authors' closing remarks must also follow the above rules.
17. A separate note should accompany the manuscript. The note should include, (i) authors' names, business and home addresses and phone numbers, (ii) brief resumes of the authors and (iii) a statement "I declare in honesty that this article is the product of a genuinely original study and that a similar version of the article has not been previously published anywhere else" signed by all authors.
18. Copyright has to be transferred to UCTEA Turkish Chamber of Civil Engineers. The standard copyright form signed by the authorised author should therefore be submitted together with the manuscript.

CONTENTS

ISSN: 1300-3453